UNIVERSITE D'AIX-MARSEILLE

ED 352 PHYSIQUE ET SCIENCES DE LA MATIÈRE

FACULTÉ DES SCIENCES
Laboratoire d'accueil :
UMR7345 - Physique des Interactions Ioniques et Moléculaires

Thèse présentée pour obtenir le grade universitaire de docteur
Discipline : Energie, Rayonnement et Plasma

Roba MOUSSAOUI

Study of negative ion surface production in cesium-free H_2 and D_2 plasmas

Soutenue le 19 octobre 2018 devant le jury composé de :

Anne lise THOMANN	GREMI, Orléans Université	DR, Rapporteur
Olivier GUAITELLA	LPP, Ecole polytechnique	HDR, Rapporteur
Caroline CHAMPENOIS	PIIM, Marseille Université	CR, Examinateur
Emilie Despiau-Pujo	LTM, Joseph Fourrier Université	MC, Examinateur
Mamiko SASAO	Doshisha Université, Kyoto	Pofesseur, Examinateur
Gilles CARTRY	PIIM, Aix Marseille Université	Professeur, Directeur de thèse

Acknowledgements

A ma mère Fatima, à mon père Zaki, à mon chérie Mohamad, à mes sœurs Marwa et Sara et mes frères : Mohamad, Ibrahim et Sayed Hassan, à mes amis : Hiba, Alaa, Labelle, Marwa et Zahraa.

Ce travail a été effectué dans le groupe Plasma Surface du laboratoire PIIM de l'Université d'Aix-Marseille dont je remercie le Directeur le Professeur Jean-Marc LAYET pour m'avoir accueilli au sein de cette équipe et de ce laboratoire exemplaires.

Ensuite, je remercie grandement mon directeur de thèse le Professeur Gilles CARTRY pour avoir été toujours à l'écoute de mes besoins et pour les discussions intéressantes et importantes.

Je remercie tous les membres de mon jury pour avoir accepté de juger mon travail, particulièrement Anne lise THOMANN and Olivier Guiatella pour avoir accepté d'en être les rapporteurs.

Un grand merci aux tout les collègues qui m'ont aidé à réaliser ce travail et en particulier Dr. Dmitry KOGUT pour ces conseils précieux, discussions nombreuses et son aide. Je voudrais aussi remercier toutes les membres de l'équipe Plasma Surface avec lesquels j'ai travaillé ou collaboré .

Je tiens à remercier également les chercheurs engagées en collaboration avec nous pendant ma thèse en particulière des autres équipes du PIIM surtout Cédric PARDANAUD et les chercheurs de Doshisha université surtout le Professeur Mamiko SASAO.

Un remerciement cordial à l'atelier mécanique en particulier à Jean-Bernard FAURE ainsi qu' a Remy RIGARD-CERISON qui ont assuré le fonctionnement des manips, les réparations et le développement. Je remercie aussi les membres de l'atelier électronique Jean-François PIOCHE et Eric GARABEDIAN pour leur participation dans le développement des manipulations et des expériences élaborées.

Je voudrais également remercier le personnel administrative de laboratoire PIIM : Annette CALISTI, Nathalie BONIFAY, Cynthia JULIEN, Marie-Pierre CARVIN, Zaïnaba KASSIM, Hulya KIRMACI et Elodie PICO pour leur attention et leur aide.

Acknowledgements

بداية اشكر الخالق القادر، معلمي الأول، الذي وهبني الحاسة ومن علي بالإدراك، فشوقني للسؤال، وأكثر إستثارة لبي بجميل ما مزج من ألوان ونفخ من أصوات، وشكل من أشكال، قادني طفلة بالنجوم وأدهشني بالقمر، حيرني بالبحر وأسلمني لخيال وصور، فله الحمد أن سيرني بعد إختياري لشق من شقوق معرفته الكثيرة، فما تهت عن حكمته إلا وأعادني إليه وما شككت به لحظة إلا وسقاني جرعة يقين من يديه. الشكر الثاني لوالدتي، لكل تفصيل من تفاصيل وجهها المتعب، لكل عضلة مرهقة في جسدها، اشكر ايقاظها لي كل صباح للمدرسة، اشكرها على كل الكتب والقصص التي روتها على مسمعي، اشكر اهتمامها بالمهم، اشكر حبها ورفقها وصبرها، اشكر رضاها ومساندتها. الشكر الثالث لأبي، لشيبته المهيبة، وكفيه الخشنين، لعطر عرقه، لنزاهته وصلابته، ولاهتمامه كذلك بالمهم. اشكر أختاي على الأمل واخواني الثلاث على السند.

بعد عائلتي، اشكر توأم روحي، من ساندني في كل أوقات الشدة والرخاء، من خفف عني ثقل الغربة وضيقها، فكان كل عائلتي، كان أخي وابي وأمي وحبيبي، صبر على تعبي وكان واحة صحرائي وكل أنسي.

لا أنسى اصدقائي في الوطن وفي الغربة. أحبكم جداً.

وأخيراً أهدي نتاج السنين الثقال إلى أهل الاستحقاق، أهديه إلى فقراء بلادي وشهداء بلادي.

Contents

Résumé français

Cette thèse porte sur l’étude de la production de surface des ions négatifs (IN) pour des applications dans la fusion thermonucléaire. Ce travail a été réalisé à l'aide d'une source plasma à haute densité et à basse pression PHISIS. Les IN formés en surface de l'échantillon lors du bombardement des ions positifs du plasma H_2 sont collectés et analysés avec un spectromètre de masse (SM). La fonction de la distribution en énergie des ions négatifs FDEIN mesurée est le résultat de la FDEIN produite en surface et modifiée par la transmission à travers le plasma et le SM. Un calcul SIMION a été effectué pour avoir une idée complète sur l'effet de la transmission SM sur la FDEIN.

Au cours de cette thèse, une technique de polarisation DC pulsée est introduite pour permettre l'étude de la production d'ions négatifs en surface sur des échantillons isolants comme le diamant non dopé. Un modèle qui calcule le taux de changement de la variation de la tension sur une surface isolante polarisée en mode pulsé est développé. Le modèle est en bon accord avec l’expérience et permet une meilleure compréhension de la technique. De façon surprenante, la production d’IN en surface sur un diamant dopé au bore ou non dopé est beaucoup plus élevée en mode pulsé qu'en mode continu. Cet effet est attribué à une surface de diamant moins défectueuse en mode pulsé.

Cette thèse traite également la production d’IN en surface dans les conditions de faible tension de polarisation. Des conditions de faibles polarisations permettent de travailler dans des conditions similaires à celles de la source d’IN d'ITER où la grille face au plasma est non polarisée. Le meilleur rendement d’IN mesuré à faible polarisation est obtenu avec du diamant dopé au bore (BDD) et il est 2 fois plus élevé que celui mesuré sur la surface du HOPG (high oriented pyrolitic graphite). L'analyse de la production d’IN en surface à différentes polarisations de surface pour différents matériaux a été effectuée afin de corréler l'évolution du rendement d’IN aux changements d'état de surface.

Une étude approfondie de la production en surface d'ions négatifs a été réalisée sur la surface de Nanoporous 12 CaO. 7 Al2O3. L'influence de la température de surface, de la polarisation et du temps d'exposition au plasma sur le rendement en ions négatifs a été étudiée. Différentes mesures FDEIN sur Nanoporous 12CaO.7Al2O3 sont comparées aux FDEIN mesurées sur notre matériau de référence HOPG et une surface de molybdène. Dans cette contribution, nous montrons que ce matériau pourrait potentiellement être utilisé dans les sources d'ions négatifs sans césium pour les injecteurs de la fusion.

Mots clés : interactions plasma-surface, ions négatifs, injecteurs de neutres, spectrométrie de masse, plasmas à basse pression.

English abstract

This thesis deals with negative ions (NI) surface production for applications in thermonuclear fusion. This work was conducted using a low pressure high density plasma source. NI formed on a negatively biased sample surface from positive ion bombardment in hydrogen plasma are collected and analyzed with energy mass spectrometer (MS). The measured negative ion distribution function NIEDF is the result of the NIEDF produced on the surface modified by the transmission through the plasma and by MS transmission function. A SIMION calculation was done to have a complete idea about MS transmission effect on the NIEDF.

In the course of this thesis, a DC pulsed bias technique is introduced to enable the study of negative ion surface production on insulating samples as non-doped diamond layers. A model that calculate the rate of change of bias on insulator surface biased in pulsed mode is developed. The good agreement between model and experiment permits the comprehension of the technique. This technique was optimized, and its feasibility was proved. Surprisingly, negative-ion surface production on boron-doped or non-doped diamond is much higher in pulsed mode than in continuous mode. This effect is attributed to a less defective diamond surface in pulsed mode.

This thesis deals also with negative ion surface production in low bias condition. Low bias conditions allow working in similar conditions as those of NI source of neutral beam injectors for ITER where the plasma grid is unbiased. The best NI yield measured at low bias is obtained with Boron doped diamond (BDD) ant it is 2 times higher than the one measured on HOPG (highly oriented pyrolytic graphite) surface. Analysis of NI surface production at different surface bias for different material were performed in order to correlate the NI yield evolution to the surface state changes.

An extensive study of negative ion surface production was performed on Nanoporous $12CaO.7Al_2O_3$. The influence of surface temperature, bias and plasma exposure time on negative-ion yield was investigated. Measurement on Nanoporous $12CaO.7Al_2O_3$ electride surface are compared to measurement on our reference material such as HOPG on molybdenum. In this contribution, we show that the electride material has potentials to be used as a production surface in negative ion sources devoted to nuclear fusion application.

Keywords: plasma-surface interactions, negative ions, neutral beam injectors, mass spectrometry, low-pressure plasmas

List of acronyms

2D: Two Dimensional
3D : Three Dimensional
a-C : amorphous carbon
a-C:H : hydrogenated amorphous carbon
C : Carbon
CCP : Capacitively Coupled Plasma
CEA : Commissariat à l'Energie Atomique et aux énergies alternatives, France
CFC : Carbon Fiber Composite
D : Deuterium
d : distance between the MS and the surface in mm
DEMO : DEMOonstration Power Plant
DLC : diamond-like carbon
E_1 : l'énergie d'entrée des ions dans le plasma
E_i : initial energy of a NI at the surface in eV
E_{MS} : energy of NI at the entrance of the mass spectrometer
ECR : Electron Cyclotron Resonance
ECRH : Electron Cyclotron Resonance Heating
EDS : Energy-dispersive X-ray spectroscopy
EELS : Electron Energy Loss Spectroscopy
EFDA : European Fusion Development Agreement
E_{impact} : impact energy of PI in SRIM calculations
$f(\theta, E)$: NIEDF emitted at the surface calculated by SRIM with a given E_{impact}
$f'(E)$: NIEDF collected by the MS calculated by the model
$f''(E)$: NIEDF detected by the MS calculated by the model
Gd : gadolinium
H : Hydrogen
H-mode : High confinement mode
He : Helium
HOPG : high oriented pyrolitic graphite
Mo: Molybdenum
MgO: magnesium oxide
HREELS : High Resolution Electron Energy Loss Spectroscopy
ICP : Inductively Coupled Plasma
ICR : Ion Cyclotron Resonance
ICRH : Ion Cyclotron Resonance Heating
IPP : Max-Planck Institute of Plasma Physics, Garching, Germany
IRFM : Institute de Recherche sur la Fusion par confinement Magnétique, CEA Cadarache, France
ITER : International Thermonuclear Experimental Reactor
JET : Joint European Torus tokamak, Culham, UK

List of acronyms

L-mode : Low confinement mode
LAPLACE : LAboratoire PLAsma et Conversion d’Energie, Université de Toulouse, France
LASER : light amplification by stimulated emission of radiation
LEED : Low Energy Electron Diffraction
LHD : Large Helical Device, National Institute for Fusion Science, Toki, Japan
LN_2 : Liquid Nitrogen (at temperature of 77 K)
LP : Langmuir Probe
MASsoft: a software for measurement and control of the MS
MATLAB : MATrix LABoratory: a numerical computing software
MC : Monte-Carlo
MCBDD : micro-crystalline boron-doped diamond
MCD : micro-crystalline diamond (non-doped)
MS : mass spectrometer
NBI : Neutral Beam Injection
NCD : nano-cristalline diamond
n_e : electronic density in m^{-3}
NI : negative ions
NIEDF : negative ion energy distribution function
NRA : Nuclear Reaction Analysis
O : Oxygen
PECVD : Plasma Enhanced Chemical Vapor Deposition
PFC : Plasma Facing Component
PI : positive ions
PWI : Plasma Wall Interactions
QMS : Quadrupole Mass Spectrometer
RF : Radio Frequency
RGA : Residual Gas Analysis
SIMION : a software for calculation of ion transport inside the MS
SOL : Scrape-Off Layer
SRIM : Stopping and Range of Ions in Matter; a group of programs designed to calculate the stopping of ions (10 eV – 2 GeV/a.m.u.) in matter
T : Tritium
ta-C : tetrahedral amorphous carbon
TDS : Thermal Desorption Spectroscopy
TPD : Temperature Programmed Desorption
T_e : electronic temperature in eV
T_{MS} : transmission inside the MS
TS Tore Supra : superconducting tokamak in IRFM, Cadarache, France
V_{ext} : extraction potential in V
V_{MS} : MS nozzle potential

V_p : plasma potential in V
V_s : surface potential in V
W : Tungsten
α : angle between the normal to the sample and the MS axis in °
θ_i : initial angle of NI emitted from the surface
θ_1 : angle of entrance of NI in the plasma
θ_{MS} : angle of arrival of NI to the MS entrance

Introduction et motivation

Nous traitons en continu avec les 3 différents états de la matière : le solide, le liquide et le gaz. Un quatrième état de la matière peut être ajouté à ces trois, le « plasma ». Linguistiquement, le mot "plasma" est un mot grec qui signifie "substance malléable". Il a été découvert pour la première fois par Irving Langmuir (1928) lors de ses travaux sur les arcs de décharge du mercure. Durant cette expérience, il a trouvé une substance diffusante dans une chambre à vide à la manière d'une gelée dans un moule et l'a appelée "plasma". Physiquement, le plasma peut être obtenu en chauffant suffisamment un gaz de manière que l'énergie cinétique de ses atomes devienne si élevée[1] que les atomes de gaz se heurtent fortement entre eux et que leurs électrons soient éliminés : un gaz ionisé se forme alors. Ce gaz ionisé est caractérisé par différents paramètres, principalement la température et la densité des électrons. En se référant aux valeurs de ces deux paramètres, le plasma peut être classé en deux catégories : Plasma chaud où la température des espèces plasma est de l'ordre de 10^7 K (cette température est portée par les ions) et plasma froid où cette température est de l'ordre de 10^4 K (cette température est portée par les électrons).

Le plasma forme 99% de notre univers visible, les étoiles dans nos galaxies, ou les aurores boréales de notre planète sont faits de plasma. Le plasma ne se trouve pas seulement dans la nature, mais il peut être artificiel comme les lampes fluorescentes et les lampes au néon. Le plasma joue un rôle important dans de nombreuses applications dans divers domaines tels que l'industrie et la médecine. Dans l'industrie, il est largement utilisé en microélectronique. A titre d'exemple, il est utilisé dans la production de circuits intégrés[2], et il est présent dans l'industrie spatiale et aéronautique. En médecine, il se révèle dans les traitements dentaires[3] ainsi que dans les traitements des cancers où il se révèle être une technique utile pour tuer les cellules cancéreuses[4].

Mais l'objectif principal des applications plasma est de produire une source d'électricité durable à partir de la réaction de fusion nucléaire. Cet objectif est inspiré du processus naturel qui se produit dans les étoiles précisément dans le soleil. En effet, la matière est chauffée à une température très élevée, elle atteint l'état plasma[5], et une réaction de fusion a lieu. Cette réaction fournie une énorme quantité d'énergie. Dans cette étude, nous allons nous intéresser à l'application plasma dans le domaine de l'énergie de fusion.

L'énergie de fusion peut faire partie de la solution au problème énergétique actuel, où nous nous tournons vers des sources d'énergie compatibles avec le développement durable. Ce problème peut être résolu par des sources d'énergie abondantes et géographiquement distribuées, où l'électricité peut être disponible pour tous les pays, en particulier ceux qui ont encore besoin de se développer. L'indice de développement des différents pays n'est pas le seul critère des sources d'énergie désirées, le monde a besoin de sources d'énergie ayant un faible impact sur l'environnement, avec de faibles émissions de gaz à effet de serre comme le dioxyde de carbone CO_2. Ces sources d'énergie doivent être sécurisées non seulement pour l'environnement mais aussi pour la population. Donc, trois critères sont nécessaires pour la prochaine génération de source d'énergie. Ces trois critères sont disponibles dans une source d'énergie basée sur la réaction de fusion.

Commençons par définir la réaction de fusion. La fusion comme déjà mentionné, est la source naturelle d'énergie dans les étoiles. Par exemple, dans le soleil de notre galaxie, quatre protons se combinent pour former un noyau d'hélium à quatre nucléons[6]. En conséquence, une énorme quantité d'énergie est produite comme le montre la **Figure 0.1**. Cette dernière montre les détails des réactions en chaîne proton-proton. La production d'énergie après une réaction de fusion provient d'un défaut de masse où la masse des réactifs est supérieure à la masse des produits. Ce défaut de masse se transforme en énergie en respectant la loi de relativité d'Einstein ($E = mc^2$).

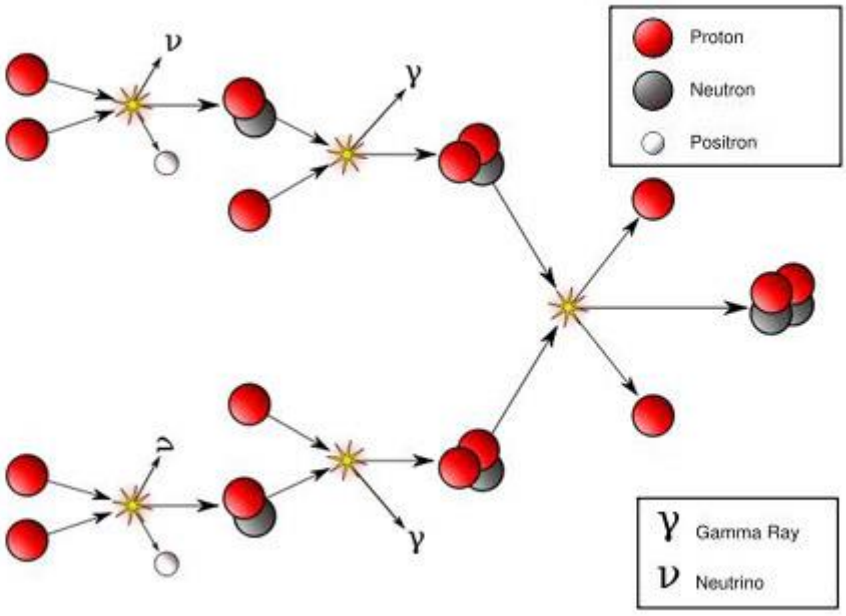

Figure 0.1 les réactions en chaine proton -proton dans le soleil

Le tritium, le deutérium et l'hélium sont les combustibles de fusion. Différentes réactions de fusion sont possibles sur terre et peuvent se produire entre différentes combinaisons de ces éléments comme suit[7]: (i) le deutérium et le tritium peuvent fusionner pour produire de l'hélium-4 et un neutron (**équation 0.1**), (ii) du deutérium et de l'hélium-3 peuvent fusionner pour produire de l'hélium-4 et un proton (**équation 0.2**), et / ou (iii) du deutérium et du deutérium peuvent fusionner pour produire deux résultats possibles un hélium -3 et un neutron (**équation 0.3**), ou un triton et un proton (**équation 0.4**):

${}_1D^2 + {}_1T^3 \longrightarrow {}_2He^4 + {}_0n^1$ équation 0.1

${}_1D^2 + {}_2He^3 \longrightarrow {}_2He^4 + {}_1p^1$ équation 0.2

${}_1D^2 + {}_1D^2 \longrightarrow {}_2He^3 + {}_0n^1$ équation 0.3

${}_1D^2 + {}_1D^2 \longrightarrow {}_1T^3 + {}_1p^1$ équation 0.4

Le processus de fusion fonctionne très bien au soleil, mais il n'est pas évident de le reproduire sur terre. La difficulté de réaliser une telle réaction de fusion sur terre n'est pas liée à l'existence des combustibles, mais elle est limitée par le principe d'une telle réaction. Dans une réaction de fusion, nous avons deux noyaux chargés positivement. Ces derniers s'éloignent les uns des autres sous l'effet de la répulsion coulombienne et la réaction de fusion ne se produit pas. Donc, pour avoir une réaction de fusion, il faut approcher les noyaux les uns des autres à une distance critique[8]. Dans telles conditions, la force nucléaire prédomine sur la force électrostatique, et les noyaux peuvent fusionner. Des noyaux énergétiques ont un mouvement aléatoire rapide, leurs collisions sont assez fortes de sorte qu'ils peuvent être assez proches les uns des autres et fusionner. Ces noyaux peuvent être obtenus en chauffant les combustibles de fusion à très haute température. A 100 millions de Kelvin[9], la réaction de fusion peut être réalisée sur terre, et les combustibles de fusion sont à l'état de plasma.

Pour quantifier la difficulté des trois réactions de fusion disponibles sur Terre (D-T, D-He et D-D), nous devons quantifier la probabilité que chacune d'entre elles se produise. Ceci est possible en regardant la section efficace. La **Figure 0.2** montre la section efficace de chaque réaction possible de fusion mesurée en fonction de l'énergie moyenne du centre de masse[10]. Comme il est montré, la réaction de fusion D-T a la plus grande section efficace (ligne noire). Par conséquent, elle est la plus probable à réaliser. C'est pour cela qu'elle a été choisie comme la réaction à utiliser pour la première génération des réacteurs de fusion.

La réaction de fusion D-T est déjà mentionnée dans l'**équation 0.1** et elle est montrée dans la **Figure 0.3**. Une fois que nous atteignons le niveau de température requis, D et T entrent en collision, fusionnent et, par conséquent, une énorme quantité d'énergie est gagnée. L'énergie totale produite par la réaction est de 17,59 MeV, et elle est répartie entre ses produits. Le noyau d'hélium 4 ou la particule α se produit avec 20% de l'énergie totale (équivalent à 3,53 MeV) et un neutron est éjecté également avec l'énergie restante (80% de l'énergie totale équivaut à 14.06 MeV) [11].

Une fois cette réaction de fusion choisie pour être utilisée dans le futur réacteur de fusion, il est important de vérifier la disponibilité de ses réactifs. En ce qui concerne le deutérium, il représente environ 14% de l'hydrogène présent sur terre, y compris les océans (1,6 g de D par litre[12, 13]), et il peut être extrait de l'eau de mer avec une technique peu coûteuse. Cependant, le tritium est un isotope de l'hydrogène qui n'existe pas dans la nature car il est radioactif avec une durée de vie courte (12,5 ans). La non- disponibilité du tritium peut être résolue par un processus pouvant le produire à partir du lithium (voir **l'équation 0.5**). Li peut être extrait de l'eau des océans. Lorsqu'un atome de Li réagit avec un neutron énergétique provenant de la réaction de fusion elle-même il est possible de produire du tritium. La production de tritium peut être effectuée dans un réacteur de fusion en plaçant une couverture contenant du lithium autour du plasma de fusion où les neutrons sont produits[14] :

$$ {}_{3}Li^{6} + {}_{0}n^{1} \rightarrow {}_{1}T^{3} + {}_{2}He^{4} $$ **équation 0.5**

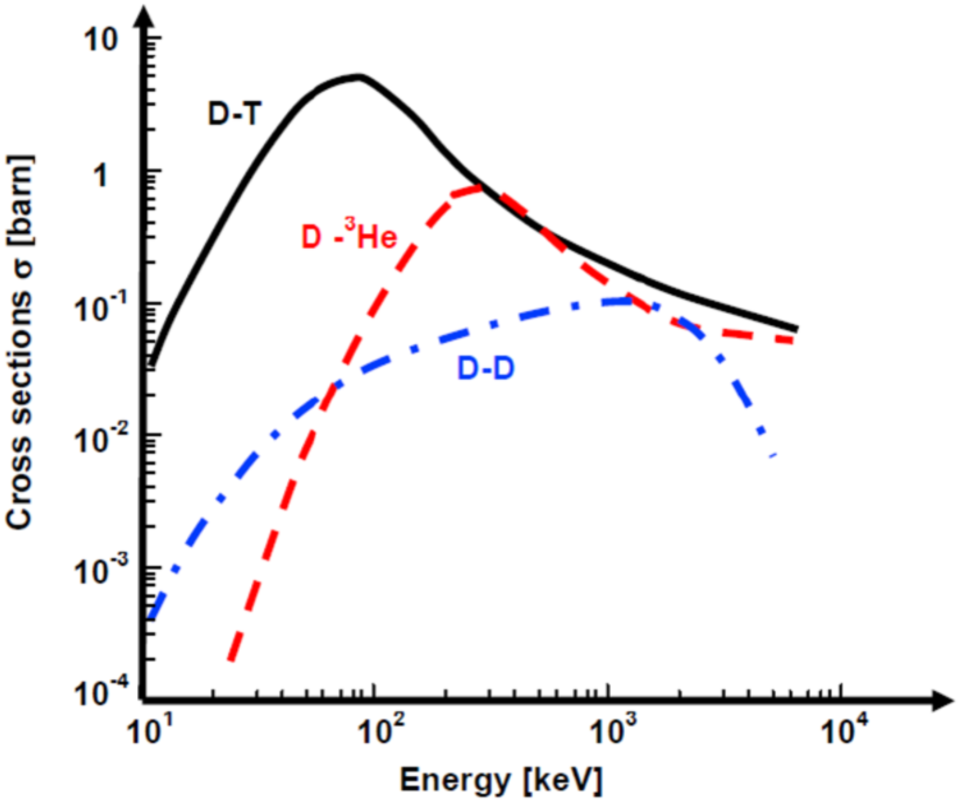

Figure 0.2 la section efficace mesurée pour des différentes réactions de fusion en fonction de l'énergie du centre de masse

La disponibilité des réactifs n'est pas la seule contrainte pour un réacteur de fusion, La difficulté principale d'un tel dispositif est l'allumage de la réaction de fusion. L'allumage est établi lorsque la puissance de gain de la fusion dépasse la puissance de perte. La puissance de perte de la fusion peut être décrite par un paramètre appelé "temps de confinement de l'énergie" 'τ_E. C'est le temps caractéristique pendant lequel l'énergie est transportée hors du système de fusion et perdue dans son environnement. Ce temps de confinement d'énergie τ_E requis est déterminé par le critère de Lawson. Ce critère est un triple produit de la densité électronique n_e, de température ionique T_i et de temps de confinement τ_E, il définit la valeur minimale requise pour allumer la réaction de fusion[15] :

$$n_e \cdot \tau_E \cdot T_i \geq 3 \cdot 10^{21} \text{ [keV} \cdot \text{m}^{-3} \cdot \text{s]} \qquad \textbf{équation 0.6}$$

Le critère de Lawson impose un rang de température allant de 10 keV à 20 keV[16]. Par conséquent, le confinement du plasma de fusion est essentiel, non seulement pour allumer la réaction, mais aussi pour protéger les parois du réacteur du flux de chaleur énorme provenant du plasma (D-T), qui est très chaud. Dans le cas où le confinement du plasma est absent, les particules heurtent le mur de la chambre de plasma, et ils se perdent. Le plasma disparaît et les parois ne supportant pas cette température sont très endommagées.

L'un des moyens efficaces de confiner le plasma de la fusion et de le séparer des parois, est le confinement magnétique. Cette approche est basée sur l'utilisation d'un fort champ magnétique pour piéger les particules chargées du plasma en fusion. Les ions et les électrons du plasma de fusion sont soumis à la force électromagnétique, et ils tournent autour des lignes de champ magnétique sans toucher les murs de la chambre plasma.

Pour appliquer le confinement magnétique du plasma de fusion, de nombreux types de configurations de lignes de champ magnétique ont été proposés. La première proposition est la configuration linéaire où le plasma est confiné autour des lignes de champ magnétique. Dans ce cas, un problème évident se produit avec les deux extrémités du dispositif linéaire. La deuxième configuration proposée est la configuration toroïdale où un champ magnétique toroïdal est produit par une machine formée de nombreuses bobines de forme toroïdale[17]. Avec une telle géométrie de bobines, les lignes de champ magnétique ont une certaine courbure et un gradient d'intensité de champ est également présent. Ces deux phénomènes conduisent à une dérive qui sépare la charge positive de la charge négative. En conséquence, cette séparation de charge crée un champ électrique E. De plus, E se combine avec le champ magnétique toroïdal B et une dérive (E x B) commence à sortir le plasma. Les phénomènes de séparation de charge peuvent être annulés sur un dispositif toroïdal en imposant un champ poloïdal qui aide les particules à se déplacer dans une direction de dérive opposée à celle causée par le champ toroïdal, et une moyenne nulle de la dérive nette est obtenue. La combinaison de la configuration de champ magnétique toroïdale avec celle poloïdale donne une configuration hélicoïdale[18].

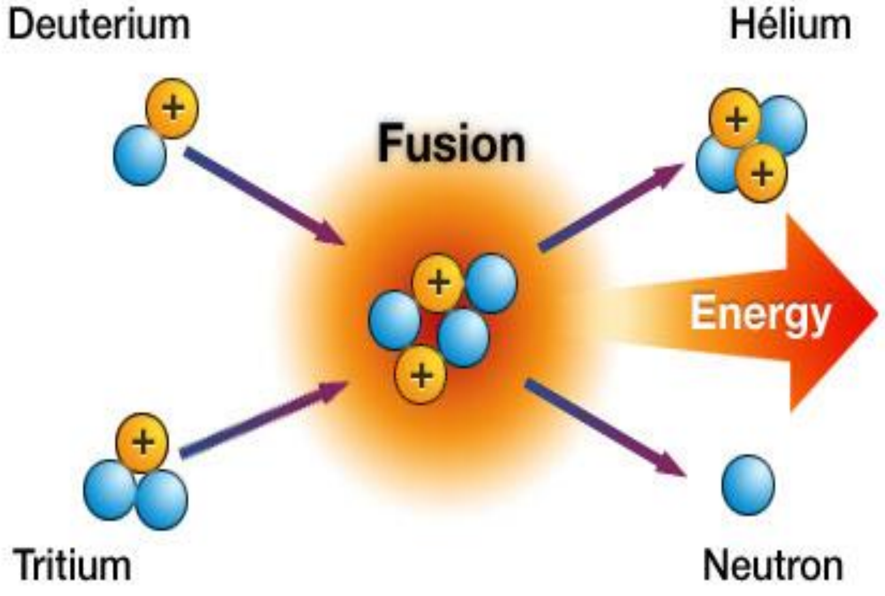

Figure 0.3 la réaction de fusion D- T

Le Tokamak est l’une des machines les plus prometteuses de confinement magnétique pour le plasma de la fusion, elle est basée sur la configuration hélicoïdale du champ magnétique. Sur la **Figure 0.4**, nous pouvons voir le champ magnétique hélicoïdal résultant du champ magnétique toroïdal, produit par les bobines de la chambre du tokamak (bobines de couleur bleue), combiné avec le champ poloïdal, produit par le courant plasma (lignes vertes). Un tel dispositif ne fournit pas seulement une qualité de confinement, mais il chauffe naturellement le plasma.

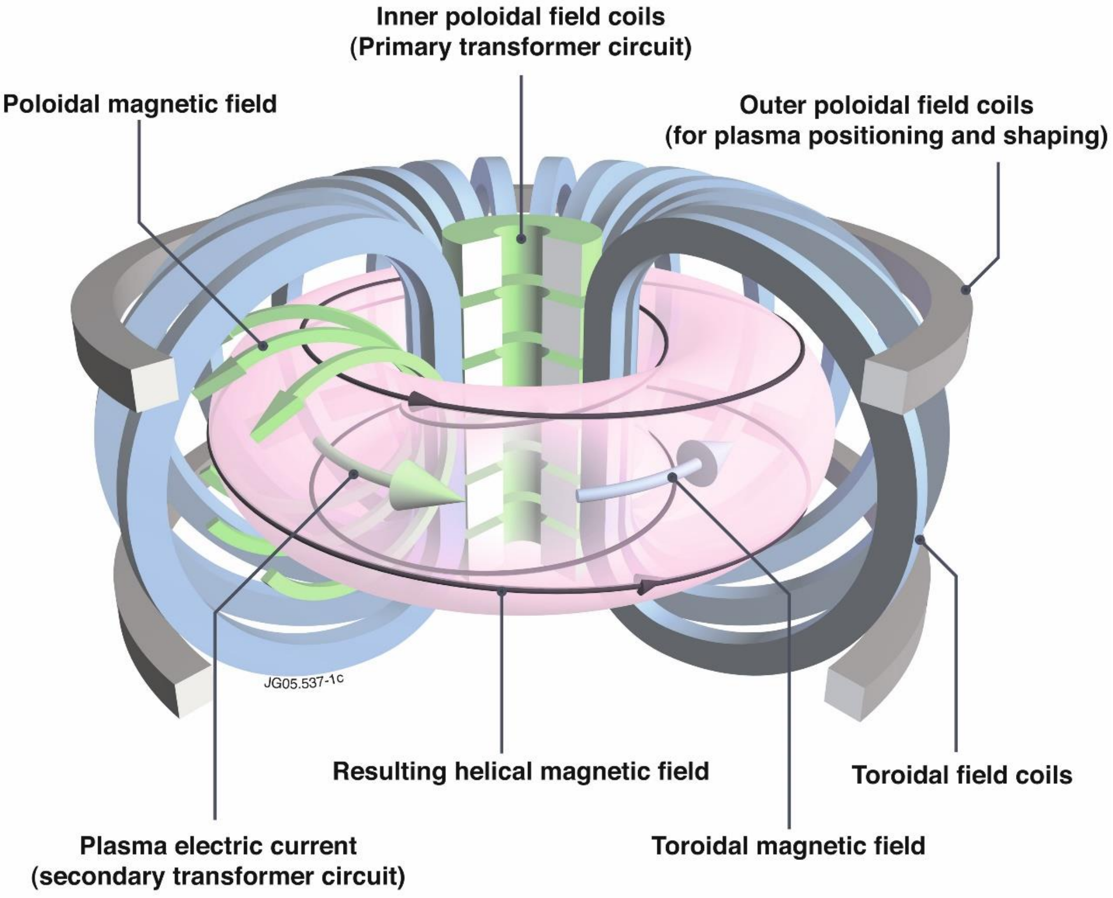

Figure 0.4 La configuration du champ magnétique dans une machine tokamak

Après cette description scientifique et technologique de l'énergie de fusion, sa faisabilité et sa sécurité doivent être démontrées. Pour cette raison, une coopération internationale de sept partenaires (Chine, Inde, Japon, Corée, Russie, États-Unis et UE) est réalisée pour construire un réacteur expérimental thermonucléaire international (ITER) à Cadarache, en utilisant la réaction de fusion basée sur le principe de tokamak. Ce projet a été officiellement lancé en 2006 et la première expérience de plasma devrait avoir lieu en décembre 2025. Le tokamak d'ITER sera le plus grand du monde avec un poids de 23 000 tonnes, un rayon de plasma de 6.2 m. La puissance fournie attendue d'ITER est d'environ la moitié du gigawatt (500 Mw) avec un gain de fusion * Q> 10. ITER nécessite une température 150 millions° C. cette valeur est égale à dix fois la température au cœur du soleil. Elle nécessite un système de chauffage performant pour l'atteindre[19].

Le premier système de chauffage est interne (le chauffage ohmique) et il est présent dans ITER comme indiqué précédemment. Il est limité et ne peut pas fournir la température désirée. Par conséquent, des systèmes de chauffage externes sont nécessaires. L'un des systèmes de chauffage supplémentaires est le chauffage par ondes électromagnétiques à haute fréquence (radiofréquence (RF)). Il est basé sur un principe que l'on retrouve dans un four à micro-ondes ou la chaleur est transférée aux aliments à travers les micro-ondes. Le plasma est chauffé par ondes radio (RF) et par transfert d'énergie à travers des interactions résonnantes à ses particules. Dans un système de chauffage à ondes électromagnétiques à haute fréquence, deux sources sont utilisées : une pour le chauffage des ions et la seconde pour le chauffage des électrons. Chaque source utilise une fréquence de résonance différente afin de correspondre à la fréquence du cyclotron de chaque espèce. Un chauffage par résonance cyclotronique ionique (ICRH) fonctionnera dans ITER à une fréquence de résonance allant de 40 MHz à 55 MHz, et un chauffage par résonance cyclotronique électronique (ECRH) fonctionnera à 170 GHz[21]. Le système de chauffage par radiofréquence (RF) n'est pas le seul système de chauffage externe à utiliser dans ITER. Un deuxième est également nécessaire pour atteindre la température demandée pour la fusion ; il est appelé injecteur de faisceau neutre (IDN). Ce système de chauffage est le plus efficace et il sera l'objectif principal de ce travail.

Le chauffage plasma par injecteur à faisceau neutre (IDN) est basé sur l'injection d'atomes neutres à haute énergie. Typiquement, le deutérium est injecté dans le cœur du plasma de la fusion. Ce faisceau est ionisé par le plasma lui-même et un courant d'ions énergétiques y est progressivement créé. Par conséquent, un transfert d'énergie se produit après les collisions coulombiennes entre les particules de plasma et le faisceau d'ions, le plasma est chauffé. Le faisceau neutre énergétique injecté par l'IDN est important non seulement pour le chauffage du plasma, mais aussi pour conduire un courant non-inductif dans le plasma. L'injection de faisceau énergétique se fait dans une géométrie tangentielle, parallèle autant que possible à la direction toroïdale du tokamak. Un courant de plasma toroïdal est créé en plus de celui inductif. Le plasma est ravitaillé et le confinement est amélioré[22].

L'idée d'utiliser un faisceau d'atomes neutres pour être injecté dans le volume de plasma de la fusion provient de sa capacité d'éviter l'effet du champ magnétique. Ce dernier règne dans le tokamak et il empêchera la pénétration des ions de l'extérieur comme il empêche l'échappement des ions de l'intérieur. Un faisceau hautement énergétique est recommandé pour obtenir une bonne pénétration dans le cœur du plasma de la fusion, cette distance augmente avec l'énergie du faisceau pour une densité de plasma donnée. Pour cette raison, une énergie élevée de 1 MeV pour le faisceau D^0 est nécessaire pour atteindre une distance de pénétration de l'ordre de quelques mètres[21] qui est la taille d'ITER et les futurs réacteurs que nous prévoyons avoir.

Après cette description des différents processus qui se produisent suite à l'injection du faisceau neutre à haute énergie dans le plasma de la fusion, il est important de savoir comment un tel faisceau peut être créé par un système NBI. La génération d'un faisceau de neutres rapides se fait en trois étapes[21] :

- génération d'un puissant faisceau d'ions de l'ordre de plusieurs MW
- neutralisation du puissant faisceau d'ions dans une cible gazeuse

- transport des atomes neutres vers le tokamak, et filtration des ions énergétiques non neutralisés

Le système d'injection de faisceau neutre (IDN) pour ITER est basé sur l'accélération et la neutralisation d'un faisceau d'ions négatifs (D^-). La raison de l'utilisation d'ions négatifs pour ITER peut être déduite de la **Figure 0.5**. La dernière montre la variation de l'efficacité de neutralisation de D^- et D^+ successivement par rapport à l'énergie du faisceau d'ions. Nous pouvons voir que les ions négatifs ont un rendement élevé de neutralisation de 55% même pour un faisceau d'ions assez énergétique, contrairement aux ions positifs où il est presque 0% après 400 KeV. Par conséquent, la génération du faisceau neutre requis D^O à 1 MeV pour ITER est impossible à partir d'un faisceau d'ions D^+ et une source d'ions négatifs performante est nécessaire pour un tel système. Différents composants de l'injecteur de faisceau neutre pour ITER sont représentés sur la Figure 6. Le premier est la source d'ions négatifs où 55 A de D- sont générés et extraits de la source pour être accélérés à 1 MeV par un champ électrique. Ce champ règne juste après dans une grille polarisée par une tension continue élevée. Un puissant faisceau d'ions négatifs (40 A à 1 MeV) pénètre dans le neutraliseur où il entre en collision avec une cible gazeuse D_2, les électrons sont facilement détachés des ions D^- qui se convertissent en atomes D^0 suivant la réaction :

$D^{-*} + D_2 \rightarrow D^{0*} + e^- + D_2^+$ **équation 0.7**

Après la neutralisation du faisceau, un filtre d'ions résiduels sépare les particules du faisceau neutre des ions énergétiques restants en les déviants à l'aide d'un aimant. Un courant de 10 A de D^+ et 10 A de D^- (1 MeV) sont filtrés. Un faisceau net neutre de D^0 à une énergie de 1 MeV et une puissance de 16,5 MW est prêt à être injecté dans le tokamak. Dans le réacteur ITER, deux injecteurs de faisceaux des neutres seront installés, chaque système a une longueur de 15 m, une largeur de 4,7 m et une hauteur de 5,3 m. La puissance totale fournie de ces deux systèmes est 33 MW[21, 24, 25, 26].

Ainsi, la source d'ions négatifs est l'élément clé pour le système de chauffage IDN pour ITER. Le développement d'un tel système est important pour un énorme appareil de fusion. Nous avons vu précédemment que les ions négatifs ont été choisis pour le système IDN pour ITER, en se référant à son efficacité de neutralisation élevée (55%) à haute énergie (1 MeV). Cet avantage des IN au niveau de la partie neutraliseur (détachement facile des électrons de H^- / D^-) joue un rôle opposé au niveau de la source (attachement difficile des électrons à H / D). Jusqu'à présent, l'exploitation de sources d'ions négatifs représente un défi scientifique du fait de la faible 'énergie de liaison de l'électron à un atome H, 0,75 eV[27]. Cette faible énergie limite la production de courant IN intense et ralentit l'exploitation de la source demandée. Le courant IN d'ions négatifs pour un chauffage efficace dans une machine de fusion de la taille d'ITER est calculé. Nous avons besoin d'un courant H^- / D^- stable de 69 A d'hydrogène et 57 A de deutérium à 1 MeV[28]. Le courant IN calculé est intense et difficile à obtenir expérimentalement. Une source performante capable de délivrer une valeur de courant IN comparable à la valeur calculée est nécessaire. Par conséquent, la compréhension des mécanismes de production d'ions négatifs dans les conditions de source est nécessaire.

Dans une source d'ions négatifs, les ions négatifs H^- / D^- sont produits dans une source de plasma à basse pression (H_2 / D_2) et ensuite extraits et accélérés. La production d'ions négatifs sur les surfaces dans les plasmas à basse pression se base sur deux mécanismes distincts. Selon l'endroit où les ions sont formés, nous distinguons deux types différents de production celle en volume et celle en surface. La production en volume de IN est associée à l'attachement dissociative d'électrons de plasma froids (<1 eV) sur des molécules vibrationnelles excitées[29, 30]. Dans une source volume, les IN produits sont caractérisés par une plage d'énergie faible (Ti <Te). La production de IN en surface est associée à la capture d'un ou de deux électrons par des atomes neutres ou des ions bombardent la surface. Les IN produits dans les sources de production en surface sont plus énergétiques que ceux produits dans une source de production en volume.

Dans un plasma à basse pression, la production en volume des IN est le mécanisme principal et le processus le plus favorable pour des applications en microélectronique et en propulsion spatiale. En revanche, la production en surface des IN est considérée dans de nombreuses études et expériences comme un mécanisme mineur. Mais, dans certaines conditions, cette production peut être très efficace. Lorsqu'une surface avec des propriétés électroniques déterminées est bombardée par un plasma, un énorme rendement d'ions négatifs est produit en surface.

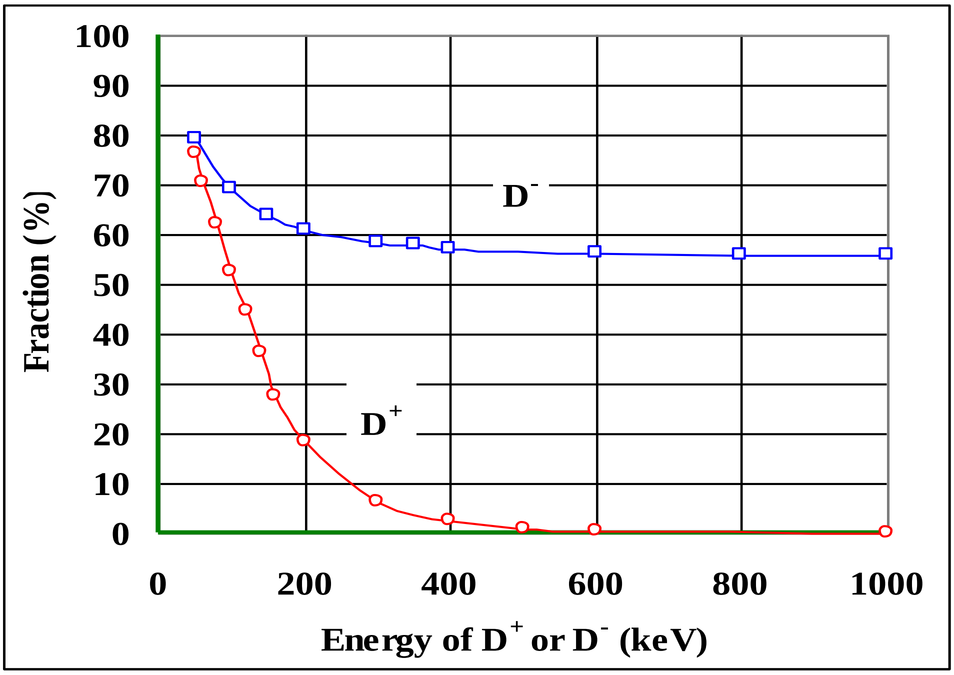

Figure 0.5. L'efficacité de neutralisation (fraction in %) des ions deutérium en fonction de leur énergie[21]

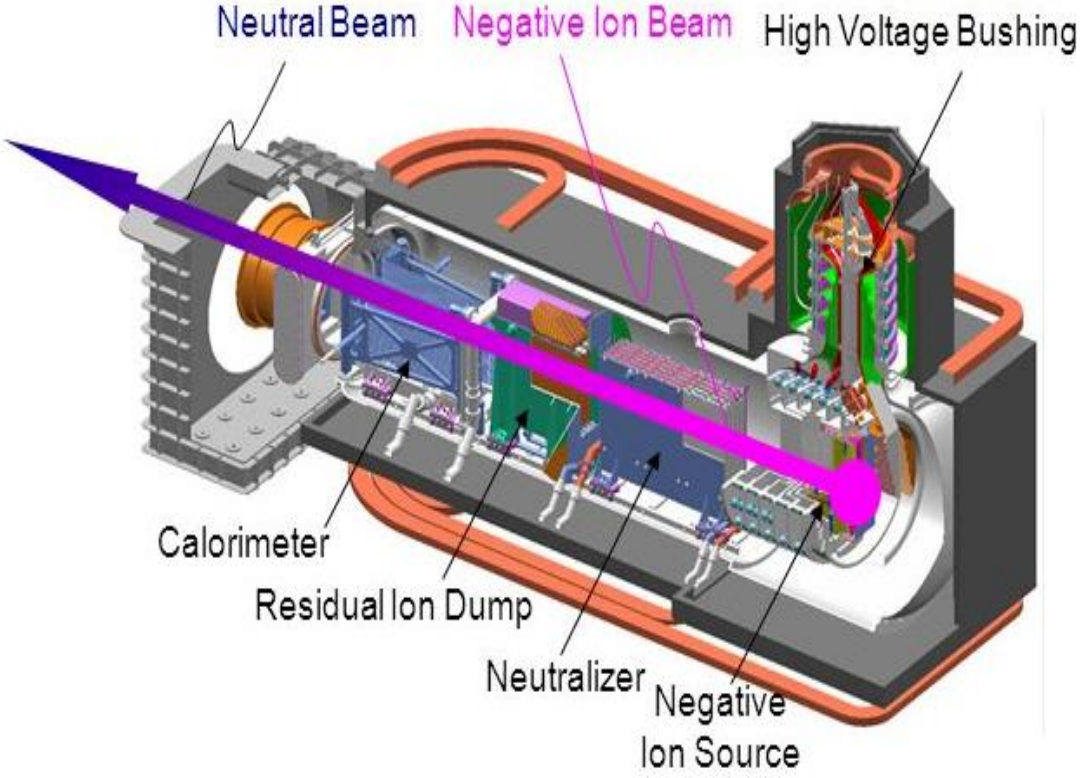

Figure 0.6 l’injecteur de faisceaux des neutres (IDN) pour ITER avec une description de ses différents composants

Ce résultat expérimental a été observé pour la première fois par Belchenko et al (1973) lorsque des surfaces couvertes par le césium (Cs) sont placées dans une source plasma à basse pression. Une énorme production en surface des IN par conversion des ions positifs ou d'atomes incidents est observée après contact entre la surface de Cs et le plasma[31, 32]. Cette observation conduit à une conclusion importante : une surface à faible travail de sortie comme le Cs est favorable à la production en surface des IN. En 1989, Leung montre que l'injection de Cs dans une source volume augmente le rendement des IN. L’amélioration de la production d'ions négatifs en surface par l’injection de césium est le principe utilisé dans une source intense d'ions négatifs. C'est la base de la source d'ions négatifs à l'hydrogène pour la fusion et les accélérateurs linéaires à haute énergie[33, 34].

La source conçue pour ITER est en cours de développement à IPP Garching en Allemagne. Elle fonctionne avec un plasma à couplage inductif à basse pression. Elle est composée de huit excitateurs. Chaque excitateur est un générateur de plasma à couplage inductif (ICP) fourni avec 100 kW de puissance RF (voir **Figure 0.7**). La source doit générer une densité de courant NI intense de 200 A.m^{-2}, sur une grande surface de 1.2 m^{2}. Un flux de D extrait avec une uniformité de 5% à 10% pendant une longue période de fonctionnement (1 heure) est demandé. Un faible courant d'électrons co-extrait (inférieur à un électron par ion négatif) est également requis. Ce dernier est possible par l'application d'un champ magnétique transversal (50 Gauss) entre la région de diffusion du plasma et la région d'extraction des IN. Les électrons chauds générés dans les excitateurs sont refroidis et filtrés à l'aide de cette barrière de champ magnétique. La source des IN d'ITER est basée sur l'injection de Cs[35]. C'est la seule solution scientifique connue à jour pour atteindre un tel courant ionique de D- et répondre aux exigences d'ITER. Le césium (Cs) est injecté sous forme vapeur à l'intérieur de la région d'extraction. Il dépose sur la surface de la grille en contact avec le plasma. Le dépôt de césium Cs sur la grille abaisse le travail de sortie du matériau à 2.3 eV. Cet effet augmente l'efficacité de capture des électrons par des particules incidentes. Ainsi, un rendement des IN élevé est obtenu.

Le développement de la source ITER NI fait l'objet de plusieurs recherches dans différents pays. En Allemagne, IPP Garching exploite deux sources d'essai : BATMAN et ELISE[36]. BATMAN est une petite source d'ions avec un seul excitateur RF (un huitième de la taille de la source d'ITER). Il offre une grande flexibilité expérimentale et il est équipé d'un ensemble de diagnostic très complet. ELISE une source d'ions composée de quatre excitateur RF (la moitié de la taille de la source NI d'ITER). Ce banc d'essai étudie principalement le comportement de la source pour de longues impulsions et des questions liées aux lois d''échelle. À Toulouse en France, le laboratoire LAPLACE a mené des expériences et modélisations dédiées sur le transport du plasma à travers le champ magnétique[37]. En Italie, il a été décidé de construire l'installation d'essai NBI PRIMA (Padova Research sur ITER Megavolt Accelator). Il comprend SPIDER (source IN complète composée de huit excitateurs) et MITICA (prototype de l'injecteur ITER complet) [38,39]. En parallèle, un travail de modélisation sur la source d'ions en Cs est réalisé à IPP Garshing, au laboratoire de Laplace[40, 41, 42, 43], à l'université de Sofia et à l'université technique de Sofia (Bulgarie) [44] en collaboration avec le CEA Cadarache.

Des études menées à IPP Garshing montrent qu'en utilisant l'injection de Cs, la source d'ions négatifs ITER peut atteindre les fortes densités de courant requises. Cependant, des inconvénients de l'utilisation du césium ont été identifiés. Tout d'abord, une forte consommation de césium dans la gamme de 5-10 $\mu g. s^{-1}$ [45, 46] est signalée. car le césium doit être injecté en continu dans la source pour obtenir un courant d'ions négatifs stable pour une longue durée. Deuxièmement, le césium diffuse et pollue l'accélérateur. Cette contamination peut provoquer des faisceaux parasites et / ou des claquageset implique une maintenance régulière et contraignante dans un environnement nucléaire. Enfin, la stabilité sur des temps longs nécessite un conditionnement en césium strict, long, et difficile de la source d'ions négatifs. Ces trois problèmes compliquent le fonctionnement de la source d'ITER. Par conséquent, les recherches concernant la source de fusion IN poussent vers une solution alternative. L'objectif est de réduire fortement la consommation de césium ou même de développer une source d'ions négatifs sans césium pour la nouvelle génération de systèmes IDN [25]. De tels systèmes seront utilisés pour le futur réacteur de fusion DEMO (Démonstration Power Plant) [48]. Le but de ce travail est d'étudier des matériaux alternatifs à des métaux revêtus de césium pour la production en surface de rendements élevés d'ions négatifs dans les plasmas H_2 ou D_2 à basse pression.

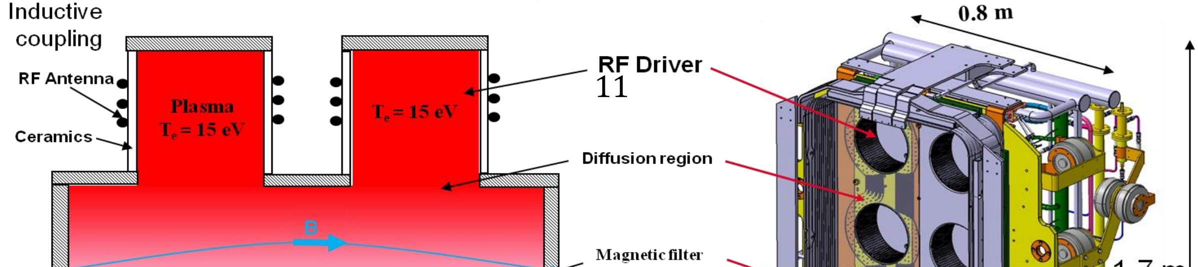

Introduction and motivation

Matter has three state: solid, liquid and gas. A fourth state of matter can be defined with these three states the so-called “plasma”. Linguistically, the word “plasma” is a Greek word that means ‘moldable substance’. Irving Langmuir (1928) discovered it for the first time during his work on mercury arc discharges. He found a substance diffusing in vacuum chamber as a jelly in a mold and named it “plasma” Physically, plasma can be obtained by heating a gas, in a way that the kinetic energy of its atoms or molecules becomes high[1]. Afterward, if the gas particles strongly collide their electrons can be stripped away and as a result, an ionized gas is formed. This ionized gas is characterized by different parameters that are mainly the electron temperature and the electrons density. Referring to the range of these two principal parameters, plasma can be classified as two categories. Hot plasma where the temperature of plasma species is in the order of 10^7 K (this temperature is carried by plasma ions and electrons $T_i \approx T_e$). Cold plasma where this temperature is in the order of 10^4 K (this temperature is carried by plasma electrons only $T_i << T_e$).

Plasma form 99% of our visible universe, starting by the stars in our galaxies to endless lighting and aurora borealis in our planet. Plasma is not only found in the nature, but it can be man-made such as in fluorescent lights and neon lamps. Plasma has a key role in many industrial applications in various fields such as microelectronics, or medicine. In microelectronics, it plays a crucial role in integrated circuit production[2], and in medicine, it intervenes in dental[3].and could help in the near future in cancer treatments[4].

One major application of plasma is in the field of energy production, more precisely in the generation of sustainable electricity from nuclear fusion reactions. This goal is inspired from natural process that occurs in stars, like the sun where the matter is heated up to a very high temperature and reaches plasma state[5]. Consequently, fusion reactions are ignited providing a huge amount of energy. Plasma application in fusion energy research is our focus and interest and is described below.

Energy consumption in the world has exploded over the last century and is continuing to grow with the development of emerging-countries. Put into the context of limited oil reserves, global warming effect, growth of world population, the international energy situation is nowadays a hot topic. The challenge is to find sustainable and non-pollutant energetic solutions with unlimited or almost unlimited reserves geographically distributed all over the world. Even energy sources with low negative impact on the environment, and in particular, with low emission of greenhouse gas as carbon dioxide CO_2, to limit pollution and its consequence on climate change must be found. These energy sources must be safe not only for the environment but also for the population. Therefore, many criteria must be considered for the next generation of energy source. Nuclear fusion is a source of energy that would meet these criteria.

Let us first define the fusion reaction mechanism. Fusion as already mentioned is the natural source of energy in the stars. In stars, four protons are put together in a way to form helium-four nucleus[6] . Consequently, a huge amount of energy is produced as shown in **Figure 0.1** the energy production after a fusion reaction comes from a mass defect where the mass of fusion fuels is higher than the mass of fusion products. The mass defect is transformed to the energy respecting Einstein’s law ($E= mc^2$).

Different fusion reactions are possible on earth using different hydrogen isotopes as follow[7]:(i) deuterium and tritium can fuse to produce helium-4 and a neutron (**Equation 0.1**), (ii) deuterium and helium-3 can fuse to produce helium-4 and a proton (**Equation 0.2**), and/or (iii) deuterium and deuterium can fuse to produce two possible outcomes a helium -3 and a neutron (**Equation 0.3**),, or a triton and a proton (**Equation 0.4**)

$$\mathbf{{}_1D^2 + {}_1T^3 \rightarrow {}_2He^4 + {}_0n^1} \qquad \textbf{Equation0.1}$$

$$\mathbf{{}_1D^2 + {}_2He^3 \rightarrow {}_2He^4 + {}_1p^1} \qquad \textbf{Equation0.2}$$

$$\mathbf{{}_1D^2 + {}_1D^2 \rightarrow {}_2He^3 + {}_0n^1} \qquad \textbf{Equation0.3}$$

$$\mathbf{{}_1D^2 + {}_1D^2 \rightarrow {}_1T^3 + {}_1p^1} \qquad \textbf{Equation0.4}$$

Fusion process occurs in sun, but it is not obvious to reproduce it on earth. The difficulty in achieving such fusion reactions is due to the presence of two positively charged nuclei that repeal from each other due to the Coulomb force. To have fusion reaction, nuclei must approach each other at a critical distance[8]. Under such conditions, nuclear force predominates electrostatic force. This situation can be reached with energetic nuclei. Energetic nuclei mean that the nuclei random motion is fast, so they can be very close to each other collide and fuse. Energetic nuclei with fast random motion can be obtained by heating up fusion fuels to very high temperature. At hundred million of kelvin[9], fusion reaction can be achieved on earth, and at this temperature, fusion fuels are in a plasma state.

To quantify the difficulty of three fusion reactions available on earth to produce energy (D-T, D-He, and D-D), we must quantify the probability of each one to happen by looking at their cross section. **Figure 0.2** shows the measured cross section as a function of the averaged center of mass energy of fusion system for different fusion reactions[10]. As can be seen, D-T fusion reaction has the largest cross section at the lowest energy (solid black line). Therefore, it is considered as the easiest one, and it was chosen for the first generation of fusion reactor.

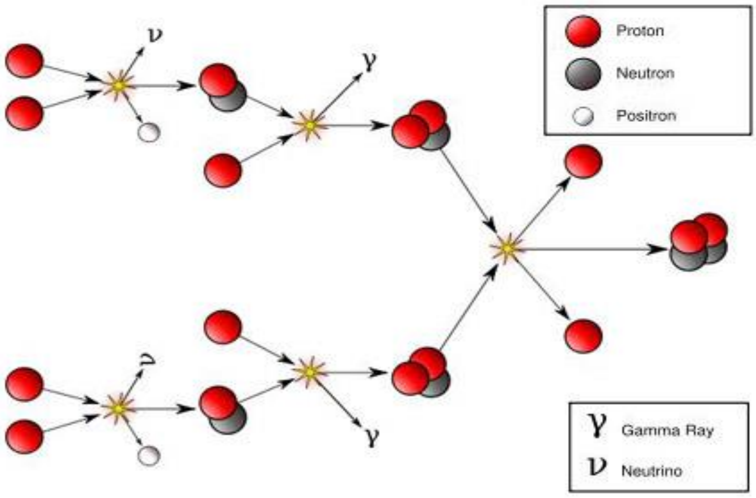

Figure 0.1. Proton- proton chain reactions in sun

D-T fusion reaction is shown in **Figure 0.3**. Once we reach the required temperature level, D and T collide, fuse and as a result, a huge amount of energy is gained. The total energy produced by the reaction is 17.59 MeV and is distributed between the products. Helium- 4 nucleus (α particle) comes up with 20% of the total energy (equivalent to 3.53 MeV) and a neutron comes up with the remaining energy (80% of total energy is equivalent to 14.06 MeV)[11].

After having chosen the fusion reaction, it is important to check its fuels availability. On the one hand, deuterium is about 1 % of hydrogen everywhere including oceans (2.10^5 mg of H per liter of water[12,13] and it can be extracted from sea water with low cost technique, so, it is easily available and for almost eternity. On the other hand, tritium is hydrogen isotope that does not exist in the nature because it is radioactive with a short lifetime (12.5 years). A process called breeding (see **Equation 0.5**) can solve tritium availability problem. The process consists of tritium production from lithium- 6 nucleus (Li can be mined from oceans 0.18 mg of Li per liter of ocean water[12,13]. Lithium reacts with a neutron coming from D-T fusion reaction. Breeding process can be done on a fusion reactor by putting a blanket containing Lithium around plasma where fusion reactions occur, and where neutrons are produced.[14]

$${}_{3}Li^{6}+ {}_{0}n^{1}\rightarrow {}_{1}T^{3}+ {}_{2}He^{4} \qquad \textbf{Equation 0.5}$$

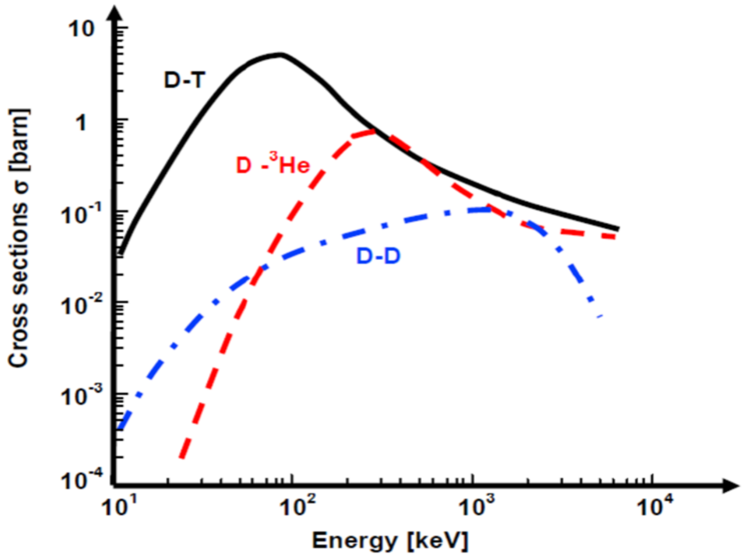

Figure 0.2. Measured cross sections for different fusion reactions as a function of the averaged center of mass energy. Reaction cross sections are measured in barn. (Image credit: M. Decreton, SCK-CEN).

One of the main challenges of fusion reactor is fusion reaction ignition. Ignition regime is established when the fusion power gain exceeds the fusion power losses. Power Losses can be described using a single parameter called “energy confinement time”’ τ_E, it is the characteristic time over which the energy is transported outside fusion system and lost in its environment. Required energy confinement time τ_E is determined by Lawson criterion. This criterion defines the minimum required value of the triple product of electron density n_e, ion temperature T_i and confinement time τ_E, required to ignite the fusion reaction[15]:

$$\mathbf{n_e.\tau_E.T_i \geq 3.10^{21}\ [keV.m^{-3}.\ s]} \qquad \textbf{Equation 0.6}$$

Lawson criterion imposes a temperature range going from 10 keV to 20 keV[16]. Vessel walls of fusion reactors would not withstand such temperature without being damaged. Hence, fusion plasma confinement is essential, not just to ignite reaction but also to protect walls of reactor vessel from the huge heat flux coming from hot D- T plasma.

One of the effective ways to confine fusion plasma and separate it from the walls is magnetic confinement. This approach is based on the use of a strong magnetic field to trap charged particles. Ions and electrons of fusion plasma are subject to electromagnetic force, they rotate and gyrate around magnetic field lines without touching walls.

To apply magnetic confinement on fusion plasma many magnetic field lines configuration were proposed. The simplest one is the linear configuration. In this case, an evident problem occurs with the two ends of the linear device where the particle can be lost. A simple solution to solve this issue is to close the magnetic field in a toroidal magnetic field configuration that can be obtained with many toroidal field coils[17]. With such coils geometry, magnetic field lines have a certain curvature and a field intensity gradient is present. This is leading to a drift that separate positive charge from negative charge. As a result, this charge separation creates an electric field E in the vessel. The E field combines with the toroidal B field and an (E x B) drift starts taking plasma out towards the walls. Charge separation phenomena can be avoided on a toroidal device by imposing a poloidal field to annihilate drift caused by toroidal coils geometry. These leads to a zero average net drift. The combination of toroidal magnetic field configuration with poloidal one provides a helical magnetic field configuration[18].

Tokamak device is the most promising design of magnetic plasma confinement; it is based on helical magnetic field configuration. In **Figure 0.4.** we can see resulting helical magnetic field from toroidal magnetic field produced by the toroidal field coils of tokamak chamber (blue coils) combined with the poloidal one produced by plasma current (green lines). Such device is providing not only a confinement quality, but also it naturally heats plasma thanks to the toroidal current that leads to ohmic heating.

In order or demonstrate feasibility and safety of fusion energy, a large cooperation involving seven partners (China, India, Japan, Korea, Russia, USA and European Union EU) has been set to construct an International Thermonuclear Experimental Reactor (ITER) in Cadarache, south of France. This project was officially launched in 2006 and the first plasma experiment is expected to be done in December 2025. ITER tokamak chamber will be the largest one in the world with a weight of 23 000 tones, a plasma radius of 6.2 m and a plasma volume of 840 m^3. The fusion power expected from ITER is about half of gigawatt (500 MW) and the fusion gainQ> 10. ITER ignition needs a temperature of 150 million °C. This temperature value is equal to ten times the temperature of the sun’s core. Such temperature value needs a performant heating system to be reached[19].

The first heating system is the ohmic heating. In a tokamak chamber, an ohmic heating power P_{ohmic} is generated by the toroidal plasma current I. Ohmic heating is not enough to heat fusion plasma up to the ignition temperature because its efficiency decreases when the plasma temperature is in the order of 2 keV[20]due to a drastic decrease of plasma resistivity. Thus, supplementary heating system must be installed One of the additional heating systems is the high frequency electromagnetic waves heating. It uses the principle of microwave oven that transfers heat to food. Plasma is heated up by radio frequency (RF) waves that transfer energy by resonant interactions with plasma particles. In a high frequency electromagnetic waves system, two sources are used: one for plasma ions heating and the second one is for plasma electrons heating. Each source uses a resonant frequency to match the cyclotron frequency of each species. An Ion Cyclotron Resonance Heating (ICRH) will operate in ITER at a resonant frequency ranging from 40 MHz to 55 MHz, and an Electron Cyclotron Resonance Heating (ECRH) will operate at 170 GHz[21]. Radio frequency (RF) heating systems are not enough to ignite and maintain plasma of ITER and will be associated to the Neutral Beam Injector (NBI). This heating system is considered as the most efficient one and is the focus of the present work.

Plasma heating by Neutral beam injector (NBI) is based on the injection in the tokamak of a high-energy neutral atom beam. In the plasma fusion core, the beam is ionized by the plasma itself and an energetic ion beam is progressively created there. Ions in plasma transfer energy by coulomb collisions with plasma particles and the plasma is heated up. Energetic neutral beam injected from NBI are important not only for plasma heating. It is possible to drive a non-inductive current in the plasma with these energetic particles[22]. Fast neutral beam is injected in a tangential geometry, parallel as possible to the toroidal direction of the tokamak. A toroidal plasma current is created in addition to the inductive one. Plasma is refueled, and confinement is improved.

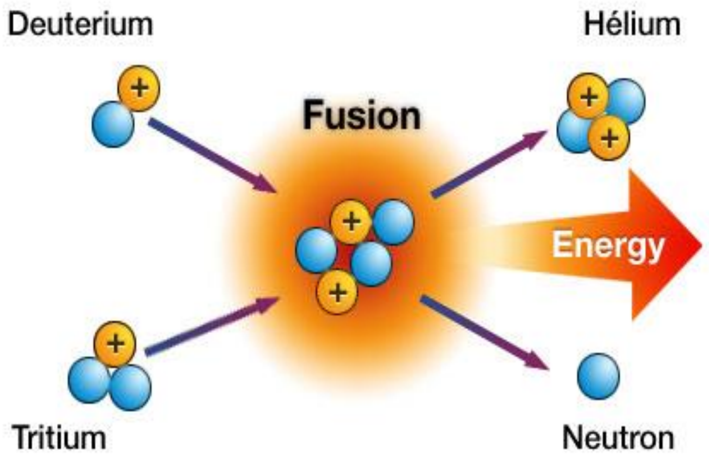

Figure 0.3. D-T fusion reaction

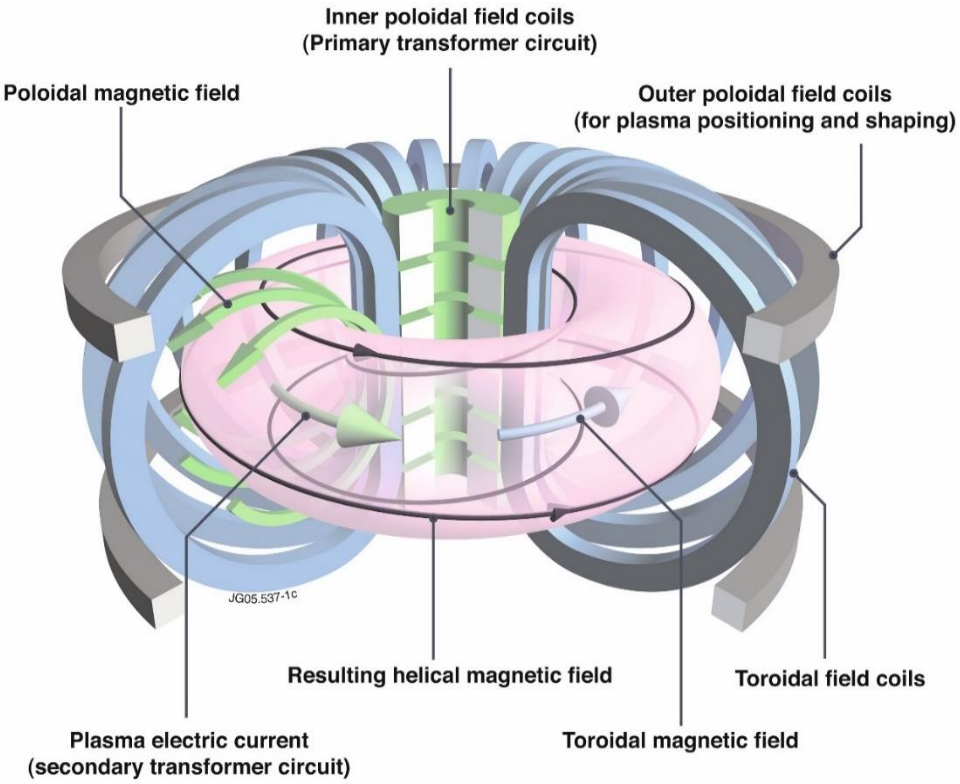

Figure 0.4. Magnetic field configuration in tokamak device[18]

The idea of using a neutral atom beam to be injected into fusion plasma volume comes from its ability to avoid the effect of magnetic fields. The later reign in tokamak chamber and would prevent the penetration of ions from outside as it prevents the escape of ions from inside. A highly energetic beam is recommended to achieve a good penetration in fusion plasma core, where the beam penetration distance increases with beam energy at a given plasma density. For this reason, a high energy of 1 MeV for D^0 beams required to reach a penetration distance of the order of few meters[21], which is the size of ITER and the future reactors that we are foreseeing to have.
The generation of fast neutral atom beam occurs in three steps[21]:

- generation of a powerful ion beam in the range of several MW
- neutralization of the powerful ion beam in a gas target
- transport of the neutral atoms to the torus, deflection of the non-neutralized ions to a so-called ion dump

The Neutral beam injection (NBI) system for ITER is based on the acceleration and neutralization of a negative ion beam (D^-). The reason of using negative ions for ITER can be concluded from **Figure 0.5.**

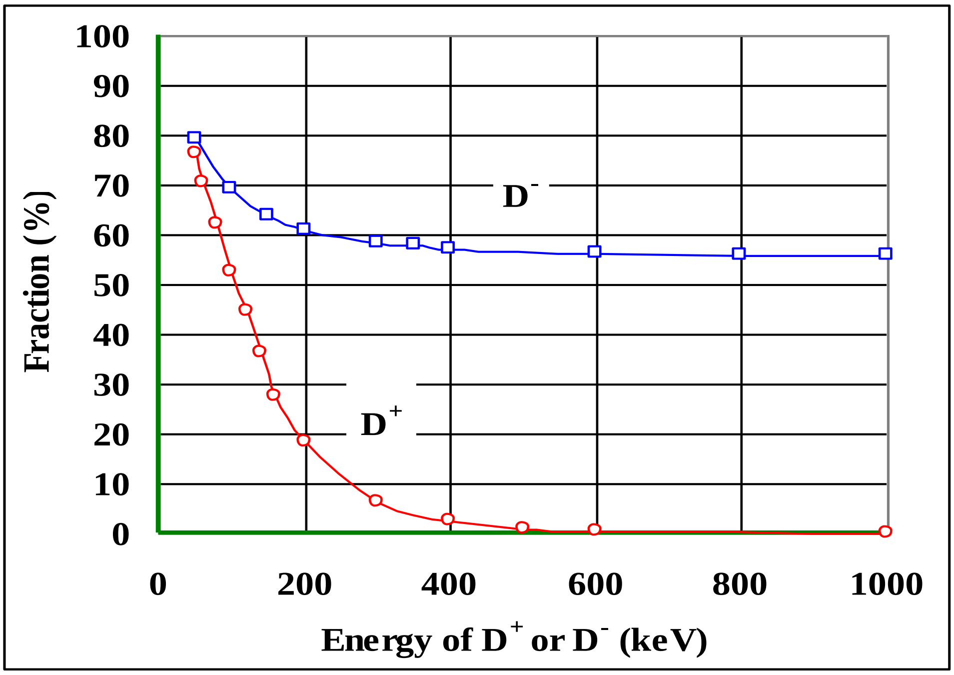

Figure 0.5. Maximum neutralization efficiency (fraction in %) of deuterium ions as a function of energy[21].

The later shows the variation of neutralization efficiency of D^- and D^+ with respect to the ion beam energy. We can see that the negative ions have a high neutralization yield of 55% even at high ion beam energy contrary to the positive ions where it is almost 0% after 400 KeV[23]. Therefore, the generation of the required neutral beam D^0 at 1 MeV for ITER is impossible from a D^+ ion beam and a performant negative ion source is needed for such NBI system. Different components of neutral beam injector for ITER are shown in **Figure 0.6.**

Principal one is the negative ion source where 55 A of D^- are generated, then extracted from the source to be accelerated to 1 MeV by an electric field which reigns just after NI source. Powerful negative ions beam (40 A at 1 MeV) enters neutralizer and collide with a D_2 gas target. Electrons are easily stripped away from D^- ions, which are converted to D^0 atoms as follows:

$$\mathbf{D^{-*} + D_2 \rightarrow D^{0*} + e^- + D_2^+} \qquad \textbf{Equation 0.7}$$

After beam neutralization, a residual ion dump actively cooled separates neutral beam particles from remaining ions by deflecting them using a magnet. Currents of 10 A of D^+ and 10 A of D^- at 1 MeV are filtered out and a net neutral beam of D^0 at an energy of 1 MeV and a power of 16.5 MW is ready to be injected in tokamak chamber. In ITER reactor, two neutral beams injector will be installed, each system has a length of 15 m, a width of 4.7 m and a height of 5.3 m. The totals delivering power of those two systems are 33 MW [21,24,25,26].

Negative ion source is a key component for NBI heating system for ITER. The development of such system is important for huge fusion device. We have seen before that negative ions were chosen for ITER NBI system, referring to their high neutralization yield (55%) at high energy (1 MeV). This NI advantage in neutralizer stage (easy electrons detachment from H^-/D) plays an opposite role in source stage leading to difficulty to produce high negative-ion current. Indeed, the binding energy of H^- electron is only 0.75 eV[27]

Negative Ions current outgoing of the source for effective heating of ITER plasma must be 69 A in hydrogen and 57 A in deuterium[28]. These currents are intense and difficult to be obtained experimentally. Therefore, to reach these goals the understanding of negative ions production mechanisms in source conditions must be improved.

In a negative ion source, H-/D- negative ions are produced in an (H_2/D_2) low-pressure plasma and subsequently extracted and accelerated. Negative ion production in low-pressure plasmas relies on two distinct mechanisms. Depending on where the ions are formed, we distinguish volume production and surface production. NI volume production is associated with dissociative attachment of cold plasma electrons (~ 1 eV) on vibrationally excited molecules[29,30]. Surface NI production is associated to the capture of one or two electrons by neutrals atoms or ions impinging on the surface.

In a low-pressure plasma, NI volume production is usually the main NI production mechanism and NI Surface production is often considered as a mechanism of minor importance. However, in certain conditions it can be very efficient. When a surface with appropriate electronic properties is bombarded by plasma, a huge negative ion yield is produced. Belchenko et al (1973) observed this experimental result for the first time by putting in contact to the plasma a surface covered by Cesium (Cs) that led to an important conclusion[31,32]: low work function surface such as Cs covered surfaces is favorable for NI surface production. Negative ion surface production enhanced by Cesium injection is the principle used in intense negative ion sources for fusion of for particle accelerators[33,34]. It is nowadays the only scientific solution known to reach high D^- negative ion current meeting ITER requirements. Cesium (Cs) is injected in vapor state inside diffusion chamber. It deposits on the surface of plasma grid. Deposition of cesium Cs on the grid lowers the material work function. This effect increases electron capture efficiency by neutral particles leaving surface after plasma bombardment.

The ITER NI source operates with a low pressure Inductively Coupled Plasma (ICP). It is composed of eight drivers. Each driver is an ICP generator supplied with 100 kW of RF power. The dimensions and main components of ITER RF driven ion source are shown in **Figure 0.7**. The source must generate an intense NI current density of 200 $A.m^{-2}$, over a large surface of 1.2 m^2. Extracted D^- flux with 5%-10% uniformity during long operation period (1 hr.) is targeted. A low co- extracted electron-current (below one electron per negative ion) is also required. This latter is possible by application of a transverse magnetic field (50 Gauss) between plasma diffusion region and NI extraction region. Hot electrons generated within the drivers are cooled down and filtered out using this magnetic field barrier. ITER NI source is based on Cs injection[35]. The development of ITER NI source is the subject of several researches in different country. In Germany, IPP Garching operates two test beds: BATMAN and ELISE[36]. BATMAN is a small ion source with a single RF driver (one eighth of the ITER source). It offers a great experimental flexibility and it is equipped with a very comprehensive set of diagnostics. ELISE is an ion source composed of four RF driver (half the size of the ITER NI source). This test bed investigates mainly the source behavior in long pulses and questions related to size scaling. In Toulouse France, LAPLACE laboratory conducts experiments on plasma transport across the magnetic field[37]. In Italy, it was decided to build the NBI test facility PRIMA (Padova Research on ITER Megavolt Accelerator). It includes SPIDER (full size NI source composed from eight drivers) and MITICA (prototype of the whole ITER injector)[38,39]. In parallel, a modeling work on Cs-seeded ion source is carried out in IPP Garshing, Laplace laboratory[40,41,42,43], Sofia University and technical University Sofia (Bulgaria)[44] in collaboration with CEA Cadarache.

Studies conducted at IPP Garshing show that by using Cs injection, the ITER negative ion source could reach the required high current densities. However, drawbacks of the use of cesium have been identified. First, a high cesium consumption in the range of 5-10 µg. s^{-1} [45,46]is observed. Since cesium is continuously injected in the source to obtain, a stable negative ion current over long shots. Secondly, cesium diffuses and pollutes accelerator. This contamination might cause parasitic beams and/or voltage breakdowns and imply a regular and restrictive maintenance in a nuclear environment. Finally, long-term operational stability with cesium requires a strict, long, difficult and controlled conditioning of the negative ion source[47]. These three issues complicate the operation of ITER NBI source and push towards an alternative solution. The goal is to reduce strongly cesium consumption or even develop a cesium-free ion source for new generation of NBI systems[25]. Such systems could be used for the future fusion reactor DEMO (Demonstration Power Plant)[48]. The aim of the present work is to investigate alternative materials to cesium for surface production of high negative ion yields in low pressure H_2 or D_2 plasmas.

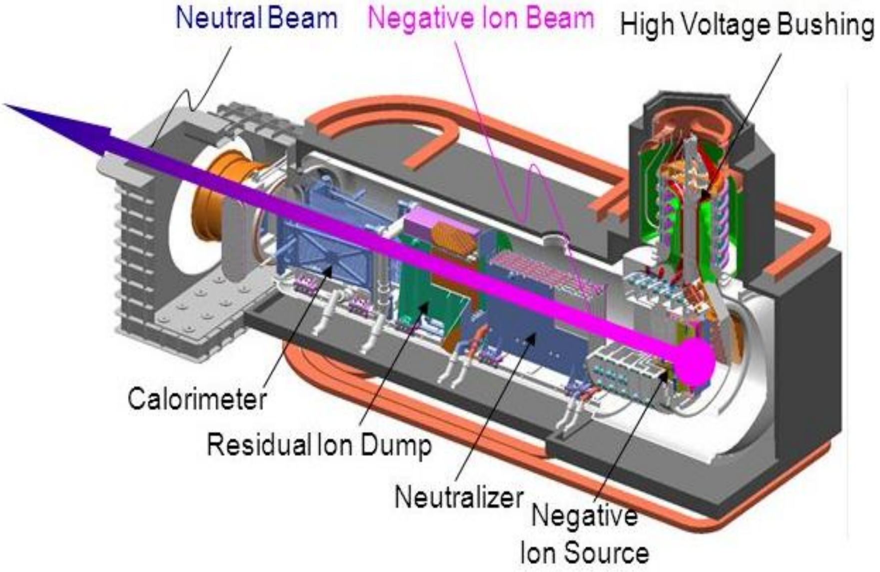

Figure 0.6. Neutral beam injector (NBI) system and the beam line for ITER with the description of main components and the process-taking place[28]

.

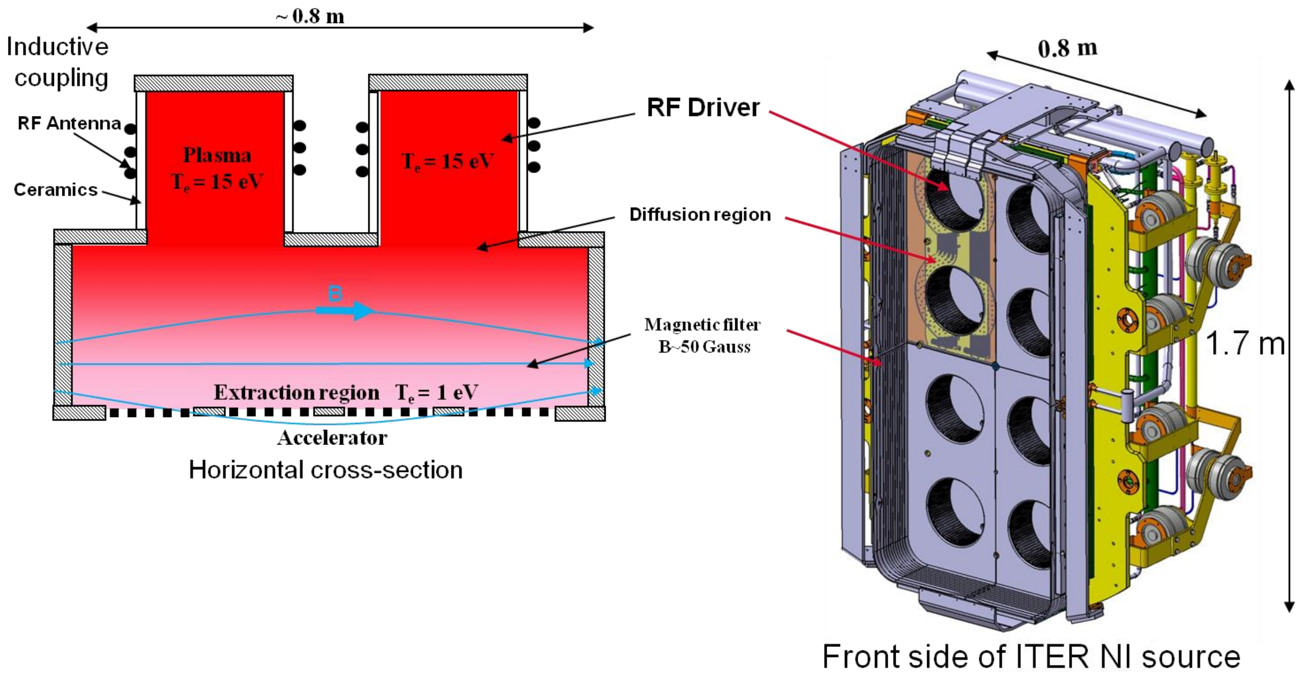

Figure 0.7. The ITER RF driven ion source: horizontal cross-section of an individual section (composed of two ICP drivers) on the left; the front side of the complete NI source on the right. Dimensions and description of the main components are given.

This thesis presents a study of NI surface production in Cs- free H_2/D_2 plasmas on different materials (HOPG, diamond and C12A7 electride surface). The research work is summarized in five chapters. **Chapter 1. Negative ion surface production measurements** explains the general principale of the negative ion surface production measurements and gives the details of the employed experimental set- up PHISIS. The experimental protocol used for several types of measurements is also specified therein. **Chapter 2. Modeling of NIEDF** is dedicated to the modeling of surface produced NI energy and angular distributions functions. A study of the impact of positive ion energy on carbon- surface (graphite and diamonds films) production of negative ion in deuterium plasmas is presented in **Chapter 3 Impact of positive ion energy on NI surface production.** The **Chapter 4. Pulsed bias approach** provides information about the newly developed method of pulsed bias which has enabled the study of NI production on surfaces of insulating materials. A model is presented to describe the behavior of insulator sample immersed in plasma and biased in pulsed mode. The last chapter entitled **Chapter 5. NI production from a nanoporous C12A7 electride surface** presents a study of negative ion surface production on a nanoporous C12A7 electride surface in different experimental conditions.

Chapitre 1 Negative ion surface production measurements

1.1 General principle of measurements

The main idea of the thesis is to study Negative- Ions (NI) surface production in low pressure hydrogen and deuterium plasmas. Surface negative ion production measurements are performed in the diffusion chamber of a plasma reactor. The sample is placed inside the plasma. It is negatively biased with respect to the plasma potential. So, the plasma positive ions are accelerated towards the sample surface by the electric field formed in the sheath (plasma-sample surface). The positive ions bombardment leads to a negative ions surface production on the surface. The produced negative ions are accelerated towards the plasma and self- extracted from the plasma towards a mass spectrometer placed in front of the sample. The mass spectrometer collects them according to their mass and energy. This measurement gives the negative ion energy distribution function (NIEDF). The general principle of negative ions surface production measurement is shown in detail in **Figure 1.1**. This experimental arrangement has two advantages. First, studied materials are not deposited on an extraction grid and they can be changed easily thanks to a fast load lock system. Second, negative ions are self-extracted leading to simple ion extraction physics. On the other hand, this experimental method represents a main disadvantage, a negative surface bias is required to get the self-extraction effect. Therefore, the positive ion bombardment damages the surface and create defects. The exposed material is different from the pristine one and its surface state must be characterized.

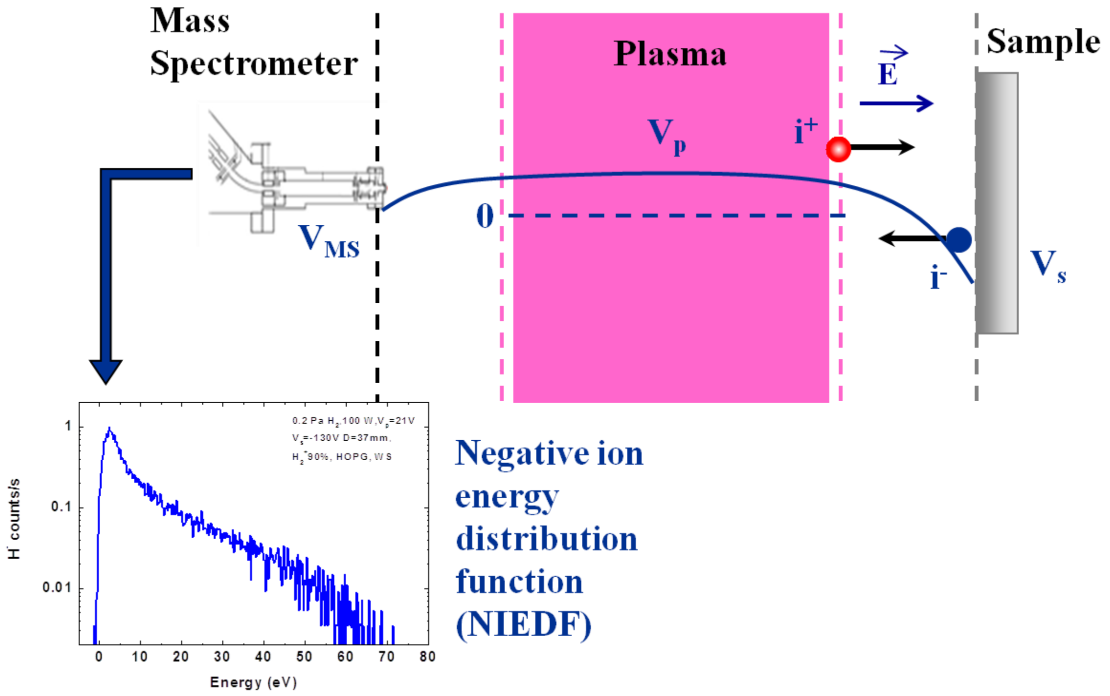

Figure 1.1. Principle of negative-ion measurements on PHISIS set-up with potential profile between the sample and the MS. V_p – plasma potential, V_s – surface bias, V_{MS} – mass spectrometer potential. Output: negative ion energy distribution function (NIEDF).

1.2 Helicon reactor PHISIS

The helicon reactor PHISIS (Plasma Helicon to Irradiate Surface in Situ)[49]is shown in **Figure 1.2**(a). This reactor is the result of a collaboration between PIIM Laboratory and Research laboratory of Australian National University (Canberra). It was done by Anutech society and installed in 1998 by Marcel Carrère and Jean-Bernard Faure. This reactor was initially developed to generate a plasma of high density (>10^{11} cm^{-3}) like plasma near tokamak walls. The goal of such device was the study of different physical phenomena related to the problem of tokamak walls erosion. Helicon design was chosen for this reactor, because it can generate a plasma of high density.

This reactor is composed from two principals' chambers:

A) The source chamber where the plasma is produced
B) The diffusion chamber where the plasma is diffusing

Source chamber is the superior part of this reactor and it has a cylindrical shape. The diffusion chamber corresponds to the inferior one and it has a spherical shape.

1.2.1 Source chamber

The source chamber consists of three main parts: an antenna, a Pyrex tube and two coils. The Pyrex tube has a length of 200 mm, an external diameter of 150 mm and a thickness of 7 mm. It is surrounding by a Boswell antenna (helicon antenna)[50] made of copper. There is a provision to use a magnetic field (vertical direction) in the source chamber of the plasma reactor[51]. However, no magnetic field was applied in the plasma reactor so that only capacitive and inductive plasma coupling could be used. All experiments have been performed in the capacitive mode (E-mode).

1.2.2 Diffusion chamber

Once the plasma is generated, it diffuses in this part of the reactor. This chamber is a sphere of 200 mm of diameter. It is formed from stainless steel. The diffusion chamber is where plasma- surface interaction takes place. The sample is localized in the center of this chamber. A mechanical grounded screen was placed horizontally (5 cm above the sample) between the source and diffusion chamber[52] (see **Figure 1.2**(c)). This screen minimizes radio frequency RF fluctuations of plasma potential in the case of RF capacitive plasma coupling. Different diagnostics tools are installed there: a mass spectrometer, a pressure gauge and a Langmuir probe. It contains several portholes to monitor the general state of plasma and sample.

1.2.3 Radio frequency generator and matchbox

The plasma is initiated by a Huttinger PFG 1600 RF generator. It operates with a frequency of 13.56 MHz and it delivered a maximum power of 1600 W. This generator is followed by a Huttinger PFM 3000A matchbox L configuration[51]. This latter minimizes reflected power by plasma towards the generator by an impedance matching. This matching is automatically controlled by the generator.

1.2.4 Gaz injection and pumping system

To work in a plasma with low rate of impurities, a performant pumping system is used. The base pressure in the reactor is provided by two pumps: a primary pump (Alcatel 2012A) which sets a vacuum pressure in the order of 10^{-4} mbar and a secondary turbomolecular pump (Alcatel ATP400, pumping velocity 400 l/s) to reach a vacuum in the order of 10^{-7} mbar. The reactor volume is 20 l. So, it is pumped quickly. The set-up is equipped with a load lock system pumped to 10^{-3} mbar by a primary pump identical to the previous one. Another pumping system is used for the mass spectrometer. The base pressure of 10^{-8} mbar is achieved in the mass spectrometer using a primary pump followed by a secondary turbomolecular pump (80 l/s). The base pressures in the reactor and the mass spectrometer were monitored by two ionization gauge[50]. The gas injection into the reactor was realized by two types of flow controller. The hydrogen/deuterium gas injection is done by BROOKS Mass Flow Controller 5850TR of 20sccm (with 5.2sccm for hydrogen and 7.6sccm for deuterium). The argon/ helium gas injection is done by 100sccm MKS mass Flow Controller. To set the desired working pressure in the chamber a 150mm inner diameter Riber gate valve is installed just before the turbo molecular pump[51]

1.2.5 Transfer rod and sample holder

The transfer rod is manufactured by the German company HGK. It is a sliding rod formed from stainless steel **(see Figure 1.2**) allowing to load the sample in the load lock system and bring it in the center of the diffusion chamber. It serves also as sample holder. The sample holder is 35 mm in length, 19.7 mm in width and 12 mm in height (see **Figure 1.2**(b) and is made of molybdenum. The sample is clamped on the sample holder by a thin (0.2 mm) molybdenum clamp with a circular central hole of 8 mm in diameter. The sample holder allows to bias the sample by an external DC bias supply (max of 1 kV). The heating of the sample is done by a current circulating in a resistive heater embedded inside the sample holder. Different details of the sample holder are shown in **Figure 1.2**(b).

1.2.6 Mass spectrometer

The main diagnostic tool employed to study NI surface production on PHISIS set-up is the mass spectrometer Hiden EQP 300 (Electrostatic Quadrupole Plasma). It combines the electrostatic analysis sector for energy with a quadrupole mass filter of high performance. The MS Hiden EQP 300 is designed for energy analysis between 0 and 1100 eV for a mass up to 300 a.m.u. Schematics of the Hiden EQP MS is represented in **Figure 1.4** with a brief description of the main components. The MS could function in two modes: Residual Gas Analysis (RGA) and Secondary Ion Mass Spectrometry (SIMS). The RGA mode is used to analyze the mass and energy of the neutral species (molecules, radicals, atoms). In the SIMS mode the ions (positive or negative) are extracted from the plasma and detected. A maximum pressure of 10^{-6} mbar inside the MS is necessary to perform the measurements to limit the collisions between the analyzed species and the gas present in the device. The entrance orifice of the MS connecting it to the diffusion chamber is 100 µm in diameter which is small enough to maintain the pressure below 10^{-6} mbar even in the presence of a gas pressure in the order of 10^{-3} mbar in the plasma chamber. The MS is controlled by a PC via MASsoft software produced by Hiden Analytical. It allows to acquire, store and manipulate the mass spectra and the energy distributions of neutrals, as well as positive and negative ions. In addition, this software allows to choose the potential values of each lens of the mass spectrometer and to visualize the spectra. It permits the MS tuning to maximize the measured signal. This is done with the help of an autotune file which is provided by MASsoft and it could be customized or generated manually. The autotunes procedure allows an automatic alignment of different MS lens. Therefore, the internal transmission of the spectrometer is optimized. Typically, when the energy of the ions arriving at MS orifice is changed significantly (by more than 20 eV) the autotune procedure should be redone to improve the collection of ions.

The MS is composed of four main parts: extractor, energy analyzer, mass filter and the detector (see for details **Figure 1.5**):

The extraction of ions is realized by a polarizable orifice of 100 µm (**Figure 1.6**). The extractor potential V_{ext} could be defined directly by MASsoft and is adjustable between –100 V and +360 V. This orifice is followed by the first focusing lens ‘’lens1’’ which isused to extract ions rapidly from the extraction region and to focus the beam on the energy filter. It also serves to remove ions during neutral measurements.

All the lenses are floating on a reference potential V_{ref} which can be varied between –1000 V and +1000 V (bias scheme of MS electrodes is shown in Figure 7). The voltage of the MS orifice is set to the sum of the voltages applied to the extractor and to the reference: $V_{MS} = V_{ext} + V_{ref}$. The orifice potential has a big influence on the shape of the sheath in front of the MS and thus on the trajectories of the NI

The ions focused by Lens 1 go through a drift tube (Axis) and reach the energy filter. The pass energy in the filter has been set to 40 eV for all experiments. Basically, the ion energy is determined from the voltage that must be set onto the "energy" power supply (see **Figure 1.7**) to slow down or accelerate the ions to the pass energy. The voltage of the "energy" power supply can be scanned from -100 to +100 V. After the energy filter the ions are focused towards the mass filter and then detected thanks to a channeltron detector giving a result in terms of counts per seconds.

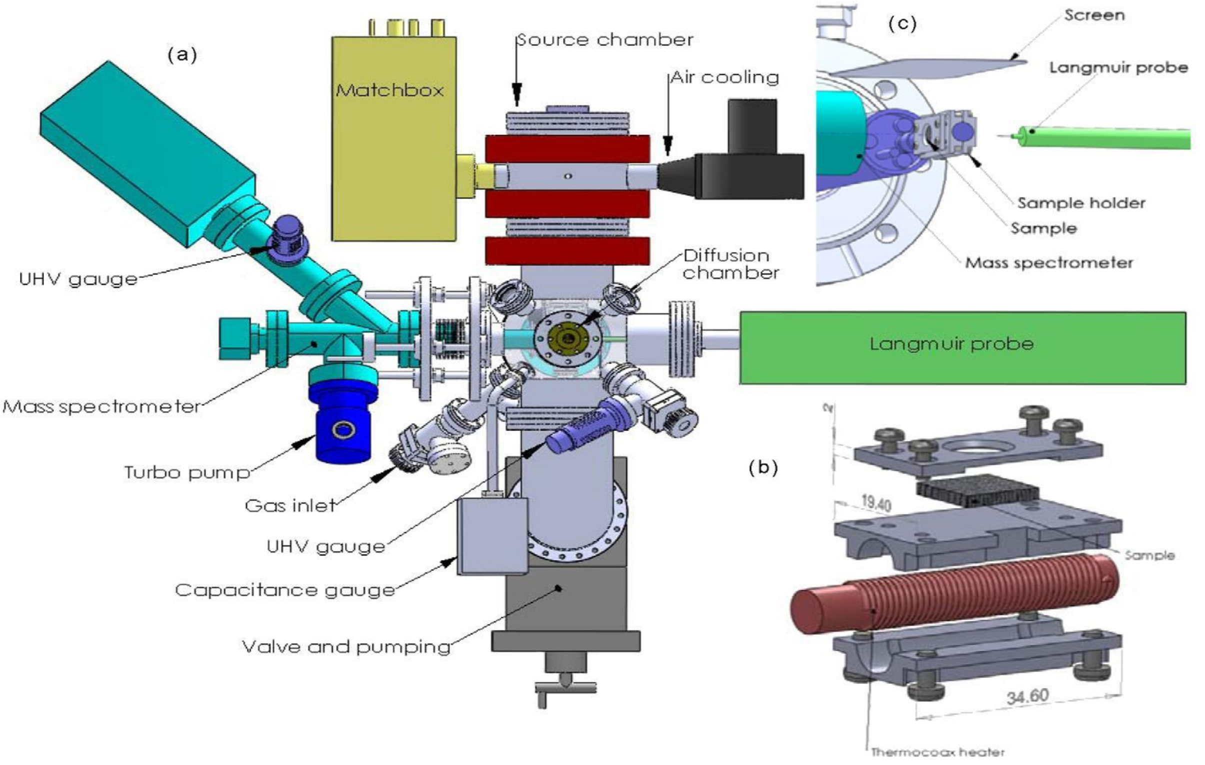

Figure 1.2 (a) Experimental set-up PHISIS, **(b)** details of the sample holder, **(c)** inside the diffusion chamber showing the sample holder, Langmuir probe and MS.

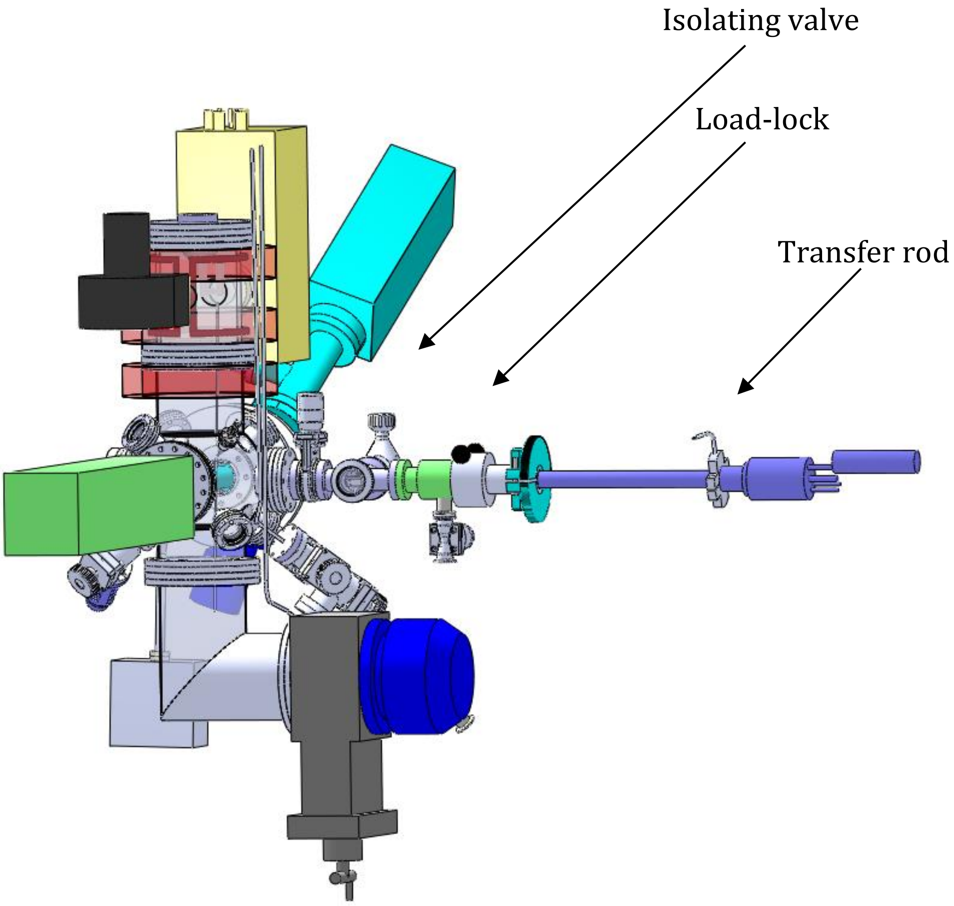

Figure 1.3 Experimental set-up PHISIS with outgoing transfer rod.

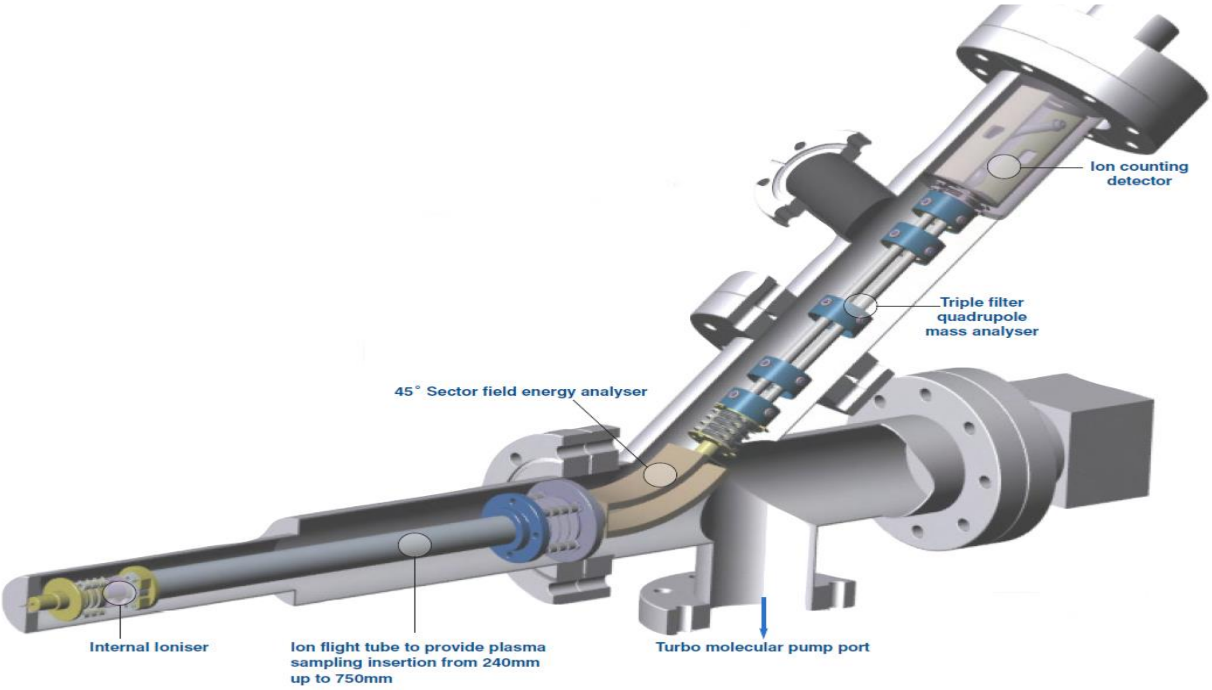

Figure 1.4. 3D schematics of the HIDEN EQP - the mass/energy analyser for plasma diagnostics and characterisation.

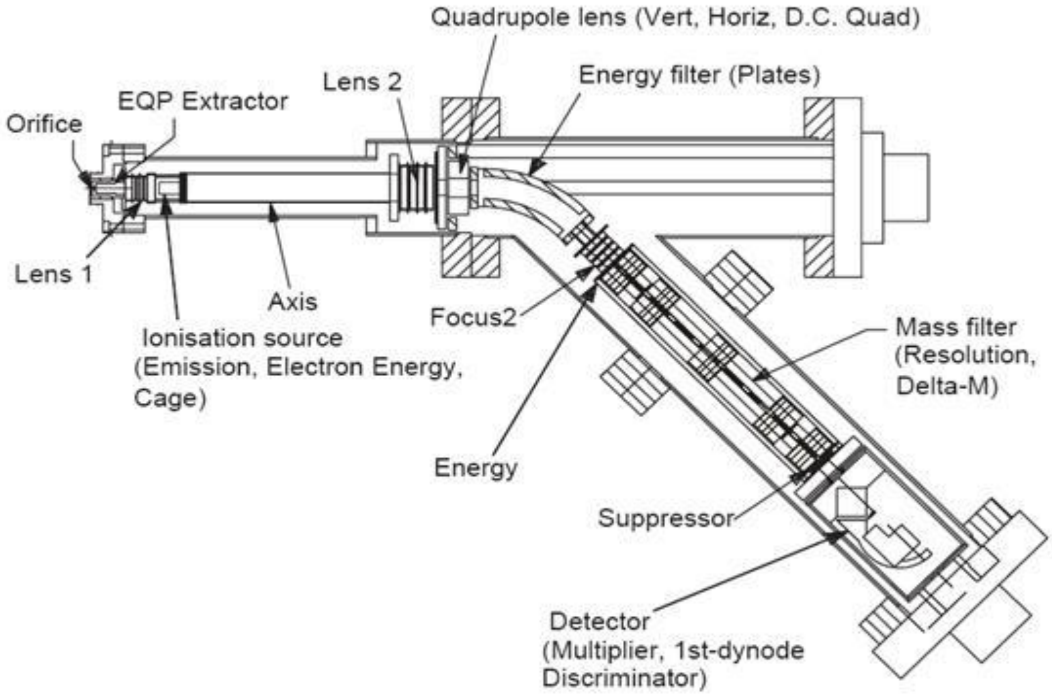

Figure 1.5 Scheme representing the HIDEN EQP MS with its main components and electrodes. For complex components like mass and energy filters the individual electrodes are specified in the brackets.

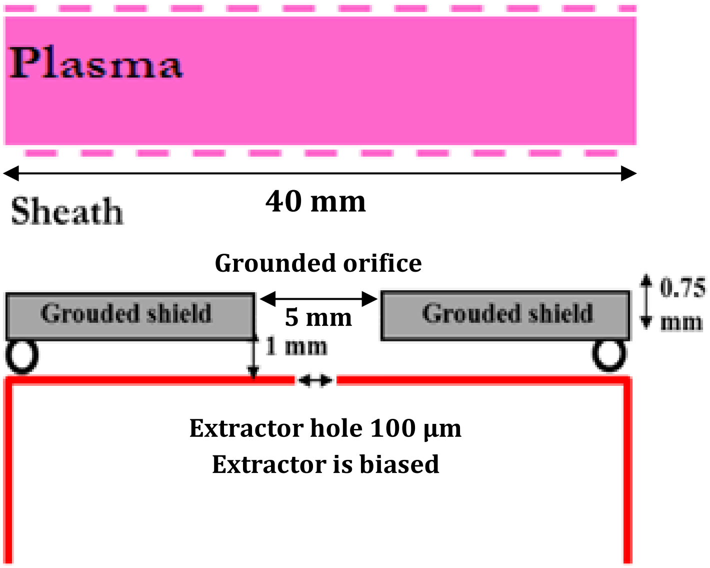

Figure 1.6 Schematic representation of the used MS nozzle configuration (grounded shield).

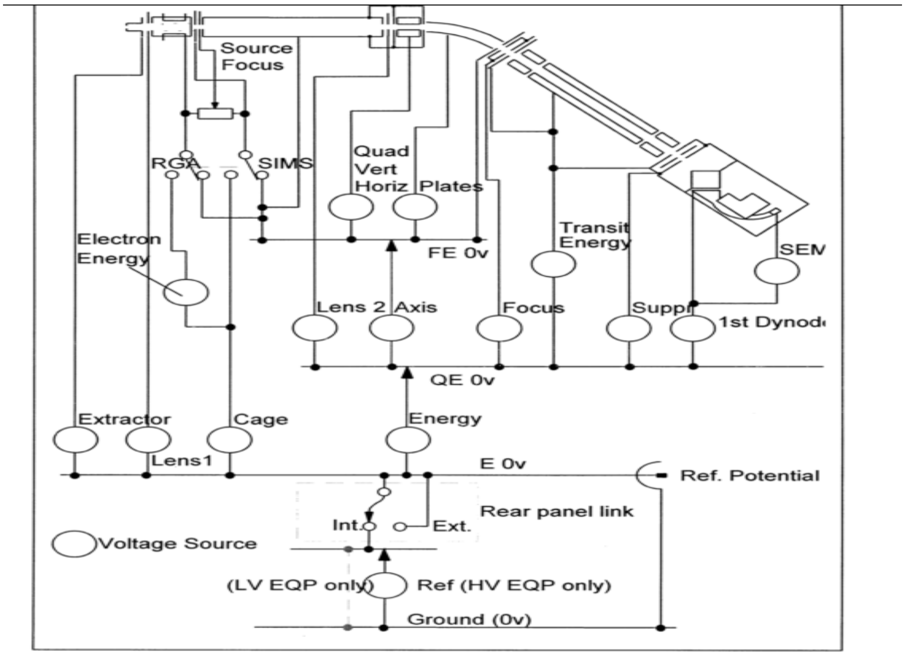

Figure 1.7 Schematic representation of the lens potentials in the mass spectrometer.

1.3. Experimental protocol

1.3.1 Materials

In our experiment, the base pressure in PHISIS setup was typically maintained below 5.10^{-7} mbar. Before introducing the sample inside the reactor, the load lock chamber was pumped down to 10^{-3} mbar, and then the valve separating the load lock system and the diffusion chamber was opened. Once a pressure of 10^{-3} mbar has been reached, plasma has been ignited at least for 10-15 minutes to condition the reactor with a sample still in load lock (the plasma was not diffusing inside the narrow arm). Consequently, the sample was introduced inside the reactor with a help of the transfer rod and the measurements were performed. The most important samples studied within this thesis are:

- **Highly Oriented Pyrolitic Graphite (HOPG)**

HOPG (Highly Oriented Pyrolytic Graphite) has been chosen as a reference material for the study because of its high production rate of negative ions[53,54,55] and because of its simplicity to cleave and clean. The HOPG material[56,57] was of ZYB type purchased from MaTeck GmbH Company. The density and electrical resistivity of HOPG were 2.265 g·cm^{-3} and 3.5 × 10^{-5} Ω·cm, respectively. Before performing any experiments with HOPG, a certain preparation procedure was followed. HOPG was cleaved by using tape which remove several monolayers from the top surface, thereby providing a “pristine” sample.

- **Diamond**

Diamond is another perspective material for high production rate of NI surface production[47]. Given its low or even negative electron affinity and variable wide energy band gap (depending on the doping), diamond present electronic properties that may be advantageous for negative-ion production[58,59]. It is well known for its ability to emit electrons at high temperature and even at low electric fields[60].Beam experiments on diamond showed surface production of H^- ions with high yiels up to 5.5%[61].Moreover, it has been observed in plasma experiment that NI production rate on boron doped diamond can be increased by factor 5 when increasing the the temperature to 400°C[52,49].This has raised the interest to study NI production on heated surfaces in plasma. Polycrystalline **MCBDD** (MicroCrystalline Boron Doped Diamond) and **MCD** (MicroCrystalline Diamond) films were deposited at LSPM laboratory by using plasma-enhanced chemical vapor deposition (PECVD) in a bell jar reactor (PLASSYS BJS 150) operating with a mixture of H_2, CH_4 and B_2H_6 gases for **MCBDD** and the mixture of H_2 and CH_4 for **MCD**[62].The films were deposited on a <100> oriented 1 mm thick silicon substrate. The deposited diamond layer for **MCBDD** had a thickness of 3.2 ± 0.1 µm (determined by the weight gain of the substrate). For **MCD** the layer thickness is 17.5 ± 0.5 µm (determined from confocal microscopy pictures). The grain size for **MCBDD** samples are about 2.5 µm in the horizontal plane and much bigger for MCD, on the order of 10 µm, as seen by scanning electron and confocal microscopy pictures. The charge carrier density for **MCBDD** was estimated to be 10^{19} - 10^{20} cm^{-3}, which leads to good electrical conductivity for biasing of the diamond layer. Hydrogenated diamond surfaces are usually conductive. However, it has been observed that under plasma exposure at surface temperature lower than 300°C, **MCD** samples loss their surface conductivity[63], most probably because of the creation of a defective layer on top of the diamond thin film. Nanocrystalline Diamond (**NCD**) films were deposited at the LSPM laboratory using the following gas mixtures: 1% CO_2 / 1% CH_4 / 98% H_2 for NCD 1% and 5% CO_2 / 5% CH_4 / 90% H_2 for NCD 5%. They were characterized at PIIM laboratory by Scanning Electron Microscopy (SEM) prior to plasma exposure. The measurements were performed on ESEM Philips XL 30 device with a resolution of *5 nm* in the Microscopy Center of Aix-Marseille University. **Figure 1.8** shows SEM images of unexposed surfaces of diamond materials. By looking at the images of microcrystalline diamond films (**a** and **b**), one could see crystals of *~ 5 µm* in size. The height of these crystals lies in the range of *µm*, as could be concluded from AFM image of MCD shown in **Figure 1.8**. On the contrary, the nanocrystalline diamonds (parts **c** and **d**) demonstrate a much finer structure. In case of NCD 1%, one could observe small grains ~ *50 nm* in size forming a homogeneous arrangement on the top surface. There are also big grains of *300-500 nm* in diameter which could produce agglomerations sizing in several µm. NCD 5%, on the other hand, exhibits the grains of a larger size (~ *100-200 nm*) which form cauliflower type structures on the top surface. The size of these structures covering completely the surface of the film varies from *0.2* to *0.6 µm*. The composition of all the grains is the same, as verified by Energy-dispersive X-ray spectroscopy (EDS). The EDS spectrum shows an intense C peak and a weak Si peak (coming from the substrate), and the peak ratio is constant for all the grains. The diamond films were originally deposited on a circular Si wafer 5 cm in diameter. They were first cleaved to getsquare samples of 1 cm by 1 cm approximately.

- ### Nanoporous 12CaO. 7Al_2O_3 electride surface

The C12A7 (12CaO. 7Al_2O_3) is an ionic crystal. It is an electrical insulator and well known as a good refractory oxide[64]. However, it can be converted to a persistent electronic conductor by utilizing its intrinsic nanostructure. The chemical formula for the unit cell of this crystal lattice is represented as $[Ca_{24}Al_{28}O_{64}]^{4+} + 2O^{2-}$: the former denotes the cage framework and the latter are called ‘free oxygen ions’. Two free oxygen ions are clathrated in the unit cell to compensate the positive charge of the cage framework. In 2003, Hosono et al. revealed that this refractory oxide 12CaO. 7Al_2O_3 (C12A7) can be transformed to an electride with a low work function [65],[66], by exchanging clathrated oxygen ions as the counter anions from the positively charged crystallographic cages of C12A7 leading to formations of high density electrons in the cages. When 100% of the clathrated oxygen ion were removed, a conductivity of approximately 1000 Siemens/cm at 300 K was observed, demonstrating that the encaged electron behaves as an anion[67]. They reported that the obtained $[Ca_{24}Al_{28}O_{64}]^{4+} + 4e^-$ could be regarded as an electride, and demonstrated the unique properties including a very low work function of 2.4 eV with a high thermal and chemical stability[68]. All those electronics properties encourage the study of negative ion surface production on C12O7 electride surface.

C12A7 electride sample was covered by a protective layer. This latter was removed by heating the sample in vaccum for 30 min under 500°. The heating was followed by Ar plasma bombardment for 10 min. This cleaning process is followed by a mass scan of different impurities in the diffusion chamber and a complete removing of the protective layer is ensured.

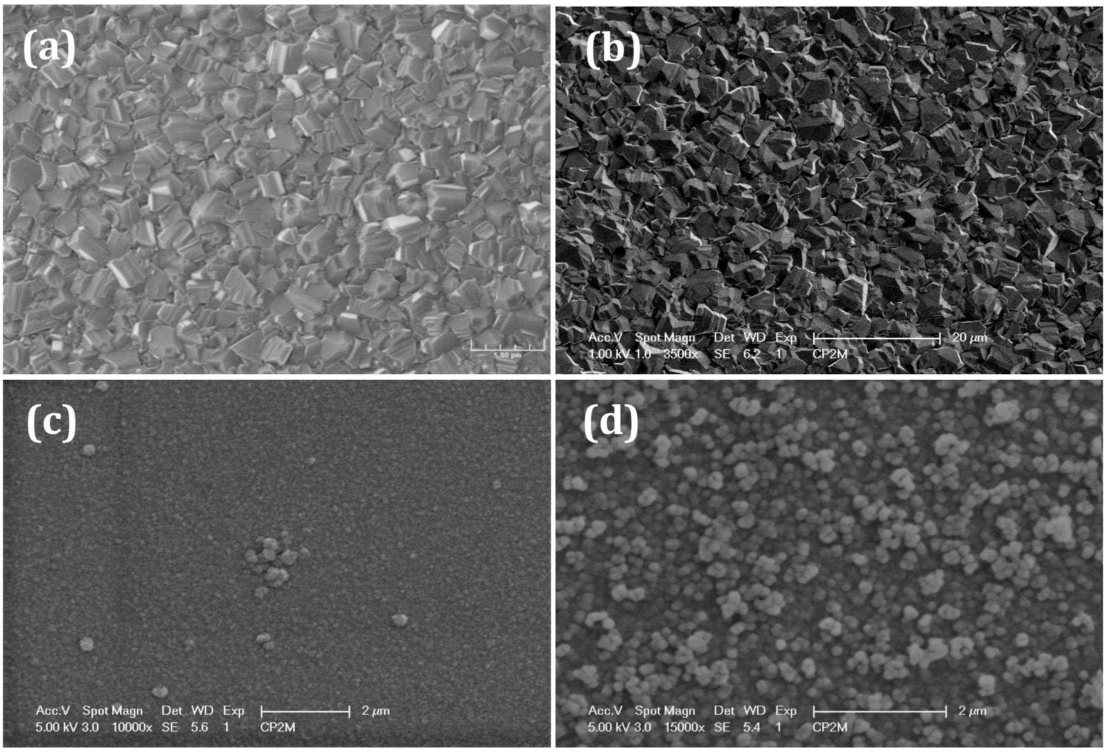

Figure 1.8 SEM images of unexposed surfaces of diamond materials: **(a)** MCBDD, scale 5 µm; **(b)** MCD, scale 20 µm; **(c)** NCD 1%, scale 2 µm; **(d)** NCD 5%, scale 2 µm.

1.3.2 Plasma conditions

A) Radio frequency (RF) plasma

To simplify the interpretation of NIEDF measurement, we have chosen to work in a plasma condition where one type of positive ions is dominant, and where fluctuations of plasma potential were as small as possible.

A. Ahmad in his thesis has performed NIEDF measurements for different RF power at low pressure (0.2 – 2 Pa). He observed that NIEDF shapes were increasingly influenced by plasma potential fluctuations when RF power was increased. He concluded that low RF power was favorable to reduce RF fluctuation effect on NIEDF measurement. Therefore, a low power of 20 W was chosen and to further decrease plasma potential fluctuation influence on NIEDF he installed a grounded screen between the source chamber and the diffusion chamber (see experimental part). We have chosen, for the same reasons, to work in the same experimental conditions.

A. Ahmad also investigated the relative percentage of each positive ion (H^+, $H_2^{+,}$ H_3^+) in hydrogen plasma. The author showed that in a RF plasma, a pressure range 0.9 Pa- 2 Pa of H_2 is ideal to get a H_2 plasma with H_3^+ dominance. At this pressure range the plasma was mainly populated with H_3^+ ions (~80%) for hydrogen and D_3^+ ions (~90%) for deuterium because of the fast conversion:

($D_2^+ + D_2 \rightarrow D_3^+ + D$).

In this thesis, we work at the same condition chosen by A. Ahmad and used then by K. Achkasov in his thesis. The RF H_2/D_2 plasmas conditions are a pressure of 2 Pa and a RF power of 20 W. At this condition, the plasma density in the diffusion chamber, as estimated by the Langmuir probe, is around $n_e = 2 \cdot 10^{13}$ m^{-3} and the electronic temperature around $T_e = 3.5$ eV. The positive ion current flux to the sample is on the order of 10^{17} $m^{-2}s^{-1}$.

Let's note that that the injected power has been slightly increased in some experiments from 20 to 26 W. This increase of the power was required to maintain the plasma density as measured by langmiur probe and inferred from sample current, at the level of our previous studies at 20 W. Most probably a change of antenna to plasma coupling has occurred maybe due to mechanical change in the position of the antenna. Anyway, plasma parameters are identical, and results are directly compared for 20 W and 26 W.

B) Electron Cyclotron Resonance (ECR) plasma

To work at higher plasma density an ECR plasma source can be punctually installed on the experiment. Indeed, increasing the RF power applied to the plasma to increase both the positive ion flux and the resulting NI flux is not a satisfying solution, since it also increases the RF oscillations of the plasma potential, perturbing the measurement. The ECR source from Boreal plasma is shown in

Figure 1.9, the antenna was positioned in a radial position 5 cm away from the sample. It operated at 2.45 GHz, which gives electron resonance for a B field of 845 G (such value is reached less than 1 cm away the magnet). A more detailed description of the ECR source can be found in K. Achkasov thesis. The later proved that the NIEDF shapes are not affected by the magnetic field of the ECR source, which is around 50 G at the sample surface. this magnetic field is relatively small and should not affect the NI trajectories. Indeed, the Larmor radius for the NI accelerated by the sheath in front of the sample is more than 33 cm, which is much larger than the distance between the MS entrance and the sample. If the antenna is moved further than 5 cm from the sample, the measured intensity gets smaller, but the shape of the NIEDF is not changed. As far as the plasma homogeneity in front of the sample is concerned, a model has shown that n_e profile is homogeneous in the axial direction from a similar ECR antenna (no noticeable gradients on the scale of 1-4 cm) for 1 Pa Ar plasma at 50 W of absorbed power[69].

The conditions in H_2/D_2 ECR plasma are 1 Pa of pressure and 60 W of power. At those conditions, H_3^+/ D_3^+ is the dominating ion, the plasma density in the diffusion chamber, as measured by the Langmuir probe is $n_e = 2 \cdot 10^{15}$ m^{-3} and the electronic temperature $T_e = 1$ eV. The plasma ion flux to the sample in ECR plasma is 7.10^{18} m^{-2}. s^{-1}.

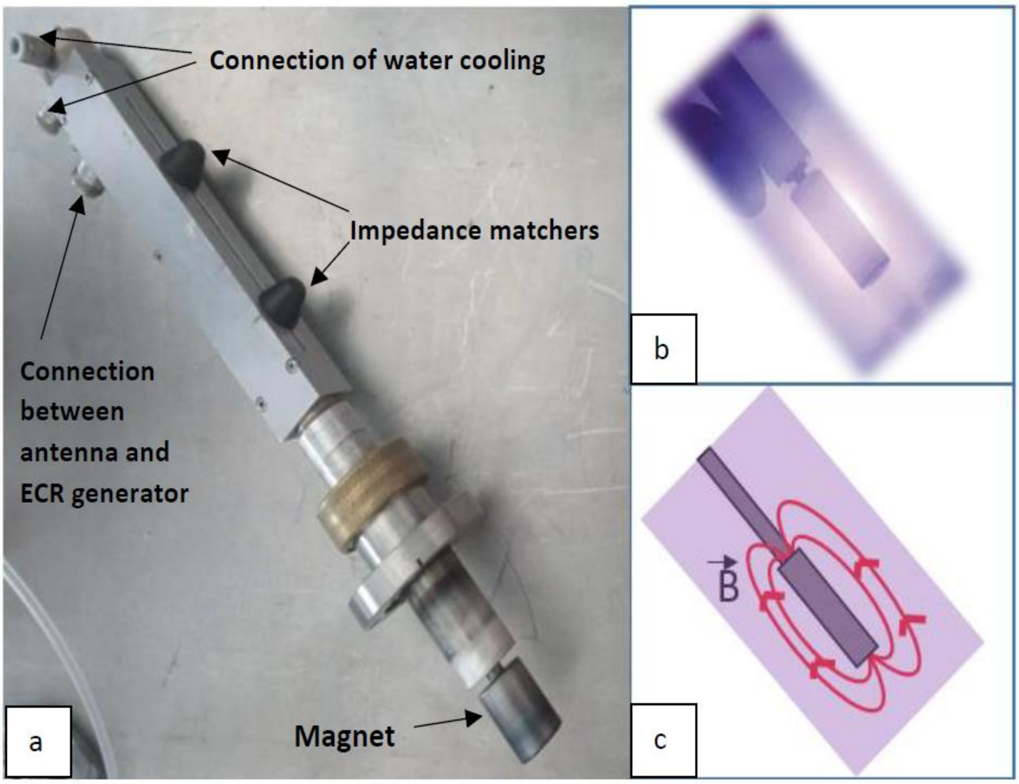

Figure 1.9(a) ECR antenna used to generate plasma in our experiments (b) photo of the ECR antenna inserted in PHISIS diffusion chamber creating H_2 plasma (c) The magnetic field lines produced by the magnet of ECR antenna

1.3.3 Sheath requirements

NIEDF modeling presented in **Chapter 2** requires calculation of negative-ion trajectories through sheaths in front of sample and in front of mass spectrometer. This requires the knowledge of the electric field inside sheaths. For that reason, experimental arrangement and experimental conditions have been chosen to ensure planar sheath in front of sample and mass spectrometer. In this situation the electric field is perpendicular to the surfaces and its magnitude can be computed from Child Langmuir law using plasma parameters measured by Langmuir probe.

As the extraction orifice of the mass spectrometer is surrounded by a large grounded surface, the extraction voltage has been set to 0 V to ensure planar sheath in front of the extraction orifice. In addition, the sample holder surface which is biased is much larger than the sample surface (circle of 8 mm of diameter) to prevent sheath edge effects (see **Figure 1.2** (b)).

1.3.4 Ion Energy Distribution (IEDF) measurements

This part gives few inputs that are required to understand ion energy distribution measurements with the mass spectrometer

A) Positive ions energy distribution function (PIEDF) spectra

A positive ion PI created in the plasma has the initial total energy $\mathbf{E_{Ti}}$:

$$\mathbf{E_{Ti} = E_{kini} + E_{poti} = eV_p}$$

Where $\mathbf{E_{kini}}$ is its initial kinetic energy (in plasma the ion temperature is assumed to be close to the gas temperature and $\mathbf{E_{kini}}$ is considered negligible), $\mathbf{E_{poti}}$ is initial potential energy in the plasma and $\mathbf{V_p}$ is plasma potential. After the energy filter the positive ion total energy is:

$$\mathbf{E_{Tf} = E_{kinf} + E_{potf} = E_{kinf} + e\,(V_{energy} + V_{axis} + V_{ref})}$$

Where (V_{energy} +V_{axis} +V_{ref}) is the local potential at the output slit of the energy filter. $\mathbf{eV_{energy}}$ is the potential which is scanned by the software when IEDF are measured, $\mathbf{V_{ref}}$ is reference potential over which the whole MS is floating (it is set to 0 V for positive ions) and $\mathbf{V_{axis}}$ is the potential that determines the pass energy of the energy filter. A pass energy of 40 eV is a good compromise between the level of signal and the energy resolution. V_{axis} must be set to - 40V to get a pass energy of 40 eV.

In the absence of collisions, the energy conservation principle gives $\mathbf{E_{Ti} = E_{Tf}}$, so we obtain:

$$\mathbf{eV_p = E_{kinf} + e\,(V_{energy} + V_{axis} + V_{ref})}$$

$$\mathbf{eV_p = e\,V_{energy}}$$

So, PIEDF measurement allows to measure plasma potential $\mathbf{V_p}$ which corresponds to the PIEDF peak position. In addition, it permits to measure the relative percentage of different positive ions in the plasma.

The positive ion flux composition can be determined by mass spectrometry. In order to measure correctly the positive ion energy distribution function (PIEDF) at the sample surface (in the case of V_s= -130 V), the mass spectrometer nozzle is polarized at V_{MS}= -130 V and the sample holder is grounded. The measured intensities are corrected for the number of protons and the energy by proton for each type of ion; the resulting total PIEDFs for RF and ECR plasmas are shown in **Figure 1.10**. It is assumed that H_2^+ and H_3^+ are immediately dissociated at the sample surface and the kinetic energy is equally distributed between the impinging protons. One may note substantial differences between two regimes in **Figure 1.10**: the peaks are more pronounced and demonstrate higher intensities in case of the ECR plasma. This is due to higher ne and thinner sheaths: positive ions experience fewer collisions on their way through the sheath, so their energy distribution is less perturbed. On the contrary, in case of RF one can observe a substantial increase of low energy part of the distribution of H_2^+ and H^+, which does not occur for H_3^+. The low-energy ions H_2^+ and H^+ are the products of charge-exchange reactions in the sheath, while the reaction $H_2^+ + H_2 \rightarrow H_3^+ + H$ is not probable as the sheath dimensions are smaller than the corresponding mean free path[70]. H^+ can also loose energy through the ro-vibrational excitation of the H_2 molecules. Charge-exchange reactions produce fast H atoms, which may contribute to the surface formation of H^-; this process is not taken into account in the model presented in **chapter 2**.

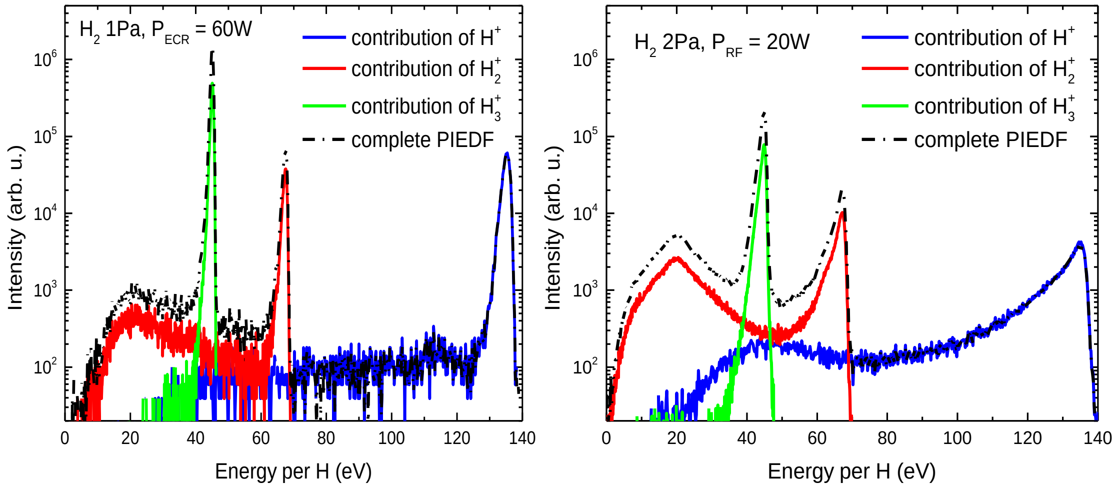

Figure 1.10 (a) Positive-Ion Energy Distribution Function measured at V_{MS} = -130 V and V_s = 0 V for the ECR H_2 plasma at 1 Pa, 60 W (b) and RF H_2 plasma at 2. Pa, 20 W.

As far as integrals of PIEDF are concerned, H_3^+ flux contributes to 91% of the total ion flux, H_2^+ flux to 8% and H^+ to 11% in the ECR plasma, while in RF plasma H_3^+ flux forms around 66% of the total ion flux, H_2^+ flux-2% and H^+ -8%.

In our experimental conditions negative ion are mainly produced by the impact of positive ion on the surface contrary to ITER NI source where hydrogen atom impact is responsible for negative ion production. This analysis is supported by measuring the NI signal variation with injected ECR power, where the NI signal on HOPG surface is linear with power. The atomic hydrogen flux Φ_{H^0} in our experimental conditions is negligible compared to Φ_{H^0} of ITER NI[74] source. The ratio between positive ion flux and atomic flux is much higher under our experimental conditions compared to ITER NI source ones. Indeed, an important remark has to be made about hyperthermal H atoms, which are created through the electron impact dissociation of H_2 in plasma with energies of few eV per H. In the present RF-based NI sources for fusion reactors the grid covered with Cs has a potential close to the plasma potential, hence most of hydrogen ions and hyperthermal neutrals have more or less the same energy when they strike the cesiated Mo surface. Given a much larger H flux compared to a positive ion flux in these sources, the dominant mechanism of H^- formation is conversion of hyperthermal H atoms on the Cs surface.

The positive ion flux variation with surface bias has been measured in the case of ECR plasma and RF plasma. Let us note that under ECR condition the positive ion flux is only slightly depending on the bias[115] and the NI yield can be defined directly as the NI total counts (area below NIEDF). Indeed, the sheath surrounding the sample holder is much thinner under this condition and remains planar in front of the sample avoiding edge effects. For RF plasma, the positive ion flux depends on the bias, and the the NI yield cannot be defined directly as the total NI yield, and it is normalized by total ion flux, this is caused by sheath broadering and RF fluctuation.

B) Negative ion energy distribution function NIEDF spectra

A negative ion NI created at the surface has the initial total energy $\mathbf{E_{Ti}}$**:**

$$\mathbf{E_{Ti} = E_{kini} + E_{poti} = E_{kini} - eV_s} \quad \ldots$$

Where $\mathbf{E_{kini}}$ is its initial kinetic energy, $\mathbf{E_{poti}}$ is initial potential energy at the surface and $\mathbf{V_s}$ is surface bias. At the energy filter exit, the negative ion total energy is:

$$\mathbf{E_{Tf} = E_{kinf} + E_{potf} = E_{kinf} - e\,(V_{energy} + V_{axis} + V_{ref})}$$

For negative-ions Vaxis has to be set to +40V for a pass energy of 40 eV.

If there is no collision between the sample surface and the MS detector, the NI total energy is conserved ($\mathbf{E_{Ti} = E_{Tf}}$**),** so we obtain:

$$\mathbf{E_{kini} - eV_s = E_{kinf} - e\,(V_{energy} + V_{axis} + V_{ref})}$$

$$\mathbf{E_{kini} - eV_s = -\,e\,(V_{energy} + V_{ref})}$$

$$\mathbf{E_{kini} = e\,(V_s - V_{energy} - V_{ref})}$$

The expression above allows the calculation of the initial kinetic energy of the NI for known surface bias, reference potential and the potential V_{energy} at which the ion is detected. Let’s take a typical example with a surface bias of -130 V and a reference potential of 0 V. In this situation a negative-ion created at rest (Ekini = 0 eV) on the surface would appear on the energy scan at Venergy = -130 V. This is outside of the scan capability of the mass spectrometer since V_{energy} can only be scanned from -100 V to +100 V. To solve this issue the reference potential is set to -110 V and the negative ion created at rest appears on the energy scan at V_{energy} = - 20 V. A negative ion created with a non-zero kinetic energy will appear at a lower V_{energy} potential. In this document no such raw data are presented. The energy scale is converted in order to give a representation of NIEDF as a function of E_{kini}, the NI energy on the surface. NIEDF should therefore starts at 0 eV and span over few tens of eV.

If a NIEDF shown on some graph in this thesis starts at negative energy, it can be connected either to a lower surface bias than expected (due to insulating properties of the sample), or to NI collisions between sample and MS, or to NI created somewhere else than the sample surface. Under our experimental conditions, the highest NI cross section is electron detachment. Therefore, NI collisions mostly lead to detachment and collisions can be disregarded when interpreting NIEDF. Typically, the separation between the MS and the sample is 37 mm which is approximately equal to the mean free path for electron detachment by collisions of H^- with H_2 at 2 Pa. Roughly 50% of the NI flux is lost due to electron detachment[49].

Chapitre 2 Modeling of NIEDF

2.1 Introduction and motivation

In cesium free plasma, negative ion (NI) surface production is usually a mechanism of minor importance. However, in certain circumstances it can be very efficient. In previous study a high amount of H^- and D^- produced on HOPG and MCBDD surfaces has been observed in low pressure H_2 or D_2 plasmas[52,54,55]. The study of NI surface production on HOPG has been performed by Loic Schiesko during his thesis[52, 53, 54].

The study of negative ion energy distribution function NIEDF of negative ions created on surfaces gives information on NI surface production mechanisms. In his work, Loic Schiesko proved that NIEDF measured on HOPG surface can be divided in two parts: the low energy peak and the tail. He demonstrated experimentally that in our experimental conditions NI are created on HOPG surfaces via two mechanisms:

a) Backscattering of incoming positive ion as a negative ion
b) Sputtering of an adsorbed H/D atom as a negative ion by incoming positive ion

The low energy peak of NIEDF results from contribution of both mechanisms whereas the energetic tail contains only the backscattering contribution. This conclusion resulted from a large experimental study that can be summarized as follows.

The sputtering mechanism measured experimentally by NIEDF on HOPG surface at room temperature and comparing it to the measured one at 1000 K. At this high temperature, hydrogen has desorbed from the surface. A large concomitant decrease of NIEDF signal at low energy was observed showing that sputtering mechanism contributes noticeably to the NIEDF low energy peak at room temperature.

To demonstrate backscattering contribution to NIEDF spectra, L. Schiesko studied the maximum energy of negative ions. In the backscattering mechanism, the energy transmitted to the newly formed negative ion is the energy of the outgoing backscattered particle. For the sake of simplicity ionization energy, work function and electron affinity were neglected in this simple analysis. A positive ion backscattered without any energy loss on the surface could create a negative ion with a maximum energy equal to the energy acquired in the sheath between the plasma and the sample. In the case of molecular ion (H_3^+), this energy has to be divided by the number of fragments ($E_0/3$ and E_0 is the energy of H_3^+ in the sheath front the sample surface), because all the ions undergo dissociation and neutralization at impact. L. Schiesko by working in two plasma conditions, the first one with dominance of H_3^+, the second one with dominance of H_2^+ Loic Schiesko has proven the formation of NI by backscattering mechanism. For first plasma condition, the maximum energy observed in NIEDF spectra was around $E_0/3$. For second plasma condition, the maximum energy observed in NIEDF spectra was around $E_0/2$.

Those experimental observations proved the contribution of backscattering mechanism to NIEDF.

In the study of negative-ion surface production by beam experiments, most of the information on the surface production mechanisms is concentrated in the scattering differential cross section of the products associated with well-defined momentum of the primary projectile. In plasma the measurement is reduced to the energy and angle distribution function of the emitted negative-ions (NIEADF) which is already difficult to obtain since the negative-ions have to be extracted before being measured. The measured NIEDF is very different from the NIEDF of emitted ions principally because of the limited acceptance angle of the mass spectrometer that does not allow collecting the full negative-ion flux. Simulations are needed to take into account this effect. Those simulations were developed previously in A. Ahmad thesis[51, 53]. A method has been proposed to obtain the distribution functions in energy and angle (NIEADFs) of the negative-ions emitted by the sample. He first chose a *priori* the NIEADF, then he calculates ion trajectories inside the sheath based on this choice, and finally produce a NIEDF at mass spectrometer restricted to the ions reaching the mass spectrometer within its acceptance angle. The computed NIEDFs are compared to the experimental ones. The a priori choice made for NIEADF on the surface was validated by the good agreement between modelled and experimental NIEDFs. The a priori choice of NIEADF was made using the help of the SRIM software[71] which is able to compute energy and angle distributions of backscattered and sputtered particles upon bombardment of a surface by positive ions[53,54, 55,72.] This model will be detailed in the first section of this chapter with two improvement done during this thesis by using the realistic PIEDFs (positive ion energy distribution function) as a SRIM input parameter. In addition, a new method (different than the one used in A. Ahmad work) of calculation of mass spectrometer acceptance angle and MS transmission function will be presented.

SRIM output includes both sputtered and backscattered particles, however it does not take into account the probability to form NI on the surface: P_{iz}. It has been suggested earlier that this probability is constant ($P_{iz} = const$) for HOPG, i.e. independent of the neutral particle energy and angle of emission, leading to a remarkable agreement of experimental NIEDFs with the SRIM-based modelling[51,73]. However, if we consider other materials, the ionization probability P_{iz} may not be constant. For instance, P_{iz} on the surface of low work function metals may depend on the perpendicular velocity of the outgoing particle. Furthermore, in order to obtain a correct NIEADF by SRIM the proper input parameters are needed, such as a surface binding energy, a surface concentration of hydrogen; these are well known for carbon owing to the decades of fusion research, however they may not be defined for other materials. Therefore, in general case, it is necessary to determine the distribution in energy and angle of NI emitted from the surface purely from the experimental data without any *a priori* assumptions about NIEADF, P_{iz} or the input parameters of SRIM. In K. Achkasov thesis, it was proposed a new method which allows to reconstruct the full NIEADF at the sample surface based on the NIEDF measurements at different tilt angles of the sample with respect to the mass spectrometer axis[74]. It does not depend on the NI surface production mechanism, so it can be applied to any type of surface and/or NI. To check the validity of the method through comparison with the SRIM modelling, K. Achkasov presents the results for HOPG and he also shows NIEADF for gadolinium as an example of low work-function metal (work function = 2.9 eV), which can be further implemented as an alternative to cesium[74].

2.2. Description of the model

A dedicated model has been developed to take into account transmission of negative ions through sheaths, plasma and mass-spectrometer[51,73,74]. It allows to determine the distribution function in energy and angle of the negative-ions (NIEADF) emitted by the sample from the MS measurements.

The yield of negative-ions measured for a given angle θ and energy E of emission is:

$$Y_{NI}(E,\theta) \propto P_{iz}(E,\theta,V_s) \times \left(Y_{sp}(E,\theta,V_S) + Y_B(E,\theta,V_S)\right) \times T_{pl}(E,\theta,V_S) \times T_{MS}(E,\theta,V_S)$$

Equation 2.1

The absolute NI yield is defined as the flux of negative-ions divided by the total flux of positive ions impinging on the surface. $\mathrm{Y}_{sp}(E,\theta,V_S)$ and $\mathrm{Y}_B(E,\theta,V_S)$ are the sputtering and backscattering yields for particles leaving the surface with an energy E and angle θ, upon the bombardment of positive ions at energy $E_0 = e(V_p - V_s)$. $P_{iz}(E,\theta)$ is the ionization probability of such particles. It is assumed constant for any E andθ. $P_{iz}(E,\theta,\mathrm{V}_s) = P_{iz}$.$T_{pl}(E,\theta,V_S)$ and $T_{MS}(E,\theta,V_S)$ are the transmission probabilities through the plasma and through the mass spectrometer respectively. The first one tells if the emitted ions can reach the mass spectrometer entrance with an angle below the acceptance angle, it is 0 or 1. The NI trajectory depends on the emission energy and angle ($E\ and\ \theta$) and on the electric field in the sheath, which is set by the sample bias (*Vs*). The calculation of NI trajectory is detailed in **section 2.3**. The acceptance angle is depending on the arrival energy of the negative-ion at the mass spectrometer E_{MS} which is set by both emission energy and sample bias where:

$$E_{MS} = E + e(V_{MS} - V_s) = E - eV_s. \qquad \textbf{Equation 2.2}$$

The second one is the transmission probability inside the mass spectrometer. It is calculated using SIMION software[75]. It depends on the arrival angle and energy at the mass spectrometer. Most of our recent calculations averages this transmission over the angles from zero to the acceptance angle (see details in section 2.5.2). Therefore $T_{MS}(E,\theta,V_S) \approx T_{MS}(E,V_S)$ = $T_{MS}(E_{MS})$.The calculation of $T_{MS}(E_{MS})$ for different surface bias V_s is detailed in **section 2.5**.

The method developed to model the measured NIEDFs (labelled *f''(E)*.) consists in assuming the ionization probability constant ($P_{iz}(E,\theta) = 1$) and integrating **Equation 2.1** Over all the angles θ:

$$\mathrm{f}''(E) \propto \int \left(\mathrm{Y}_{sp}(E,\theta,V_S) + \mathrm{Y}_B(E,\theta,V_S)\right) \times T_{pl}(E,\theta,V_S) \times T_{MS}(E,V_S)\ \mathrm{d}\theta$$

Equation 2.3

The NIEDF calculated by the model without taking into account $T_{MS}(E,\theta,V_S)$ is labelled *f'(E)*.:

$$\mathrm{f}'(E) \propto \int \left(\mathrm{Y}_{sp}(E,\theta,V_S) + \mathrm{Y}_B(E,\theta,V_S)\right) \times T_{pl}(E,\theta,V_S)\ \mathrm{d}\theta$$

Equation 2.4

The difficulty of the model is to get backscattering and sputtering yields, $\mathrm{Y}_{sp}(E,\theta,V_S)$ and$\mathrm{Y}_B(E,\theta,V_S)$, as a function of energy and angle of emission. SRIM software[51,72] has been used to compute the energy and angle distributions of backscattered and sputtered particles $\mathrm{Y}_{sp}(E,\theta,V_S)$ and $\mathrm{Y}_B(E,\theta,V_S)$.

The energy and angle distributions of backscattered and sputtered particles computed by SRIM are assumed to be those of sputtered and backscattered negative-ions (NIEADF). As SRIM does not take into account the surface ionization probability, the model implicitly assumes that the surface ionization probability is independent of the angle and energy of the particles emitted. This is a strong assumption that has been a posteriori validated by the good agreement between model and experiment[73].

Results of the model are the modelled NIEDFs at the mass spectrometer (*f''(E)* from **Equation 2.1**) and the NIEDFs on the surface *f(E)* as computed by SRIM:

$$f(E) \propto \int \left(\mathrm{Y}_{sp}(E,\theta,V_S) + \mathrm{Y}_B(E,\theta,V_S)\right)\ \mathrm{d}\theta$$

Equation 2.5

f ''(E) can be directly compared to the measured NIEDF $f_{\mathrm{exp}}''(E)$ in order to validate the model. In this chapter the model is used up to know to analyse data obtained at V_s = -130 V.

2.3. Calculation of negative ions NI trajectories

Determination of $T_{pl}(E,\theta,V_S)$ requires knownledge of ions trajectories between the sample surface and the mass spectrometer nozzle as a function of ion emission angle and energy.

Each ion emitted from the surface passes through three different regions before arriving to the mass spectrometer (see **Figure 2.1** Sketch (not to scale) of trajectories for four negative-ions leaving the surface from three different locations with the same angle and two different energies.):

- Sheath 1 in front of the sample (ionic sheath)
- Plasma
- Sheath 2 in front of the mass spectrometer (ionic sheath)

In our experimental arrangement sheaths are planar in front of mass spectrometer and sample surface[51]. In this situation, the local electric field in the sheaths is perpendicular to sample surface, and it can be calculated using Child Langmiur law knowing the electron density and temperature, the plasma potential and the surface bias. The first three parameters are taken from Langmuir probe experiments. Ion trajectories in the sheath are then simply determined by numerically solving the Newton's equation of motion. For each ion emitted from the surface, the arrival angle θ_{MS}, arrival energy E_{MS} and deviation d are calculated using initial energy E_i and initial velocity vector (v_{xi}, v_{yi}, v_{zi}).

The negative ion NI emitted from the surface is detected by the mass spectrometer MS if it fulfills two requierements:

- Its deviation must be inferior to d_{max}= 4 mm (sample radius) assuming that the sample is centered with respect to the MS axis.
- Its arrival angle should be smaller than the MS acceptance angle. The acceptance angle is known from the simulation of the MS performed with SIMION software (this calculation will be detailled in section 2.5.1).

Figure 2.1 shows a sketch (not to scale) of trajectories for four negative ions leaving the surface from three differents location with the same angle and two differents energies. The tilt angle (α) is the angle between the sample normal and the mass spectrometer axis . When rotating the sample, ions emitted at higher angles and/or higher energy can be collected. Ion 1 is not collected, its energy is low so its trajectories is strongly modified by the electric field in sheath 2, leading it to miss the mass spectrometer (MS) entrance. Ion 3 has got the same energy as ion 1 but its location allows it to reach the MS entrance. Ion 2 reaches the mass spectrometer but at an angle greater then the MS acceptance angle, so it is not collected. Ion 4 has got the same energy of ion 2 and starts at a radially symmetric location on the sample, but is emitted from a surface tilted with respect to the mass spectrometer sheath. Ion 4 is collected as its arrival angle at the MS entrance is lower than the acceptance angle. For the sake of simplicity, trajectory in sheath 1 are not correctly represented (electric field is much lower in sheath 1).

The ions trajectories inside the sheath are calculated after choosing an a prioi NIEADF on the sample surface. As it was mentionned in the introduction, the a priori choice made for NIEADF on the surface is validated once a good agreement between modelled and experimental NIEDFs at different tilts of the sample is obtained[73]. So, this method requires an accurate initial guess of the solution. To generate initial angular and energy distributions (NIEADFs), we used the SRIM software.

.

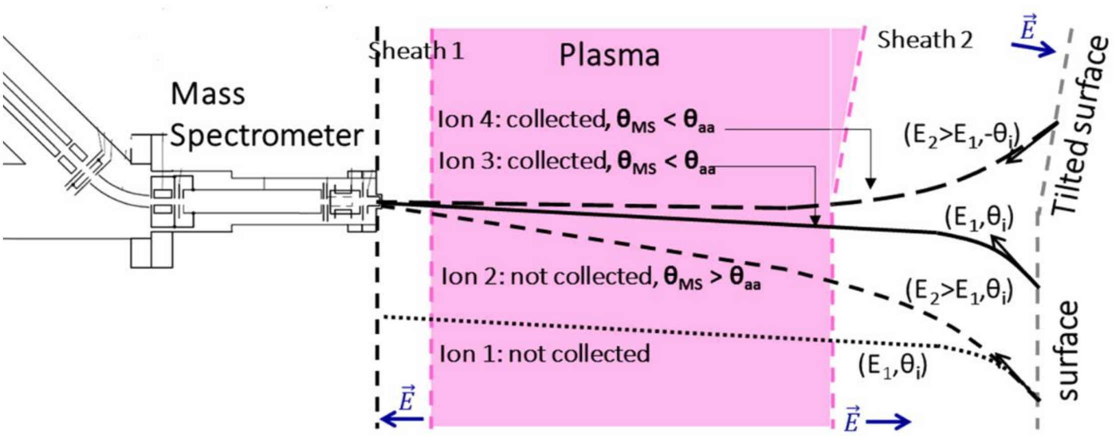

Figure 2.1 Sketch (not to scale) of trajectories for four negative-ions leaving the surface from three different locations with the same angle and two different energies.

2.4 The initial guess of *f (E, θ)*

2.4.1 SRIM software

SRIM software (Stopping and Range of Ions in Matter) is a group of programs designed to calculate the stopping of ions (10 eV – 2 GeV/a.m.u.) in matter. It is intended to calculate the interactions of energetic ions with amorphous targets. SRIM is based on Monte Carlo approach based on the binary collision approximation (BCA)[76,77,78] which assumes that collisions between atoms can be approximated by binary elastic collisions described with an interaction potential[79,80]. With SRIM one could calculate the final distribution of ions in 3D with all the kinetic phenomena associated with ion energy loss: target damage, sputtering and ionization [81]. The target material is considered to be amorphous with atoms occupying random positions and a mean distance which corresponds to interatomic distance of given material[82,83].

The energy and angular distribution of backscattered and sputtered particles computed by the SRIM code has been chosen as the initial guess for *f(E,θ).*

2.4 2 SRIM inputs parameters: case of HOPG sample

For HOPG case, a good agreement has been shown between the measured NIEDF and the modelled one[74]. The HOPG sample material is assumed to be an amorphous a-C: H layer (30%) [84,85,86,87,88,89], since the graphite surface exposed to plasma is subjected to hydrogen implantation and defect creation in the subsurface layer, which has been confirmed by Raman spectroscopy measurements[49]. The target material density was taken as $\rho=2.2$ g/cm^3 for HOPG (and later as $\rho=3.5$ g/cm^3 for diamond films). The chosen type of calculation was "Surface Sputtering/Monolayer Collision steps", since it is more adapted to treat backscattered and sputtered particles. The other input parameters were:

- **Displacement Energy** - the energy necessary for a recoil to overcome the lattice forces and to move more than one atomic spacing away from its original site. It was fixed at 25 eV for carbon and 2.5 eV for H/D.[90,91,92,93,94,95]
- **Surface Binding Energy** - the energy that target atoms have to overcome in order to leave the surface of the target. It is approximated by the sublimation energy for mono-element material and is unknown for composite materials. Surface binding energy is a key parameter to estimate the sputtering yield (number of target atoms leaving the target surface). The value of 4.5 eV was taken for carbon and 3 eV for H/D.[90,96,31]
- **Lattice Binding Energy** - the energy lost by every recoiling target atom when it leaves its lattice site and recoils in the target. For both carbon and H/D the value of 3 eV was chosen.[90,31]

Calculations have contained 10^6 or 10^7 hydrogen/deuterium ions impinging on 10 nm of target material. In A. Ahmad and K. Achkasov calculations, we don't take into account all three populations of hydrogen ions present in plasma H_3^+, H_2^+ and H^+, when calculating *f(E, θ)* with SRIM. Mono-energetic ions were assumed. In the case of mono-energetic ions, the choice of energy was derived from the experimental conditions. As an example, for the applied bias V_s = -130 V and plasma potential V_p = 5 V the ion energy before contact with the surface is E_0 =

$e(V_p - V_s) = 135$ eV. In the case of a H_2 plasma ignited under conditions: 2 Pa of gas pressure and 20 W of RF power, the dominating ion population is H_3^+, after the dissociation of the molecular ion, energy is equally divided between three fragments: $E_{impact} = E_0/3 = 45$ eV.

In this thesis, we extend the calculation of $f(E,\theta)$ in the case of realistic positive ions energy distribution function PIEDFs presented previously in **Figure 1.10**, which were used as input to the SRIM code .

Because of the sheath, ions are considered to impact the surface perpendicularly in SRIM calculations.

SRIM provides calculation results in the form of text file which contains all the emitted particles with the origin of their emission (backscattering or sputtering), atomic number, initial energy E_i, depth (x), lateral position (y, z) and the direction of their movement: $\cos(x), \cos(y), \cos(z)$. From these parameters, the initial emission angle θ_i and the initial velocity $\vec{\upsilon}_i$ can be calculated for each ion with the help of a routine written in Scilab. Thereby, the distribution function of emitted ions in energy and angle $f(E,\theta)$ can be deduced from the file given by SRIM. The distribution $f(E,\theta)$ is the first output of the model.

SRIM calculates the angle and energy distribution function of neutral on the surface. We have assumed that these distributions are those of negative ions. The energy distribution function of ions on the sample are calculated by SRIM in the case of mono-energetic ions (case 1) and realistic PIEDFs (case 2) and will be compared in the **section 2.6**.

2.5 Transmission of mass spectrometer $T_{MS}(E_{MS})$

NIEDF at mass spectrometer are produced by selecting ions reaching the mass spectrometer within its acceptance angle. Then NIEDF at mass spectrometer detector are produced by multiplying the previous NIEDF by the MS transmission function. In this section a new method of calculation of MS acceptance angle and MS transmission will be presented.

2.5.1 SIMION software

SIMION software[97,98] calculates in 2D and 3D the electric and magnetic fields and the trajectories of the charged particles in those fields. SIMION is used to simulate ion analyzer and specially the mass spectrometer[99,100,101]. SIMION permits to create virtual electrode of all shapes and sizes. To model a system as the mass spectrometer, pieces are constructed in planar or circular symmetry (2D construction), or directly in 3D; the latter case calculation are more difficult but essential for pieces with no geometric symmetry (see **Figure 2.2**).

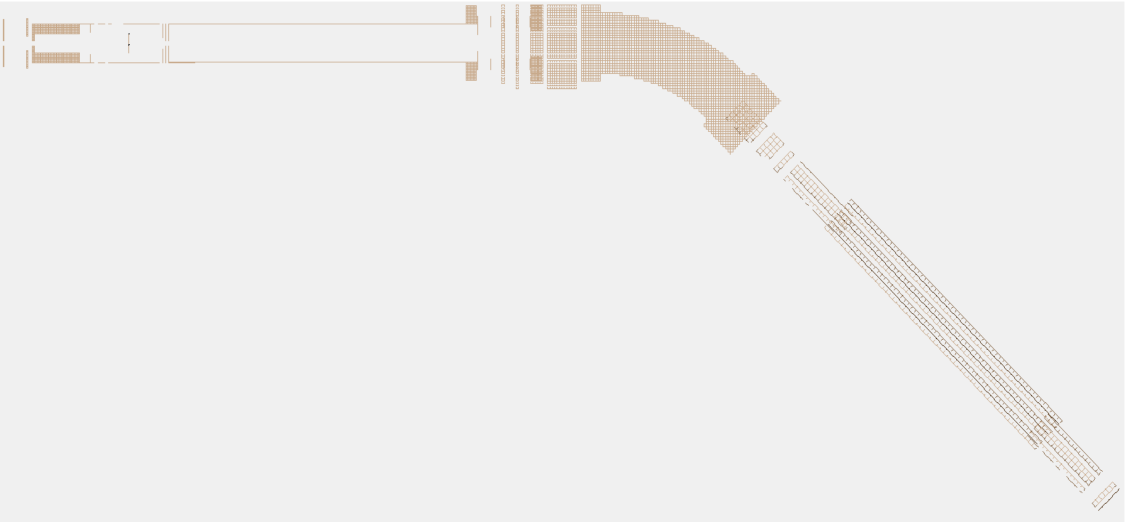

Figure 2.2 Mass spectrometer given by SIMION graphic interface

2.5.2. Calculation of MS transmission T_{MS} (E_{MS})

After the construction of the modeling program SIMION of the mass spectrometer (EQP) (see **Figure 2.2**) and its validation by different tests (work done by Pasquet Thimotée during internship), the calculation of mass spectrometer acceptance angle θ_{aa}. and of mass spectrometer transmission T_{MS} are possible. The aim of this work is to give a good and realistic estimation of these two parameters to be used in NIEDF modeling.

In this thesis we will present a new method to calculate these two parameters as a function of ion energy at the MS nozzle. Before detailing the method and showing results, let's define the acceptance angle θ_{aa} and the MS transmission $T_{MS}(E_{MS})$. The acceptance angle θ_{aa} is the angle value for it **1 ion** minimum arrives to the MS detector. The MS transmission $T_{MS}(E_{MS})$ is the transmission probability of different ions arriving MS orifice to be transmitted to MS detector. Each ion reaches the MS orifice with an angle θ_{MS} and an energy E_{MS}. For $\theta_{MS} > \theta_{aa}$, $T_{MS}(E_{MS})$. = 0.

After the construction of EQP 300 model under SIMION software (see **Figure 2.2**)) and its validation by different tests (work done by Pasquet Thimotée during internship), the calculation of mass spectrometer acceptance angle θ_{aa}. and of mass spectrometer transmission T_{MS} are possible. The aim of this work is to give a good and realistic estimation of these two parameters to be used it in NIEDF modeling. The acceptance angle θ_{aa} and the transmission probability T_{MS} are calculated for all surface bias values V_s: -20 V, -40 V, -60 V, -100 V, -130 V and -170 V. The optimized experimental setting of the mass spectrometer at each bias is used as input for SIMION calculations.

A. Ahmad in his thesis defined the acceptance angle as the maximum angle leading to ion transmission through the first collimating lens which is located just after the sampling orifice. Let us note that the geometrical acceptance angle of the sampling orifice, defined by width and length of the orifice, is equal to 45° and is much higher than the acceptance angle defined by A. Ahmad. Indeed, many ions passing through the orifice have too large angle to be collimated and end up their trajectory there. It gave acceptance low angle, around 2.5° for Vs = - 60 V and below 2° for Vs = - 130 V. The acceptance angle in A. Ahmad's thesis was a fixed value for each experimental condition (θ_{aa} = cte) and was calculated for ions creating at rest on the surface and accelerated to the MS by the potential difference. No dependence with the ion initial kinetic energy was introduced. However, A. Ahmad calculated a transmission probability though the mass spectrometer for all ion energies at each angle. In this way the dependence of the acceptance angle with the energy was indirectly considered since some ions at high energy had zero transmission probability despite their arrival angle was below the acceptance angle. The transmission probability was calculated with 5 eV steps in energy and 0.1 to 0.5° steps in angle, requiring numerous very long calculations to get $T_{MS}(E,\theta)$.

In the present thesis we have changed the definition fo the acceptance angle and have introduced a new method to calculate faster the mass spectrometer transmission probability and the acceptance angle as a function of ion energy. The acceptance angle θ_{aa} is now defined as the maximum angle for which at least 1 ion at a given energy arrives to the MS detector. The acceptance angle is calculated as a function of the negative ion initial kinetic energy: θ_{aa}(E). The MS transmission T_{MS} is averaged over all the arrival angles at each individual NI energy: $T_{MS}(E) = \frac{1}{2\theta_{aa}}\int_{-\theta_{aa}(E)}^{+\theta_{aa}(E)} T_{MS}(E,\theta)d\theta$. Each ion reaches the MS orifice with an angle θ_{MS} and an energy E_{MS}. For $\theta_{MS} > \theta_{aa}$, $T_{MS}= 0$.

We are interested to calculate θ_{aa} and T_{MS} of negative ion H^- emitted by the surface and reaching the MS spectrometer with an angle θ_{MS} and an energy E_{MS}. For $H^{-,}$ E_{MS} is equal to $E_{MS}=E_i + e(V_{MS}- V_S)$. As the mass spectrometer does not have a perfect cylindrical symmetry, ions in our SIMION computations are distributed over a cone (see **Figure 2.3**) for acceptance angle calculations, and inside the cone for transmission calculations, to cover all possible value of Φ angle. For good statistics, calculations are done using at each NI energy 2500 ions distributed on or inside the cone (see **Figure 2.3**).

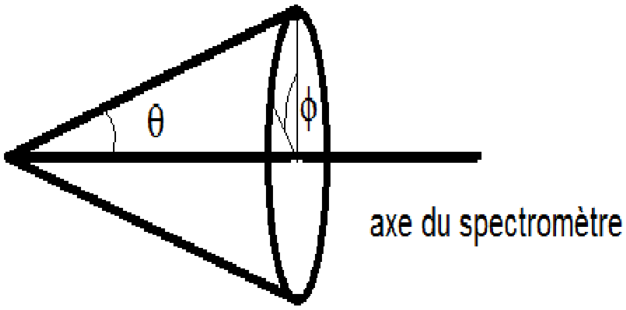

Figure 2.3 cone distribution of ion beam reaching the MS orifice

For an initial NI kinetic energy E_i, it is easy to determine theoretically the value of potential V_{energy} at which the ion is passing through the energy filter of the MS. The relation between E_i, and V_{energy} has been defined previously as $eV_{energy}= eV_s-eV_{ref}- E_i$ (see **chapter 1**). For ion beam in non-normal incidence, this value is slightly modified. For this reason, in our case, we do an energy scan around the theoretical value of V_{energy} ($V_{energy\text{-}th}$-5 eV to $V_{energy\text{-}th}$+5 eV). The energy step is 0.2 eV. The number of ions by step is 50 ions giving a total number of 2500 ions as mentioned before.

To show the method of calculation more clearly, let us take the particular example of V_s= -20 V in the case of RF plasma (2 Pa H_2, 20 W of RF power). The initial energy E_i of H^- created on surface in that case ranges from 0 to a maximum value of $e (V_p- V_s) = 40$ V, where Vp is the plasma potential and it is equal to 20 V if one takes into account all positive ions including H^+. The H^- energy at MS entrance $E_{MS}=E_i +e (V_{MS}- V_S) = E_i +20$ V since $V_{MS}= 0$ V:

- For $E_i =0$ V, E_{MS} =20 V, and $eV_{energy}= eV_s-eV_{ref}- E_i= -20$ V since in that situation we used $V_{ref}= 0$ V. In this case the theoretical potential at which these ions are passing through the filter is V_{energy} = 20 V. In SIMION calculations we scaned V_{energy} between -25 V and -15 V.
- For $E_i =5$ V, E_{MS} =25 V, and $eV_{energy}= eV_s-eV_{ref}- E_i= -25$ V with $V_{ref}= 0$ V. In this case eV_{energy} is scaned between -30 V and -20 V.

For a given Ei, the scan of V_{energy} is performed at increasing value of the θ_{MS} with ions distributed on the surface of a cone with half opening angle θ_{MS}. As long as at least one over the 2500 ions of the scan is reaching the MS detector the angle θ_{MS} is increased. When no more ion is arriving at the MS detector, the acceptance angle is found.

- For $E_i =0$ V, E_{MS} =20 V, the calculated acceptance angle θ_{aa} is 3.8° (see **Figure 2.4**(a)
- For $E_i =5$ V, E_{MS} =25 V, the calculated acceptance angle θ_{aa} is 2.6°. (see **Figure 2.4**(a))

shows calculated acceptance angles as a function of NI energy at the entrance of MS E_{MS} for different surface bias Vs in following plasma conditions: 2 Pa of H_2 gas pressure, 20 W of RF power. As one can see in **Figure 2.4** (a) (b) (c), for Vs= -20 V, -40 V and -60 V respectively θ_{aa} decreases with E_{MS}. The tendency in high bias range (-100 V, -130 V, -170 V) is different from the case of low surface bias. A chromatic aberration is observed[102] for high surface bias (see **Figure 2.4** (d) (e) (f)).

In order to calculate T_{MS} we follow the same methodology. The main difference is that for each E_i the 2500 ions are distributed inside a cone of half opening angle θ_{aa}. $T_{MS}(E_i)$ is defined as the maximum transmission obtained over the scan from $V_{energy\text{-}th}$-5 eV to $V_{energy\text{-}th}$+5 eV (see **Figure 2.5**)

- For $E_i =0$ V, E_{MS} =20 V, the calculated T_{MS} is 1. All the ions created at the surface with 0 eV kinetic energy and arriving at mass spectrometer entrance within the acceptance angle are collected. This is due to their quite low energy which allows for an efficient collimation by the MS. (see **Figure 2.5**).
- For $E_i =5$ V, E_{MS} =25 V, T_{MS} is 0.65. 65% of the ions created at the surface with 5 eV energy and reaching the mass spectrometer within the acceptance angle (2.6°) are collected (see **Figure 2.5**).

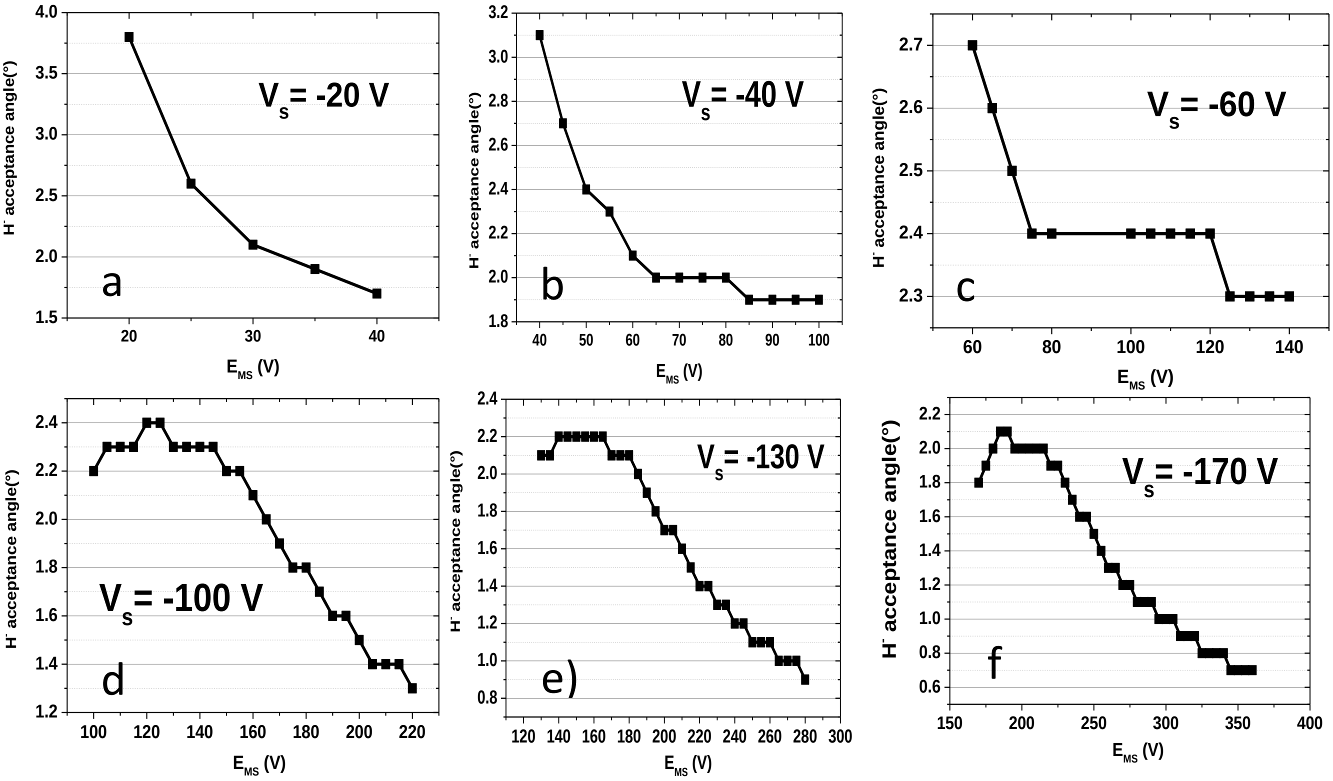

Figure 2.4 H_2 plasma: 2 Pa and 20 W RF power. Calculated acceptance angle for H^- ion in the case of V_p= 20 V and V_{MS} = 0 V as a function H^- energy at mass spectrometer entrance E_{MS} for different surface bias V_s: a) -20 V b)-40 V c)-60 V d)-100 V e)-130 V f)-170 V

Figure 2.6 shows the calculated T_{MS} as a function of the initial NI kinetic energy for different surface bias. For all surface bias (-20 V in (a) , -60 V in (b), -170 V in (c) and -130 V in (d)), the transmission decreases wit NI energy. This tendency is normal. When a high energy NI beam enters the MS orifice, the MS lens has difficulty to focalize the beam. When the MS lens success to focalize all the arriving ions in the beam T_{MS}= 1.

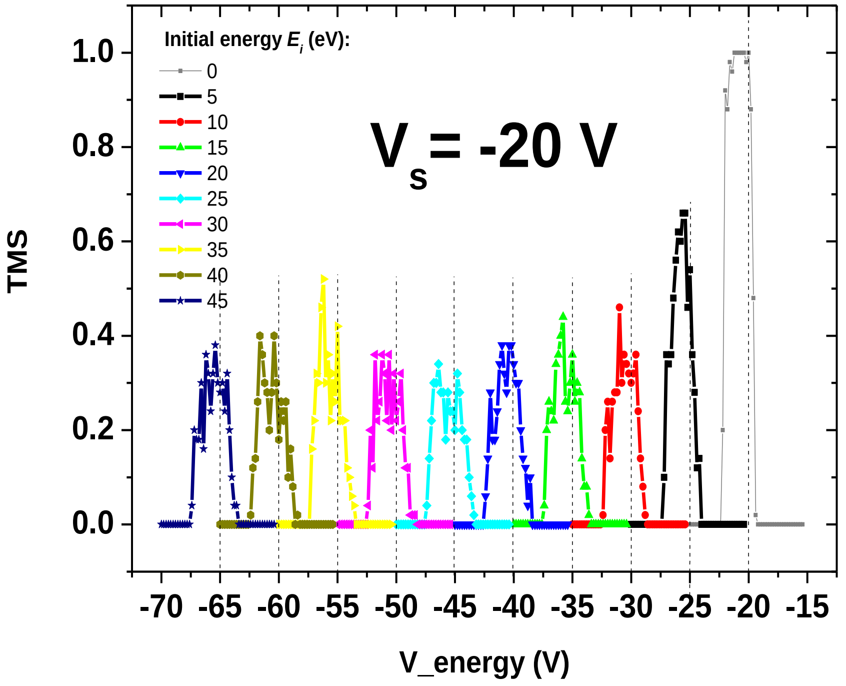

Figure 2.5 Transmission calculation of H^- in the case of V_s= 20 V for different initial energy E_i. T_{MS} value is the peak of the signal of each E_i.

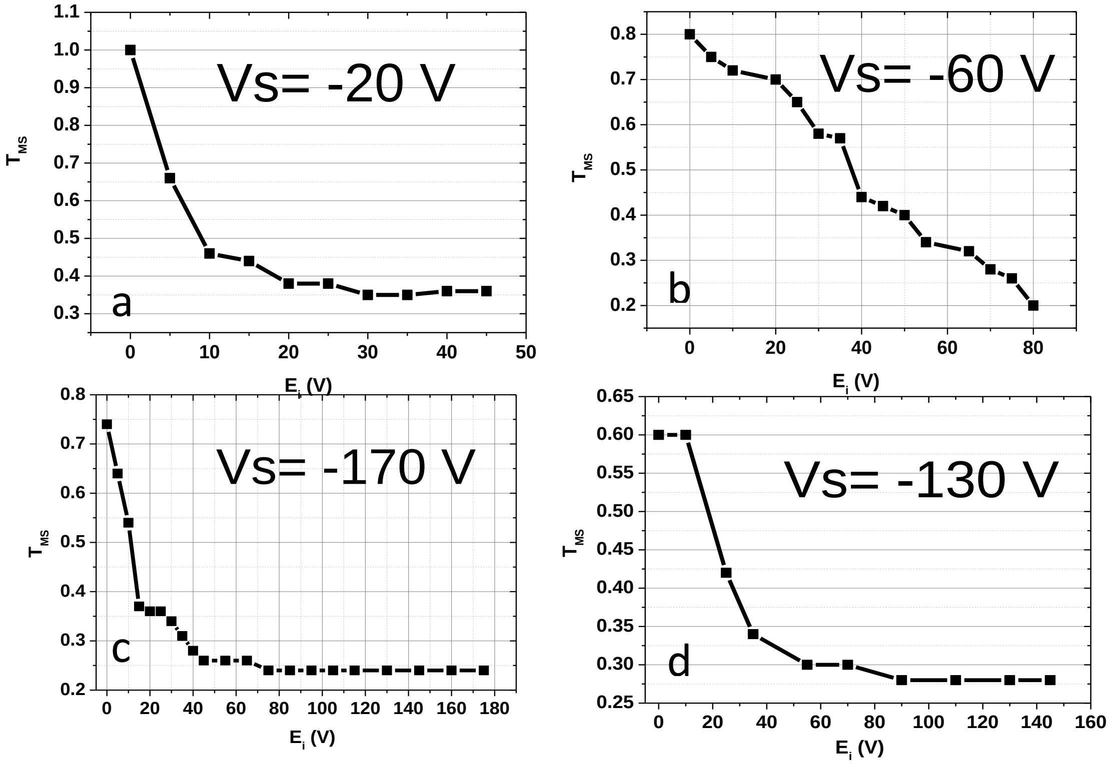

Figure 2.6 Calculated transmission probability for H^- ion in the case of V_p= 20 V and V_{MS} = 0 V as a function H^- initial energy at sample surface E_i for different surface bias V_s: a) -20 V b)-60 V c)-170 V d)-130 V

Finally, let us note that we did not observe any major change of the modelling results with the new definitions and new methods of calculation of acceptance angle and transmission probability. However, calculations are fastened. Therefore, comparisons with results obtained in previous PhD thesis are possible.

2.6 Modeling results

In this section a comparison between computed and experimental NIEDFs in case 1 (mono energetic ions) and case 2 (real PIEDF) is presented for HOPG sample in different plasma conditions. All those calculations are done for zero tilt angle.

2.6.1 Case 1: mono-energetic incoming ions:

The results of the model compared to the experimental data (measured for HOPG at room temperature) in the case of mono –energetic incoming ions case are presented in the **Figure 2.7**. This figure is extracted from K Achkasov’s thesis. The agreement is excellent. The RF-fluctuations of the plasma potential were suppressed by using the ECR source. When using the RF source, the broadening of the peak can be observed for high input power, but for P_{RF} = 20 W the fluctuations are minimized efficiently by using the grounded screen. As one can see in **Figure 2.8**, the modeling compares quite well with the experiment also in the case of RF plasma.

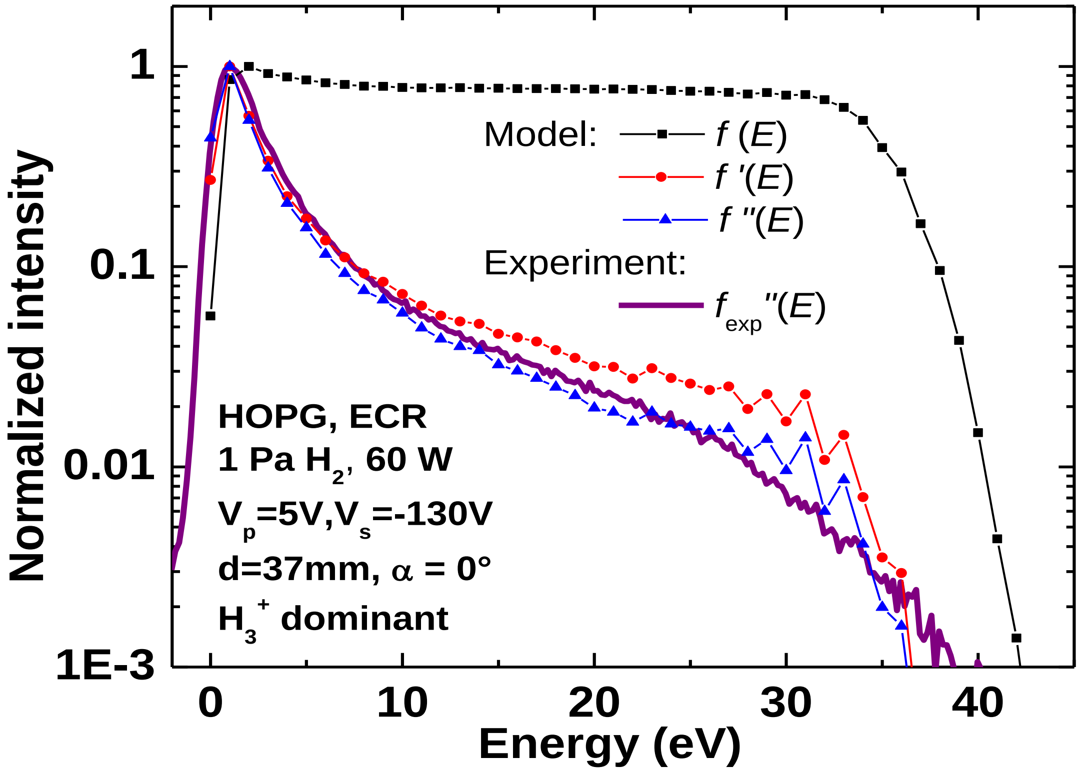

Figure 2.7 Comparison between experimental NIEDF (purple) and calculated NIEDF for HOPG in hydrogen: f(E,θ) emitted from the surface as given by SRIM (black squares), f '(E) at the entrance of the MS given by the model (red with dots), f “(E) at the MS detector given by the model (blue with dots). $E_{impact} = E_0/3 = e\ (V_p-V_s)/3 \approx 45$ eV. Experimental conditions: 1.0 Pa of H_2 plasma, Q = 5.2 sccm, P_{ECR} = 60 W, V_s = -130 V, V_{MS} = 0 V, without screen.

One of the important SRIM input parameters influencing the shape of the modeled NIEDF is H/D surface coverage *Θ*. The typical value used in the calculations is 30% of H/D atoms and 70% of carbon atoms. However, this percentage could vary depending on the material type, surface temperature, etc.

The modeling performed for different values of hydrogen surface coverage *Θ* ranging from 40% to 0% with the step of 10% is shown in **Figure 2.9**. The value of surface binding energy of hydrogen was kept $U_b = 3\ eV$ for all calculations. Note that the curves are normalized by the maximum value. As can be seen from the graph, the tail of NIEDF grows as the coverage diminishes This is due to a decrease of the sputtering contribution to NI production. Indeed, NI created by sputtering are mostly located at low energy. Therefore, the increase of the tail contribution or NIEDF, or decrease of the peak contribution to NIEDF, is a sign of a higher relative contribution of backscattering to NI production (see**Figure 2.9**).

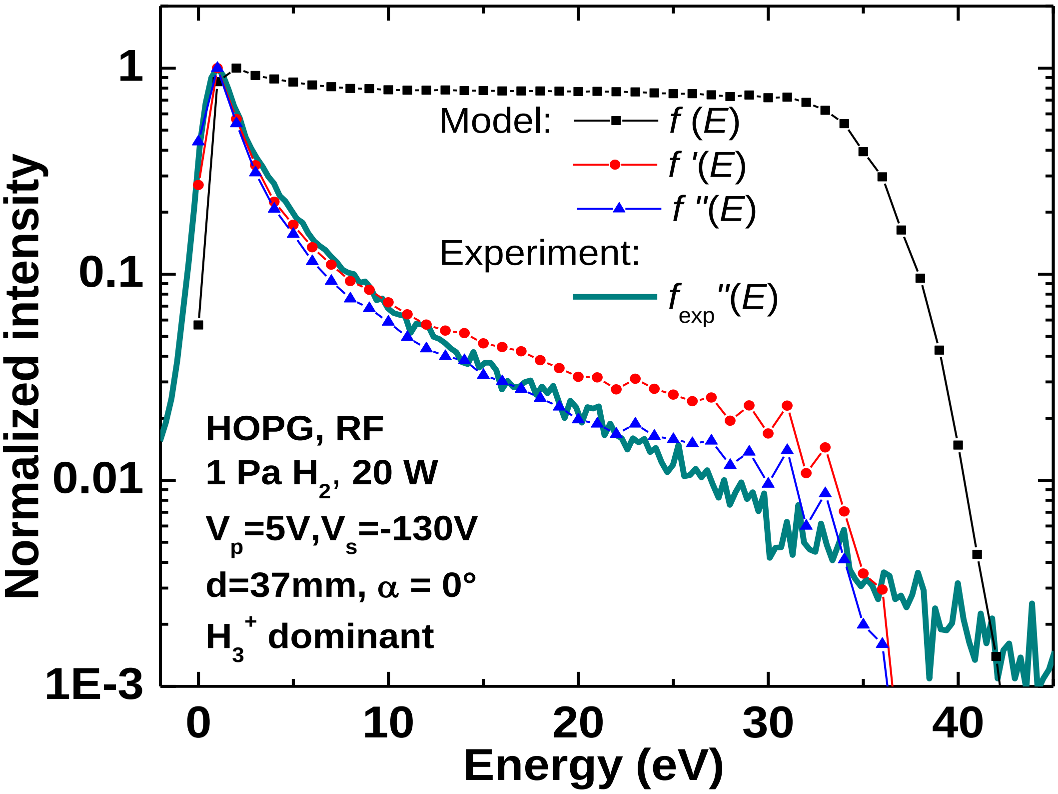

Figure 2.8 Comparison between experimental NIEDF (cyan) and calculated NIEDF for HOPG in hydrogen: f(E,θ) emitted from the surface as given by SRIM (black squares), f '(E) at the entrance of the MS given by the model (red with dots), f "(E) at the MS detector given by the model (blue with dots). $E_{impact} = E_0/3 = e\ (V_p\text{-}V_s)/3 \approx 45$ eV. Experimental conditions: 2.0 Pa of H_2 plasma, Q = 5.2 sccm, P_{RF} = 20 W, V_s = -130 V, V_{MS} = 0 V, with screen.

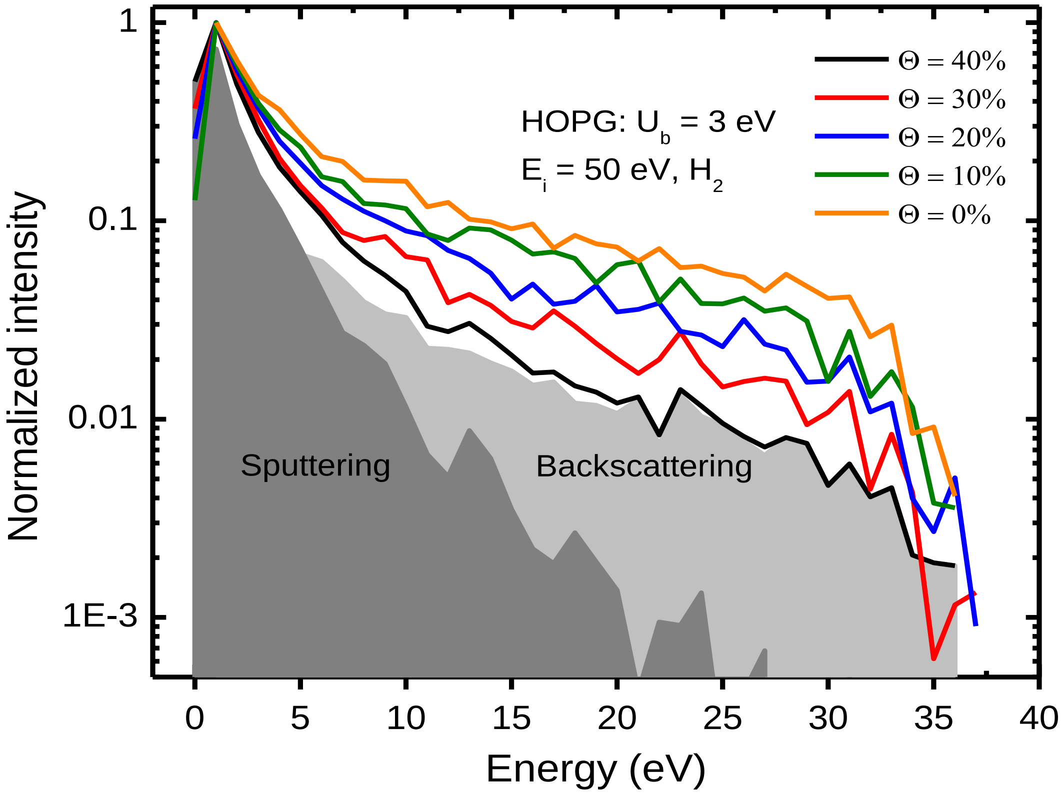

Figure 2.9 Comparison between calculated f "(E) at the MS detector given by the model for HOPG in hydrogen for different values of hydrogen surface coverage Θ. The contributions of sputtering and backscattering are shown for Θ = 40%.

Another parameter having a similar effect on the NIEDF shape is the surface binding energy. The effect of binding energy is shown in K. Achkasov thesis. The higher the binding energy, the lower the sputtering contribution is.

2.6.2 Case 2 : realistic PIEDFs

In this section we extend the comparison of $f_{exp}''(E)$ and $f''(E)$ to the case of realistic PIEDFs ((**Figure 1.10**), which were used as input to the SRIM code.**Figure 2.10** shows a comparison between the measured NIEDF (blue) in the ECR plasma and the computed one. Let us note that NIEDF modelling with monoenergetic ions was giving a good agreement with experiment over three decades of signal. In the **Figure 2.10** NIEDF measurement is presented over 5 decades of signal. In order to measure precisely the NIEDF over 5 orders of magnitude, the MS has been operated in the accumulation regime for 20 min; it has been checked that the shape of NIEDF is not changing with time.

The model reproduces quite well the shape of $f_{exp}''(E)$ over the five decades of signal. $f_{exp}''(E)$ presents a main peak at low-energy (0–10 eV), a tail with a slight decreasing slope at intermediate energy (10–30 eV) and breakings of the slope around 30 eV and 50 eV followed by the high energy tail. Each change of the slope corresponds to the disappearance of the contribution of a certain positive ion population. Indeed, the energy of the ejected particle (the NI) cannot exceed the maximum impact energy of the corresponding positive ion. The maximum impact energy for H_3^+ fragments is $E_0/3$ and $E_0/2$ for H_2^+ fragments. Above $E_0/3$ and $E_0/2$ H_3^+ and H_2^+ fragments respectively do not participate anymore to NI production. This can be seen from **Figure 1.10**. It explains why there are 3 steps in f(E) (**Figure 2.10**). The experimental NIEDF is changing more smoothly in the range of ion energies 30–40 eV compared to the modelled one; this probably indicates a small inaccuracy in the determination of input PIEDF. It is possibly due to a variation of the MS transmission with ion energy and mass for H^+, H_2^+, H_3^+ or due to a contribution of fast H atoms created in the sheath, which is neglected here. We use the raw measured PIEDF as an input for modelling, so we do not aim for the perfect matching of the curves but rather to compare the tendencies: all the slope changes, the low-energy part and the high-energy tail are reproduced remarkably well by the model. Besides, let us note that the modelled H_3^+ contribution provides a good agreement of *f ''(E)* with $f_{exp}''(E)$ for 95% of the negative-ion population, as only few negative-ions have energy higher than 35 eV.

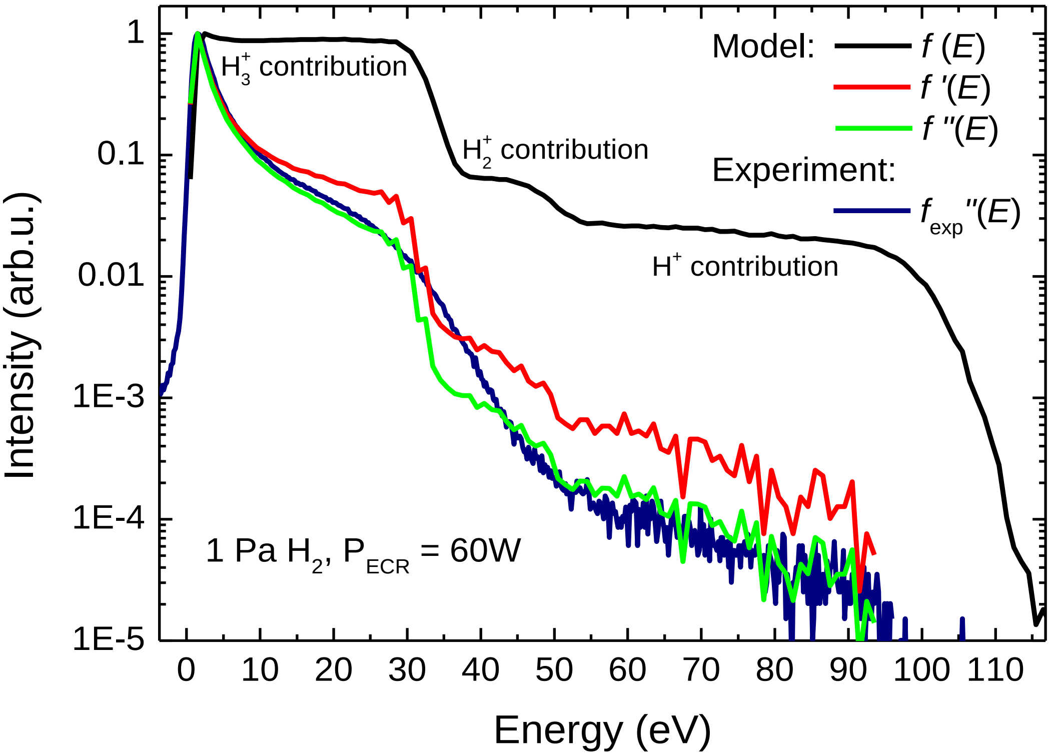

Figure 2.10 Comparison between the calculated energy distribution function *f ''(E)* of the negative ions at the MS detector (green line) and the experimental one $f_{exp}''(E)$ (blue line) obtained at 1 Pa, 60 W with the ECR source, $\alpha = 0°$. The energy distribution function of ions on the sample *f(E)* calculated by SRIM and used as input in the model is shown with a black line. Red line shows *f '(E)* at the MS entrance. All NIEDFs are normalized to the peak value.

Figure 2.11 shows a comparison between $f_{exp}''(E)$ and the computed *f ''(E)* for $3 \cdot 10^7$ incident ions in case of the RF plasma. A good agreement between the modelled *f ''(E)* and $f_{exp}''(E)$ is demonstrated, although the experimental NIEDF again appears to be smoother than the modelled one. The slope changing of *f(E)*, *f '(E)* and *f ''(E)* is less pronounced in the RF plasma compared to the ECR case, as the PIEDF in the RF plasma has a smeared shape due to the ion collisions in the sheath.

Finally, **Figure 2.10** and **Figure 2.11**demonstrate that only a part of the emitted ions is collected by the mass-spectrometer: the distribution function of the collected ions *f ''(E)* differs strongly from the distribution function of the emitted ions *f(E)*.

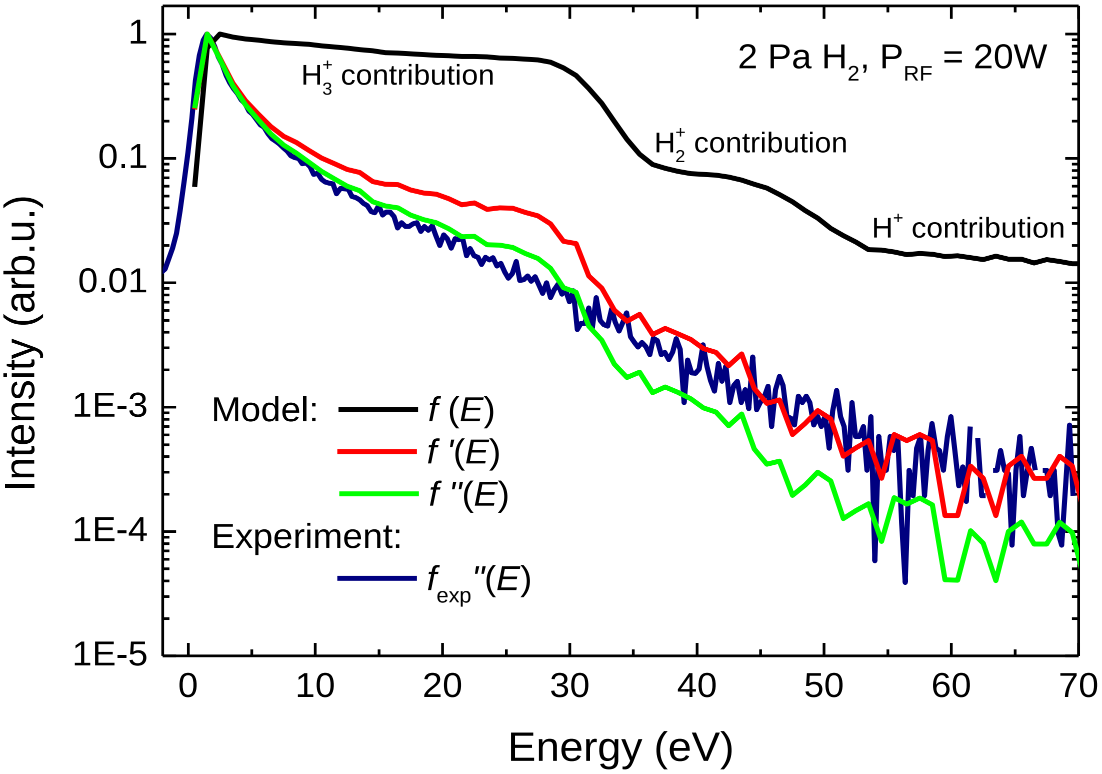

Figure 2.11 Comparison between the calculated energy distribution function *f ''(E)* of the negative ions at the MS detector (green line) and the experimental one f_{exp}*''(E)* (blue line) obtained at 2 Pa, 20 W with the RF source, $\alpha = 0°$. The energy distribution function of ions on the sample *f(E)* calculated by SRIM and used as input in the model is shown with a black line. Red line shows *f '(E)* at the MS entrance. All NIEDFs are normalized to the peak value.

2.7 Conclusion

In this chapter, we have presented the model used to determine the initial NIEADF of NI emitted from the sample surface in H_2 plasma. This model is validated by good agreement of the model with the experiment. Indeed, using SRIM distribution function as an initial NIEADF, the model can reproduce the NIEDFs measured by the mass spectrometer. The NIEDF on HOPG surface is close to the neutral distribution function given by SRIM. It implies that the NI formation probability on the graphite surface, under the present experimental conditions. Furthemore, the model shows that hydrogenated materials will probably present high negative ion signal contrary to non-hydrogenated materials.

Chapitre 3 . Impact of PI energy on carbone surface production of NI in D_2 plasmas

3.1 Introduction and motivation

This work focuses on the production of negative-ions on graphite and diamond surfaces in low pressure plasmas of H_2/D_2. In this chapter, the changes in negative-ion production mechanisms and production yields versus the positive ion energy are analyzed. It is shown that surface defect creation by positive ion bombardment has opposite effects on diamond and graphite.

In the previous works the surface bias of the sample was fixed at -130 V. The surface bias and the plasma potential determine the positive ion energy impact on the surface. Impact energy of the incident particle was 45 eV per proton or deuteron in our previous experiments since the ion population is largely dominated by H_3^+ or D_3^+ ions under the experimental conditions used, and because the plasma potential was around 5 V[74]. In the present work we study the influence of the ion energy upon the NI surface production down to 10 eV/nucleon. A special focus is put on low bias exposure as it is relevant to low ion/atom impact energies on cesiated grid in real NI sources for NBI systems. We first study the possibility to self-extract the ions at low bias. We then focus on negative-ion yield kinetic effects.

3.1 NIEDF measurement at different surface bias V_s

Measurements are performed in PHISIS setup. Plasma discharge is created with RF power at 2 Pa D_2, 20 W of injected power. Sample is placed in the chamber center with a molybdenum substrate holder.

The positive ion flux repartition determined by mass spectrometry is D_3^+ (90%) followed by D_2^+ (9%) and D^+ (1%). The sample can be biased to negative voltages in order to get the positive ion impact energy of ~10–50 eV per deuteron if one restricts the analysis to D_3^+ ions. The plasma potential V_p in the vicinity of the sample holder depends on surface bias V_s and ranges from 18 V at $V_s = 0$ to 5 V at $V_s = -130$V. The impact energy of the dominant incident ion D_3^+ can be estimated as $e(V_p - V_s)/3$ per deuteron. All the present measurements have been done at room temperature.

A set of measured NI energy distribution functions NIEDFs for HOPG (Highly oriented pyrolytic graphite) and MCBDD (MicroCrystalline Boron Doped diamond) surfaces exposed to D_2 plasma at different surface biases V_s is shown in **Figure 3.1** and **Figure 3.2**. A relatively high and noiseless signal can be acquired even with a bias as low as -10 V. In this situation the self-extraction is ensured by the 10 V difference between the sample surface and the mass spectrometer entrance. Below 10 V measurements start to become difficult as the signal level is strongly decreasing. The maximum value of the NIEDFs and its evolution with the surface bias differ noticeably for HOPG and MCBDD. On the contrary the shapes of NIEDFs are quite similar (**see Figure 3.3**). The NIEDFs include low-energy peak (1–4 eV region shown in red) and higher energy part that extends up to an impact energy of positive ion minus minimum energy transfer to the solid[54]. It has been shown earlier that the negative ions are formed by backscattering of positive ions as NI and by sputtering of adsorbed hydrogen (deuterium) atoms as NI[53,55].

In order to understand experimental results and interpret the shape of the measured NIEDF.for different surface bias V_s, the model presented in Chapter 2 will be used[51, 73, 74].

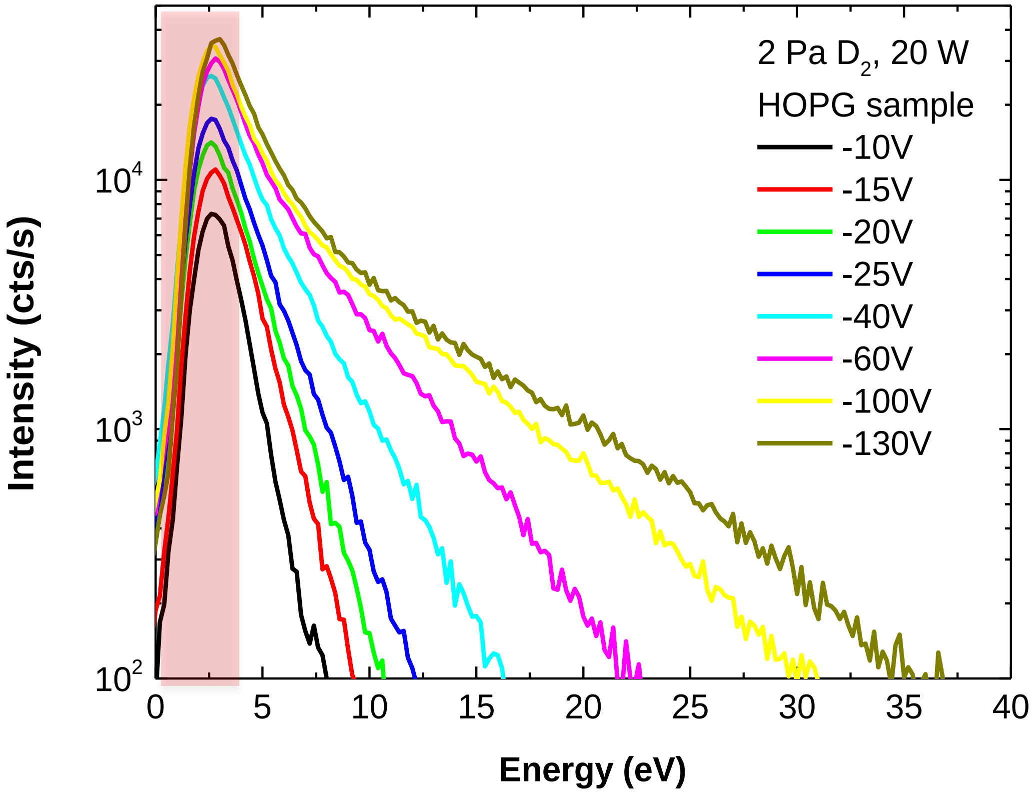

Figure 3.1 NIEDF measured for HOPG sample exposed to 2 Pa D_2 20 W RF plasma at different surface biases at room temperature. Pick values of the distributions represent low-energy part (1–4 eV) of negative ions, shown by a transparent red region.

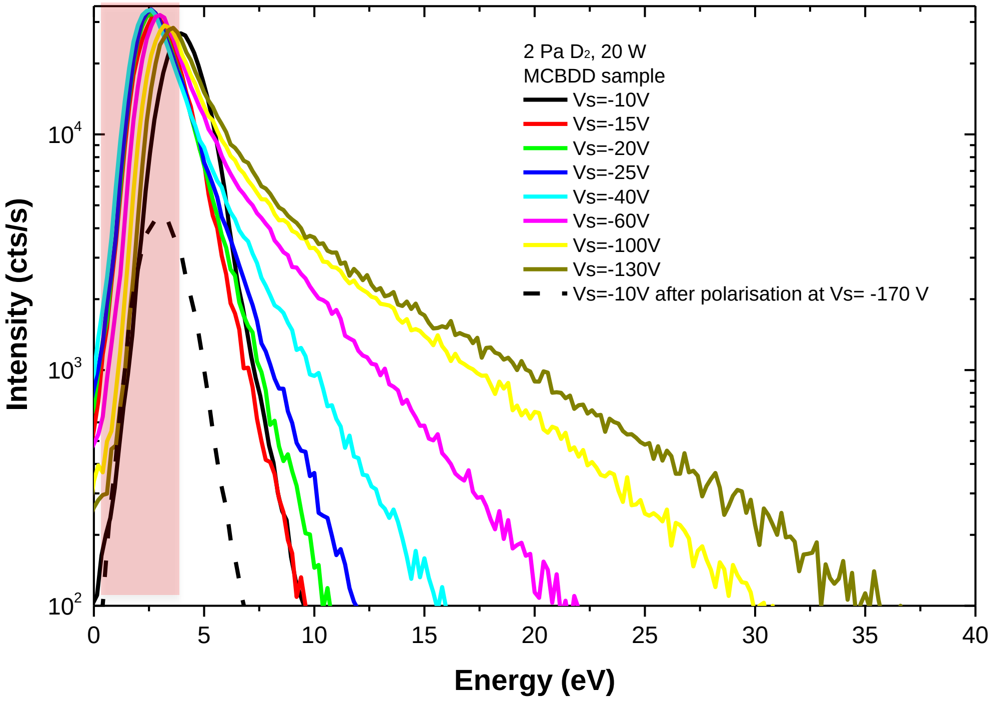

Figure 3.2 : NIEDF measured for MCBDD sample exposed to 2 Pa D_2 20 W RF plasma at different surface biases at room temperature. Pick values of the distributions represent low-energy part (1–4 eV) of negative ions, shown by a transparent red region.

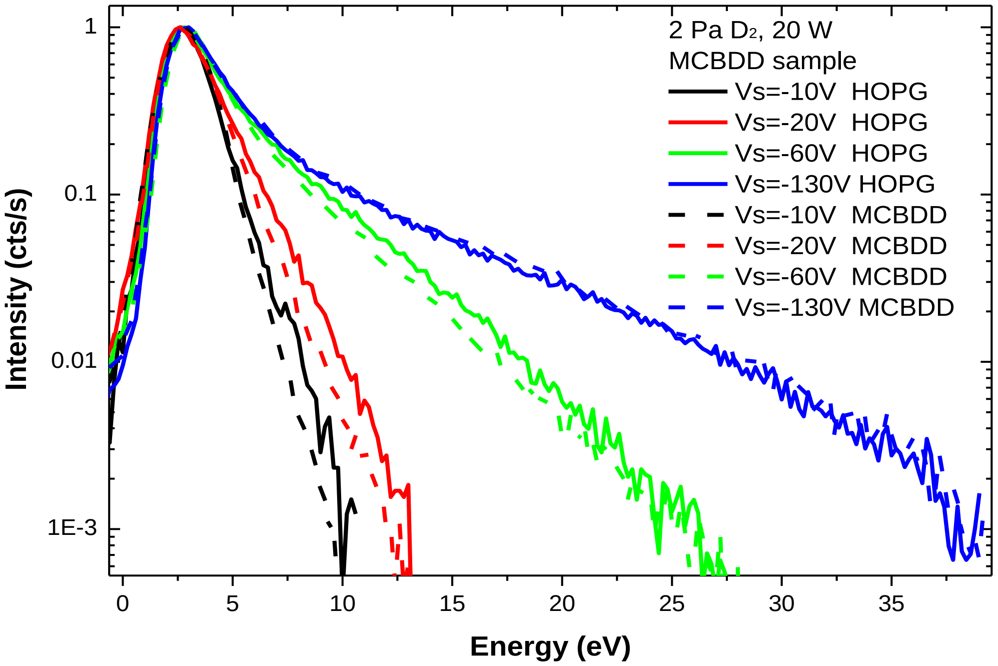

Figure 3.3 Normalized NIEDF measured for MCBDD and HOPG sample exposed to 2 Pa D_2 20 W RF plasma at different surface biases at room temperature. MCBDD NIEDFs at -10V and -130V have been slightly shifted on the horizontal axis to match the maximum of all NIEDFs and favour the comparison of the shapes.

3.2 Modeling of NIEDF measured at different surface bias:

It has been shown in **Equation 2.1** that the yield of negative-ions measured for a given angle θ and energy E of emission depends on surface bias V_s Where $Y_{sp}(E, \theta, V_S)$ and $Y_B(E, \theta, V_S)$ are the sputtering and backscattering yields for particles leaving the surface with an energy E and angle θ, upon the bombardment of positive ions at energy $E_0 = e(V_P - V_S)$. It was assumed that $P_{iz}(E, \theta)$ (ionization probability) is constant for any E and θ. P_{iz} might depends on V_s only through a change of the surface state with the bias. $T_{pl}(E, \theta, V_S)$ depends on the electric field in the sheath, which is set by the sample bias (Vs) (see **section 2.2**). $T_{MS}(E_{MS})$ was calculated for different (Vs), details of transmission functions calculation were presented previously in **section 2.4.**

In the present experiments the sample bias is varying between -10 V and – 130 V giving an impact energy per deuteron (D_3^+ is the dominant positive ion in the plasma) between ~10 eV and 45 eV taking into account the plasma potential and its changes versus sample bias.

f'''(E) (See **Equation 2.3**) is more accurate than *f'''(E)* (**Equation 2.4**) but requires time consuming calculations to get T_{MS}. We often use *f'(E)*. only to fasten and simplify the analysis. We have noted previously that the differences between f' and f'' are not huge, and f' calculation is often enough to interpret the shape of NIEDF (see **section 2.5**). The transmission through the MS mostly modifies the signal intensity. Modeling is done using SRIM code[51,72]. As it was presented in **section 2.4.1**, the SRIM code is based on the binary collision approximation (BCA) which assumes that collisions between atoms can be approximated by binary elastic collisions described by an interaction potential. As discussed by Eckstein et al[103], the validity of the assumptions behind the BCA is expected to decrease below around 30 eV. In chapter 2, model has been used until now to analyse data obtained at V_s = -130 V. Under this condition the positive ion energy is around 50 eV/nucleon and SRIM assumptions are probably fulfilled. In the present work, lower positive ion energy (lower bias in absolute values) are explored and SRIM results must be taken with cares.

SRIM does not take into account the surface ionization probability, the model implicitly assumes that the surface ionization probability is independent of the angle and energy of the particles emitted. This is a strong assumption that has been a posteriori validated by the good agreement between model and experiment (see **Figure 2.8**, **Figure 2.9**, **Figure 2.10** and **Figure 2.11** in **section 2.5**). Another recent method for reconstruction of the surface emitted NIEADF without any a priori assumption confirms that for HOPG at V_s = -130V the SRIM model provides a relatively good approximation[74].

The sample material in the model is assumed to be an amorphous a-C:H layer (30% H) or a-C:D (30% D). The dominant positive ion in the present experiment is D_3^+. It is assumed that it dissociates at impact on the surface and that the energy is shared between the three fragments. Therefore, the D_3^+ bombardment is modelled in SRIM by the impact of mono energetic D^+ ions at energy $E_0/3$ between 10 eV and 45 eV. Other parameters of the SRIM calculations was listed in **section 2.3.2**[71].

Results of the model are given in **Figure 3.4** showing the modelled NIEDFs at the mass spectrometer (*f' (E)* from **Equation 2.4**) and the NIEDFs on the surface *f (E)* as computed by SRIM:

An important outcome of the model is that the fraction of emitted NI which is collected by MS is relatively small. Many ions are missing the entrance of the mass spectrometer or reaching it with an angle θ_{MS} higher than the acceptance angle θ_{aa}. In particular ions emitted at high energy are not efficiently collected since their trajectories are not sufficiently rectified by the electric field in the sheath and they arrive at mass spectrometer with a too high angle.

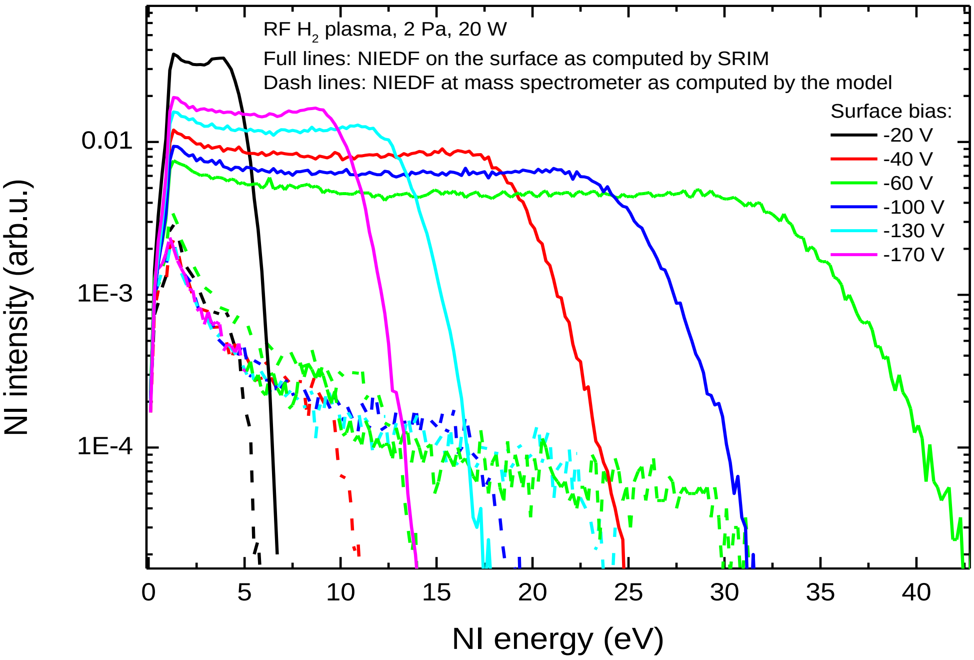

Figure 3.4 NIEDFs on the sample surface (full lines) computed by SRIM. NIEDF at the mass spectrometer (dash lines) computed using SRIM results and NI trajectory calculations. Parameters for the calculations are those of a D_2 RF plasma 20 W, 2 Pa.

All SRIM calculations have been made assuming a 30% constant deuterium percentage on the surface whatever the bias. This choice, validated at high bias (V_s = - 130 V), is here arbitrary. Two sets of calculations have been performed, one with a layer density of 2.2 g/cm^3 and one with 3.5 g/cm^3 corresponding respectively to deuterated HOPG and deuterated diamond. No major difference was observed between both sets of calculations, neither on the yields nor on the NIEDF shapes. Therefore, only one set of result is presented (2.2 g/cm^3) in **Figure 3.4**. Comparison of model and experiment are given in **Figure 3.5**. Distribution functions are normalized, and only shapes can be compared in this figure. Obviously, the differences between *f'(E)* and *f''(E)* are light and *f'(E)* can be used to study the shapes of NIEDF. The agreement between experiments and calculations at Vs = - 130 V, if not perfect, is quite satisfactory. One must keep in mind that in RF plasma the NIEDF are slightly broadened by the RF fluctuations of the plasma potential and therefore the model never perfectly matches to the experiment[51]. However, the validity of the model has been proven using microwave plasma (ECR excitation)[51] (see **Figure 2.10** Comparison between the calculated energy distribution function *f "(E)* of the negative ions at the MS detector (green line) and the experimental *one fexp"(E)* (blue line) obtained at 1 Pa, 60 W with the ECR source, α = 0°. The energy distribution function of ions on the sample *f(E)* calculated by SRIM and used as input in the model is shown with a black line. Red line *shows f '(E)* at the MS entrance. All NIEDFs are normalized to the peak value.) It is also possible to improve the agreement between experiment and modelling as demonstrated in a by taking into account the relative ratio of D_3^+, D_2^+ and D^+ ions as well as their real energy distribution[74]. However, this is not the goal of present chapter and to speed up the calculations only mono-energetic D_3^+ ions have been considered for the modelling.

Still at Vs = – 130 V, it has been shown that changing $Y_{sp}(E,\theta,V_S)$ and $Y_B(E,\theta,V_S)$ or changing hydrogen coverage noticeably affects the computed distribution (see **Figure 2.9** Comparison between calculated f "(E) at the MS detector given by the model for HOPG in hydrogen for different values of hydrogen surface coverage Θ. The contributions of sputtering and backscattering are shown for Θ = 40%.). However, as can be seen from**Figure 3.5**, for the low bias case, changing the hydrogen coverage is not affecting too much the computed NIEDF. The agreement between model and experiment at low bias is therefore only showing that angle and energy distribution functions computed by SRIM are roughly correct. There is not enough dynamics on the signal to fully validate SRIM calculations at low positive ion energy (low bias in absolute values). One more difficulty in analysing the low bias results is coming when considering the total NI counts (integral of NIEDF) rather than shapes of NIEDF. This is detailed in next paragraph.

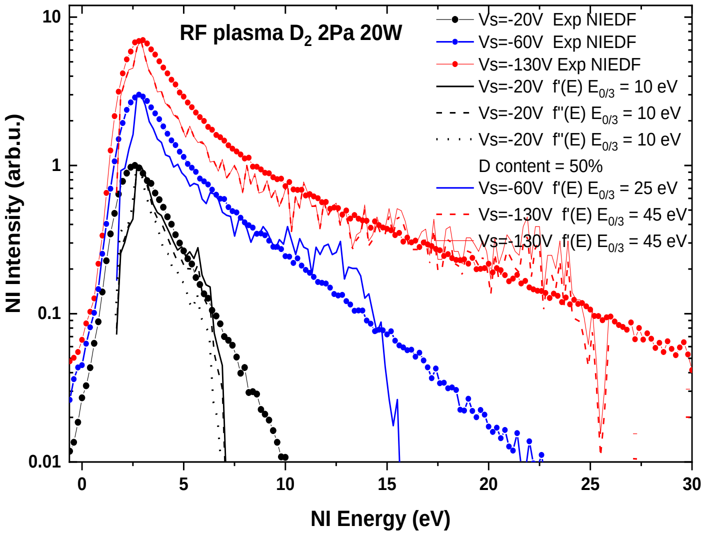

Figure 3.5 comparison between experimentally measured NIEDFs (line plus symbols) and computed ones (lines). f''(E) and f'(E) stand for NIEDFs computed with or without the mass spectrometer transmission function. Experimental conditions are D_2 RF plasma 20 W, 2 Pa, bias surface of -20 V (results normalized to one), -60 V (results normalized to three) and -130 V (results normalized to seven for sake of clarity). Considering results of calculations, the impact energy is indicated in the figure and the deuterium content on the surface is 30% except for one calculation (50%).

3.3 Analysis of negative ion yield behavior with surface bias

Figure 3.6 shows measured NI yields as a function of V_s for MCBDD (filled red squares) and HOPG (filled black circles) in D_2 plasma. The measured yield is defined as the ratio between the measured NI total flux (integral of the measured NIEDF) and the positive ion flux. It is given in arbitrary units since the mass spectrometer signal scale is not absolutely calibrated. The positive ion flux onto the sample has been measured versus the sample bias by isolating completely the sample from the sample holder and measuring its current independently of the sample holder current (the sample holder was acting as a guard ring during the measurement). The positive ion current on the sample was found to increase from 2.5 µA at -10 V to 5.7 µA at -170 V. It can be seen that both materials demonstrate different behaviour. The yield is increasing for HOPG while it decreases with V_s (in absolute values) for MCBDD. MCBDD is the best NI producer at biases lower than -60 V. The open symbols in **Figure 3.6** show peak intensities normalized by the PI current as a function of surface bias. The normalized peak intensity is used as a representation of the yield of low energy emitted NI (0 – 5 eV) since the peak is always located between 0 and 5 eV whatever the surface bias. Again, the signal is stronger for MCBDD between -10 V and -60 V and higher for HOPG between -60 V and -170 V, and the signal is decreasing for MCBDD while it is increasing with V_s for HOPG. The measurements were done on a pristine sample starting at V_s = -10 V and proceeding till -170 V. Let us note that all measurements are done at steady state when the yield stabilizes. It requires usually few minutes[47].

The use of SRIM assuming a unique amorphous a-C:D (30%) top layer for both diamond and graphite is immediately questioned by the results presented in **Figure 3.6** since both materials behave completely differently in terms of yields. The variations of yield computed by SRIM with a-C:D (30%) top layer are presented in **Figure 3.7**. If one neglects the transmission function of the mass spectrometer T_{MS} the yield slightly increases with bias but not as much as observed for graphite in **Figure 3.6**, and the peak intensity slightly decreases contrary to graphite in **Figure 3.6**. When considering T_{MS}, yield and peak intensity noticeably decrease with bias which is in contradiction with graphite behaviour in **Figure 3.6**.

In **Figure 3.3** it is shown that NIEDFs on HOPG and MCBDD have similar shapes. It suggests that for both material the normalized angle and energy distribution of emitted negative ions (NIEADF) are globally similar. As it has been shown that NIEDF shapes obtained at V_s = -130V are determined by the relative contribution of backscattering and sputtering processes to the negative-ion emission, it also suggests that this relative contribution is identical for both materials, at least at -130V. Indeed, materials with different backscattering and sputtering contribution lead to marked differences in NIEDF shapes as demonstrated in 74.

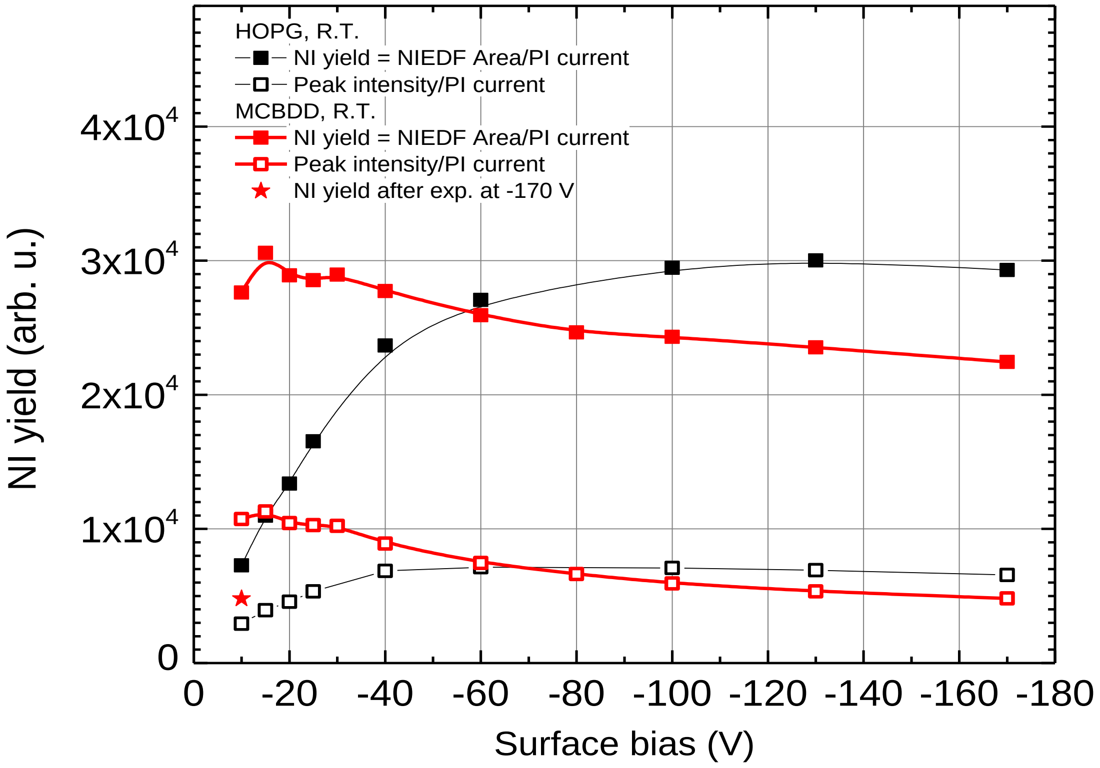

Figure 3.6 NI yield and peak intensity of NIEDF measured for MCBDD and HOPG exposed to 2 Pa D_2 20 W RF plasma at room temperature.

In order to interpret yields behaviour, let us come back to **Equation 2.3** cited in chapter 2 and dropping any assumption on the ionization probability:

$$f''(E) \propto \int \mathrm{P_{iz}}(\mathrm{E}, \theta, \mathrm{V_s}) \times \left(\mathrm{Y}_{sp}(E, \theta, V_S) + \mathrm{Y}_B(E, \theta, V_S)\right) \times T_{pl}(E, \theta, V_S) \times T_{MS}(E, V_S)\ \mathrm{d}\theta$$

Equation 3.1

If one assumes that NIEADF are globally similar for both materials, then the plasma and mass spectrometer transmission functions $T_{pl}(E,\theta,V_S)$ and $T_{MS}(E,V_S)$ are identical for both materials. Nevertheless, it is instructing to study their variations with surface bias. To do so, the fraction of collected ions has been computed versus the surface bias using the model with a uniform negative-ion energy and angle distribution function (NIEADF) on the surface. The uniform distribution is simply defined by $\mathrm{f}(E,\theta) = 1\ \forall E, \forall\theta$. The fraction of collected ions is the total number of collected ions (integral of *f'(E)* or *f''(E)* distribution between 0 and $E_0/3$) divided by the total number of emitted ions (integral of *f(E)* distribution between 0 and $E_0/3$). The fraction of low energy collected ions (represented in the experiment by the peak intensity of the NIEDF) has been also computed by integrating *f'(E)*, *f'(E)* and *f''(E)* between 0 and 5 eV. The results are presented on **Figure 3.8.**

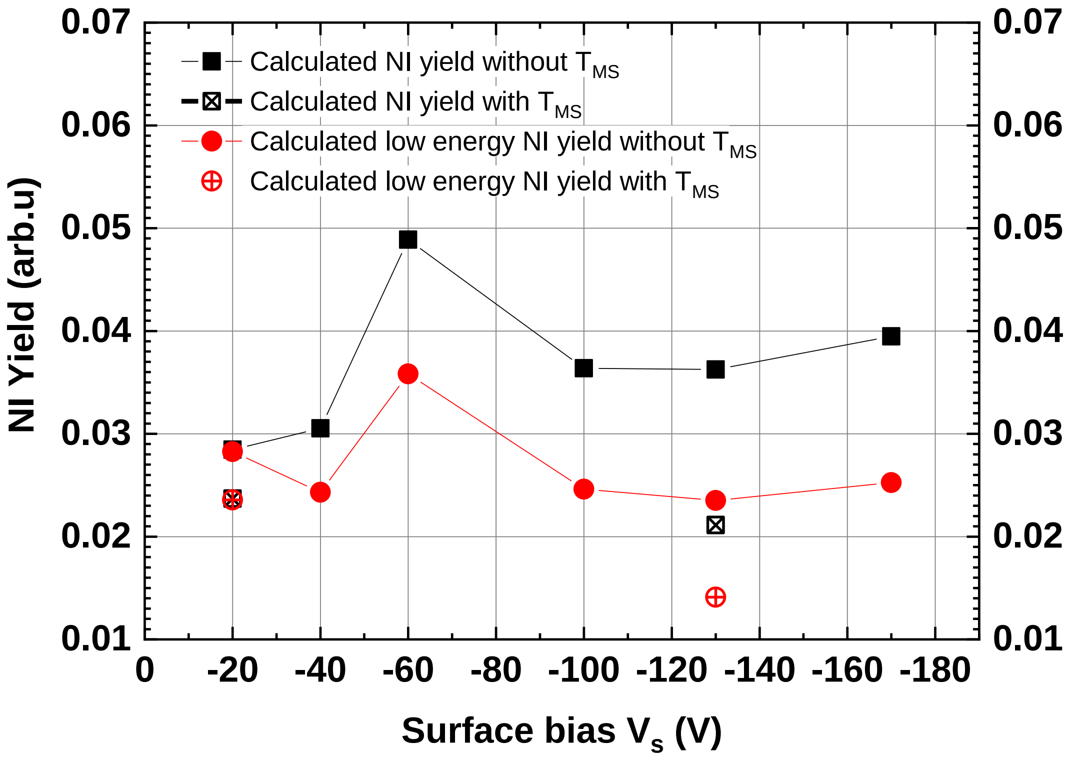

Figure 3.7 Calculated NI (square) and low energy NI (circle) yields. Fill/open symbol are for calculations without/with taking into account T_{MS}. Parameters for the calculations are those of a D_2 RF plasma 20 W, 2 Pa.

First of all, it has been checked that all negative ions collected emerged from the sample surface and no negative-ion can be collected originating from the surrounding surfaces such as the clamp. The model shows that all negative-ions collected originate from a spot on the sample surface (~2 mm in diameter) which does not exceed the sample dimensions (8 mm in diameter) for any V_s studied here, even at low bias. The calculations also show that only about 4-8 % of the emitted ions are measured, this fraction being higher if one considers the low energy ions rather than the whole NIEDF (12-15 %). The better collection efficiency of low energy ions was already observed[51]. Explanation comes hereafter.

Without taking into account the transmission function of the mass spectrometer T_{MS} the extraction efficiency is almost constant with surface bias. When increasing the bias in absolute values, the arrival energy of the negative-ion at the mass spectrometer E_{MS} is increasing leading to a decrease of the acceptance angle (see **Figure 2.4**). However, at the same time the higher electric field in the sheath tends to decrease the NI arrival angle at the mass spectrometer Θ_{MS}. Both effects compensate to give an almost constant extraction efficiency when neglecting T_{MS}. However, when E_{MS} is increasing this transmission function is decreasing due to the difficulty to focus high energy ions inside the mass spectrometer (see **Figure 2.6**). Therefore, the extraction efficiency is globally decreasing when increasing the bias. It can be noted it worth taking into account T_{MS} to analyse yield variations while NIEDF shapes can be analysed ignoring T_{MS} (**Figure 3.5**).

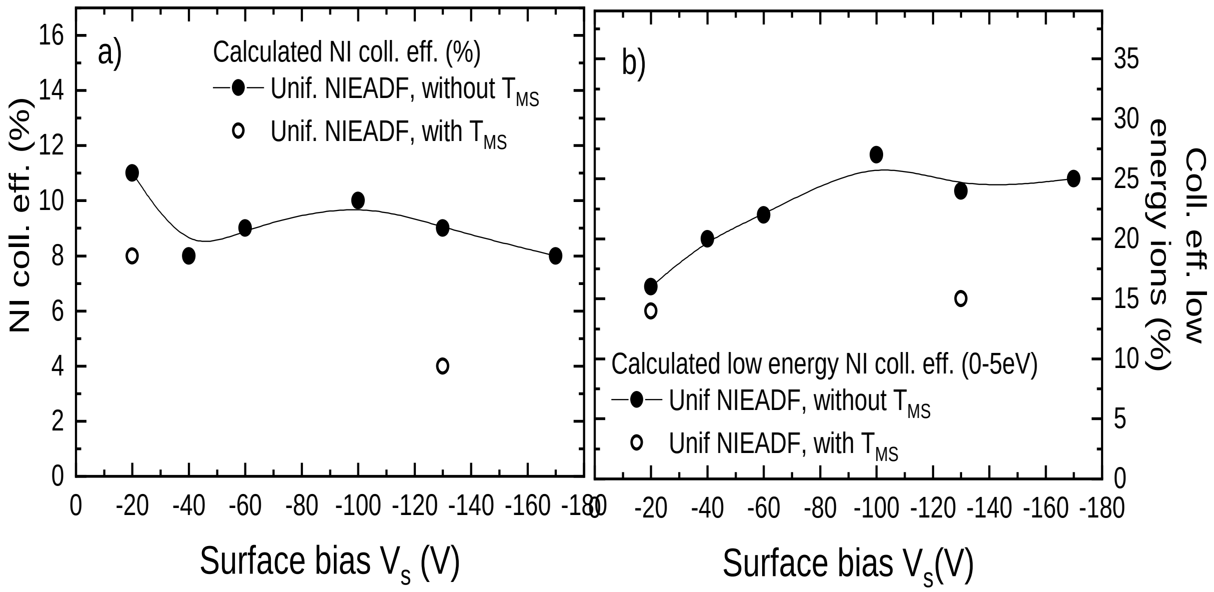

Figure 3.8 Collection efficiency (all energy on top and only 0-5 eV energy range on bottom) computed by the model using a uniform NIEADF. The fill/open symbols are for calculations without/with the transmission function of the mass spectrometer taken into account. Parameters for the calculations are those of a D_2 RF plasma 20 W, 2 Pa.

The collection efficiency for low-energy ions (0 – 5 eV) is increasing when ignoring T_{MS}. The decrease of the acceptance angle is compensated by the fact that the trajectories of low energy ions are easily modified by the electric field in the sheath leading to Θ_{MS} well below the acceptance angle. This explains their better collection efficiency. If one considers now the calculations taking into account the mass spectrometer transmission function, the collection efficiency is constant for low energy NI. The conclusion to this part is that the collection efficiency is expected to be at best constant or to decrease over the whole bias range. Any increase of the yield such as observed for HOPG material cannot be interpreted by an increase of the NI extraction and collection efficiency.

It is not easy to get direct information on the ionization probability from plasma experiment such as those presented here. For metals, the ionization probability is expected to depend on the perpendicular velocity of the outgoing particle. Here, when the bias is increasing in absolute values, the mean energy of the D particles leaving the surface is also increasing as shown by the NIEDF tail which is expanding to higher energy in **Figure 3.1** and **Figure 3.2**. Such increase of the mean energy could lead to an increase of the ionization probability. In order to rule out this possibility we have plotted the peak intensity variations in **Figure 3.6**. NIEDF peak is always located around 3-4 eV and therefore corresponds to NI emitted at constant low energy whatever the surface bias. For such ions, the ionization probability cannot increase because of an increase of the perpendicular velocity. As the peak intensity variation is following the yield variation, we assume that the increase of the mean NI energy is not playing a crucial role and is not affecting strongly the ionization probability. We can maintain the assumption we made in previous works of no dependence with energy and angle of the ionization probability for graphite and diamond[47,51,73,74].

The ionization probability could still change with sample bias if the surface state is changing. Indeed, the ionization probability is defined for one material with given electronic properties. Changing the electronic properties changes the ionization probability. In order to investigate this possibility, we have measured NI yields at low bias after high bias experiment. The idea is to measure NI under low bias condition with a surface state corresponding to the high bias condition. If after a complete scan of V_s HOPG is exposed again at low bias the same NI yield as before is immediately obtained, and no time evolution is observed. The experiments were done with a time resolution on the order of the second which is usually enough to observe surface modifications due to the ion bombardment[47] since the ion flux is rather low in the present experiments. A fluence of roughly one mono layer of material (10^{15} ions cm^{-2}) is reached after about 20 seconds. Let us note that a complementary experiment has been performed in which after high bias exposure, the bias has been modulated between -100 V (duration 5 ms) and -20 V (duration 50 µs). In this situation the sample is exposed to high bias most of the time. The mass spectrometer acquisition was performed during the low bias (-20 V) phase. The yield at -20 V was the same during the modulated bias experiment as the initial yield at -20 V before high bias exposure. It clearly shows that when switching from high bias to low bias, the yield comes back immediately to its initial low bias value without any time evolution. As the surface state, determined by parameters such as the sp2 over sp3 ratio or the deuterium content, cannot change fast, it demonstrates that the change of surface state between low and high bias, if any, is not promoting the ionization probability for HOPG material. For HOPG, the ionization probability can be considered as a constant over the whole bias range.

In the case of MCBDD its surface produces 7 times less NI at V_s = -10 V after exposure to -170 V (see **Figure 3.6**). The initial signal is recovered after several tens of minutes of exposure at -10 V. Same results are obtained with – 20 V bias. There is here a remarkable difference between both materials. When the bias is increased in absolute values the energy of the positive ions impacting on the surface and creating defects is increased, leading to i) a deeper ion implantation and a thicker defective layer on top of the pristine material ii) possibly creation of defects of different nature in the defective layer. These effects can be summarized as a change of the surface state. This change of surface state is obviously unfavourable for NI surface production on MCBDD since after a complete scan in bias, the signal is strongly decreased when coming back to -10 V. The ionization probability of the surface exposed at high bias is obviously lower than the ionization probability of the diamond surface exposed at low bias. This conclusion is in line with previous papers showing that defect creation on diamond is unfavourable for NI production[104,47]. Electronic properties of diamond are promoting NI surface production, defect creation is modifying electronic properties and lowering NI yield.

The sputtering and backscattering yield $Y_{sp}(E,\theta,V_S)$ and $Y_B(E,\theta,V_S)$ in **Equation 3.1** have now to be considered. Let us remind that NIEDF in **Figure 3.5** are normalized and the comparison between experiment and calculation is just giving information on E and θ dependence of yields but not on their absolute value. In SRIM software the surface state is an input of the calculation and the choice of surface state parameters (deuterium content, surface binding energy…) strongly influences the results given. The set of parameters chosen for calculations at Vs = - 130 V, validated in our previous works, has been used here for lower bias but nothing ensures it is valid. Calculations with this set of parameters show a sputtering yield increasing from 0 at 10 eV impact energy to 0.6% at 50 eV. The backscattering yield is increasing from 13.5% at 10 eV to 15.5% at 25 eV and is then constant. Let us note that despite sputtered particles are in a minority they have a strong influence on measured NIEDF. Indeed, they are emitted at lower energy[72] and are more efficiently collected (**Figure 3.8**) than high energy ions. From the model at – 130 V, they represent 30% of the collected NI. So, both sputtering and backscattering yield computed by the model with this set of parameters are increasing with positive ion energy (ie with surface bias in absolute value). This increase is not enough to compensate the decrease of the collection efficiency (**Figure 3.8**) and the model is not predicting an increase of NI signal for HOPG. Other surface state parameters could lead to higher increase of backscattering and/or sputtering yields and could explain the HOPG behaviour. There are no in-situ surface analyses on the present set-up to help tracking surface state changes. Some measurements and MD simulations can be found in the literature, but they do not match exactly with the present experimental conditions. Davydova et al have studied the impact of H+ ions on multi-layer graphene at increasing energy[105]. At energy below the penetration threshold through the first basal plane (5e V) ions hydrogenate the top surface. At 10 eV H^+ ions have enough energy to penetrate through the first plane but not through the second. They create a strongly disordered and hydrogenated top layer and etching starts. Once the a-C:H layer is formed H^+ ions lose less energy to pass through it and start to hydrogenate the third and fourth layers. An equilibrium is reached between erosion and hydrogenation. At 25 eV the process is globally identical, but the first three layers are initially hydrogenated by the impact of ions. Bombardment by 25 eV and 50 eV H_2^+ ions show similar trend to 10 eV and 25 eV H+ bombardment since a large fraction of H_2^+ ions dissociate at impact and the energy is shared between the fragments. From Davydova et al work it is seen that the number of CH, CH_2 and CH_3 bond ratio in the defective layer is changing with the positive ion energy, as well as the hydrogen content which is increasing with the ion energy. However, this defective layer seems to be highly hydrogenated and porous whatever the positive ion energy and could present identical electronic properties, those of a soft a-C:H layer, whatever the ion energy explaining why the ionization probability is found constant. The effect of increasing positive ion energy would be therefore mostly to reach deeper graphene layers rather than drastically change the top surface layer composition. This would make a huge difference with diamond for which increasing ion energy would help moving carbon atoms from their lattice sites. Dunn et al al have compared diamond and graphite irradiation by 15 eV tritium positive ions thanks to MD simulations[106]. They have shown that the rigid structure of diamond maintains carbon atoms in place despite they may lose their sp3 hybridization due to the hydrogenation. The parallel layers and less dense structure of graphite allows more mechanical deformation, expansion which lead to a higher penetration of ions and more retention. No calculation versus positive ion energy were made in this study but we can expect that the increase of impact energy will help destroying the diamond structure and create a porous and hydrogenated a-C:H film. De Rooij has shown thanks to MD simulation that the penetration threshold for H in diamond is around 7 eV[107]. This result is close to the value found by Kogut et al[108], around 4 eV at room temperature. De Rooij showed that even at 20 eV impact energy only 0.2 nm are modified, H ions went through one monolayer only. Yamazaki et al[109] demonstrated experimentally that impact of H_2^+ ions on diamond with energy between roughly 10 and 50 eV seem to create a defective layer with constant dangling bond density and CH bonding configuration, but with increasing depth reaching about 1 nm at 50 eV. This observation seems to be in contradiction with the assumption that the increase of impact energy would help destroying the diamond structure and thus changing the CH bonding configuration. It shows that it is hard to infer diamond transformation in the present experimental condition. However, we can expect the ionization probability to be affected, whether by the fact that the top layer composition is changing strongly from diamond like to a-C:D, or by the fact the electronic properties of the underlying pristine diamond material are no more influencing ionization as the modified layer depth is growing. Let us note to conclude that none of the MD simulations referenced above consider the concomitant impact of low energy neutral H atoms with ions while in the experiment the atomic flux is much higher that the ion flux. In 110 a MD study of H impact on Si and SiN layer has been conducted with increasing atom to ion ratio. From these results we can expect that H atom impacts on diamond or graphite will increase the top layer hydrogenation and its etching, thus limiting its depth.

After examining all parameters in **Equation 3.1** we come to the conclusion that HOPG yield increase with surface bias can only be explained by an increase of backscattering and/or sputtering yields. The same increase probably occurs also for diamond but is mitigated by the strong decrease of the ionization probability. This conclusion is reinforced by a complementary experiment performed with HOPG material. The bias scan was performed in a high-density plasma, using ICP mode rather than CCP mode. The injected power was 200 W. The measured plasma density was 3 10^9 cm^{-3}, and the positive ion flux was around 100 µA/cm^2 (~6 10^{14} ions/cm^2s, around ten times higher than for the low-density case). Under such high-density condition, the sheath in front of the sample is much thinner than in low density conditions and is no more collisional for positive ions. This has been demonstrated in reference 74 where distribution functions of positive ions crossing a high voltage sheath were measured. In high density mode the distribution functions are much more peaked and closer to monoenergetic distributions than in low bias conditions. Under such a situation, the NI yield on HOPG is of course higher due to the much higher positive ion flux. But more interesting is the observation of an abrupt increase of NI yield between Vs = - 20 V and Vs = - 40 V (see **Figure 3.9**). Such threshold effect is most probably corresponding to the onset of sputtering. This onset is not seen in low density mode since positive ion distribution functions are more distributed in energy and at any bias a large distribution of positive ion energy is impacting the surface, smoothing the threshold effect. The sputtering threshold explains that the NI yield immediately comes back to its initial value when switching the bias from high value to low value since positive ion energy is immediately lowered.

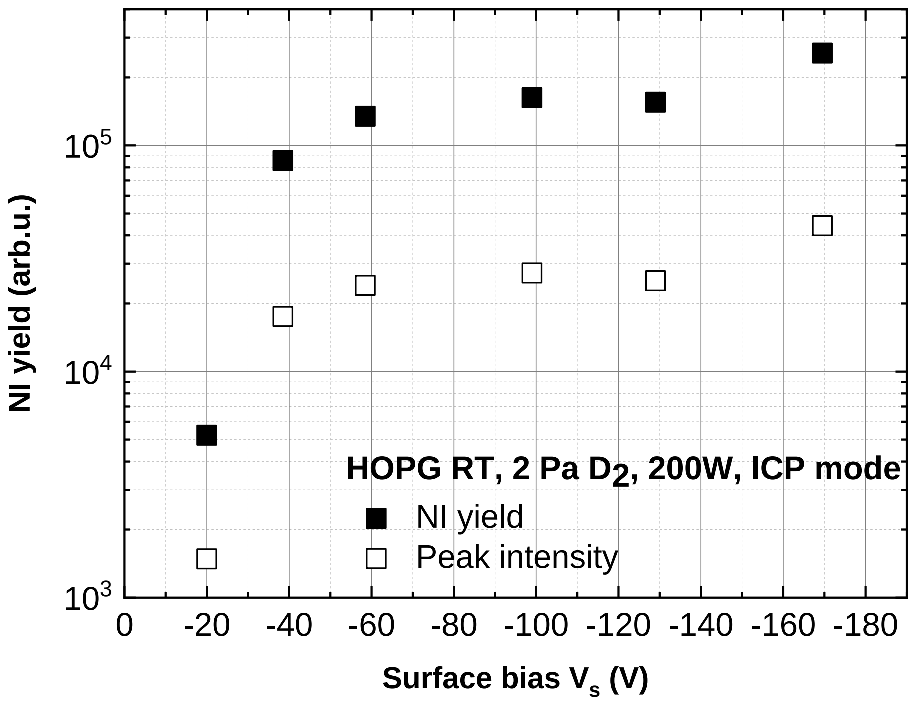

Figure 3.9: NI yield and peak intensity of NIEDF measured for HOPG exposed to 2 Pa D_2 200 W ICP plasma at room temperature.

We therefore conclude that NI yield on HOPG is increasing with surface bias due to an increase of backscattering and/or sputtering yields and despite a decrease of the collection efficiency. This increase of backscattering and sputtering yields cannot be predicted due to the lack of knowledge on the surface state versus the sample bias. Molecular dynamics simulations could help solving this issue and will be the subject of future works. It has also been demonstrated that the ionization probability is not changing for HOPG with surface bias. On the contrary the ionization probability is strongly decreasing for diamond due to a loss of diamond electronic properties because of defect creation by positive ion impact. Consequently, despite backscattering and/or sputtering yields are probably increasing also for diamond, the NI yield is decreasing.

Another way to observe the surface state change of diamond is to take a pristine sample and to trace NI yield in time upon plasma exposure at a given bias. The sample was pre-heated in vacuum to desorb any possible impurities and cooled down. **Figure 3.10 (a)** shows such time evolution for MCBDD in a D_2 plasma at V_s = -10 V. One can observe a rapid increase of NI yield during the first 3 min of exposure and then a gradual decrease on the timescale of 1 hour. The initial increase can be due to activation and hydrogenation of the surface in the beginning; this initial increase is only observed at low bias. At higher bias, starting from – 20 V the yield decreases with time (see **Figure 3.11**. Time evolution of NI yield and NIEDF peak intensity for HOPG in 2 Pa D_2 20W RF plasma at R.T.: filled symbols refer to a short exposure of 30 s at each surface bias, while open symbols show equilibrium values after long-term continuous exposure. for time variation of yield at -130 V). At higher bias yet later the surface is degrading until equilibrium is reached. In **Figure 3.10** (**b)** another MCBDD sample was put in a H_2 plasma (in order to have lower mass and lower transferred momentum to the surface) at V_s = 0 V. It is hard to extract NI without bias towards MS, so the signal is relatively small, nevertheless an increasing tendency was found for NI yield with time. In the latter case 90% of ions impinge with 6 eV/H (H_3^+), 9% with 9 eV/H (H_2^+) and 1% with 18 eV/H (H^+). Therefore, it is possible to observe a certain threshold of the ion impact energy at which the diamond surface starts to degrade decreasing the NI production rate. No such decrease with time was observed with HOPG at low bias.

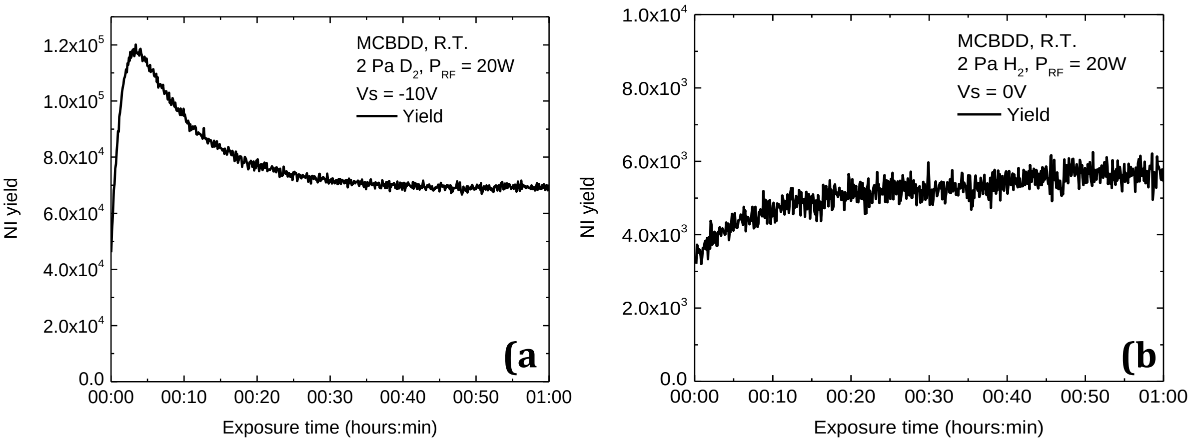

Figure 3.10. Time evolution of NI yield produced on MCBDD surface: (a) 2 Pa D_2 20W RF plasma, surface bias -10 V; (b) 2 Pa H_2 20W RF plasma, surface bias 0 V.

Figure 3.11 and **Figure 3.12** present NI total signal and NI peak signal variations with time for short exposure duration at each bias for respectively HOPG and MCBDD. No normalization by the positive ion flux have been made here. The data shown are in counts/s or counts/s/eV and have been directly taken from the mass spectrometer measurements. In this experiment, the plasma was switched on at -10 V bias using pristine samples. After 30 seconds (20 seconds for MCBDD) of exposure the bias was increased to -15 V and measurements were recorded again for 30 seconds (20 seconds for MCBDD). This procedure was repeated for each bias. The total NI signal is shown by black full symbols and the NI peak signal is shown by red full circle symbols. The figures also indicate yield and peak intensity values obtained at steady state in separate experiment (full symbols). These are the data of **Figure 3.6** before normalization by the ion flux.

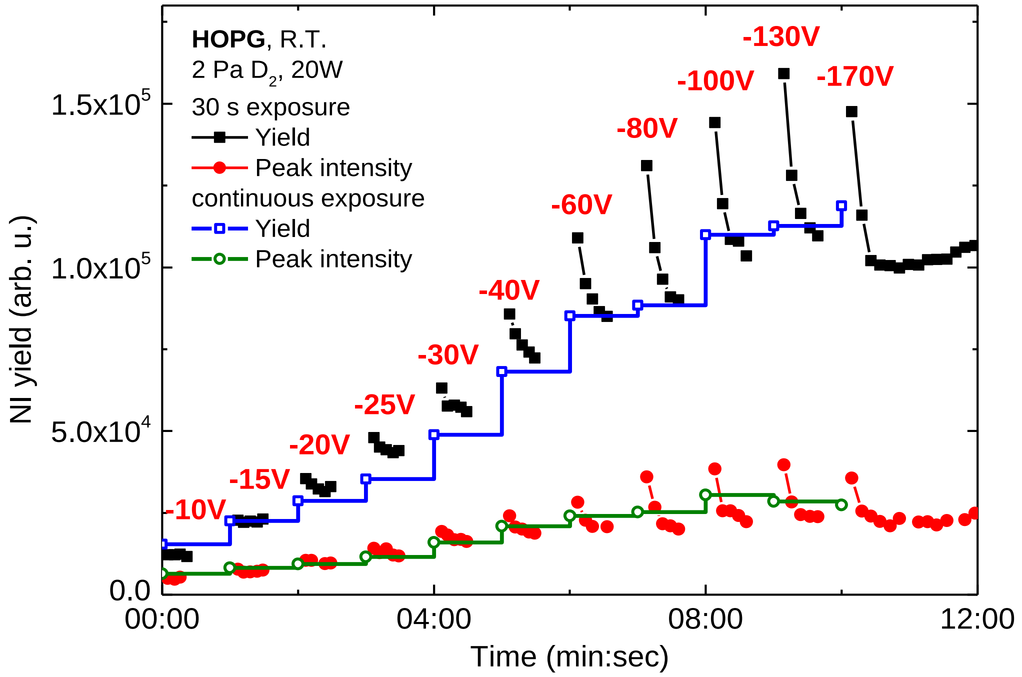

Figure 3.11. Time evolution of NI yield and NIEDF peak intensity for HOPG in 2 Pa D_2 20W RF plasma at R.T.: filled symbols refer to a short exposure of 30 s at each surface bias, while open symbols show equilibrium values after long-term continuous exposure.

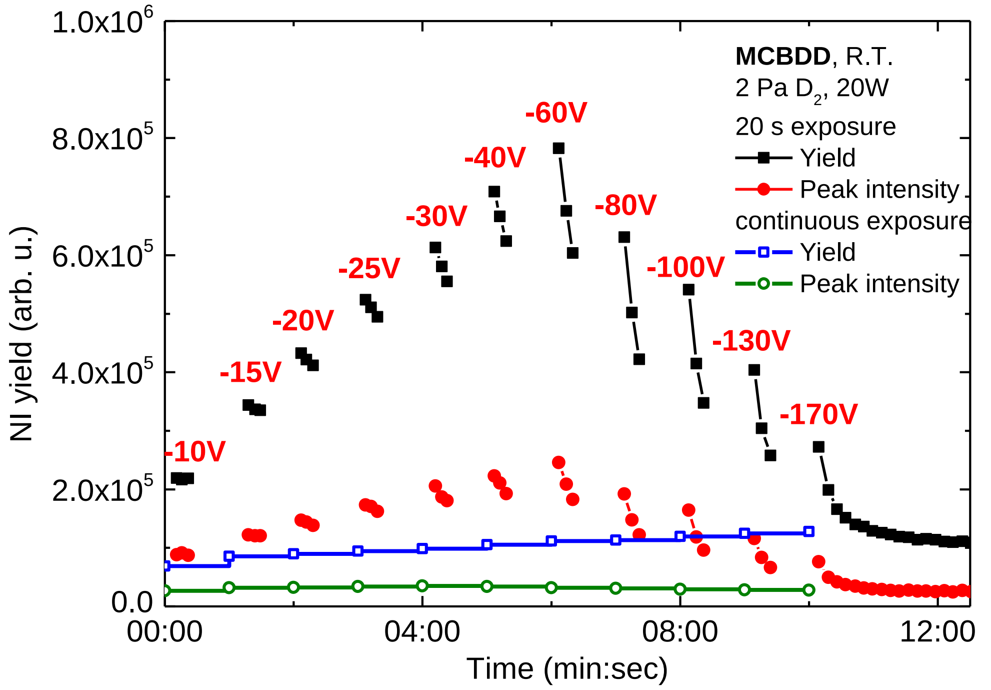

Figure 3.12. Time evolution of NI yield and NIEDF peak intensity for MCBDD in 2 Pa D_2 20W RF plasma at R.T.: filled symbols refer to a short exposure of 30 s at each surface bias, while open symbols show equilibrium values after long-term continuous exposure.

There is one common trend to both materials. When the bias is increased, the signal is initially higher than after 20 or 30 seconds of exposure. So, the increase of positive ion energy leads to a temporary increase of the signal. Coming back to, we attribute this effect to a temporary increase of the backscattering yield due to the fact that the positive ions reach a depth where no previous hydrogen implantation has occurred. In this region the material is the pristine one, made of carbon only, and is denser than the modified one. MD simulations show indeed a decrease of carbon material densities with hydrogen bombardment. SRIM is predicting a decrease of backscattering yield by about 25% when going from a pure carbon layer to a deuterated carbon layer at 50 eV D impact energy. As the material is denser and as the energy transfer from deuterium to carbon is much less efficient that deuterium to deuterium, we can expect that impacting particles on pure carbon are initially not slow down efficiently and have higher chance to reverse their momentum. It explains the higher initial backscattering yield. Then the hydrogen implantation mitigates this effect and the signal comes back to its stationary value for HOPG. Concerning MCBDD the signal is also decreasing with time during the short exposure duration but is still much higher than at steady state. Indeed, the signal at -60 V for instance is initially 7 times higher and still 5 times higher after 20 seconds of exposure. It can be observed that the signal starts to decrease at bias higher than -60 V. At – 170 V the signal reached its steady state value within the course of the short 20 seconds exposure duration. This is a consequence of the defect creation with the accumulated dose of positive ions. Up to – 60 V, the dose and the energy of the positive ions are not high enough to have created defects noticeably changing surface state. Consequently, the ionization probability is probably still high. After – 60 V the signal is decreasing because the ionization probability is decreasing. When switching on the bias at – 170 only the temporary higher backscattering yield is observed, and the signal is reaching its steady state value within the 20 seconds exposure duration.

The experiments presented in **Figure 3.11** and **Figure 3.12** confirm previous conclusions made in this chapter. The surface state of HOPG is probably similar for all bias, only the depth of the modified layer is changing. Indeed, due to the layer structure of HOPG, when positive ion energy is increased a new layer is reached and fast modified. The signal comes fast to its steady state value. For MCBDD, the accumulation of impacts at increasing energy slowly destroy the hard structure of the diamond material and the signal slowly decreases to its steady state value.

Conclusion

The changes in negative ion production mechanisms and production yields versus the positive ion energy are analysed. It is shown that surface defect creation by positive ion bombardment has opposite effects on diamond and graphite. For the surface state of HOPG is probably similar for all bias, only the depth of the modified layer is changing. Indeed, due to the layer structure of HOPG, when positive ion energy is increased a new layer is reached and fast modified. The signal comes fast to its steady state value. For MCBDD, the accumulation of impacts at increasing energy slowly destroy the hard structure of the diamond material and the signal slowly decreases to its steady state value.

Chapitre 4 Pulsed bias approach

Introduction and motivation

Previous works have shown that diamond is an interesting material to promote NI surface production in hydrogen plasmas. A comparison between NI yield on diamond and graphite surfaces is shown versus surface temperature in **Figure 4.1**. We can see clearly that Micro Crystalline Boron Doped Diamond (MCBDD) presents a NI yield which is maximum around 500°C and about 3 times higher than at room temperature. Unfortunately the same measurement could not be performed with Micro Crystalline non-doped Diamond (MCD) since these layers turned to be non-conductive when exposed to plasma at temperature below 300°C[63]. This has motivated the development of a solution, the pulsed DC bias method, which allows studying NI surface production on insulating materials using the same technic as those developed for conductive materials. This technique extends the measurement of NI surface production to potentially interesting materials. Indeed, electron capture on insulators is difficult, but electron loss is limited, resulting in a potentially high ionization probability.

A similar method has been used by Samara et al[111] to measure the ion saturation current in simpler manner as compared to the RF-biased probe. Wang and Wendt[112] and Kudlacek [113] et al have used this approach to control the ion energy in industrial plasma processes dealing with insulators. They have applied a modulated pulse shape, where the voltage during the pulse is sloped and thus exactly compensates for the drop of voltage due to the charging of the substrate being processed. Barnat et al[114] showed that a pulsed direct current bias is capable of discharging insulating surface and provides a good means of controlling the energy of the ions extracted from the sputter magnetron plasma when using insulating targets.

This chapter is separated in six parts. The first one concern the presentation of the principle of the surface bias method. The second part is dedicated to our different experimental consideration. The third part shows results obtained in pulsed bias mode with a conductive sample while the fourth part is dedicated to an insulating layer. A model has been developed to explain the insulator behavior in plasma with pulsed bias mode. Model results are compared to experimental ones. In the fifth part pulsed bias parameters are optimized. The last part shows negative ion signals obtained in pulsed mode versus surface bias and surface temperature for several samples.

4.1 Pulsed Direct Current (DC) bias technique principle

To begin the discussion, a definition of a pulsed waveform is given in the scheme presented in **Figure 4.2**. The pulse is defined as having a frequency f and a period T. The amplitude of the pulse V_a is defined as the difference between ground potential and the negative potential applied by the generator. The pulse is assumed to have an infinite slew rate during the transition between V_a and zero. Because of this infinite slew rate, rise times are neglected and the duty cycle of the pulse is defined by the ratio of the time the pulse is at V_a defined as T_{pulse} to the total period of pulse T.

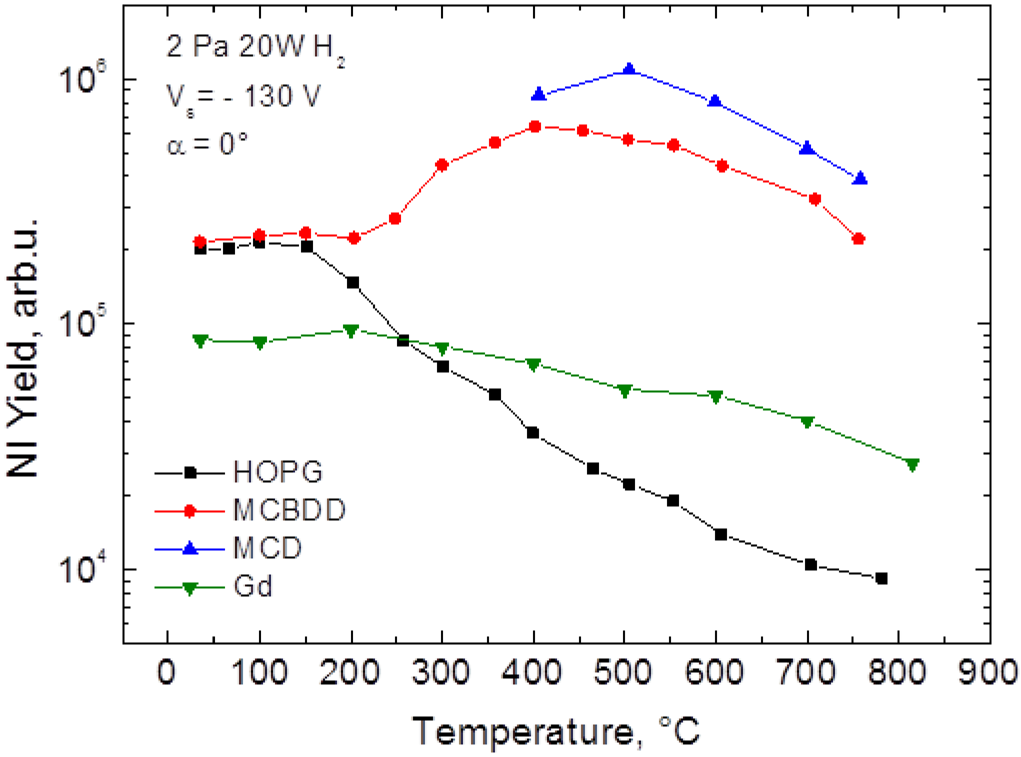

Figure 4.1 NI yield dependence on the surface temperature for HOPG, MCBDD and MCD samples at 2.0 Pa of H_2 plasma, Q = 5.2 sccm, P_{RF} = 20 W, V_s = -130 V, V_{MS} = 0 V, with screen

Having defined the properties of the pulse, we discuss the role the shape of the waveform has on the energy spectra of positive plasma ions and surface produced negative ions. To study NI surface production on conductive samples, a constant DC bias is applied. The DC bias leads to positive ion bombardment of the sample with a well-defined energy. It also permits the self-extraction towards the mass spectrometer of negative-ions created on the surface. When using the same technique for insulating samples, charge is quickly built up on the surface. As a result, the applied negative voltage does not appear anymore on the surface which is floating, so negative-ion can no more be self-extracted preventing the measurements of NIEDF. To eliminate the surface charging an RF bias can be used but its capability to control the energy of the bombarding ions is limited and furthermore it would strongly modify NIEDF shape and complicate their interpretation. The method of pulsed DC bias described in the present chapter was developed to enable the study of NI production on surfaces of insulating materials using the same tools as those developed for conductive materials. The idea is to use a pulse which is short enough to get small charge build up during the pulse and thus negligible voltage change and use a period long enough after the pulse for the plasma to neutralize the charge on the surface. During the pulse positive ions bombard the sample at well-defined energy, negative-ions are self-extracted and NIEDF measurements are performed. In the present work, only rectangular shape pulses were used. As a first step, the pulse DC bias technique was tested on a conductive material, HOPG.

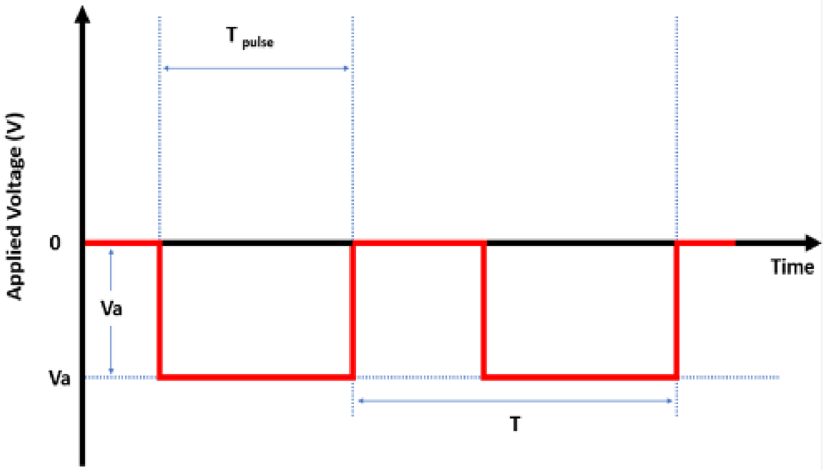

Figure 4.2 Illustration of rectangular pulse and the terminology used to describe the pulse

4.2 Pulsed Direct Current (DC) bias: experimental considerations

Pulsed DC bias experiments are done on PHISIS set- up. Measurements are performed in H_2 and D_2 plasma under following experimental conditions: 2 Pa, RF power of 26 W. The usual sample holder (rectangular Molybdenum clamp) and the other one (circular ceramic sample clamp) are used to install sample. The latter was mounted on the diffusion chamber on the flange usually dedicated to the Langmuir probe (see **Figure 1.2**). Sample was held in place on the sample holder by a 2 mm thick molybdenum clamp or by a 3 mm thick ceramic clamp. The reason for using two different materials as clamp is to test the influence of the sheath shape in front of the sample on the results. The clamp material used for the measurements will be indicated in the figures.

The system used in pulsed bias experiment is showed in **Figure 4.5**. Samples are biased thanks to a DC voltage source connected to a homemade electronic chopper controlled by a function generator. The bias duration T_{pulse} and the bias frequency f are determined by the function generator. A delay generator synchronized with the function generator is used to define the delay T_{delay} between the DC bias pulse and the acquisition, as well as the duration of the acquisition T_{acq}. The $12\ \mu s$ H^- transit time between the sample and the mass spectrometer detector has been measured accurately by observing on a scope counts at the output of the mass spectrometer detector. $T_{delay} = 13\ \mu s$ has been chosen to get rid of NI created during the first microsecond of the pulse when the applied bias is establishing. In the same way the acquisition duration T_{acq} was usually set shorter than the applied bias in order prevent the collection of NI created during the fall down of the sheath in front of the sample at the end of the pulse. This is summarized in **Figure 4.3**.

The surface charging during pulse application can be easily observed using this experimental setup. Since the value of surface bias Vs can be determined directly from NIEDF spectra, as explained in the experimental protocol. All NIEDF raw data are processed assuming a surface voltage equal to the applied voltage, like for the conductive sample case. If the surface voltage is higher than expected because of charging this leads to a NIEDF onset shifted towards negative value on the energy scale. As it is shown in **Figure 4.4** the NIEDF onset shift at time t is a measurement of the voltage change at time t compared to t = 0 (beginning of pulse).

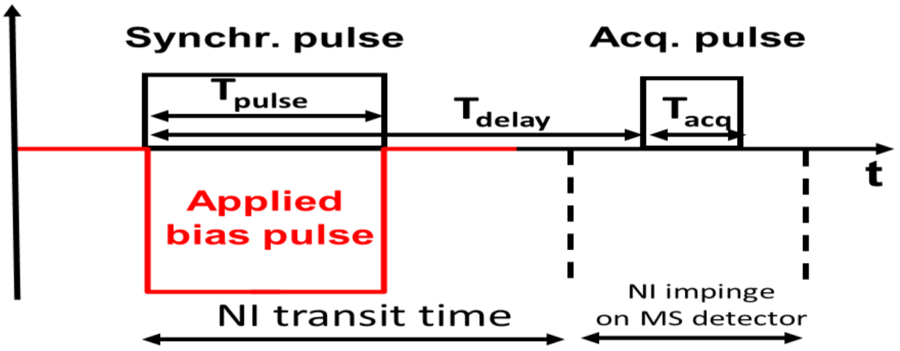

Figure 4.3 Synchronization scheme for pulse bias measurements

This technique give use the ability to measure the surface bias on sample biased in pulsed mode in order to further investigate the pulse bias method and to get some information on the OFF period, when the applied bias is switched off, we have also measured the sample current. A homemade microampermeter is connected in series between the sample holder and the pulsed DC bias supply (see **Figure 4.6**). This microampermeter can measure current in the µA range even in the presence of pulsed common mode voltage as high as hundreds of volts. Within the framework of our measurements its sole drawback was its relatively low-resolution time on the order of 5 µs. Sample current measurements are only possible with the ceramic clamp since with the molybdenum one all the sample holder is drawing a current and not only the sample.

Thanks to these measurement charging effects on surface can be explored, the pulse parameters can be adjusted, and the bias can be optimized in order to get a constant surface bias during T_{acq}.

4.3 Pulsed DC bias: test on conductive material

The feasibility of pulsed bias technique was tested on HOPG sample during the PhD thesis of Kostiantyn Achkasov [115]. However, these measurements were reproduced during the present thesis for sake of verification and to complete the data set.

We have confirmed that no charging happens on HOPG surface during the pulse. The NIEDF were measured in the case of a long pulse (T_{pulse} = 1 ms) and a low duty cycle (dc= 10%). The acquisition (T_{acq}= 50 us) was done for different T_{delay} going 13 µs 953 µs. As NI transit time between sample and MS detector is 12 µs these delays correspond respectively to time t = 1 µs after the start of the pulse and to 60 µs before the end of the pulse. No shift of NIEDF was observed (not shown here) showing that the applied bias equals the surface bias all along the pulse.

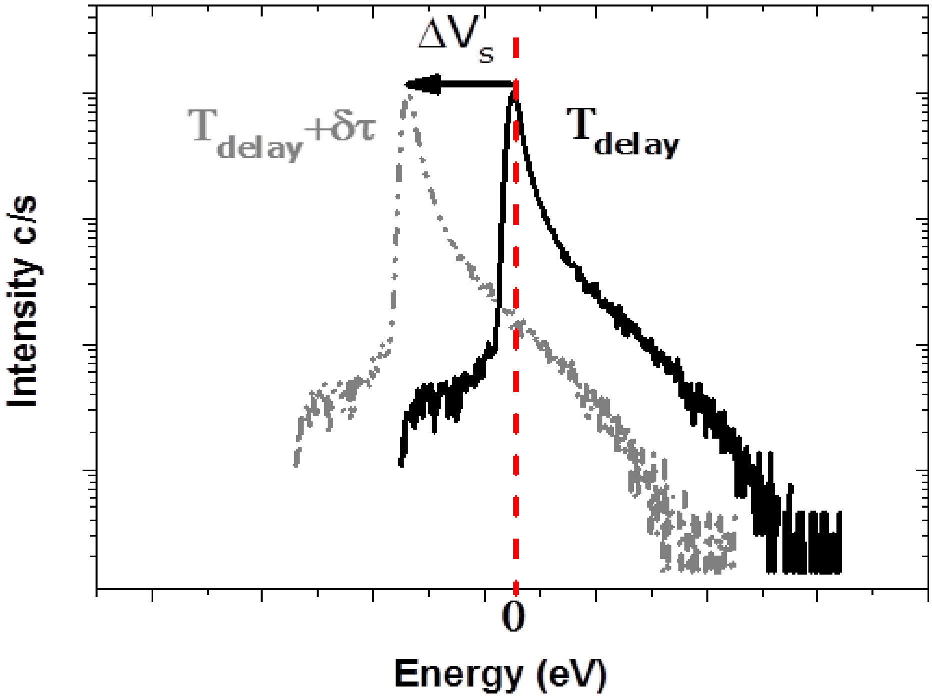

Figure 4.4 Variation of surface bias is observed experimentally by NIEDF shift with T_{delay}

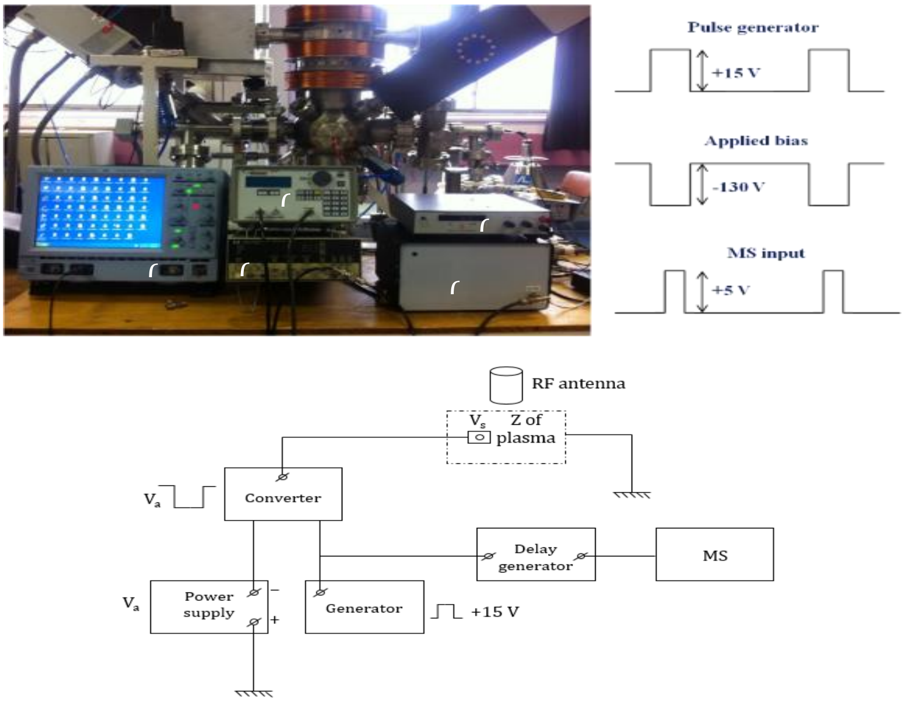

Figure 4.5. Photo of the system used for the pulsed bias experiment: (a) constant DC bias source; (b) primary pulse generator; (c) Homemade electronic chopper used to convert constant DC bias into pulsed bias; (d) delay generator; (e) oscilloscope. The output produced by components (b), (c) and are sketched on the right. The schematic circuit of the system used for the pulsed bias experiment is below the actual photo.

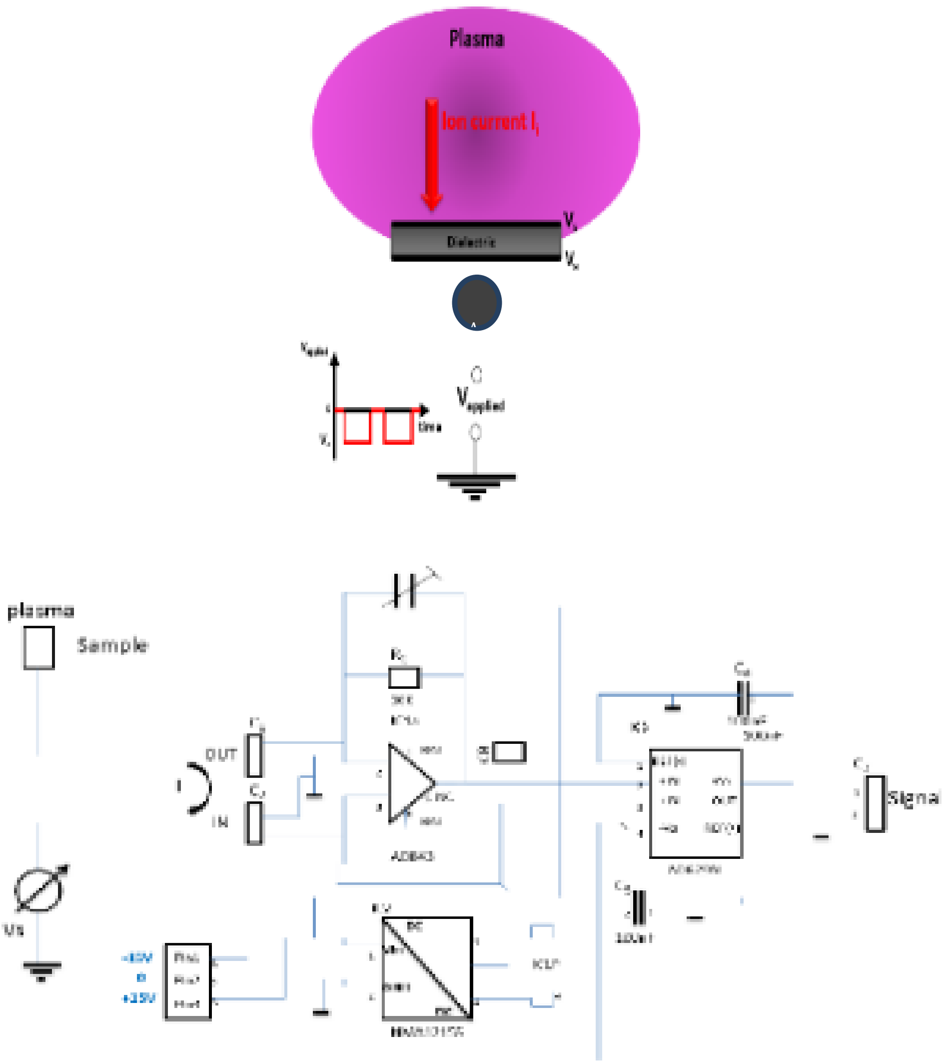

Figure 4.6 Schematic diagram of microampermeter (µA) installed between the transfer rod and the pulsed bias source. Below, the detailed circuit of the microampermeter used for surface current measurement is showed.

However, the change of the bias frequency has proven to influence the hydrogen surface dynamics. **Figure 4.7** demonstrates the NI yields measured with T_{pulse}= 10 us, T_{acq}= 8 us and T_{delay}= 13 us as a function of frequency varied from 0.25 kHz to 90 kHz. The red symbols represent the measured NI yield in the case of constant DC bias and pulsed MS acquisition. The black symbols represent the measured NI yield in the case of pulsed DC bias and pulsed MS acquisition. In the case of constant DC bias, NI yield is constant for different acquisition frequency. This constant NI yield is similar to what we measure in the case of a constant DC bias and a constant MS acquisition (orange star). In the case of a pulsed DC bias, measured NI yield decreases with bias frequency and reaches at 90 kHz the value of NI yield measured at constant DC bias. The NI yield measured at low frequency (0.25 kHz) is the double of what we measure at high frequency (90 kHz).

The NI yield behavior with bias and acquisition frequency bring us to two important conclusions. First, the NI yield decrease with frequency during the pulsed bias is not connected to the pulsed mode of MS acquisition. Second, NI yield behavior with bias frequency can only be explained by a surface change of material. This hypothesis of surface change induced by bias frequency can be confirmed by looking at the shape of normalized NIEDF's measured at different bias frequency.

As can be seen from **Figure 4.8** (c), the normalized NIEDF measured at 1 kHz has the lowest tail. The tail of normalized NIEDF grows progressively with bias frequency and it approaches at high frequency the situation of constant DC bias. The variation of the shape of normalized NIEDF (variation of the tail with respect to the normalized peak) is related to the variation of relative contribution of different mechanisms (sputtering/backscattering) to NI surface production as explained before in **Chapter 2** and as shown in **Figure 4.8** (a) and (b) where the SRIM based model[73,74,51] has been employed to compute NIEDF for hydrogenated Carbone surface with different hydrogen coverage (see **Figure 4.8** (a) &(b)). The hydrogenated Carbone surface with low hydrogen coverage corresponds to a low sputtering contribution[51]. As one can see in **Figure 4.8** (d), the NIEDF calculated in the case of HOPG surface with 40% of hydrogen coverage has approximately the same normalized shape of NIEDF measured at 5 kHz. For 30 kHz, the hydrogen coverage which is best fitting the experiment is 35%, and for f > 70 kHz it approaches 30% which is the value of surface hydrogen coverage in the case of constant DC bias. So, the decrease of measured NI yield with bias frequency is related to a loss in hydrogen surface coverage which leads to a diminution of sputtered NI production.

Hydrogen surface coverage is increased by hydrogen atoms and ions impinging surface and it is decreased by self-sputtering and by physico-chemical etching.

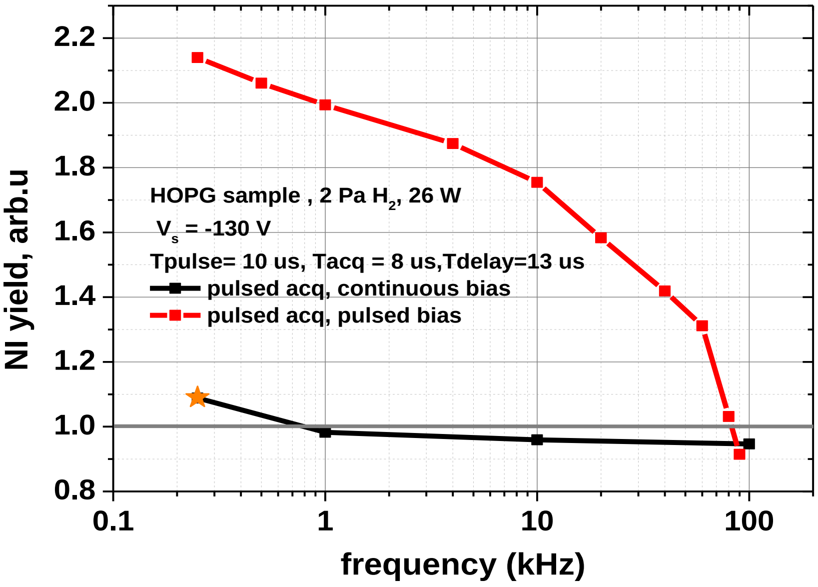

Figure 4.7 The NI yield dependence for HOPG with the pulsed bias frequency. The DC bias signal has been taken as a reference level and set to 1. The grey line is the averaged of NI yield at constant DC bias with pulse MS acquisition

A hydrogen atom is self-sputtered if it is sputtered from the surface by a hydrogen ion. In the case of pulsed DC bias, the surface is not bombarded continuously which leads to a non-continuous self-sputtering, and also probably a non-continuous physico-chemical etching. For low duty cycle (low frequency) the period without bombardment is long and allows for efficient coverage of the surface by hydrogen. This analysis can explain the high NI yield between 0.25 kHz and 1 kHz, and its decrease for higher frequency where the duty cycle is high.

As a summary, the pulsed bias tests performed on HOPG have proven that no charging effect is observed on this conductive surface. The NI yields measured in pulsed mode and continuous mode were different. The change of pulsed bias frequency (and duty cycle) leads to an HOPG material with different hydrogen surface coverage and hence different surface states. At a frequency below 1 kHz, the hydrogen coverage is higher than in continuous mode and a NI yield increase of 100% is measured. This is due, at least partly, to an increase of the contribution of the sputtering process to the NI production. At high frequency 90 kHz, the hydrogen coverage is equal to the continuous mode value[51], giving a similar NI yield value.

Let us note that the pulsed bias method does not represent a way to increase the NI surface production. As no NI production occurs when the applied bias is off during (T- T_{pulse}), the total production yield in pulsed mode is the product of the NI yield produced during T_{pulse} by the duty cycle. The product value is well below the NI yield value in continuous mode

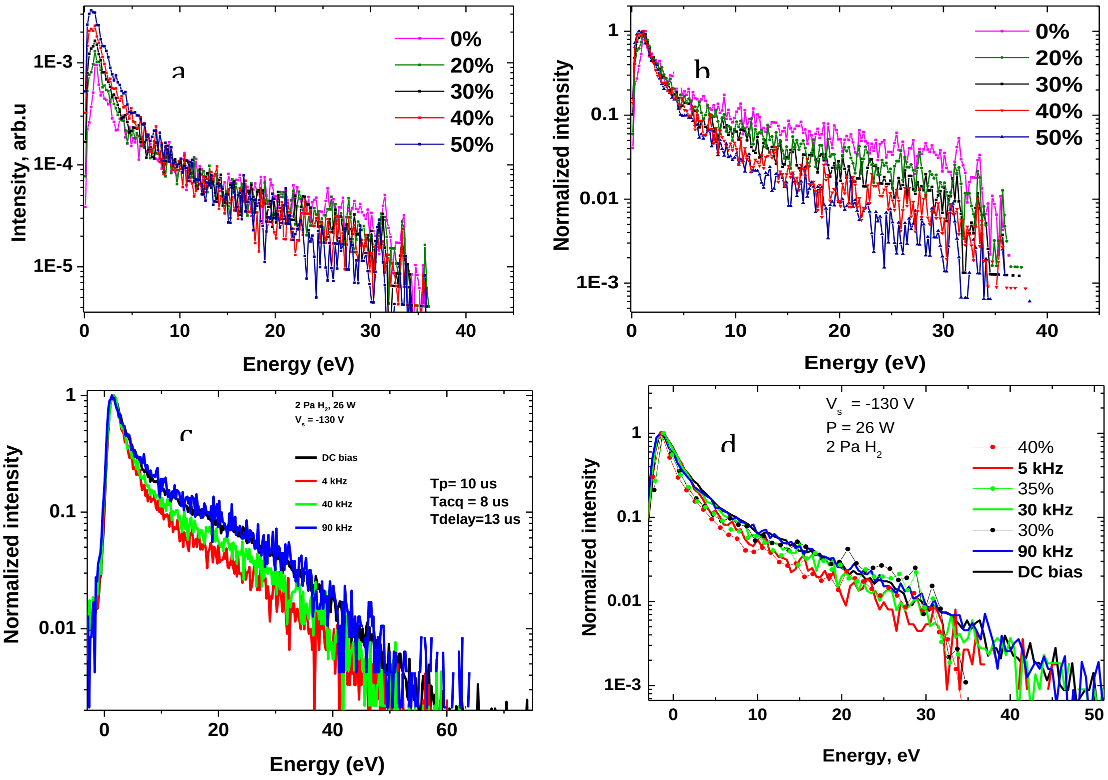

Figure 4.8 (a) NIEDF calculated by SRIM modeling for HOPG surface for different hydrogen surface coverage (b) Normalized NIEDF calculated by SRIM modeling for HOPG surface for different hydrogen surface coverage (c) Normalized NIEDF measured on HOPG surface for different pulsed bias frequency (d) Comparison of normalized NIEDF measured on HOPG surface for different pulsed bias frequency with Normalized NIEDF calculated by SRIM modeling for HOPG surface for different hydrogen surface coverage

4.4 Pulsed DC bias: insulating materials

This paragraph is dedicated to the application of the pulsed DC bias technique to insulating materials. It starts with theoretical considerations to describe the expected behavior of insulators immersed in a plasma and submitted to a pulsed DC bias.

4.4.1 Modelling

A) Modeling of non-conductive samples

To describe quantitatively the charging and discharging of insulator surface under pulsed DC bias, a model was developed. It deals with surface potential and sample current as a function of time. The model considers that an insulator immersed into plasma acts as a planar capacitor. The surface of insulator sample was treated as one plate of a parallel plate capacitor with surface potential V_s (t). The sample substrate acts as the second plate and it is in contact with the biased holder with applied potential amplitude V_a. The voltage across the capacitor is related to its charge which is in this case delivered by the current flux from the plasma. The model is qualitatively represented in**. Figure 4.9.**

For a capacitor, the potential difference can be written as:

$$V_s - V_a = \frac{Q}{C} \longrightarrow \frac{dV_s}{dt} = \frac{1}{C}\frac{dQ}{dt}$$

Equation 4.1

In this model, C represents the effective capacitance of the insulator, and Q is the charge placed on the insulator surface. As charge variation is equal to the current $dQ = I(V_s).dt$.

Where $I(V_s)$ is the surface current as a function of the surface potential) we obtain a first order differential equation for the surface bias:

$$\frac{dV_s}{dt} = \frac{1}{C}.I(V_s)$$

Equation 4.2

This simple first order differential equation can then be solved numerically to give the time evolution of the surface potential on the insulator, once a relation for the current $I(V_s)$ as a function of surface potential V_s is obtained. Basically, at large negative voltage only ions reach the sample and the surface current I_s is the ion saturation current. The surface bias V_s increases linearly with time (I_S is a constant). At lower negative voltage V_s some energetic electrons can overcome the potential barrier and reach the sample, and the current *Is* is the sum of the ion and electron current. Some theoretical predictions of $I(V_s)$ are possible (see Langmuir probe theory for instance) but is it not easy to account for all experimental particularities.

Indeed, predicting the current requires a good knowledge of the sheath formed around the sample. This is possible without too much effort only for simple geometries such as infinite planar sample, infinite cylindrical sample… Therefore, rather than trying to compute the sample current, it has been chosen to measure the $I(V_s)$ relation using HOPG sample (conductor sample) placed in H_2 plasma under usual experimental conditions: 2 Pa, RF power of 26 W. To do this measurement we bias HOPG over a large V_s range using a constant DC bias source, and we measure with an amperemeter the corresponding current value $I(V_s)$ [114].

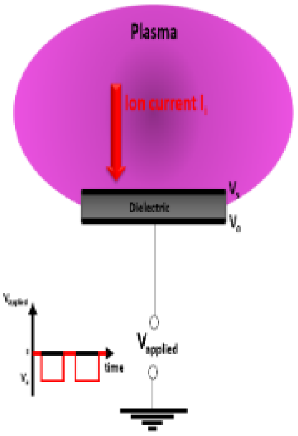

. **Figure 4.9** Schematic diagram of C equivalent circuit of the insulator biased and immersed in plasma

There is however one difficulty. If one is using a conductive clamp to hold an insulating sample under pulsed DC bias, the clamp will remain biased at the applied bias while the sample bias will evolve with time due to charging effects (see **Figure 4.10** (a)). It is not possible to reproduce such a situation with the HOPG sample, both the clamp and the sample bias are equal to the applied bias (see **Figure 4.10** (c)). For that reason, we have chosen to work with an insulating clamp using a different sample holder where the clamp is made from insulator (see **Figure 4.11**). It is a circular ceramic piece with 8mm in diameter internal hole (see **Figure 4.11**. (d)) allowing to expose the sample to the plasma in identical manner as the with the standard holder The use of this ceramic clamp allows measuring sample current versus sample potential on HOPG in identical conditions as those encountered with an insulating sample (see **Figure 4.10** (b) and (d)), and thus allows comparing model calculations and experiments. Indeed, the sheath area is equal to the collection surface of charged particles (ions or electrons) by sample surface. Therefore, the sheath area must be identical in HOPG case and insulator case when we measure $I(V_s)$.

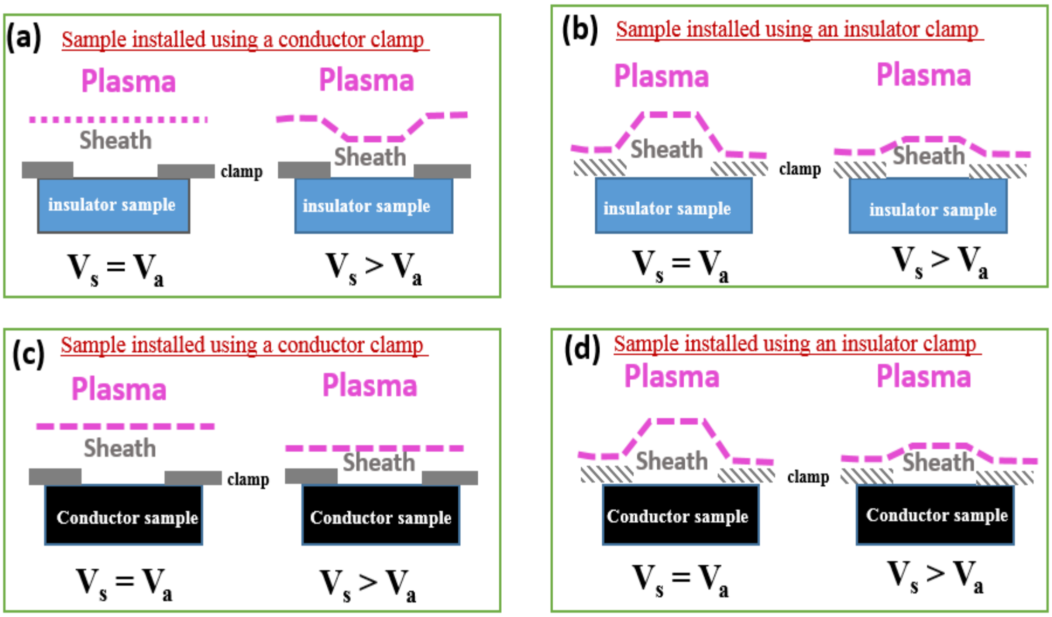

Figure 4.10 (a) Sheath in front of insulator sample installed using a conductor clamp in the case of $V_s= V_a$ and $V_s > V_a$ (b) Sheath in front of insulator sample installed using a insulator clamp and biased in the case of $V_s= V_a$ and $V_s > V_a$ (c) Sheath in front of conductor sample installed using a conductor clamp in the case of $V_s= V_a$ and $V_s > V_a$ (d) Sheath in front of conductor sample installed using a insulator clamp and biased in the case of $V_s= V_a$ and $V_s > V_a$

The incoming current from H_2 plasma to HOPG surface is measured manually as a function of the surface potential. **Figure 4.12** shows I- V characteristic of H_2 plasma for HOPG surface installed on a sample holder with ceramic clamp. As we can see, measured I- V characteristic is similar to typical Langmuir probe I-V curve. The floating potential can be determined from **Figure 4.12**, and it is equal to about 7 V (similar value to the floating potential V_f, ≈ 6 V measured in same plasma condition near HOPG sample using a Langmuir probe). Using the obtained experimental I- V data, an interpolation table is computed, from the applied bias to +70V with a step of 5.10^{-3} V. Interpolated current values are used in the modelling as $I(V_s)$ input values.

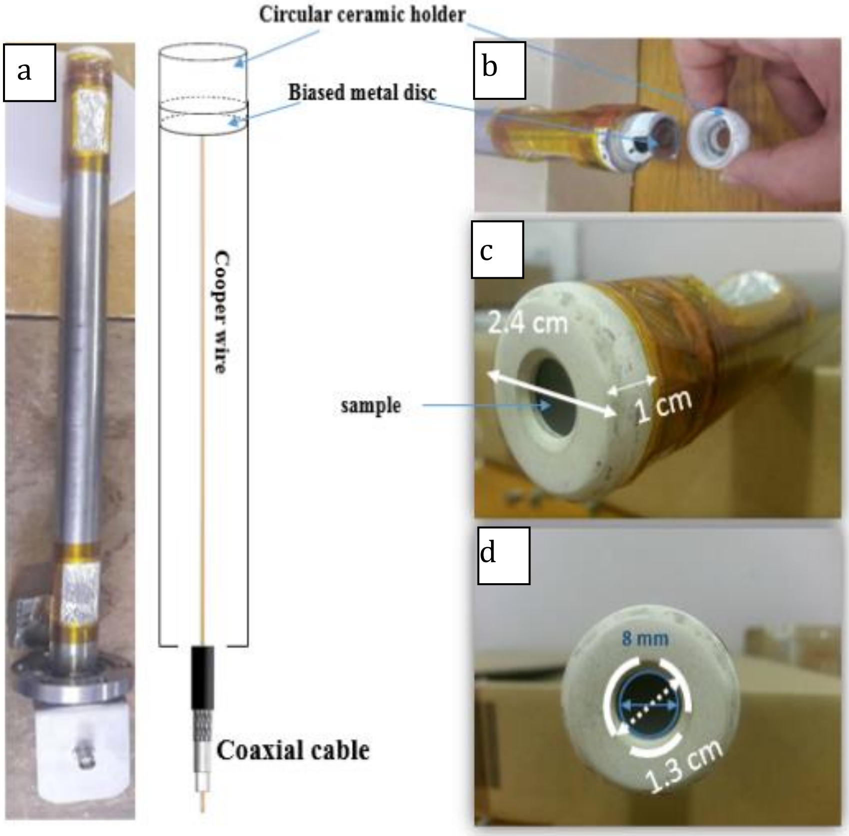

Figure 4.11 (a) sample holder with ceramic clamp, (b) Circular ceramic clamp and biased metal disc, (c) side view of ceramic clamp and dimensions details, (d) Top view of ceramic clamp with sample surface

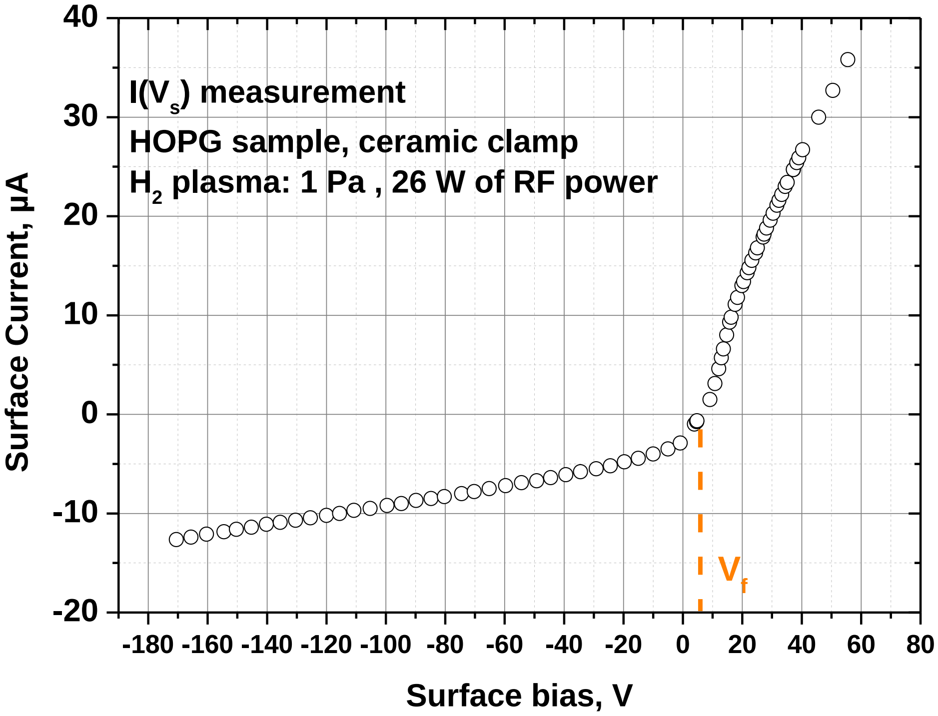

Figure 4.12 I- V characteristic of H_2 plasma (2 Pa of gas pressure and RF power of 26 W) for HOPG surface installed with a ceramic clamp. A floating potential V_f of 7 V is measured

a) Results of the model for a unique long pulse

To obtain the value of insulator effective capacitance diamond was considered as a dielectric. As we mention before, the sample is treated as a planar capacitor. The capacitance is equal to ($\varepsilon_0 \cdot \varepsilon_r \cdot S.\ d^{-1}$), where ε_0 is permittivity of free space and it is equal to $8.85 \cdot 10^{-12}$ *(F/m)*, ε_r is the relative permittivity of diamond and it is equal to 5.7, *S* is the surface of the planar insulator and it is equal to the diamond disc exposed to plasma $S = 5.10^{-5}\ m^2$ and d is dielectric thickness and it is equal to 12.5×10^{-6} (m). It gives for MCD diamond sample used in this experiment a capacitance C equal to 2×10^{-10}(F). Using I- V data and C value, surface potentials variations with time V_s *(t)* are modeled and plotted for various pulsed DC bias conditions. In **Figure 4.13**, a DC bias of -139 V is applied to MCD sample assuming that the initial surface bias is at V_a., It takes about 5 ms to fully charge and reach the floating potential of 7 V.

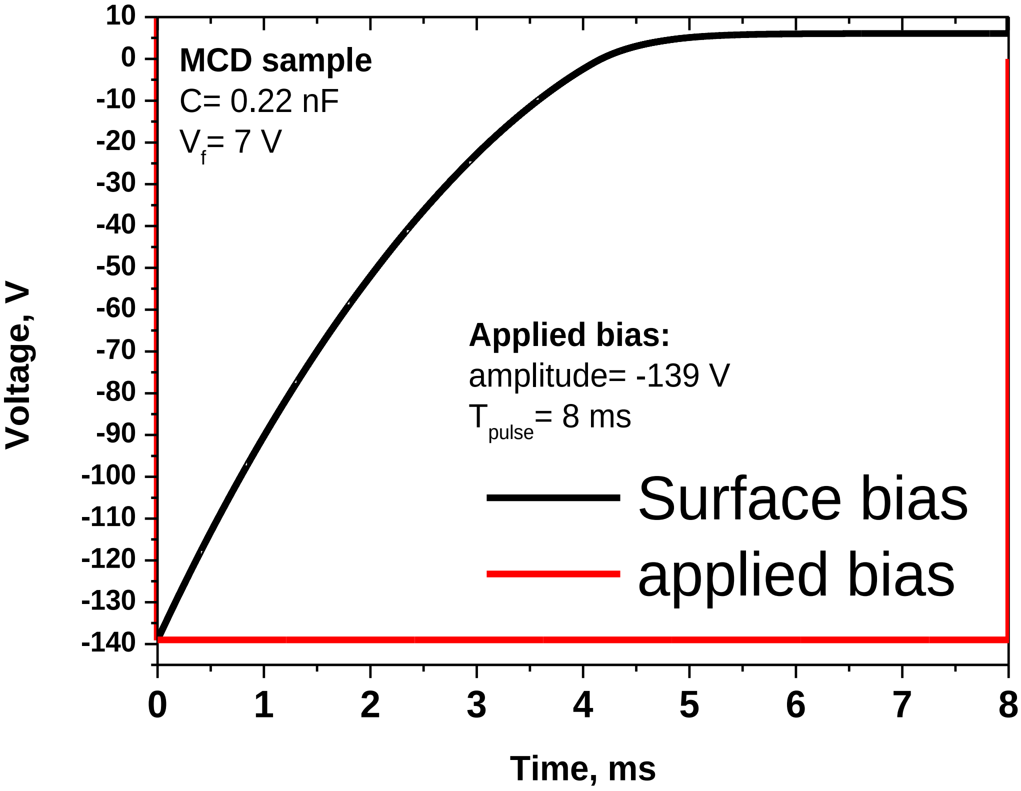

Figure 4.13. Calculated surface charging for MCD sample biased by a long DC bias pulse. C model parameters: V_f = 7 V, C= 2 x 10^{-10} (F), Va = -139 V, T_{pulse}= 8 ms.

As shown on **Figure 4.12**, the sample current can be considered as more or less constant between -140 V and -100 V (I_S = 10µA +/- 1µA). Under this situation the **Equation 4.2** can be solved analytically. The surface bias V_S (t) can be obtained by integrating its time variation, taking into account the initial condition V_S $(t= 0)$ of the surface bias before the pulse application:

$$Vs(t) = \frac{I_S}{C} \times t + Vs(t=0) \qquad \textbf{Equation 4 1}$$

At t = 0^-, just before the application of pulsed DC bias (V_a (0^-) = 0 V), the sample is immersed in plasma and the surface bias V_S (t) is assumed to be close to the floating potential V_f (V_s (0^-) ≅ V_f). The initial charge Q (0^-) can be deduced from the following equation:

$$V_s(0^-) - V_a(0^-) = \frac{Q(0^-)}{C}$$

$$V_f = \frac{Q(0^-)}{C}$$

At $t = 0^+$, just after the application of pulsed DC bias ($V_a(0^+) = V_a$), the sample is biased and immersed in plasma and the surface bias $V_s(t)$ is written as $V_s(t=0^+) = V_a + V_f$ and the initial charge $Q(0^+) = Q(0^-)$, so:

$$V_f = \frac{Q(0^+)}{C}$$

The **Equation 4.3** reads as:

$$Vs(t) = \frac{I_S}{C} \times t + V_f + V_a \qquad \textbf{Equation 4.4}$$

The voltage change is linear with time with a slope equal to $\frac{I_S}{C} = 41$ V/ms. It is the slope observed in **Figure 4.13** at t = 0. Therefore, in the ion saturation regime, the system can be simply seen as the charge of a capacitance under DC current.

b) Results of the model for a unique period

As described in the previous paragraph, an insulator sample immersed into plasma acts as a capacitor. Before the bias is applied, the insulator surface is at floating potential V_f. Right after the pulse is applied, the insulator surface voltage is negative: ($V_a + V_f$). If the applied bias V_a is sufficiently negative a large sheath is formed in front of the surface and the ion current to the sample saturates. The surface is loaded by positive charges.

Right after the pulse, the insulator surface is positively biased by the accumulated charge. If the accumulated charge is high enough, the surface bias is higher than V_p. So, a huge electron flux is attracted towards the sample during the first instants due to high electrons mobility. This causes a perturbation in the plasma, resulting in an increase of the plasma potential. This high plasma potential value limits the electrons loss towards the sample surface. The sample then unloads at potential close to the (disturbed) floating potential V_f. In the situation where the initial charge Q is low, and the surface bias is not higher than the plasma potential, there is no disturbance of the plasma.

In order to study sample unloading, we have modelled a 1 ms pulse followed by an unlimited period of time without any applied bias. All other conditions are identical to those of **Figure 4.13** and therefore the surface charging phase during the pulse can be observed on

Figure 4.14 during the first millisecond.

Let us call t_1 the end of the pulse:

At $t = t_1^-$:

$$V_s(t_1^-) - V_a(t_1^-) = \frac{Q(t_1^-)}{C} = 48.7(V)$$

At $t = t_1^+$:

$$V_s(t_1^+) - V_a(t_1^+) = \frac{Q(t_1^+)}{C} = 48.7(V)$$

This high positive potential on the surface disturbs plasma potential which increases probably above the surface voltage to limit the electron loss and maintain charge equality. Therefore, the surface voltage is reaching a value that is probably close to the disturbed floating potential. The surface unloads at a quite slow rate since electron current is low. This behavior is observed on

Figure 4.14. It can appear surprising that the model catches the perturbation of the plasma and the increase of the plasma potential since no explicit assumption has been made to do so. In fact, the model catches this behavior through the measurement of I(Vs) on the HOPG sample. When the HOPG sample is biased positively, the plasma potential is disturbed for the same reasons and in the same way as with insulating materials. This can be observed on **Figure 4.12** where the electron current to the HOPG sample is on the same order of magnitude as the ion current.

We have seen that an insulating material immersed in a plasma and submitted to a DC bias pulse accumulates charge during the pulse. If the charge accumulation is high, right after the pulse the plasma potential is increased, and the unload of the accumulated charge occurs at a quite slow rate. Let us now consider the situation where repetitive pulses are applied.

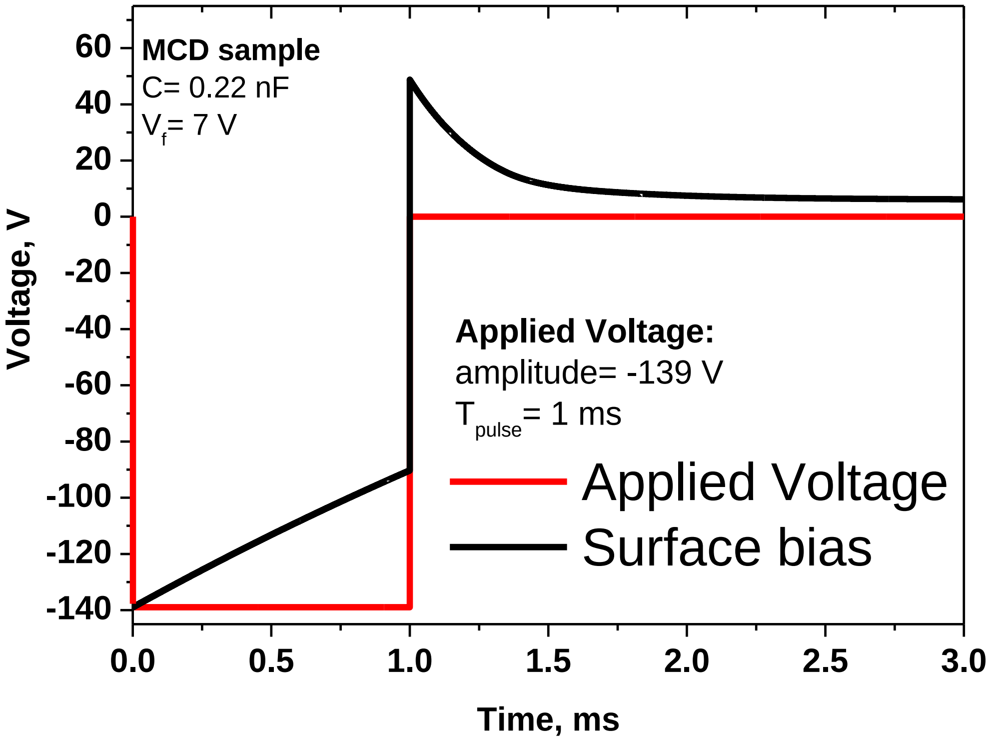

Figure 4.14 The surface voltage behavior modeled in the case of 1 ms pulse followed by an unlimited period of time without any applied bias. Surface charging (during 1 ms) and surface discharging (after 1 ms) is calculated for MCD sample biased by a long DC bias pulse. C model parameters: $V_f = 7$ V, C= 2 x 10^{-10} (F), Va = -139 V, T_{pulse}= 1 ms.

c) Results of the model for repetitive pulses

As we said before, the pulsed DC bias is employed to neutralize the positive ion charge up on insulator surface. It is seen that neutralization efficiency depends strongly on DC pulse parameters especially pulse duty cycle.

Figure 4.15 demonstrates surface charging as a function of time for a 1 kHz pulse, with a variable duty cycle. It is seen that at a duty cycle not exceeding 30% (pulsing frequency 1 kHz), the neutralization is effective and the surface voltage at the beginning of the pulse is close to the applied one. If duty cycle is higher, the diamond film does not have enough time to discharge between the pulses (see

Figure 4.15(c)) and the surface voltage noticeably differs from the applied one.

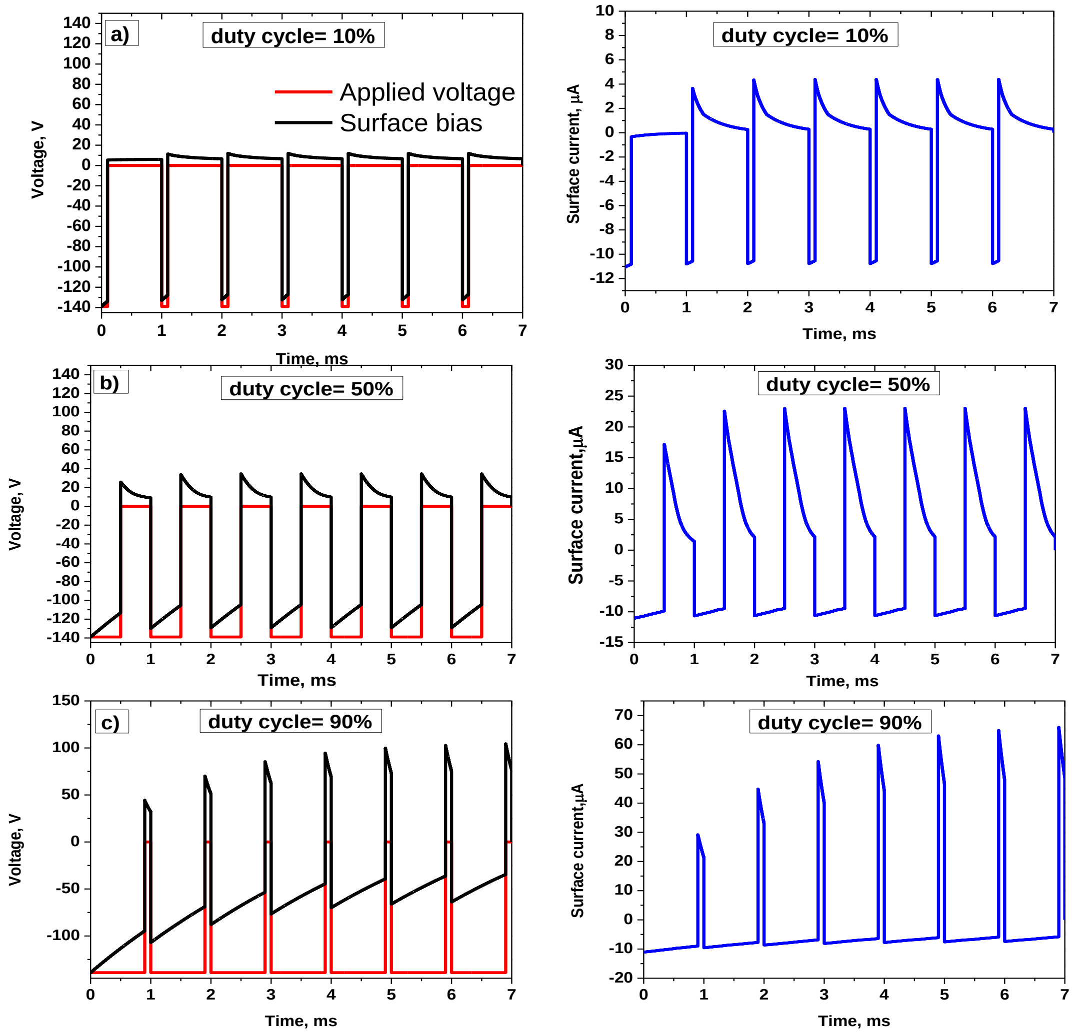

Figure 4.15 Surface bias (black lines) and corresponding surface current (blue lines on the right) calculation for MCD surface, V_f= 7 V, V_a= -139 V, f= 1 kHz, C=0.2 nF, with different duty cycle: a) 10% b) 50% c) 90%

As we can see in **Figure 4.14** and **Figure 4.15**, as soon as the bias is applied the surface starts accumulating ionic charge bias and the surface voltage increases. When the applied bias returns to ground the accumulated positive charge on the surface creates a positive bias higher than the floating. The positively charged surface is exposed to a net electronic flux neutralizing it. It is important to note again that the net electron flux towards the sample disturbs the charge equilibrium in the plasma leading to a plasma potential increase up to a value close to the surface voltage. As a consequence, the net flux of electrons towards the sample remains small and the discharging is slow. If the duty cycle is low, the surface is at the floating potential after one period **Figure 4.15** (a)). If the duty cycle is high, the diamond film does not have enough time to discharge between the pulses, a remaining positive charge persists when the cycle is complete (**Figure 4.15** (c)), and the sample surface does not reach the undisturbed floating potential. Right at the beginning of the next cycle, the surface voltage is lower than the applied bias because of the positive charge still there ($Vs = V_a + V_{endofpreviouscycle}$). So, duty cycle parameter must be optimized to get an effective surface neutralization.

B. Modeling for partially conductive samples

Let us consider now the situation of a partially conductive sample. This situation is analog to a capacitance with a resistance in parallel. A schematic diagram of RC equivalent circuit of the insulator biased and immersed in plasma is showed in **Figure 4.16**.

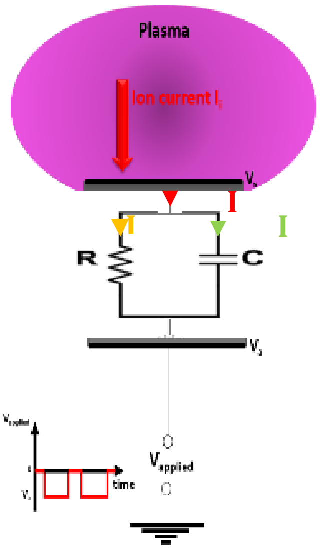

Figure 4.16 schematic diagram of RC equivalent circuit of the insulator biased and immersed in plasma

When the pulse is applied, the capacitor will gradually charge up. The manner in which the capacitor charges up is showed below:

$$V_s - V_a = \frac{Q}{C}$$

$$\frac{dV_s}{dt} = \frac{dQ}{dt} \times \frac{1}{C}$$

$$\frac{dV_s}{dt} = \frac{I_c}{C}$$

Where I_c is the current passing through the capacitor. The total current flowing into the circuit the current from the plasma I_{total} (V_s) and it is equal to $I_c + I_R$, where I_R is the current passing through the resistor R and it is expressed using Ohm law as follows:

$$I_R = \frac{V_s - V_a}{R}$$

One can deduce the charging current I_c as a function of V_s, V_a and I_i:

$$I_C = I_i - \frac{V_s - V_a}{R}$$

Replacing I_c by its expression, a simple first order differential equation is obtained:

$$\frac{dV_s}{dt} = \frac{I_c}{C}$$

$$\frac{dV_s}{dt} = \frac{I_i}{C} - \frac{V_S - V_a}{RC}$$

$$\frac{dV_s}{dt} + \frac{V_s}{RC} = \frac{RI_i + V_a}{RC}$$

Equation 4.5

a) Results of the model for a unique long pulse

Using I-V data measured on HOPG sample, surface bias is modeled for diamond sample (MCD) and plotted as a function of time (**Figure 4.17**) for a long unique pulse of -139 V of amplitude and having a duration of 8 ms. The surface is assumed to be initially at -139 V. The resistance value R is chosen to be 1 MΩ. As one can see in the **Figure 4.17**, the surface bias takes about 1 ms to reach a saturation level at -128.5 V. If one considers that the current I_{total} (V_s) is constant and equal to I_i, the equation can be solved analytically. Interpolated current values used in this RC modelling are showed in **Figure 4.12**. As one can see $I_{(Vs= -128.5V)} \cong 11$ µA.

The solution of this differential equation (**Equation 4.5**) can be written as $Vs(t) = V_{s1}(t) + V_{s2}$. Where $V_{s1}(t)$ is the solution of the differential equation without a second member and $V_{s2}(t)$ is the particular solution of the differential equation:

$$V_{s2} = RI_i + V_a$$

$$V_{s1}(t) = Ae^{-\frac{t}{\tau}}$$

$$V_s(t) = Ae^{-\frac{t}{\tau}} + RI_i + V_a$$

Where $\tau = R \times C$ . .

At t = 0^-, just before the application of pulsed DC bias (V_a (0^-) = 0 V), the sample is immersed in plasma and the surface bias V_s is assumed to be close to the floating potential V_f (V_s (0^-) ≅ V_f). The initial charge Q (0^-) can be deduced from the following equation:

$$V_s(0^-) - V_a(0^-) = \frac{Q(0^-)}{C}$$

$$V_f = \frac{Q(0^-)}{C}$$

At t = 0^+, just after the application of pulsed DC bias (V_a (0^+) = V_a), the sample is biased and immersed in plasma and the surface bias V_s is written as V_s (0^+) = V_a +V_f and the initial charge Q (0^+) = Q (0^-) is:

$$V_f = \frac{Q(0^+)}{C}$$

The constant A can be determined from initial condition at t= 0^+:

$$V_s(0^+) = Ae^0 + RI_i + V_a$$
$$V_a + V_f = A + RI_i + V_a$$
$$A = V_f - RI_i$$

So, the surface bias V_s *(t)* at any instant in time during the charging period of the first pulse is given as:

$$\boldsymbol{V_s(t) = V_f e^{-\frac{t}{\tau}} + RI_i(1 - e^{-\frac{t}{\tau}}) + V_a}$$

Equation 4.6

Contrary to C model, the surface bias doesn't reach the floating potential, this result is expected and can be deduced from $V_s(t)$ expression when $t \to \infty$ (still assuming that the ion current is saturating):

$$t \to \infty : e^{-\frac{t}{\tau}} \to 0$$

$$V_s(t \to \infty) = RI_i + V_a$$

$$V_s(t \to 8ms) = 1M\Omega \times 11\mu A - 139V = -128.5V$$

The previous model solution can be simply deduced from the present model by assuming $R \to \infty$:

$$R \to \infty : \tau \to \infty$$

$$\tau \to \infty : e^{-\frac{t}{\tau}} \to 1-\frac{t}{\tau}$$

$$V_{s(R\to\infty)} = V_f(1-\frac{t}{\tau}) + RI(1-(1-\frac{t}{\tau})) + V_a$$

$$V_f(1-\frac{t}{\tau})_{(\tau\to\infty)} \to V_f$$

$$V_{s(R\to\infty)} = V_f + RI \times \frac{t}{\tau} + V_a$$

$$V_{s(R\to\infty)} = V_f + I \times \frac{t}{C} + V_a$$

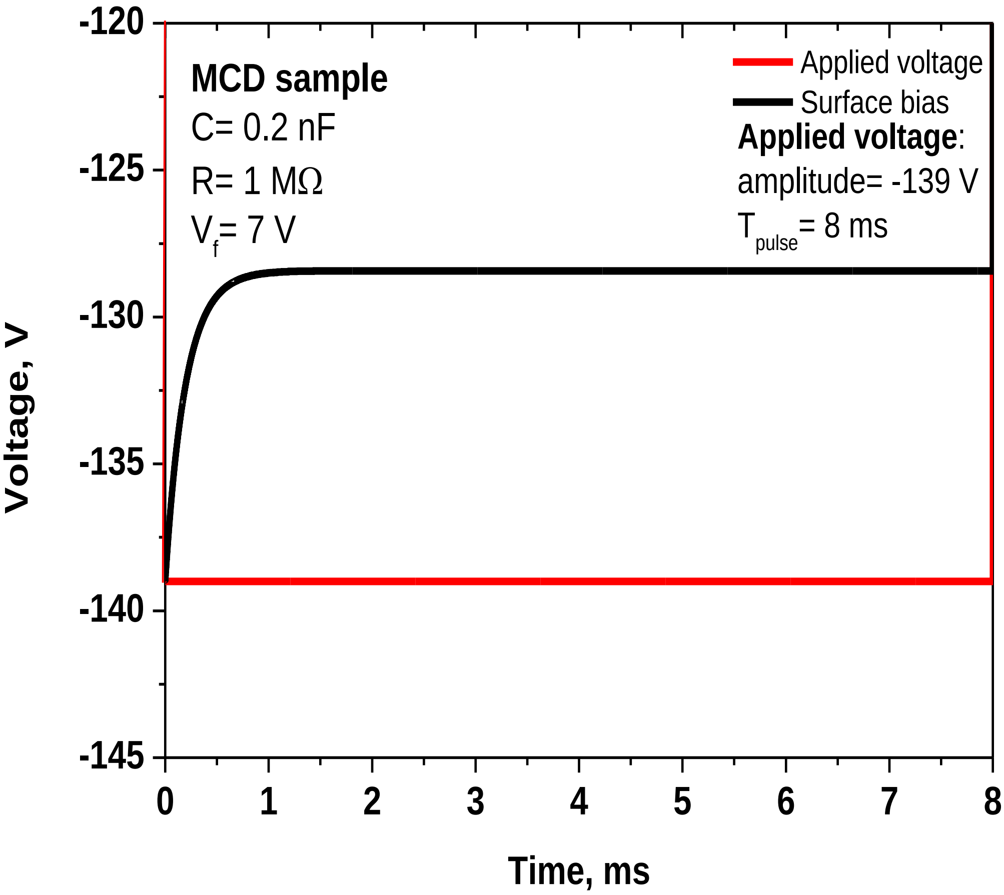

Figure 4.17 Calculated surface charging for MCD sample biased by a long DC bias pulse. RC model parameters: V_f= 7V, R= 1 MΩ, C= 2 x 10^{-10} (F), V_a = -139 V and T_{pulse}= 8ms

With this model the surface bias variation is linear with time as long as the ionic current can be considered as constant. With the RC model the surface bias is varying exponentially with time. However, a Taylor expansion of the exponential term at t=0 shows that the initial slope is identical to the one of the C models in the case $R \to \infty : \frac{dV_s}{dt}_{(t=0)} = \frac{I_i}{C}$

a) Results of the model for a unique long period

We have modelled a 1 ms pulse followed by an unlimited period of time without any applied bias. All other conditions are identical to those of **Figure 4.17** and therefore the surface charging phase during the pulse can be observed on **Figure 4.18** during the first millisecond.

Let us call t_1 the end of the pulse.
At $t=t_1^-$:

$$V_s(t_1^-)-V_a(t_1^-)=\frac{Q(t_1^-)}{C}=4(V)$$

At $t=t_1^+$:

$$V_s(t_1^+)-V_a(t_1^+)=\frac{Q(t_1^+)}{C}=4(V)$$

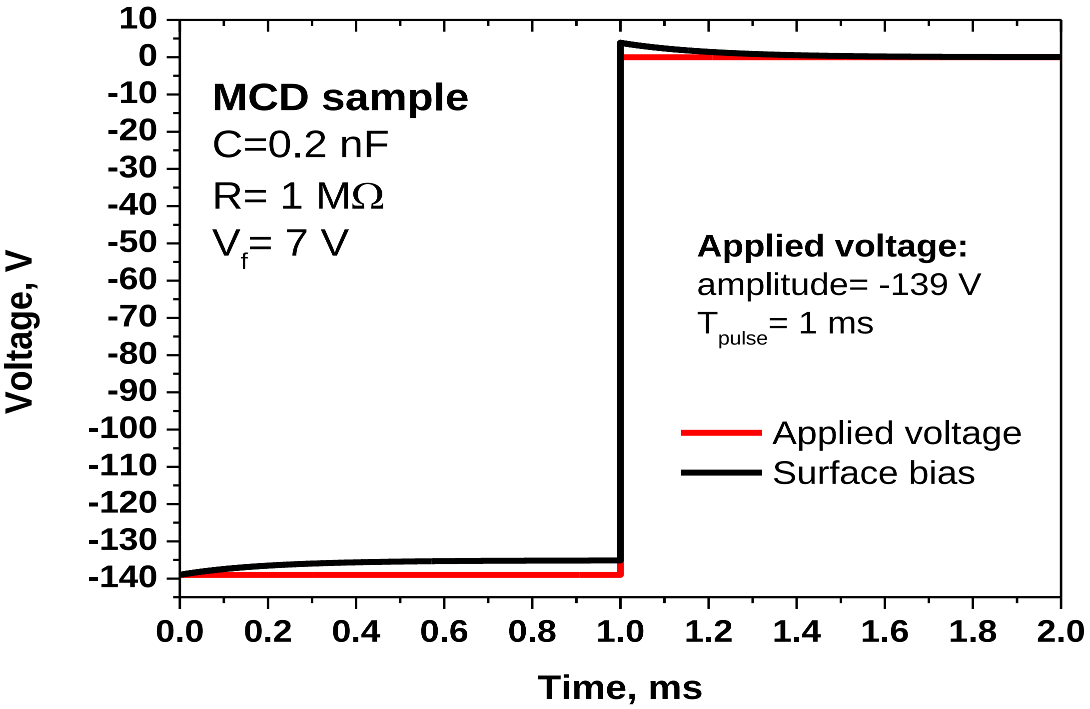

Figure 4.18 The surface voltage behavior modeled in the case of 1 ms pulse followed by an unlimited period of time without any applied bias. Surface charging (during 1 ms) and surface discharging (after 1 ms) is calculated for MCD sample biased by a long DC bias pulse. RC model parameters: V_f = 7 V, R= 1 MΩ, C= 2 x 10^{-10} (F), Va = -139 V, T_{pulse}= 1 ms.

The surface voltage after the pulse (4 V) is close to the undisturbed floating potential (7 V). No perturbation of the plasma occurs.

Of course, this result strongly depends on the value of the resistance R. With a higher resistance, the accumulated charge after 1ms is higher and we come back to a situation where the surface voltage is high and disturbs the plasma potential. The surface is then unloaded slowly by a flow of electrons (similar to the case of model C see

Figure 4.14). This is shown in **Figure 4.19** where the surface voltage behavior is modeled for R= 10 MΩ, all other conditions are identical to those of **Figure 4.18**. As one can see in **Figure 4.19** for t_1 (the end of the pulse):

At $t=t_1^-$:

$$V_s(t_1^-)-V_a(t_1^-)=\frac{Q(t_1^-)}{C}=34(V)$$

At $t=t_1^+$:

$$V_s(t_1^+)-V_a(t_1^+)=\frac{Q(t_1^+)}{C}=34(V)$$

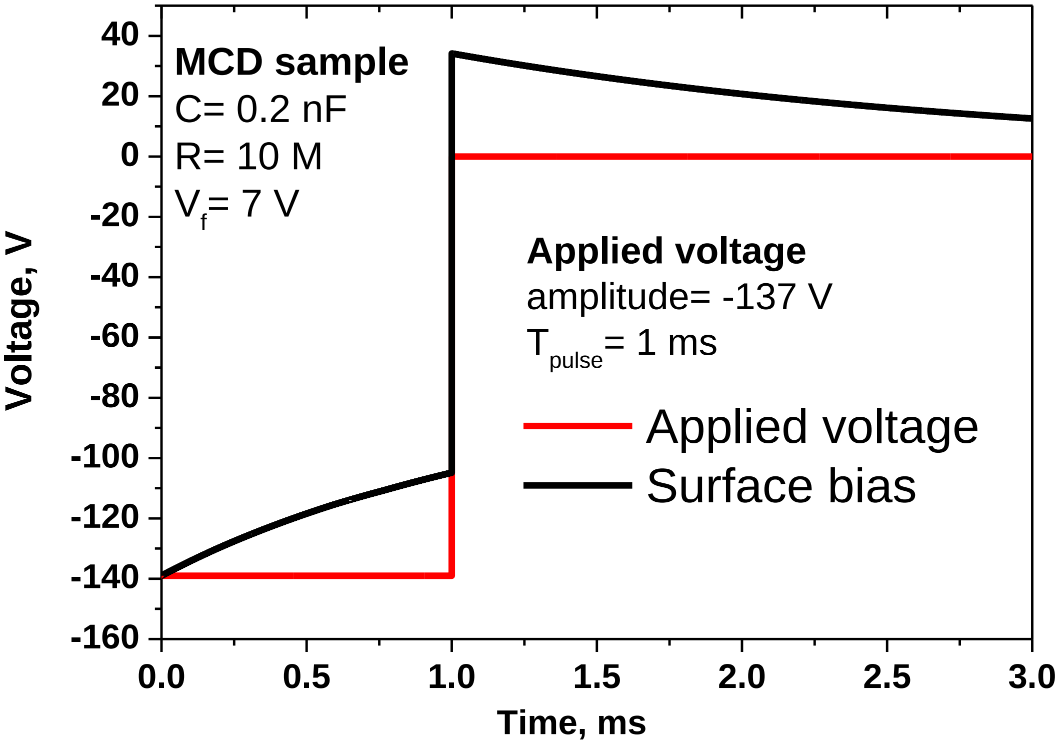

Figure 4.19 The surface voltage behavior modeled in the case of 1 ms pulse followed by an unlimited period of time without any applied bias. Surface charging (during 1 ms) and surface discharging (after 1 ms) is calculated for MCD sample biased by a long DC bias pulse. RC model parameters: V_f= 7 V, R= 10 MΩ, C= 2 x 10^{-10} (F), Va = -139 V, T_{pulse}= 1 ms.

b) Results of the model for repetitive pulses

As it was previously discussed for C model (

Figure 4.15), the neutralization efficiency depends strongly on pulse duty cycle. For RC model, duty cycle is also a key parameter for neutralization efficiency. **Figure 4.20** demonstrates surface charging as a function of time for a 1 kHz pulse, with a variable duty cycle for RC model in two different cases (case 1 for R=*10 MΩ* and case 2 for R =*1MΩ*). For R= 1 *MΩ* (case 2 presented in **Figure 4.20** in dash line), the surface voltage after the pulse is close to the undisturbed floating potential (7 V). No perturbation of the plasma occurs for different duty cycle and the neutralization efficiency is high. For R= 10 *MΩ* (case 1 presented in **Figure 4.20** in solid line), we return to the case of C model.

If the duty cycle is low, the surface is at the floating potential after one period (**Figure 4.20** (a)). If the duty cycle is high, the diamond film does not have enough time to discharge between the pulses, a remaining positive charge persists when the cycle is complete (**Figure 4.20** (c)), and the sample surface does not reach the undisturbed floating potential. Therefore, neutralization efficiency doesn't depend only from pulse parameters (duty cycle) but it depends from sample parameters such as its thickness and its conductivity.

In the next part, measurement of surface bias and current will be done using insulator sample surface biased by a pulsed DC bias and immersed in low pressure H_2 or D_2 plasma. Those measurement will be compared with surface bias and surface current calculations in the case of C and RC models.

4.4.2 Experiments

1) First observations and choice of the model to describe the experiment

The sample current measurement gives a direct information about plasma response during pulsed DC bias experiment. Indeed, the plasma plays the role of current source that delivers current towards sample surface.

The surface current measurement presented on **Figure 4.21** are done on MCD surface having a thickness of 12.5 µm at room temperature with a very long pulse (T_{pulse}= 11 ms) a low frequency (9 Hz) and an applied bias V_a of -140 V. Those pulse parameters are chosen in such a way to see the full charge and discharge of the surface and determine the time that takes each phase respectively. **Figure 4.21** shows the measured surface current on MCD surface measured in the case of H_2 plasma (2 Pa) ignited at an RF power of 26 W. The charge phase is defined as the period of time during which the bias pulse is applied. Its duration is T_{pulse}. During this phase the ion current is attracted towards the surface. The discharge phase is defined as the period where no bias is applied (V_a = 0). Its duration is (T-T_{pulse}). During this phase the electron current is attracted towards the surface.

Figure 4.21 shows that the sample current decreases during 11 ms with exponential like shape and saturates at the end of the long pulse. Contrary to C model consideration, the measured surface current does not reach 0 µA. This indicates that the surface is not a perfect capacitor and its low conductivity cannot be neglected. **Figure 4.22** (a) and **Figure 4.22** (b) show the calculated sample current in charge phase on MCD sample biased by long pulse in the case of C model and RC models (**Figure 4.21**). The relevant parameters in our calculation are the sample capacitance value and the resistance of MCD surface. The capacitance of MCD sample is calculated from its thickness and it is equal to 0.2 nF. The resistance R value was choosen equal to 1 MΩ. Obviously the C model is not relevant here. As one can see, the saturation current calculated using RC model is twice the measured one and it is reached after 2 ms. The trends of the model are good but apparently the C and R parameters chosen must be corrected to match the experiment.

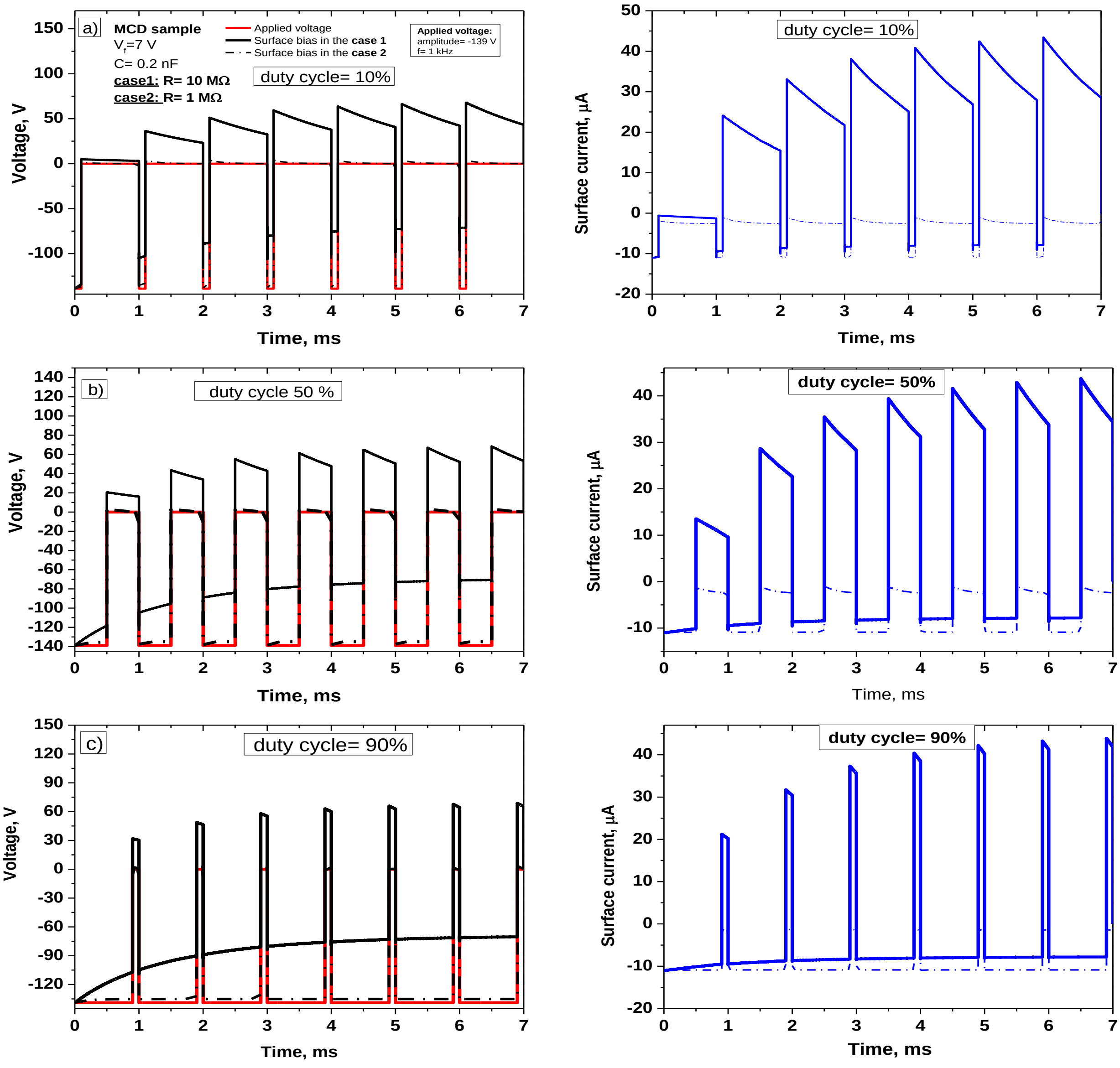

Figure 4.20 Surface bias (black lines) and corresponding surface current (blue lines on the right) calculation for MCD surface, V_f= 7 V, V_a= -139 V, f= 1 kHz, C=0.2 nF with different duty cycle in **case1 R= 10 MΩ (solid line)** and case2 R= 1 M Ω (dash line): a) 10% b) 50% c) 90%

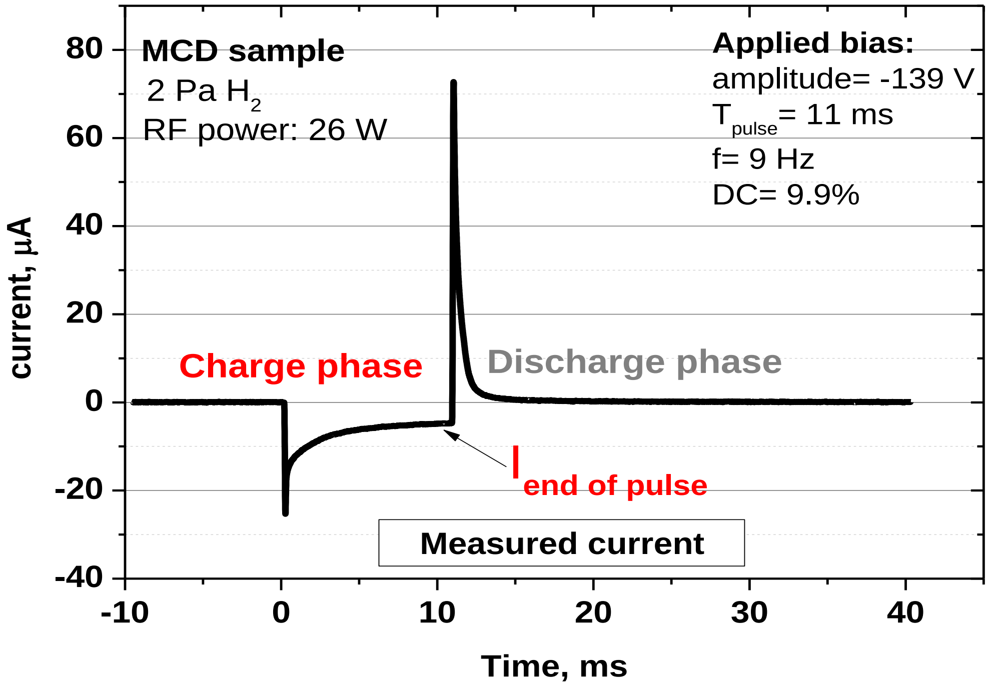

Figure 4.21 Measured surface current on MCD sample biased by a long pulse. In the case of $V_f = 7$ V, Va = -139 V, T_{pulse}= 11 ms, f= 9 Hz

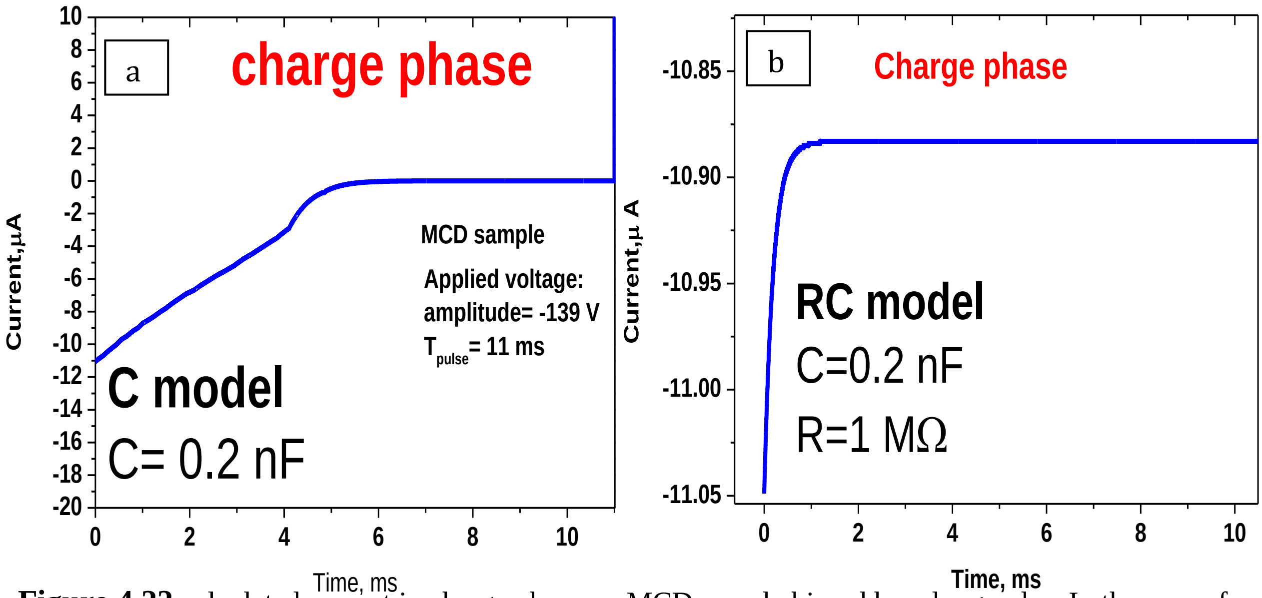

Figure 4.22 calculated current in charge phase on MCD sample biased by a long pulse. In the case of $V_f = 7$ V, Va = -139 V, T_{pulse}= 11 ms, f= 9 Hz (a) for C model C= 0.2 nF (b) for RC model C= 0.2 nF and R= 1 M *Ω*

For the discharge phase, a quick surface discharge in exponential manner is observed and the surface reach 0 µA after 4 ms.

So, the surface current variation with time measured on insulator sample surface prove our hypothesis about plasma response to sample surface biased in pulsed DC mode. It shows that the RC description (partially conductive sample) is better suited than the C model (insulating sample) for the description of pulse bias experiments with MCD sample.

2) Observation of plasma disturbance after the pulse

The plasma potential V_p perturbation can be detected using positive ion energy distribution function PIEDF. The PIEDF peak position is related directly to plasma potential V_p (**$eV_p = e V_{energy}$**). Therefore, any perturbation in plasma potential V_p implies a shift in PIEDF peak position

Different PIEDF measurements were done on MCD sample at room temperature in H_2 plasma under the following experimental conditions: a gas pressure of 2 Pa and a RF power of 26 W. The effect of introducing the sample holder in the plasma without any bias is shown in **Figure 4.23** (a). First, PIEDF is measured when the sample holder is outside plasma chamber, a peak position value of 21 V is observed. The sample holder is immersed into plasma, the PIEDF is measured (solid line). As it can be seen, a peak shift of 6 V is observed. The sample holder is then biased in DC mode (V_{DC} = -130 V is showed in **Figure 4.23** (b)). We can see that PIEDF peak intensity is low and it is positioned at 2.5 V. This plasma response to constant DC bias can be explained. The applied (V_{DC} = -130 V) is largely more negative than the plasma potential V_p. A large sheath is formed in front of the surface. The electric field that reigns in the sheath accelerates positive ions towards the surface and trap energetic electrons in the plasma. Therefore, for this low density H_2 plasma, the plasma potential decreases dramatically and it appears at around 3 V. This effect is reinforced by the fact that the plasma dimension is rather small between the sample holder and the mass spectrometer while the sheath is large in such low density plasma. In **Figure 4.24** (a), the PIEDF measured in the case of a biased MCD sample by a long pulse (T_{pulse}= 1 ms) and a high duty cycle (80%) is presented. The applied bias V_a is equal to -139 V. As one can see in that case, the PIEDF spectra demonstrates three different peak values. The first PIEDF peak is located at 3 V, the second one is located at 15 V and the third one is located at 35 V. The dominant peak corresponds to the plasma potential observed in the case of unbiased MCD sample. The second peak is characterized by a plasma potential value equal to what we observe in the case of an MCD sample biased by a constant DC bias (2.5 V). The third one is characterized by a plasma potential value equal to 35 V. It is important to note that those measurement were done in accumulation mode, PIEDF measurement was accumulated during 1 h of plasma exposure. Right after the bias is pulsed from low (applied bias V_a) to high (ground 0 V), the insulator surface is positively biased by the accumulated charge. In the case of this long pulse and high duty cycle, the accumulated charge is high, and the surface voltage becomes higher than 15 V. So, a huge electron flux is attracted towards the sample during the first instants due to high electron mobility. This causes a perturbation in the plasma, resulting in a local increase of the plasma potential to 35 V. This high plasma potential value limits the electrons loss towards the sample surface. So, the presence of the plasma potential peak at 35 V for a long pulse and a high duty cycle confirms our expectations on the plasma potential perturbations.

Contrary to the case of long pulse with high duty cycle, a short pulse (T_{pulse}= 10 µs) with low duty cycle (1%) does not perturb plasma (see **Figure 4.24** (b)). The accumulated charge during 10 µs is so low and the duty cycle is low enough to discharge completely the MCD surface before the beginning of the next pulse cycle. The absence of charge accumulation effect gives a PIEDF peak at 15 V. This study demonstrates the complex surface charge dynamics during the (T-T_{pulse}) duration, and possible plasma potential disturbances due to the accumulated charge on the surface.

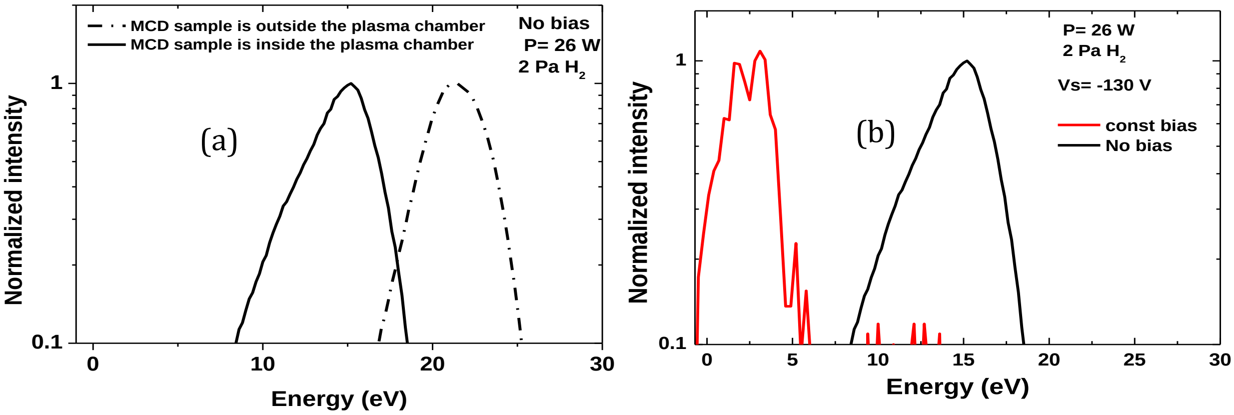

Figure 4.23 (a) Normalized PIEDF (H_2^+) measured before and after the immersion of sample holder at ground in plasma chamber (b) Normalized PIEDF (H_2^+) measured before and after the biasing of sample holder in DC model

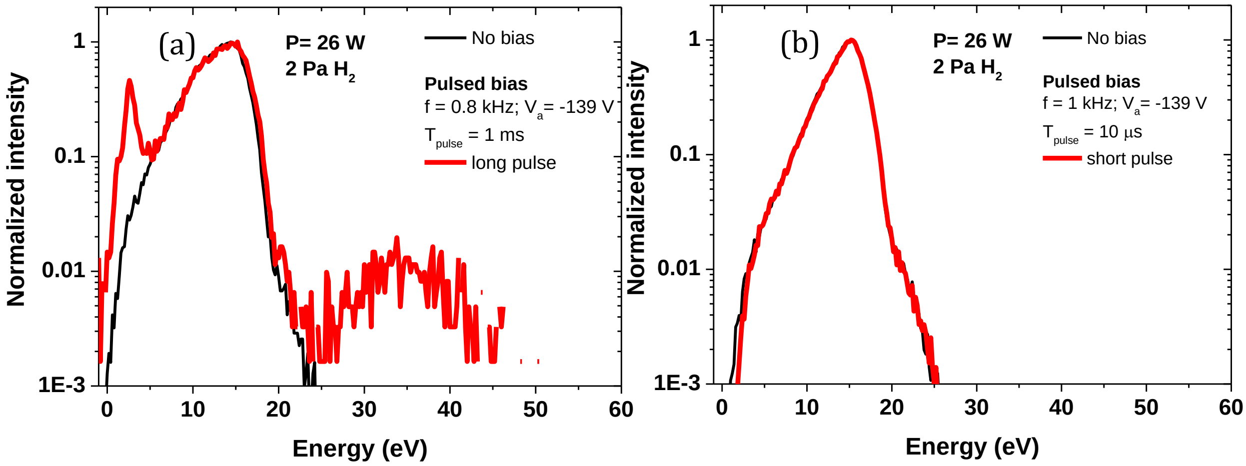

Figure 4.24 (a) Normalized PIEDF (H_2^+) measured in the case of MCD sample biased by a long DC pulse compared to normalized PIEDF (H_2^+) measured in the case of unbiased MCD sample (b) Normalized PIEDF (H_2^+) measured in the case of MCD sample biased by a short DC pulse compared to normalized PIEDF (H_2^+) measured in the case of unbiased MCD sample

3) Exploration of the pulse DC bias method

3.A Surface charging on MCD sample during long pulse

To get insights onto surface charge accumulation, model and experiments are compared in the case of a long DC pulse. This measurement is done on MCD surface at room temperature using a long pulse (5 ms) with a low pulse frequency (100 Hz, duty cycle 50 %). A molybdenum clamp was used in this experiment. The MCD thickness was 12.5 µm. The acquisition time has been set to 50 µs (T_{acq} = 50 µs) and the delay was 21 µs (T_{delay} = 21 µs correspond to D^- fly time). **Figure 4.25** (a) shows that NIEDF measurement can be recovered using the pulse DC bias method. The onset of the NIEDF is at 0 on the energy scale indicating that for this measurement the surface bias is indeed equal to –19 V.

To study the charge accumulation on the surface during the pulse NIEDF acquisitions have been performed at different delay times (T_{delay} from 21 µs to 4 ms) and are represented in **Figure 4.25**. All NIEDF acquisitions have been processed assuming a surface bias of -20 V. As can be seen NIEDF peak positions as well as NIEDF onsets are shifting towards negative values indicating that the surface bias is increasing and is no more equal to -20 V. This shift is equal to the difference between the actual surface bias and the bias initially present on the surface (V_s *~ –20 V*). The NIEDF onset has therefore been used to get the actual surface bias V_s present on the surface at different times in the pulse (different T_{delay}). In such a way, the charging of the sample was followed in real time as demonstrated in **Figure 4.25** (b). The surface initially is at ~ -19 V and it varies with time. It takes about 2 ms to fully charge and obtain a saturated potential of -13.2 V. The measured surface bias on MCD sample during a long pulse does not reach the floating potential (V_f= 7 V in our experimental conditions) showing again that the RC model is more appropriate than the simple C model. The comparison of measured surface bias on MCD sample with calculated one in the case of RC model and C model respectively is essential and it will be the subject of our discussion in the next part.

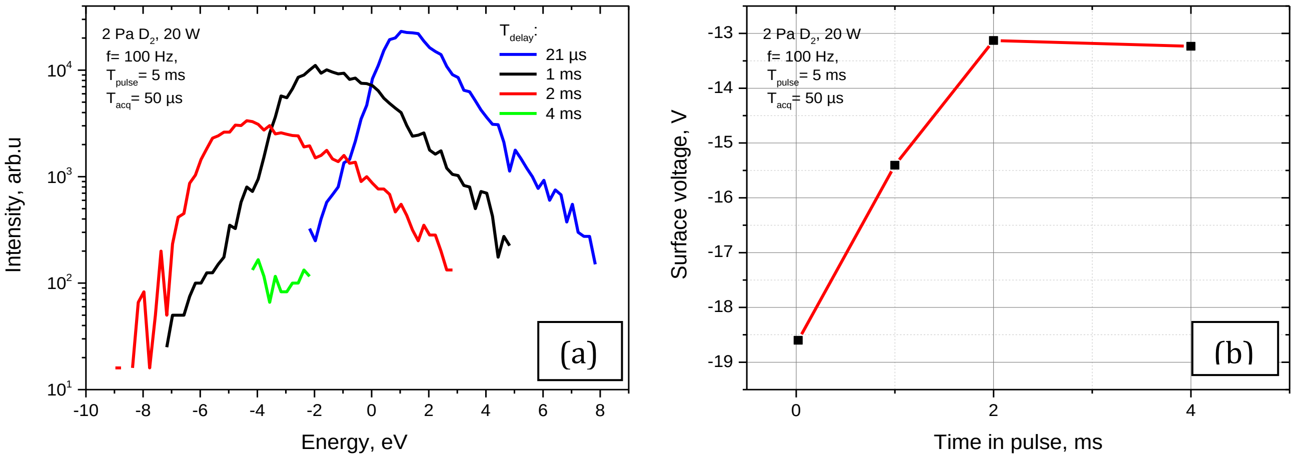

Figure 4.25(a) NIEDF measured at different moment (defined by T_{delay}) of the bias pulse in the case of a long pulse of 5 ms (b) surface voltage V_s of MCD material at different moment of the 5 ms bias pulse.

The relevant parameters in surface bias calculations are MCD sample resistance R and MCD sample capacitance C. Those sample parameters can be deduced from experiment or calculated from known surface parameters (thickness, permittivity). The sample resistance can be defined experimentally in two way: it can be measured directly by an ohmmeter put in contact with the sample surface layer. This is approximate since this measurement only gives the resistance of the unmodified diamond layer (the measured value is 50 MΩ). A second estimation of the sample resistance R_{exp1} can be deduced from surface voltage saturation level at t= 4 ms. The resistance experimental value R_{exp1} (1.25 MΩ) is deduced from our experiment using **Equation 4.6**:

$$R_{exp1} = \frac{V_s(t = 4ms) - V_a}{I_i}$$

Where I_i is the current value corresponding to V_s= -13 V and it is equal to ~ 4.3 µA. This current value is deduced from **Figure 4.12** and it is an approximated value because in this experiment we use a molybdenum clamp and *$I(V_s)$* measurement on HOPG sample was done in the case of ceramic clamp. The experimental sample capacitance C_{exp} can be deduced from R_{exp1} value by using the slope of experimental Vs (t) curve at t= 0 (The slope is equal to 2.9 V/ms) respecting RC model **Equation 4.5**:

$$\frac{\Delta V_s}{\Delta t}(t = 0) = \frac{I_i}{C_{exp}} - \frac{V_f}{R_{exp1} C_{exp}}$$

Where I_i is the current value corresponding to V_s= -19 V and it is equal to ~ 4.5 µA (see **Figure 4.12**) and V_f= 5 V the slope $\frac{\Delta V_s}{\Delta t}(t = 0) = \frac{-19V + 13V}{2ms}$. Using R_{exp1}= 1.25 MΩ, the deduced C_{exp}= 0.1 nF.

For sample capacitance, the theoretical sample capacitance C_{theo} can be calculated using the value of sample thickness (12.5 µm) and it is equal to 0.2 nF (planar capacitor consideration).

The surface bias on MCD sample is calculated using RC model consideration. Comparison between experiment and calculation are done at steady state (after a series of several pulses). The applied pulsed DC bias parameters are identical to the experimental one.

Figure 4.26 (a) shows calculated surface bias (black line) for MCD using C_{exp} (0.1 nF) and R_{exp1} (1.25 MΩ) parameters. The surface bias in steady state just after the first pulse. The calculated surface bias Vs is compared to the experimental one as shown **Figure 4.26**(c). Calculated V_s varies exponentially with time and it takes about 1 ms to fully charge and obtain a saturated potential of -13.7 V. The calculation result compared to the experiment is satisfactory.

Figure 4.26(b) shows calculated surface bias (black line) for MCD using C_{theo} (0.2 nF) and R_{exp} (1.25 MΩ) parameters. The use of Ctheo doesn't change largely the calculation result (see **Figure 4.26** (d)).

As we have shown before, trends of the model RC are good, but C and R parameters must be chosen correctly to match the experiment.

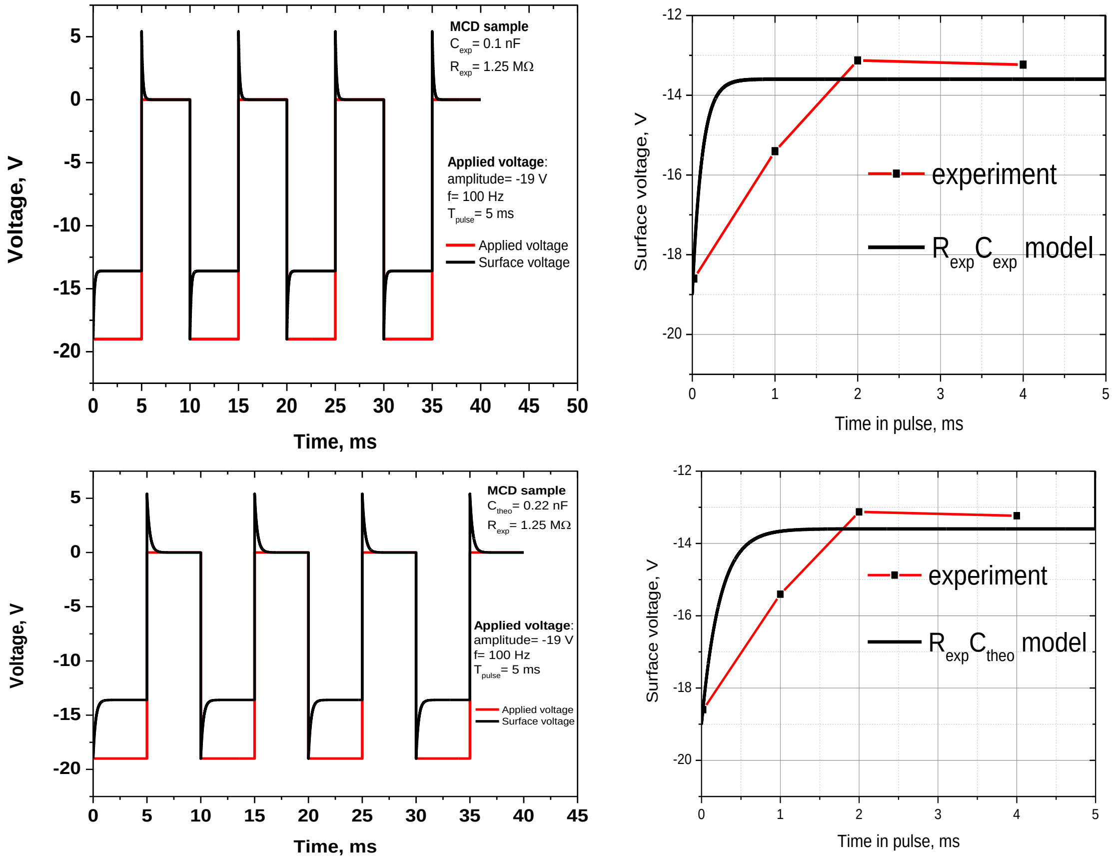

Figure 4.26 (a) calculated surface bias (black lines) and corresponding surface current for MCD surface, V_f= 7 V, V_a= -139 V, f= 1 kHz, R_{exp}= 1.25 M Ω nF with (a) C_{exp}= 0.1 nF (b) Ctheo= 0.2 nF. Comparison of experimental surface charging (red line black square symbol) with model result (black line) (c) $R_{exp}C_{exp}$ model (d) $R_{exp}C_{the}$o model

3.B. Surface charging on MCD samples having different thickness

The pulsed DC bias method has been also applied in the case of a short100 µs DC pulse (T_{pulse} = 100 µs) with a repetition frequency of 1 kHz (duty cycle = 10 %). The acquisition time has been set to 10 µs (T_{acq} = 10 µs) and the delay was 13 µs (T_{delay} = 13 µs). Such a situation, short pulse and low duty cycle is ideal to study NI surface production on insulating materials since the long period without pulse allows for unloading accumulated charges on the surface. As only the first instants (100 µs) of surface charging are considered in such experiment, it is interesting to see whether the simple C model can be applied. Indeed, it has been shown previously that the C model and the RC model both demonstrate surface voltage linear variation with time as long as the ion current can be considered as saturated. To ensure this condition the applied bias was high for this experiment (Va = -140 V).

As can be seen in **Figure 4.27**(a) the onset of the NIEDF is at 0 on the energy scale indicating that for this measurement the surface bias is indeed equal to –130 V. Let us note that a bias V_a equal to -140 V has been applied to get a surface bias of about -130 V.

NIEDF acquisitions have been performed at different delay times (T_{delay} from 13 to 103 µs) and are represented in **Figure 4.27**(a) All NIEDF acquisitions have been processed assuming a surface bias of -130 V. As can be seen NIEDF peak positions as well as NIEDF onsets are shifting towards negative values indicating that the surface bias is increasing and is no more equal to -130 V. In such a way, the charging of the sample was followed in real time as demonstrated in **Figure 4.27**(b) One can observe that charging of MCD is happening as expected in a linear manner with a rate of ~1V/10 µs. **Figure 4.27**(b) shows the linear variation of the surface bias with time using a ceramic clamp and a sample of 17.5 µm thickness (sample 1), and the same result obtained with a molybdenum clamp and a sample of thickness 12.5 µm (sample 2). In the case of the metallic clamp, the voltage on the holder surrounding the sample remains at -140 V during the measurement while the voltage on the sample varies from -130 V to -120 V. An opposite situation is obtained with the ceramic clamp, the voltage on the holder surrounding the sample is always at floating potential (few volts above 0) during the measurements. However, no noticeable effect of the holder material was observed for such a short pulse. Furthermore, the slopes obtained are in the ratio of sample thicknesses which reinforces the simple picture of the C model:

$$\frac{17.5\mu m}{12.5\mu m}=\frac{0.14V/\mu s}{0.1V/\mu s}=1.4$$

The charging of the sample during the pulse decreases the value of bias voltage V_s on the surface. Therefore, T_{acq} must be sufficiently short to get undistorted NIEDF shape which can be compared to NIEDF obtained with conductive samples biased at a well-defined voltage. The acquisition time of T_{acq} = 10 µs seems reasonable to provide a quasi-constant surface bias V_s during measurement (V_s increases by only 1 V over 130 V during the measurement).

The experimental sample charging is compared to the calculated one. As the experimental surface charging happens in a linear manner, it is compared only with calculated surface charging using C model. The relevant parameter in our calculations is sample capacitance C. This parameter can be calculated from known sample thickness and permittivity C_{theo}, or it can be determined from the best fit of the experiment by the model. For sample 1, Cexp and Ctheo values are ~0.08 nF and ~ 0.14 nF respectively. For sample 2, Cexp and Ctheo values are ~ 0.11 nF and ~0.2 nF respectively. Calculations are compared to our measurements in **Figure 4.27**(c) and **Figure 4.27**(d). The difference between the theoretical and experimental values probably comes from the fact that the sample does not act as a perfect infinite planar capacitance.

To conclude, for short pulses with low duty cycle, the simple C model is accurate enough to describe the accumulation of charges during the pulse. This will be confirmed in the next paragraph.

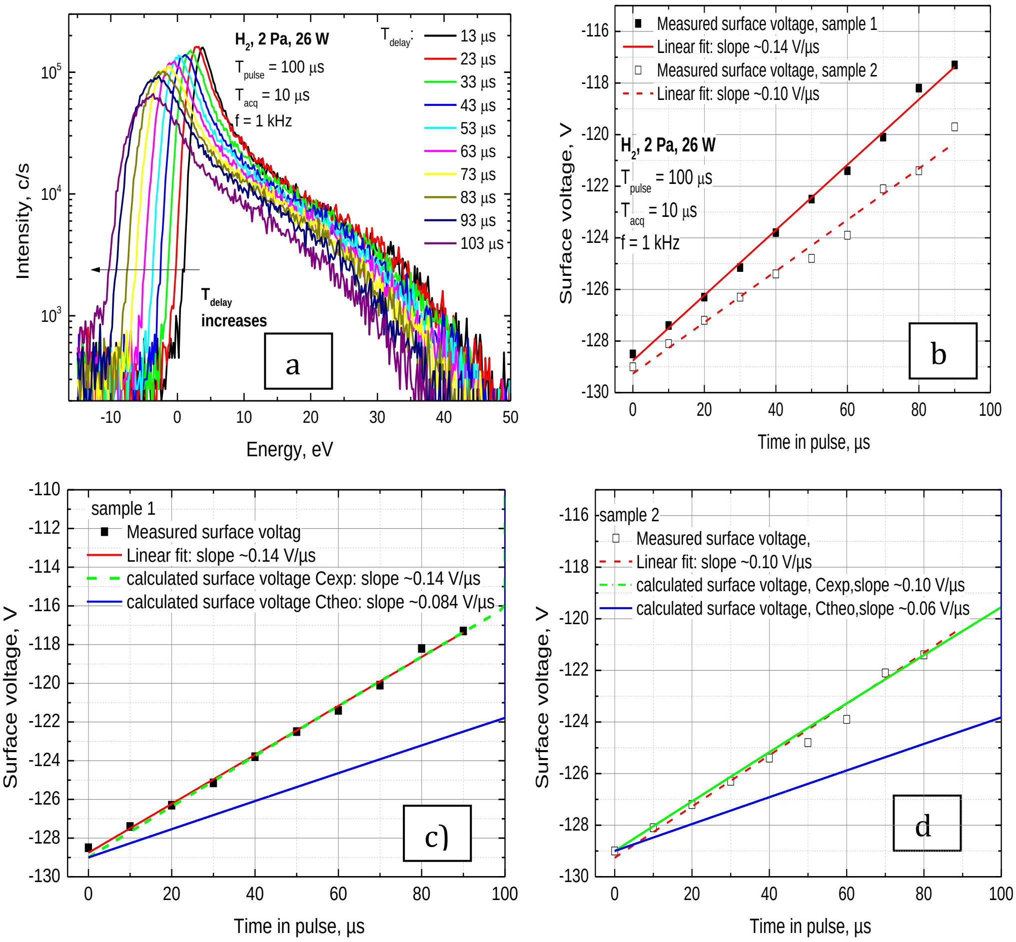

Figure 4.27 (a) NIEDF acquisition at different moment of the 100 µs bias pulse for sample1 (thicknesses is 17.5 µm) (b) surface voltage V_s of MCD material at different moment of the 100 µs bias pulse for two different sample thicknesses (sample 1 is 17.5 µm while sample 2 is 12.5 µm). (c) comparison of measured surface charging of sample 1 with calculated surface charging using C_{theo} model (blue line) and C_{exp} model (dash green line) respectively (d) comparison of measured surface charging of sample 2 with calculated surface charging using C_{theo} model (blue line) and C_{exp} model (green line) respectively

C. Surface charging on different insulator material: MCD sample and SiO_2 sample

After the discussion of sample thickness effect on surface charging we come now to the effect of the permittivity by using two different insulators. The pulsed DC bias method has been applied in the case of high V_a using a 100 µs DC pulse (T_{pulse} = 100 µs) with a repetition frequency of 1 kHz (duty cycle = 10 %). The acquisition time has been set to 10 µs (T_{acq} = 10 µs) and NIEDF acquisitions have been performed at different delay times (T_{delay} from 13 to 103 µs). A bias V_a equal to -140 V has been applied to get a surface bias of about -130 V.

Erreur ! Source du renvoi introuvable. shows the linear variation of the surface bias with time using a ceramic clamp and a MCD sample of 12.5 µm thickness with a relative permittivity of 5.7 immersed in plasma ignited at 26 W, and the same result obtained with a SiO_2 sample of 1 µm thickness and a relative permittivity of 3.9. One can observe that charging is happening as expected in a linear manner with a rate of ~1V/10 µs for MCD sample and a rate of 10 V/10 µs for SiO_2 sample.

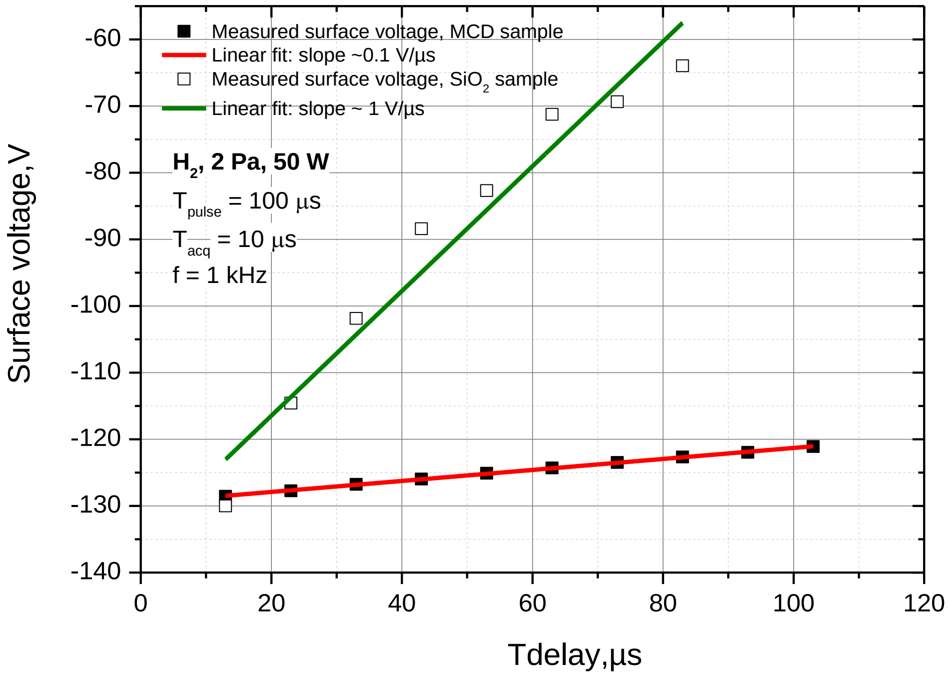

Figure 4.28 surface voltage V_s at different moment of the 100 µs bias pulse for two different insulators samples MCD and SiO_2

The slopes obtained in the case of MCD sample and SiO_2 sample are in the ratio of samples capacitance (thickness and relative permittivity):

$$\frac{rate_{MCD}}{rate_{SiO_2}} = \frac{\varepsilon_{MCD}}{\varepsilon_{SiO2}} \times \frac{d_{SiO2}}{d_{MCD}}$$

In the case of SiO2 sample, it is obvious that the C model has to be used since the resistivity of this material is very high (~ 10^{17} Ω.cm). It is interesting to note that for short pulse and low duty cycle the MCD sample which is partially conductive behaves identically to the SiO2 material.

3.D. Surface charging on MCD sample for different pulse duty cycle

While the frequency of the pulse determined the total time of the duty cycle, the duty establishes the ratio between the time within the cycle where the bias V_a is applied (this time is called T_{pulse}) and the time where there I sno applied bias Va = 0 V (this time is called T_{off}). The duty cycle will be varied in two different manners:

1) Scan of pulse duration T_{pulse} at a constant pulse frequency f
2) Scan of pulse frequency f at a constant pulse duration T_{pulse}

3.D.1) Influence of pulse duration T_{pulse} at constant pulse frequency f

It was discussed previously in modeling that the charge accumulation on the surface depends on the choice of pulse duty cycle (see **Figure 4.15** and **Figure 4.20**). In **Figure 4.29**(a), NIEDF are measured **at the beginning of the pulse** for MCD sample (thickness 12.5 µm) using a constant pulse frequency (1 kHz) and different pulse duration T_{pulse}, thus varying the duty cycle. T_{pulse} plays an important role in shaping NIEDF spectra. For longer T_{pulse}, NIEDF spectra is shifted from its initial position measured at T_{pulse} = 10 µs. Surface bias is deduced from the NIEDF onset shift and is be plotted as a function of T_{pulse} and duty cycle in **Figure 4.29**(b) and **Figure 4.29** (d). As one can notice, the surface voltage at the beginning of the pulse is almost constant with a T_{pulse} up to 200 µs (duty cycle of 20%). After that the surface voltage varies fast with T_{pulse}. A voltage variation of 54 V is measured between T_{pulse} = 100 µs and T_{pulse} = 900 µs. This behavior of surface bias V_s with pulse duration T_{pulse} is a consequence of surface charging effect. As explained before if the OFF period is too short charges accumulate on the surface due to incomplete unloading during the OFF period. It leads at steady state to an important voltage drop (Q/C) through the insulating diamond layer and a surface voltage much lower than the applied voltage.

Surface voltage variation with time during the pulse has been measured in the case of MCD sample (thickness 12.5 µm) using a pulsed DC bias with high V_a and repetition frequency of 1 kHz for different duty cycle (10 %, 30% and 50%). The surface variation for different pulse duty cycle has also been calculated using C model and RC model (R= 1.25 MΩ and C= 0.1 nF: parameters values deduced from experiment). The calculated surface variations and current are compared to measure ones (see

Figure 4.31). Comparaison are done in steady state of surface voltage. In the case of C model, whatever the pulse duration (duty cycle from 10 to 50%), the model and the experiment demonstrate a surface voltage variation linear with time with a rate of ~1V/10 µs. In the case of RC model an exponential variation with time is observed with a slope value at t= 0 of ~1V/10 µs (

Figure 4.31(a) & (c) & (e)). We can see that in the case of a duty cycle of 10%, the positive charge accumulated during 100 µs leads to a voltage drop of 10 V when the pulse is switched off. This value is close to floating potential (7 V) and charges can be eliminated before the start of the next pulse. For a duty cycle of 50%, the accumulated charge leads to a voltage drop of 50 V when the pulse is switched to ground. The surface has a large positive bias ($V_{accumulated\ positive\ charge} > V_f$). Electrons are attracted resulting in a high loss and a consecutive increase of the plasma potential. This results in a quick initial unload of the surface first ($V_{accumulated\ positive\ charge} > >V_f$) and then the unloading happens in a slow regime when the surface voltage gets close to the disturbed floating potential ($V_{accumulated\ positive\ charge}$ is close to V_f). If the time before the start of the next pulse is not enough, the accumulated charge is not eliminated completely and a remaining one exists. This reasoning is supported by surface current measurement at different duty cycle (see **Figure 4.31)**. In

Figure 4.31(b) & (d) & (f) the measured surface current at different duty cycle (10% to 50%) is presented and it is compared to calculate ones using C and RC models. A general good agreement is obtained. This is really interesting in particular for the off period where no comparison is possible between calculated and measured surface voltages. This shows that the

C model works well also for unloading phase in the off period. Let us note that the model does not catch the fast variations of current at the beginning of the pulse and at the beginning of the off period. These variations are due to the displacement current convoluted with the slow time response of the amperemeter (5 µs time resolution at best). However, at the beginning of the pulse, this transient is much longer (50µs) which might indicate that we miss something with the models.

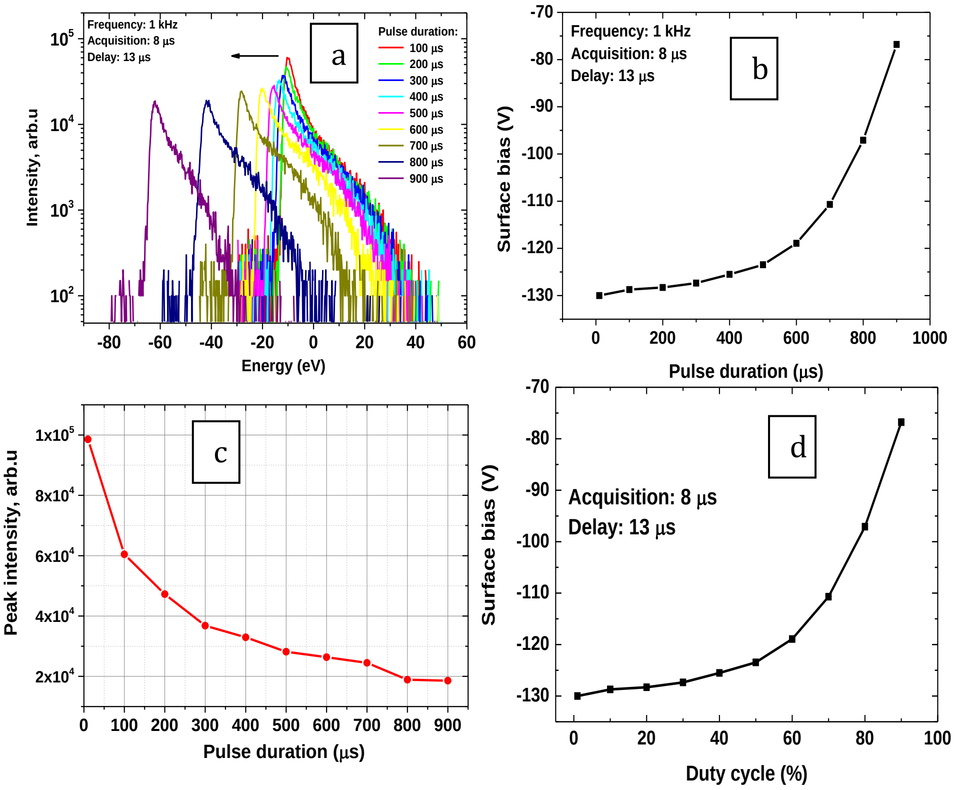

Figure 4.29 a) NIEDF measurement at beginning of pulse for pulse duration T_{pulse} from 10 µs to 900 µs, ceramic head (b) Vs at beginning of pulse as a function of T_{pulse} (c) NIEDF peak intensity measurement at beginning of pulse for pulse duration T_{pulse} from 10 µs to 900 µs (d) Vs at beginning of pulse as a function of duty cycle

One can note in **Figure 4.29**(a) and (c) that the NIEDF peak intensity decreases as the pulse duration grows. Indeed, the mass spectrometer (MS) is set to optimize the transmission of ions created at Vs= -130 V. However, when the pulse duration increases, the surface bias is no more -130 V and the transmission of ions is no more optimized for the correct negative ion (NI) energy. In order to prevent the signal loss resulting from unsuitable autotune, the following experiment was performed as depicted **Figure 4.32**: the pulse duration was varied from 100 µs to 900 µs, while increasing the applied bias V_a in order to have Vs = -130 V on the sample surface. The adjusted value of V_a in order to get V_s= -130 V at different pulse duration is presented in **Figure 4.32** (c). The surface bias remained at desired value for different pulse duration, the transmission of ions is optimized, and the situation is comparable to the use of a conducting sample. As can be seen from **Figure 4.32** (a), the NIEDF onset is now occurring at the same value whatever the pulse duration. It can also be observed that the tails of measured NIEDF superimpose and only the distribution maximums decrease. So, the NI intensity decrease with pulse duration is not mainly caused by the tuning of MS (see **Figure 4.32** (d)). The origin of signal decrease can be deduced from the shape of normalized NIEDF measured at different $T_{pulse.}$ (**Figure 4.32** (c)).

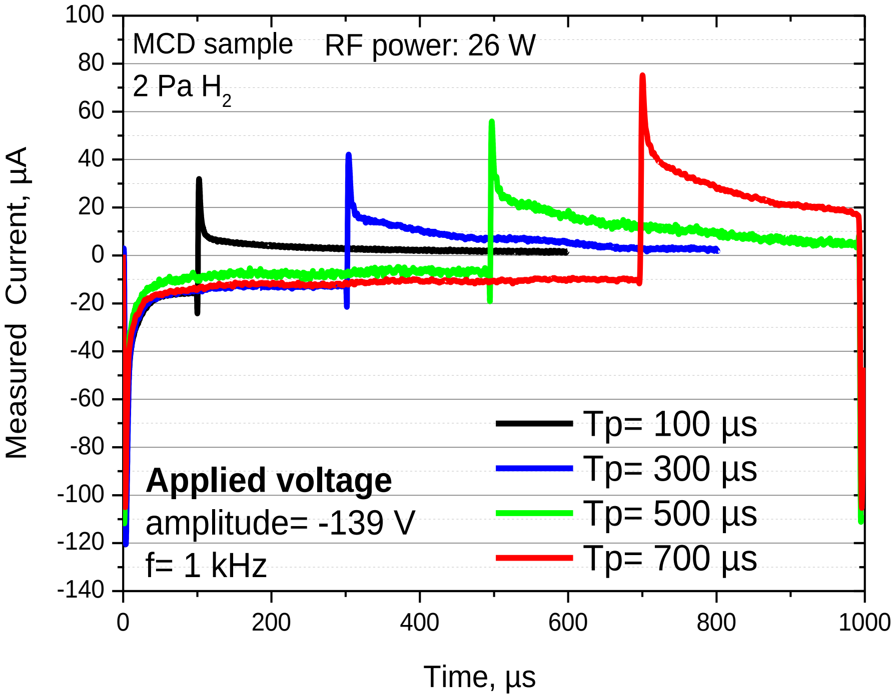

Figure 4.30 comparison of measured surface current on MCD sample at different duty cycle

For longer T_{pulse}, the tail of normalized NIEDF increases with respect to the peak. This indicates the decrease of the sputtering contribution to the NI production. This latter depends on the hydrogen surface coverage. Therefore, this behavior can result from the hydrogen surface coverage decrease. As it was discussed before (see **Figure 4.8**), the hydrogen surface coverage depends on T_{off}. Therefore, the decrease of the signal is attributed to the decrease of sputtering contribution to NI production due to a decrease of hydrogen coverage, similarly to the HOPG case.

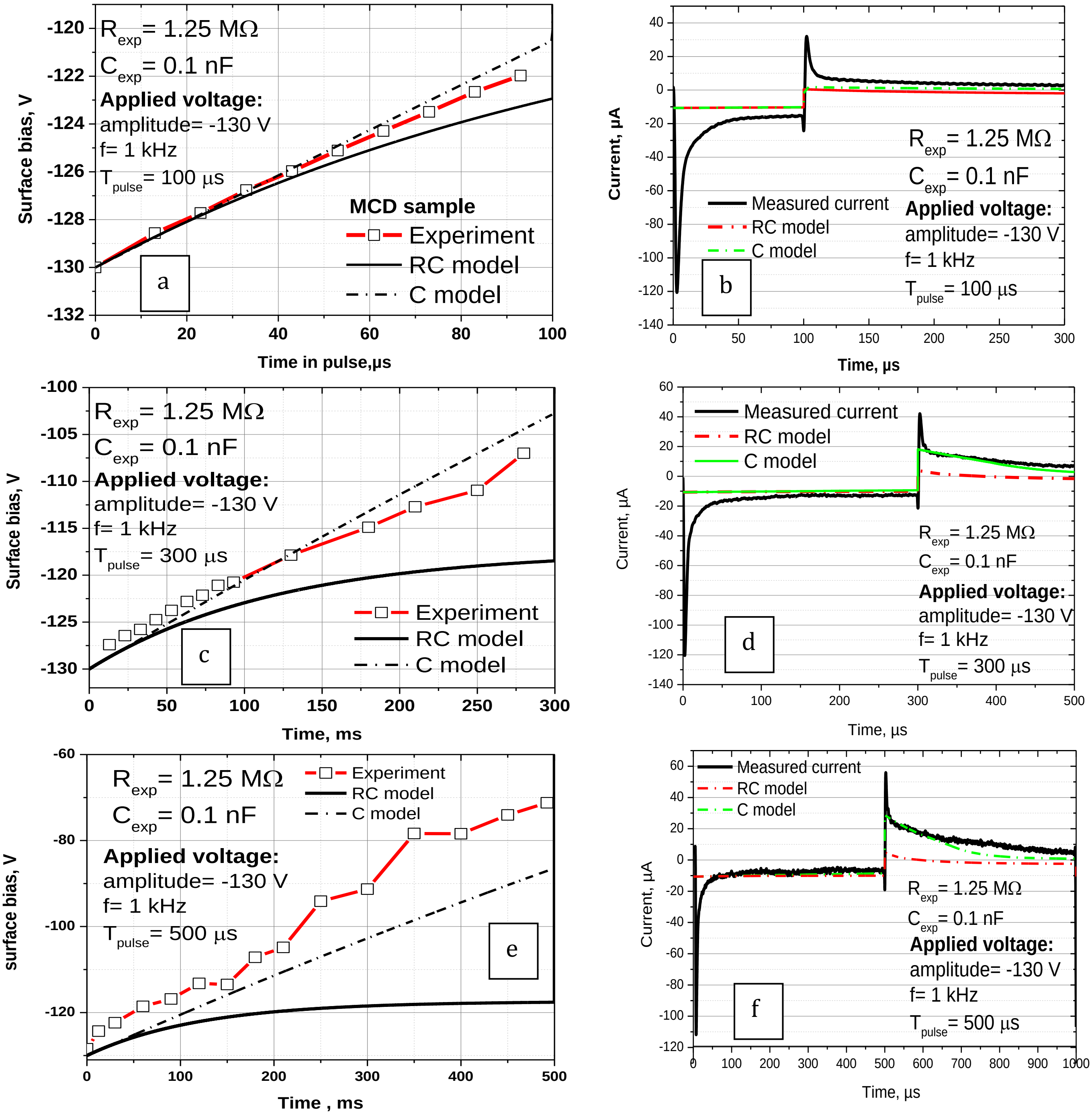

Figure 4.31 Surface voltage V_s (red line black square) of MCD material at different moment of the (a)100 µs , (c)300 µs and (e)500 µs bias pulse compared to calculated one in the case of C_{exp} model (black dash line) and C_{exp} R_{exp} model (black solid line).Current of MCD material (solid black line) at different moment of the (b)100 µs , (d)300 µs and (f)500 µs bias pulse compared to calculated one in the case of C_{exp} model (green dash line) and C_{exp} R_{exp} model(red dash line)

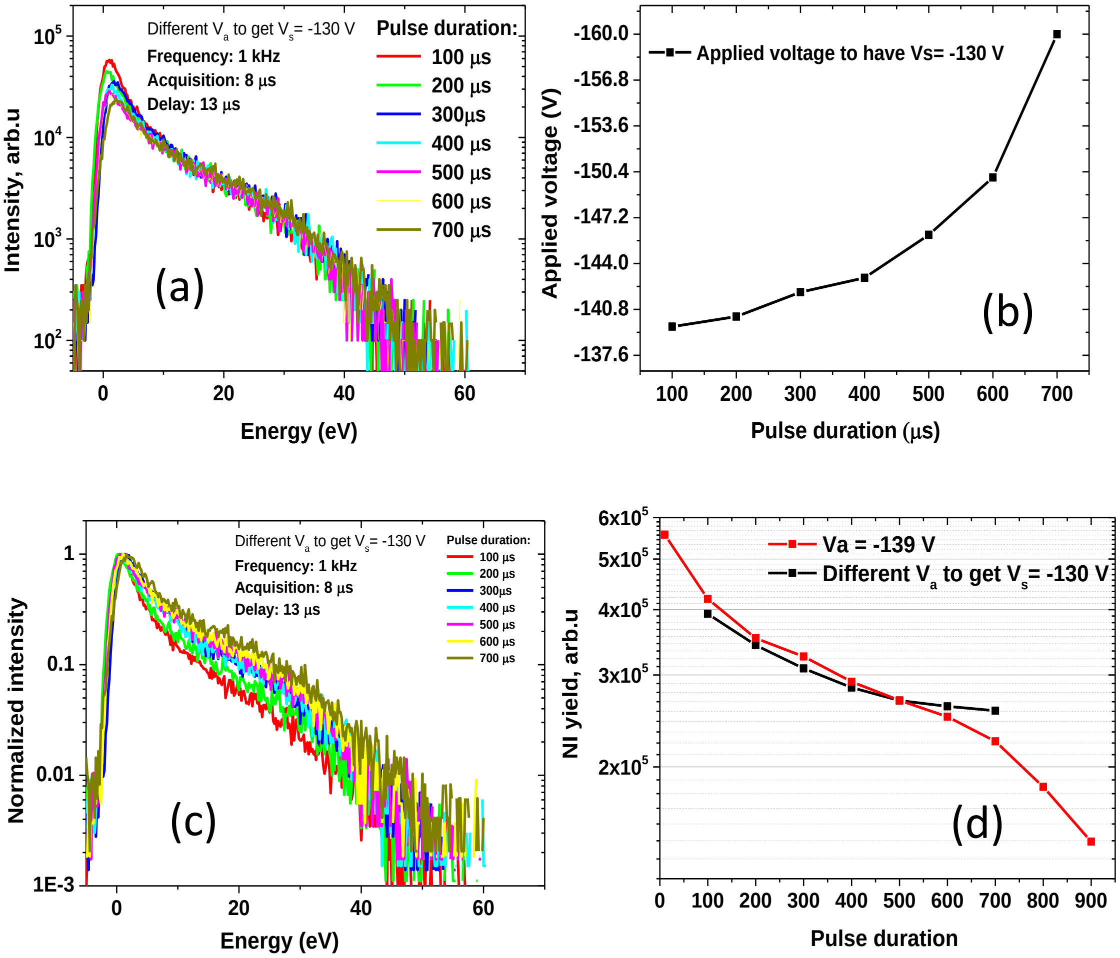

Figure 4.32 (a) NIEDF measurement at beginning of pulse for pulse duration T_{pulse} from 10 µs to 900 µs, ceramic head in the case of adjusted Va (b) Applied Va at beginning of pulse as a function of T_{pulse} in order to get Vs= -130 V (c) normalized NIEDF measurement at beginning of pulse for pulse duration T_{pulse} from 10 µs to 900 µs, ceramic head in the case of adjusted Va (d) comparison of NI yield measured in the case of different Va to get Vs = -130 V with the case of Va= -140 V at beginning of pulse for pulse duration T_{pulse} from 10 µs to 900 µs

3.D.2) Scan of pulse frequency f at constant pulse duration T_{pulse}

In **Figure 4.33** (a) are shown the measurements with an applied bias $V_a = -140\ V$ and for $T_{pulse} = 10\ \mu s$ at different frequencies from 0.25 to *90 kHz* which gives duty cycle from *0.25%* to *90%* and OFF duration from 3990 µs to 1 µs. As observed in **Figure 4.29** the NIEDF is shifted and its intensity is decreased. For high frequencies (high duty cycle) the MCD sample cannot discharge completely during T_{off} because the bias arrives too quickly. It means that for the bias duration used in the experiment ($T_{pulse} = 10\ \mu s$), the frequency should not be higher than *5–10 kHz* (see **Figure 4.33** (b) square symbols) to get a surface bias of *–130 V* with an applied bias of *–140 V*. For higher frequency, the applied bias must be increased to get the appropriate surface bias.

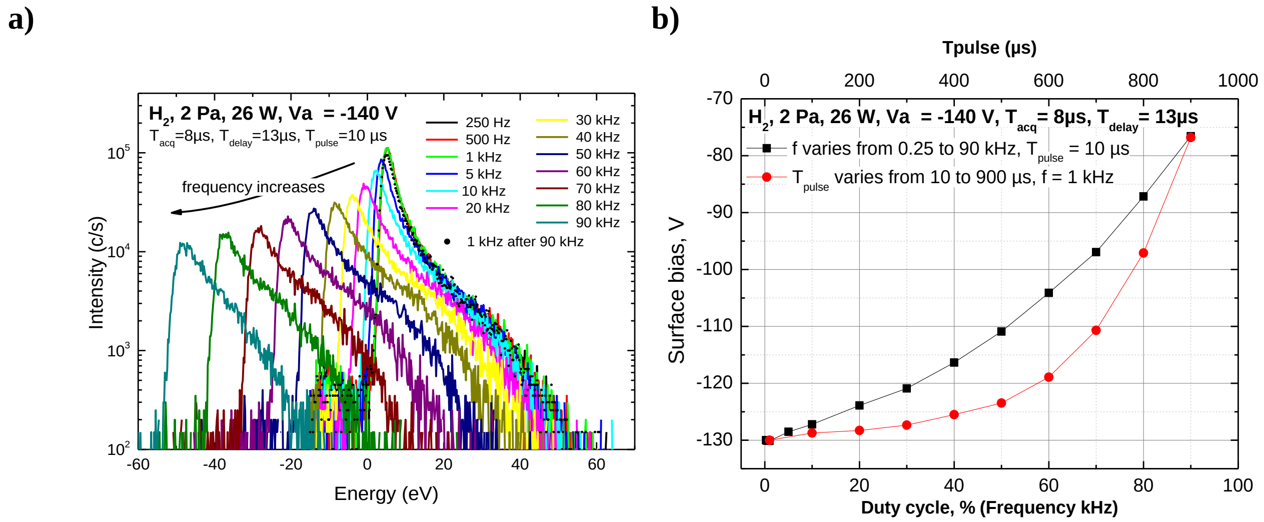

Figure 4.33 H_2, 26 W, 2 Pa, $V_a = –140$ V, Tacq = 8 µs and Tdelay = 13 µs, ceramic clamp a) NIEDF versus pulse frequency from f = 0.25 kHz to 90 kHz with $T_{pulse} = 10$ µs, $T_{acq} = 8$ µs and $T_{delay} = 13$ µs b) NI total signal versus duty cycle when varying frequency (square symbols deduced from a) at constant pulse duration (T_{pulse} = 10 µs), and when varying pulse duration from 10 to 900 µs at constant frequency (f = 1 kHz)

In **Figure 4.33** (b) the surface bias V_s is plotted versus the duty cycle for both experiments, when varying pulse duration at constant frequency (deduced from **Figure 4.33** (a)), and when varying frequency at constant pulse duration (V_s deduced from **Figure 4.33** (a)). First, as expected the duty cycle is a key parameter, the highest its value are, the highest is the charge on the surface and the lowest (in absolute values) is the surface bias during the pulse for a given applied voltage. Second, the discharge rate of the surface is clearly slower than the charging rate, otherwise up to a duty cyle of 50 % the surface bias would be -130 V. Third, the discharge rate is non-linear with the charge of the surface, it is higher for a higher charge, otherwise no negative stationary surface bias would be reached for high duty cycle and the sample would reached floating potential. Due to this non-linearity, the two type of experiments do not give the same surface bias for the same duty cycle. Indeed, the two curves on the plot cover very different situations. A duty cyle of 50% corresponds to 500 µs of bias ON, 500 µs of bias OFF in one situation, and to 10 µs ON and 10 µs OFF in the other situation (frequency variation), leading to two different surface biases during the pulse ~-124 V (T_{pulse} variation) and ~-111 V (frequency variation). As the charging rate is expected to be the same and equal to I_i/C in both experiments, it appears that the discharge rate is faster in the situation with 500 µs ON, 500 µs OFF. Most probably, the high charge of the surface in this situation (ΔV~50 V at the end of the pulse, **Figure 4.27**) is provoking a huge flux of electrons in the first instants of the OFF period leading to a fast-initial unload of the surface. At low duty cycle there is no difference between both experiments since the OFF period is long enough in both cases to completely unload the surface (990 µs OFF in the case of T_{pulse} variation, 4 ms in the case of frequency variation). However, it is not clear why both experiments merge at high duty cycle.

One can note in **Figure 4.33** (a) that NIEDF shapes are modified as the pulse bias frequency grows. They are quite usual and similar to the ones obtained on conductive samples[47] at low frequency and broaden and loose the marked low energy peak at higher frequency. In the same time NI signal (area below NIEDF) noticeably decreases. It cannot be interpreted easily because, as the surface voltage is changing, the mass spectrometer tuning is not optimized anymore for the correct NI energy. To prevent the signal loss resulting from unsuitable tuning, the applied bias V_a has been increased in order to have $V_s = -130\ V$ on the sample surface whatever the pulse frequency. In such a way, the situation was comparable to the use of a conducting sample as the surface bias remained at desired value. As can be seen from **Figure 4.34** (a), the tails of measured NIEDF superimpose up to $f = 90\ kHz$ and only the distribution maximum decreases. This may indicate the decrease of the sputtering contribution to the NI production resulting from the hydrogen surface coverage decrease. However, the suppression of the sputtering mechanism could account at maximum for a decrease of the signal by a factor two[73]. Therefore, as observed for HOPG, the decrease of the hydrogen surface coverage most probably leads to a change of top surface electronic properties and thus to a change of the ionization probability[49]. A modification of incoming positive ion flux and energy for short T_{off} (high frequency) cannot be excluded as well but has not been investigated here. It will be the subject of future works. Let us note that NIEDF modelling cannot be used here since the model assumes a planar sheath in front of the sample to calculate negative-ion transport to the mass spectrometer[51]. In the present situation, because of the ceramic clamp surrounding the sample the sheath cannot be planar. In the case of molybdenum clamp the sheath can neither be planar since the applied bias appears on the clamp while only the surface bias appears on the sample. The same experiment done with the molybdenum clamp leads to basically the same results, with similar value of the applied biases at each frequency, and a more pronounced decrease of the signal probably due to higher distortion of the sheath in front of the sample. Finally, one can note that adjusting the applied bias to get a constant surface bias at any frequency has permitted to solve the issue of unappropriated mass spectrometer tuning and has increased a bit the signal (**Figure 4.34** (b)).

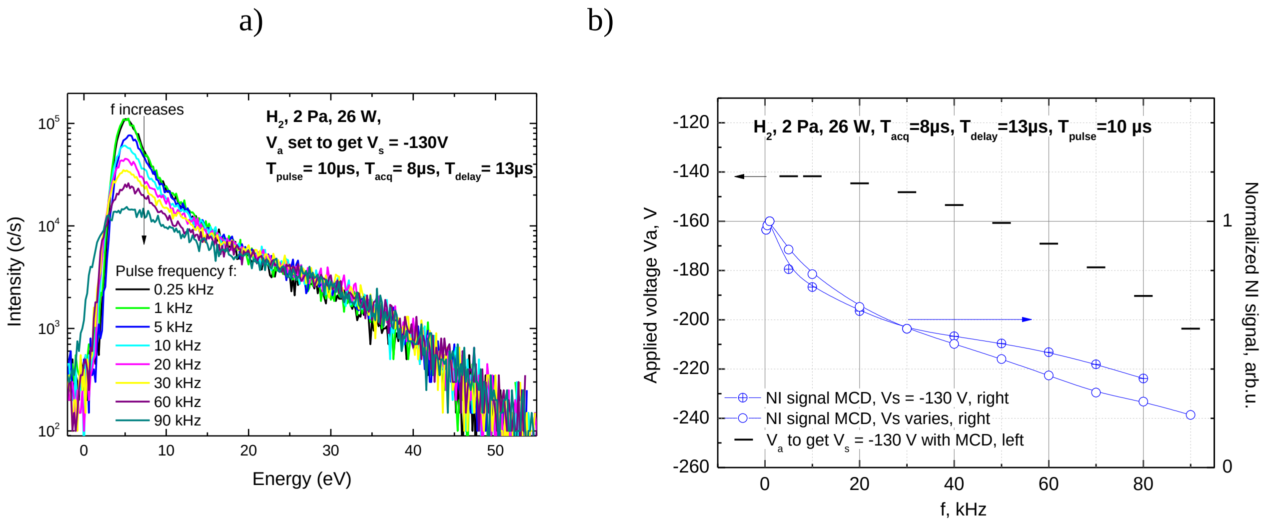

Figure 4.34: H_2, 26 W, 2 Pa, Tpulse = 10 μs, Tacq = 8 μs and Tdelay = 13 μs, ceramic clamp
a) NIEDF versus pulse frequency from f = 0.25 kHz to 90 kHz with applied voltage set to maintain surface voltage equal to -130V b) Normalized NI total signal versus frequency for MCD with Vs = -130 V (cross-circle symbols, deduced from Figure **4.34**a, right scale), MCD with Vs varying (open circle symbols, deduced from Figure **4.33**a, right scale), and value of the applied voltage set to get surface voltage of -130V (line symbols, left scale)

3.E. Optimization of pulsed bias technique

As it was mentioned in **Chapter 3**, studying NI surface production at low bias is of interest for applications since NI sources usually operates at low positive ion bombardment energy. In this part we perform an optimization of acquisition parameters for NIEDF measurements on insulating materials using low bias (- 20 V).

The main purpose of this optimization is to eliminate surface charging effect over several pulses and maintain an almost constant bias during NIEDF measurement. The surface bias stability during measurement allows for a constant positive ion bombardment energy. Under these conditions, the NIEDF measured with an insulator is treated in the same way as a NIEDF measured with a conductor.

As it was mentioned before, the pulse is characterized by its frequency f and its duration T_{pulse}. The optimization of these parameters is done in two steps. First, we set the frequency as constant and we vary the duration of the pulse to find the best signal. Second, after getting the best signal level at a precise duty cycle, the frequency and pulse duration are varied simultaneously keeping the duty cycle constant.

Different measurements were done on MCD sample immersed into a D_2 plasma (gas pressure 2 Pa, RF power 20 W). The acquisition parameters are as follows: T_{acq}= 10 μs and T_{delay} ~ 21 μs (m_D= 2m_H the fly time of D^- is ~ 2 times the fly time of H^- and it is determined using output of MS detector). The applied potential V_a is equal to -30 V, this is sufficient to obtain Vs= -20 V. To determine the optimal duty cycle, a pulse with a frequency f= 1 kHz is used. **Figure 4.35** (b) and **Figure 4.35** (d) illustrates the variation of NIEDF peak intensity and NI yield with respect to duty cycle. As we can see the highest NI yield and NIEDF peak intensity is measured at a duty cycle equal to 10 %.

After determining the duty cycle, the pulse frequency f and the pulse duration T_{pulse} are varied simultaneously keeping their product equal to 0.1. The variation of NIEDF peak intensity and NI yield with respect to pulse frequency variation (f) and pulse duration (T_{pulse}) are shown in **Figure 4.35** (a) and (b). The increase of pulse frequency leads to a faster MS acquisition but it decreases the measured NI signal. For pulse duration, the NI signal increases up to ~ 15 - 20µs and is then more or less constant. To choose optimal pulse frequency and pulse duration values, we ensure a high NI signal in a reasonable total NIEDF acquisition time with a low change of surface bias during the MS acquisition window (Tacq). As shown in **Figure 4.21** the surface voltage variation with time is very slow in these conditions, 6 V over 2 ms. So, during the acquisition window no noticeable variation of the surface bias occurs. Following these criteria, 5 kHz is chosen as an optimal pulse frequency and it corresponds to an optimal pulse duration of 20 µs.

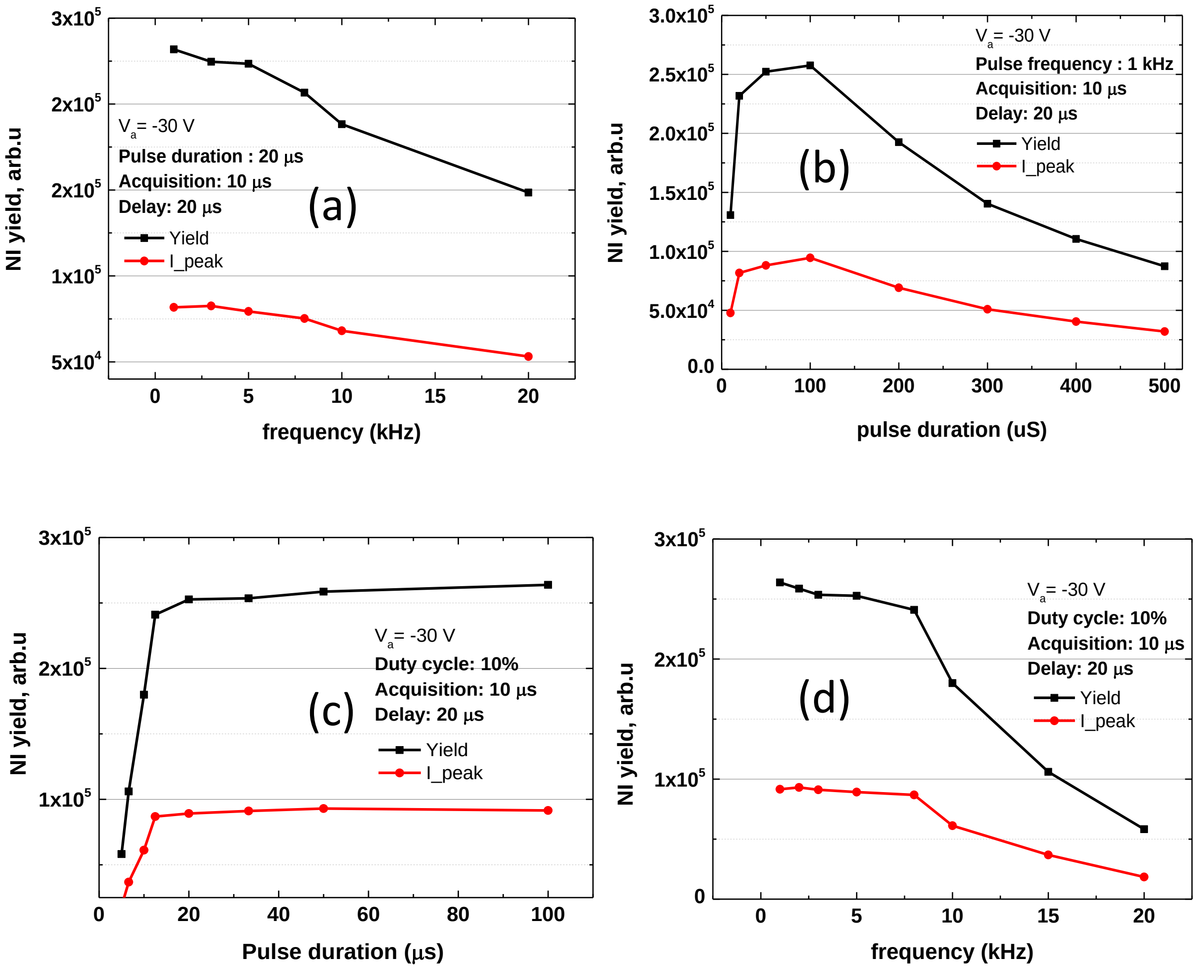

Figure 4.35 D_2 plasma: 2 Pa of gas pressure, 20 W of RF power. Measurement in pulsed bias mode on MCD sample. (a) NI variation with pulse frequency at a constant pulse duration (b) NI yield variation with pulse duration at a constant pulse frequency (c) NI yield variation with pulse duration at a constant duty cycle = 10% (d) NI yield variation with pulse frequency at a constant duty cycle = 10%

4.5 Study of NI surface production on insulating materials

a) Different materials at low bias and room temperature

After the optimization of different parameters of pulsed DC bias at Vs = -20 V, NI measurements were done on different samples at different surface bias V_s values. In **Figure 4.36** the negative ion yield is measured in D_2 plasma under the following conditions: a gas pressure of 2 Pa and an RF power of 20 W. The used pulsed bias parameters values are the optimal ones (f= 5 kHz and T_{pulse} = 20 µs). The MS acquisition conditions are: T_{acq}= 10 µs and T_{delay}= 20 µs.

Two conclusions can be deduced from NIEDF measurement done in the case of optimized pulsed bias. First, the pulsed DC bias technique gives the ability to study the NI surface production at room temperature on insulator surfaces for different surface bias values since NIEDFs were measured on MCD surface and MgO surface with success. (MgO material has been used referring to its interesting electronic properties for NI surface production such as high secondary electron emission and it has application in plasma screen).

Second, the pulsed bias mode leads to higher negative ion signal for all materials. For all materials the hydrogenation of the top layer, deduced from the SRIM modeling, is higher in pulsed mode than in DC bias mode. However, this is not enough to explain the large increase observed for diamond materials. This large increase of the signal is attributed to the weak number of defects created on diamond when exposed to pulsed DC bias at low duty cycle (10% here). The diamond surface is close to the pristine diamond surface which electronic properties are probably favorable to surface ionization of outgoing hydrogen particles. In pulsed mode one acquisition lasts around 20 minutes. It represents about 12 seconds of positive-ion bombardment and therefore measurements in pulsed mode can be considered as done with a poorly defective material. Furthermore, atomic bombardment during the OFF phases (without bias) might help removing defects created during the ON phases. The situation is close to the one obtained at the first instants of plasma exposure where the surface is not too much damaged and the signal is found higher than at steady state. However, as we have said before, the total NI production in the case of pulsed DC bias is the product of measured one by the duty cycle. The pulsed DC bias is not a method to increase the NI surface production, but it gives the ability to study insulators surface with less defective surface state.

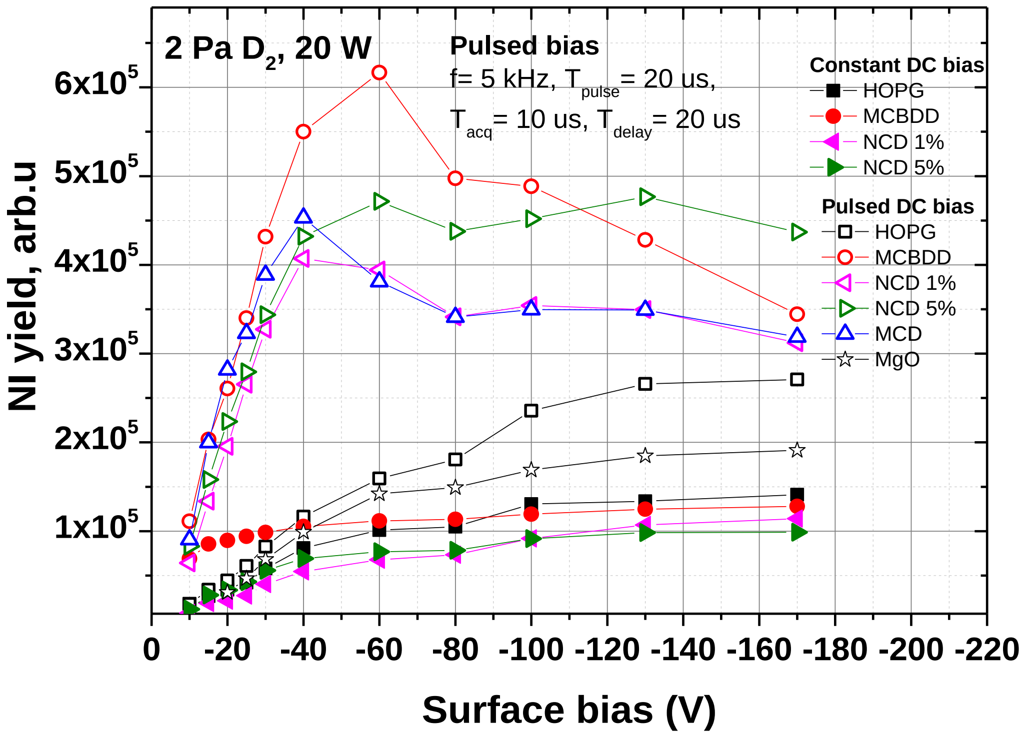

Figure 4.36 NI yield measured at beginning of pulse for pulse duration of 20 µs and a pulse frequency 5 kHz on different surface materials.

b) Different materials at high bias and high temperature

Top layers of samples exposed to plasma are modified by the ion and atomic bombardment. At low temperature the top layer formed on MCD sample is probably insulating and does not permit to bias the sample. As observed previously [63], at higher temperature, above 300 °C, this top layer becomes conductive and the sample can be biased through the clamp contact (if clamp is metallic). The pulsed bias method allows studying negative-ion surface production on MCD sample on the whole temperature range without any restriction and allows comparing directly pulsed and DC bias at high temperature. Previous works have shown that the total negative-ion count on different kind of diamond samples is increasing with temperature reaching a maximum around 400-500 °C and decreasing above. This has been attributed to the enhanced etching of sp2 carbon phases at higher temperature allowing to obtain a top layer which is closer to the pristine diamond sample. Recovering the diamond electronic properties seems therefore to be favorable for negative-ion surface production. It has also been noticed that the hydrogenation of the top layer is increasing between room temperature and 400-500 °C and decreasing above. The decrease of the signal has been attributed to the decrease of the hydrogenation, leading to a decrease of the negative-ion creation by sputtering, and also probably to a change of electronic properties which may become less favorable to surface ionization.

Results obtained are presented in **Figure 4.37** for HOPG, MCBDD and MCD materials. For MCD and MCBDD materials two samples from the same batches have been used in two different experimental campaigns in pulses mode. The signal from the two campaigns are slightly different which might come from different alignment of the sample in front of the mass spectrometer or problem of temperature calibration. As the temperature is measured on the sample holder and not on the sample itself, the surface temperature might be different from the indicated one due to variations of thermal contact. One can note that MCD samples are giving lower signal than MCBDD ones in several situations, in particular in DC mode. We do not think that this has something to see with the doping as MCD material has already demonstrated identical negative-ion yields to MCBDD one[47,63]. **Figure 4.37**shows total negative ion NI yield versus surface temperature both in pulsed bias mode at 1 kHz and in DC bias mode. The comparison of NI yield measured at pulsed DC mode to the one measured at DC mode leads to the same observation discussed previously. The pulsed bias mode leads to higher negative ion signal, almost one order of magnitude, for diamonds materials. At room temperature NI signal on MCBDD material is lower than signal on HOPG while it becomes higher by a factor 4 in pulsed mode.

This previous interpretation is supported by **Figure 4.37** presenting MCD total counts versus temperature in pulsed and DC mode and showing the timing of the experiment. The measurements are first done in pulsed mode up to 600°C and then back to 400°C. No hysteresis is observed. As the top MCD surface is conductive at 400°C the bias was then switch to DC mode. The graph shows that the signal is decreasing with time to reach a steady state with a much lower signal after around 15-20 minutes. This decrease is attributed to defect creation by the positive ion bombardment. Considering the low positive ion flux in this experiment, a fluence of 3. 10^{15} ions/cm^2 (roughly three mono layers of material) is reached after about 1 minute, and this slow evolution over 20 minutes is not surprising. Then the pulsed bias is turned ON again and a memory effect is observed. The signal is increasing, probably due to the higher material hydrogenation, but not as much as it was before DC bias irradiation. This is attributed to the defects created during the DC bias exposure.

Both in pulsed and DC mode the negative-ion signal is increasing with temperature for diamond materials. This is attributed to the enhanced sp2 phases etching at higher temperature. The decrease above 400-500°C is explained as in DC bias mode by the decrease of the material hydrogenation. Concerning HOPG the results are very similar in pulsed and DC bias mode, except the increase of the signal at room temperature due to the higher material hydrogenation. At higher temperature, as shown previously, hydrogen is desorbing, and the graphite material is recovered, leading to a strong decrease of the signal[47,49,52].

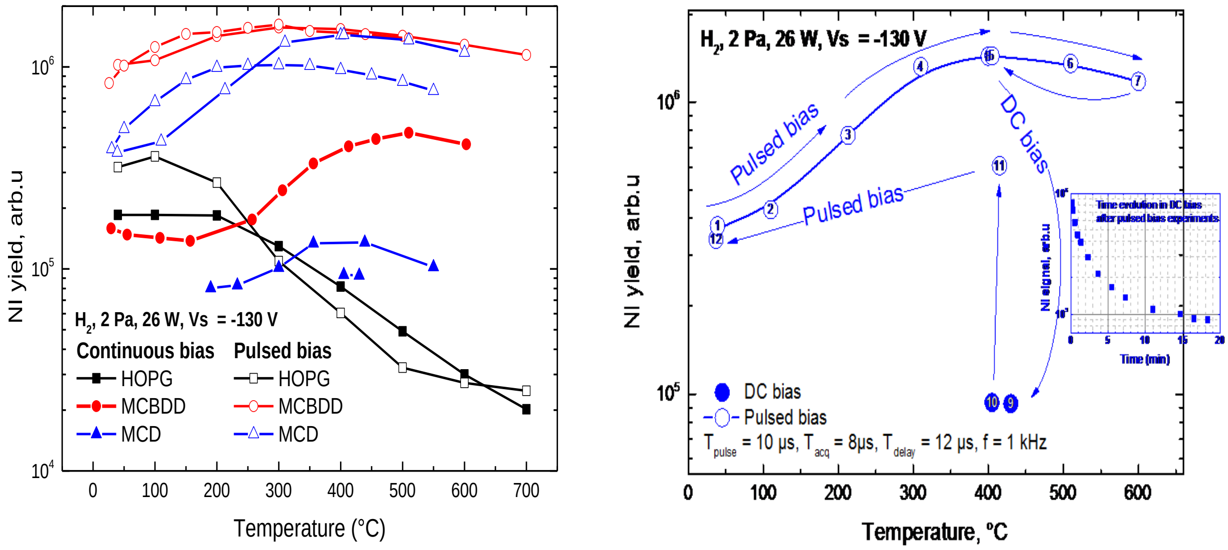

Figure 4.37 H_2, 26 W, 2 Pa, Vs = -130V, pulsed bias conditions: Tpulse = 10 µs, Tacq = 8 µs and Tdelay = 13 µs, 1 kHz, molybdenum clamp. Negative ion total signal versus surface temperature in DC (full symbols) and pulsed mode (open symbols) a) for three different material: HOPG, MCBDD and MCD b) for MCD material with the timing of the experiment. The numeric labels correspond to the chronological order of the experiment. The insert shows NI signal versus time between experiment #8 and #9.

Conclusion

In previous works we have developed experimental methods to study NIsurface production in plasmas. A sample is negatively biased. Upon positive ion bombardment some negative-ions are formed on the surface and are accelerated towards the plasma. Thanks to the energy gained in the sheath they can be self-extracted on the other side of the plasma towards an energy and mass analyzer. Up to now this method was limited to conductive material due to the use of a DC bias. In the present chapter, the method of pulsed bias was developed to enable the study of NI production on surfaces of insulating materials. The idea is to apply a brief DC bias pulse on the surface and perform a synchronized negative-ion acquisition. Between pulses the surface is let floating to ensure unload. The present technique has enabled to study NI surface production on MicroCrystalline Diamond (MCD) for a temperature range starting from RT to 750°C. The pulsed-bias tests were first performed on Highly Oriented Pyrolitic Graphite (HOPG), a conductive material, to demonstrate the feasibility of the method. By changing the pulsed-bias frequency (and the duty cycle) it was possible to obtain HOPG material with different hydrogen surface coverage and hence a different surface state (with the NI yield increase up to *30-50%*). After proving the feasibility of the pulsed bias approach on HOPG, the optimization of the experimental parameters was performed on MCD by taking into account the charging effects. It has been shown that the MCD sample behaves in plasma as a RC circuit loaded by a constant current (the positive ion saturation current) during the pulse. A low duty cycle is required (<10 %) to ensure between bias pulses a complete removal of charges accumulated during the pulse. A pulse duration of 10 µs with a repetition frequency of 1 kHz allows for measurements on MCD material under the present low positive-ion flux experimental conditions.

The total negative-ion signal strongly increases between DC and pulse mode, for the three materials tested: HOPG, MicroCrystalline Boron Doped Diamond and MCD. Factors from 1.5 (HOPG) to around 10 have been observed and the highest negative-ion yield ever measured under the present experimental conditions have been obtained in pulsed mode at high temperature. The results bring us to the conclusion that in pulsed bias case the diamond surface is less degraded and more hydrogenated, which is favorable for NI surface production. This situation is similar to biasing a fresh diamond sample with constant DC bias for a very short exposure time. Most probably, under ion bombardment, diamond samples lose their attractive electronic properties. With a very short exposure time, or using the pulsed bias technique, it is possible to maintain electronic properties close to the pristine diamond ones and obtain higher NI yields.

Pulsing the bias at low duty cycle is a solution only for fundamental studies and could not be used in a real NI source due to the low time average negative-ion production. However, the present study shows that electronic properties of diamond are favorable for NI production, and diamond placed in appropriate experimental conditions could be potentially interesting for NI surface production as also shown in beam experiments. Considering the overall result of the pulsed bias measurements, one can conclude that to optimize the NI yield on diamond, one has to work with a less degraded surface. This can be obtained by rising the surface temperature to 400°C–500°C which allows restoring intrinsic properties of diamond. The less degraded surface state can also be obtained by reducing positive ion energy.

Chapitre 5 NI production from a nanoporous C12A7 electride surface

Introduction and motivation

In previous works[49,115,52] NI surface production has been studied putting a strong focus on carbon materials such as diamond and graphite. They have been compared to common metals such as molybdenum or stainless steel but also to two low work function metals gadolinium and cesium-implanted molybdenum.

In this chapter, a new material with interesting electronics properties for NI surface production is studied. The accumulated knowledge on NI production mechanisms and surface state influence on NI surface production, as well as it is the dependence on plasma parameters will be used to deeply understand negative ion surface production on nanoporous $12CaO.7Al_2O_3$ electride surface or C12A7 electride surface for short. This material characterized by a low work function (2.4 eV) will be compared to our reference material for NI surface production HOPG, and our reference material for low work function metals Gadolinium. In previous study, HOPG has been chosen as a reference material for NI surface production due to its unique properties such as easy cleavage and high NI yield. The Gadolinium (Gd) has served as reference for low work function metals. Its work function is only 2.9 eV comparing to 4.6 for HOPG and it has an enhanced hydrogen storage capacity.

C12A7 is a candidate to enhance negative-ion surface production in negative-ion sources [116] Therefore we have studied NI surface production as a function of bias voltage, including low biases which are relevant for NI sources. This study which directly refers to **chapter 3** of the present document is presented **section 5.4** In order to better understand the influence of plasma exposure on C12A7 surface state, and the possible role of defects on NI production, pulse bias method will also be employed despite C12A7 is a conductor (**section 5.4**). This work directly refers to **chapter 4** of the present document. The effect of surface temperature has also been investigated as the plasma grid in NI sources is often heated to high temperature (200°C - 550°C) .

5.1 Bands structure of C12A7 electride surface

The C12A7 (12CaO. 7Al_2O_3) was descripted in **chapter 1** (1.3.1 Materials). This material has interesting electronics proprieties and high thermal and chemical stability.

The main properties that encourages the study of negative ion surface production on C12O7 electride surface is its low work function as shows the schematic energy diagram of C12A7 electride. For electride (chemical formula is $[Ca_{24}Al_{28}O_{64}]^{4+} + 4e^-$), anionic electrons are accommodated in the sub nanometer-sized cages, which relate to each other[64]. The connected cages form a new conduction band (called “cage conduction band (CCB) below the cage flame conduction band minimum (FCBM) (see **Figure 5.1**). The work function (WF) is 2.4 eV, comparable to potassium metal, but chemically and thermally stable owing to that electrons are sitting within the cages composed of rigid Ca-Al-O network.

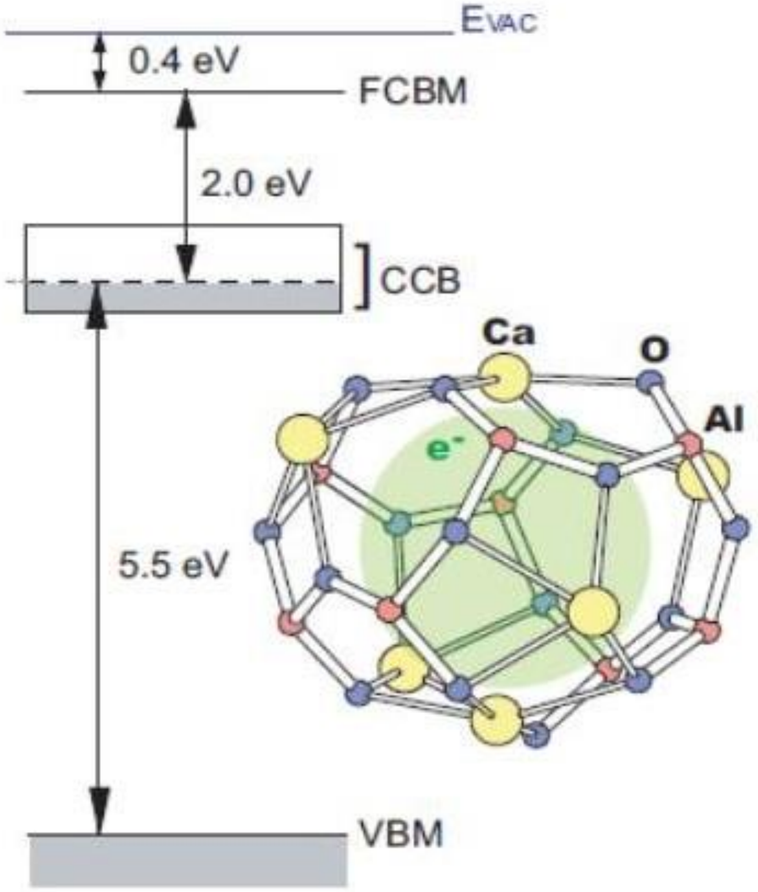

Figure 5.1 Energy diagram of the C12A7 electride: CCB (cage conduction band), FCBM (flame conduction band minimum), WF (work function and it is equal to 2.4 eV). EVAC (vacuum level), VBM (valence band maximum. The band gap is 7.5 eV.

5.2 12CaO. 7Al_2O_3 electride surface preparation

The 12CaO. 7Al_2O_3 electride surface is protected by a layer to prevent pollution and surface oxidation. Before measurement, protective layer must be removed. The removing of protective layer is done in two steps. First, we heat sample under vacuum (10^{-7} mbar) for 3 h under 550°C. Second, we bombard sample surface by Ar plasma. The used Ar plasma in protective layer sputtering is ignited under conditions: 0.1 Pa, 30 W ECR power. The sample is biased at -30 V. During removing of the protective layer, two measurement are done in parallel (not shown here):

1- Mass scan of different protective layer elements during Ar bombardment
2- Detection of emission ray by an optical spectrometer during Ar bombardment

.

2.2 Positive ions contribution to NI surface production on C12A7 electride

The atomic hydrogen flux Φ_{H^0} in our experimental conditions is negligible compared to Φ_{H^0} of ITER NI source. The ratio between positive ion flux and atomic flux is much higher under our experimental conditions compared to ITER NI source ones.

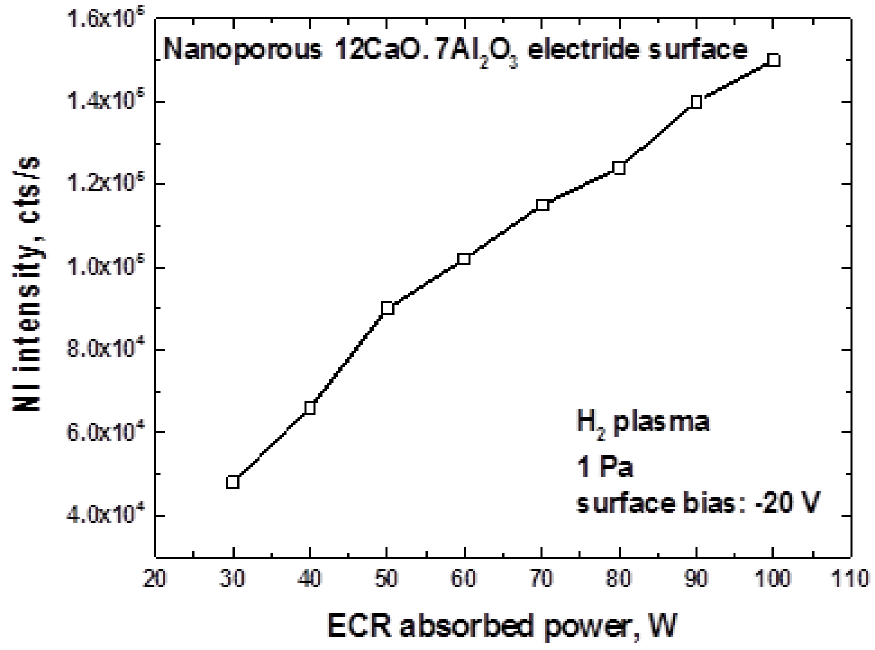

Figure 5.2 NIEDF peak intensity measured on nanoporous 12CaO. 7Al2O3 electride surface in H_2 plasma at 1 Pa and a surface bias of -20 V at different ECR power. The NIEDF peak intensity varies linearly with increasing ECR power.

So, we assume in our experimental conditions negative ion are mainly produced by the impact of positive ion on the surface contrary to ITER NI source where hydrogen atom impact is responsible for negative ion production. This analysis is supported by measuring the NI signal variation with injected ECR power. As it shown in **Figure 5.2**, the NIEDF peak intensity measured on nanoporous 12CaO.7Al2O3 electride surface biased at -20 V and immersed in H2 plasma (1 Pa of gas pressure) varies linearly with absorbed ECR power going from 30 W to 100 W. As the positive ion flux is increasing linearly with ECR power, this result is going in the direction of our conclusion, NI are mainly created by the impact of PI on nanoporous 12CaO.7Al2O3 electride surface.

5.3 NIEDF measurement for C12A7 electride surface

The negative ion NI surface production on C12A7 electride surface is studied as a function of relevant experimental parameters:

- Impinging positive ion energy defined by surface bias amplitude
- Bombardment time defined by bias duration and bias mode
- Surface temperature

The NI surface production on C12A7 electride surface is compared with those of HOPG, Gadolinium (Gd). The comparison of NIEDF shapes will help determining the relative contribution of each mechanism (backscattering and sputtering) to NI surface production on C12A7 electride surface. The comparison of NIEDF yield and NIEDF peak intensity will help to classify the C12A7 among the interesting NI enhancers.

5.3.1 NI surface production mechanisms on C12A7 electride surface

The methodology followed in this section is based on the comparison of NIEDF shape observed for C12A7 electride surface and different materials previously studied.

The NIEDF shapes obtained with carbon materials exposed to high bias is well understood thanks to modeling presented in detail in **Chapter 2**. The NIEDF modeling has been developed in A. Ahmad thesis and improved in K. Achkasov work. In A. Ahmad work, it was proved that the measured signal comes only from the sample surface, and no NI coming from the sample holder are collected. It was demonstrated that NIEDF shape is determined by the relative contribution of two production mechanisms: sputtering and backscattering.

In **Figure 5.3**, we present normalized NIEDF spectra measured at room temperature (RT) in H_2 plasma. The normalized NIEDF measured on C12A7 electride surface is compared to the measured one on HOPG surface, Gd surface and Mo surface. Obviously, NIEDF shapes are different for different materials. As long as hypothesis made to model NIEDF on HOPG are still valid for other materials, this result means that the relative contribution of NI production mechanisms (sputtering and backscattering) is not the same for different sample surfaces. As one can see in **Figure 5.3**, the normalized NIEDF shape of C12A7 electride surface is an intermediary result between HOPG and Gd.

The contribution of NI surface production mechanisms to NIEDF measured on HOPG and Gd surfaces was studied in detail in the work of K. Achkasov. In previous work, it was demonstrated that HOPG and Gd show comparable integrated NI yield with key differences in mechanisms of NI production. These differences were identified by using the reconstruction method (this method is detailed in reference 74). It was shown that for Gd the major process is backscattering of ions with a peak of production at 36 eV. This results in a measured NIEDF with a slight maximum at low energy due to the high collection efficiency of low energy ions, and a long more or less constant tail. In case of HOPG the sputtering contribution due to adsorbed H on the surface is also important and there is a production peak at low energy. As low energy ions are easily collected this results in a NIEDF shape with a well pronounced peak found around 5 eV, and a tail decreasing monotonously at higher energy. So, basing on Figure 3, we can assume that on C12A7 the relative contribution of sputtering to NI production is higher than on Gd and lower than on HOPG. In future works, this expectation can be validated by the application of reconstruction method on C12A7 electride surface, and by comparing the results with the case of HOPG and Gd. By analogy with HOPG, NIEDF peak is attributed to a strong contribution of sputerring mechanism while the NIEDF tail refers to backscaterring contribution. The analogy of C12A7 electride surface with HOPG is not enough, a study of NI yield behavior with different experimental conditions is needed. For HOPG, the ionization probability has been considered as a constant, this validity of this assumption for C1A7 electride surface must be tested.

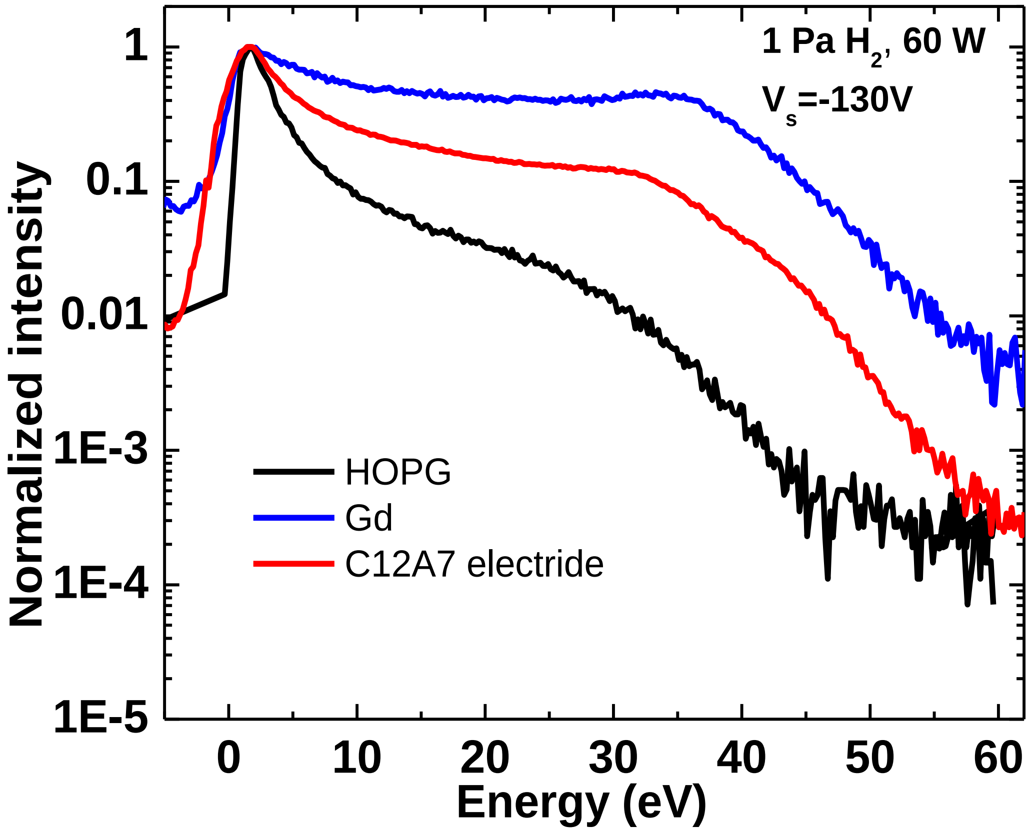

Figure 5.3 Comparison of normalized NIEDF measurement in 1 Pa H_2 plasma and 60 W ECR power for different materials: Gd, C12 A7 electride surface and HOPG for Vs= -130 V

5.3.2 NI production efficiency on C12A7 electride surface

After the discussion on the relative contribution of different NI surface production mechanisms for C12A7 electride surface, we present in this part the NI production efficiency on C12A7 electride surface under different experimental conditions (plasma and surface conditions) compared to others surfaces studied previously. **Figure 5.4** shows NIEDF measured for different surfaces including C12A7. As one can see the NIEDF peak intensity measured for C12A7 electride surface is 21 times higher than for Gd surface.

As shown by Achkasov and Kogut[74] comparing directly NIEDF signals obtained with different materials is not enough to compare NI production efficiency since NIEDF measured at MS detector are strongly different from NIEDF emitted by the surface. The collection efficiency may vary from one material to the other depending on the NI emission angle and energy. Therefore, the NIEDF produced on C12A7 must be reconstructed from measured one. Reconstructed NIEDF on C12A7 electride surface must be compared with previous result obtained by reconstruction method application on different materials.

However, it is essential to keep in mind that NI production efficiency is influenced by experimental conditions. In coming part, NI production efficiency on C12A7 electride surface will be measured under different experimental conditions (surface bias, surface temperature, gas pressure, and ECR or RF power). The effect of bombardment time (bias duration and bias mode, DC mode or pulsed mode) will also be investigated.

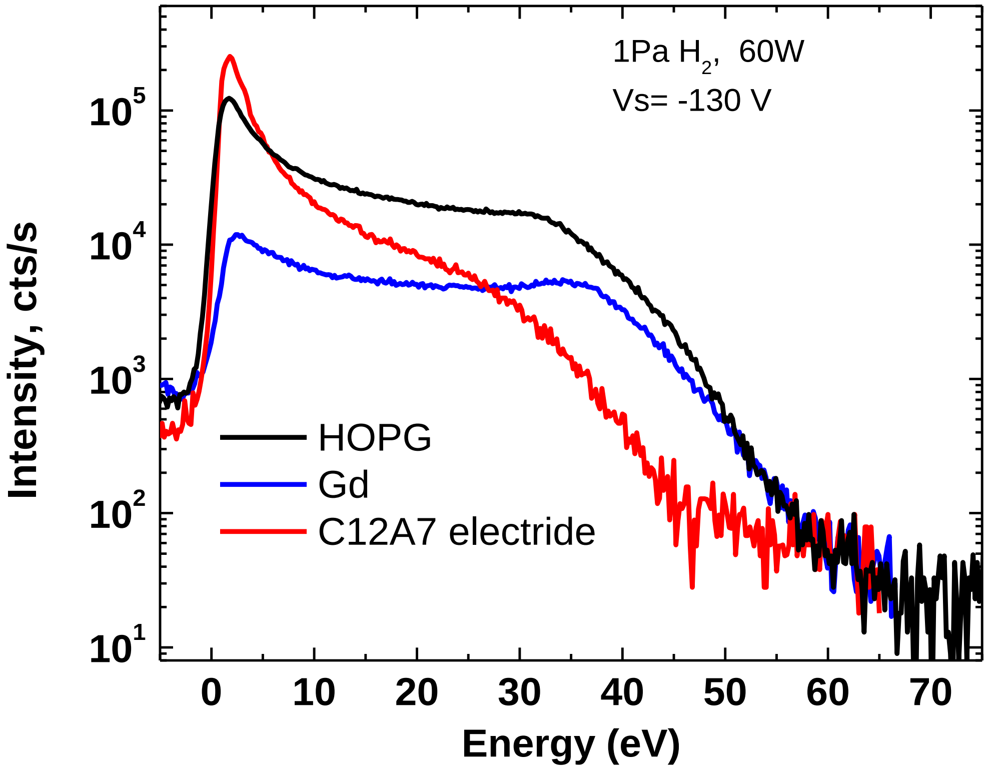

Figure 5.4 NIEDF measurement in H2 plasma 1 Pa and 60 W ECR power at Vs= -130 V for Gd, HOPG, and C12A7 electride surface.

5.4 Effect of surface bias parameters on NI production efficiency

IN this section, the variation of NI surface production efficiency on C12A7 electride surface as a function of bias amplitude will be compared to our previous observation in the case of different materials. Second, the pulsed bias approach will be applied to C12A7 electride surface, and the effect of bias mode on measured NI surface production will also be analyzed in regards of previous interpretations.

5.4.1Variation of NI surface production efficiency with surface bias amplitude

The NIEDF measurements have been performed on C12A7 electride surface in H_2 plasma under two experimental conditions. Condition 1 is 1 Pa of gas pressure and 60 W of ECR power. Condition 2 is 0.1 Pa of gas pressure and 60 W of ECR power. Condition 2 is chosen because it is closer to ITER NI source conditions where the pressure is very low (0.3 Pa of H_2 gas). The dominant positive ion in the plasma is not the same for these two conditions. At 1 Pa of gas pressure the H_3^+ is dominating while for 0.1 Pa H_2^+ is dominating.

Figure 5.5 shows the NIEDF time evolution in the case of Vs= -20 V and condition 1. The NI yield and NIEDF peak intensity increase with time and reach steady state after about 30 min. All measurements presented hereafter are performed at steady state.

Figure 5.6 (a) and **Figure 5.7** (a) show NIEDFs measured for C12A7 electride surface for different DC bias going from -10 V to -170 V in the case of condition 2 and condition 1 respectively. We get same tendencies for both conditions. As one can see in **Figure 5.8** the NI yield and NIEDF peak intensity increase with bias. Similar signal tendency is observed for condition 2 (see **Figure 5.9**).

Let us note that under ECR condition 1 the positive ion flux is only slightly depending on the bias (Achkasov thesis) and the NI yield can be defined directly as the NI total counts (area below NIEDF).

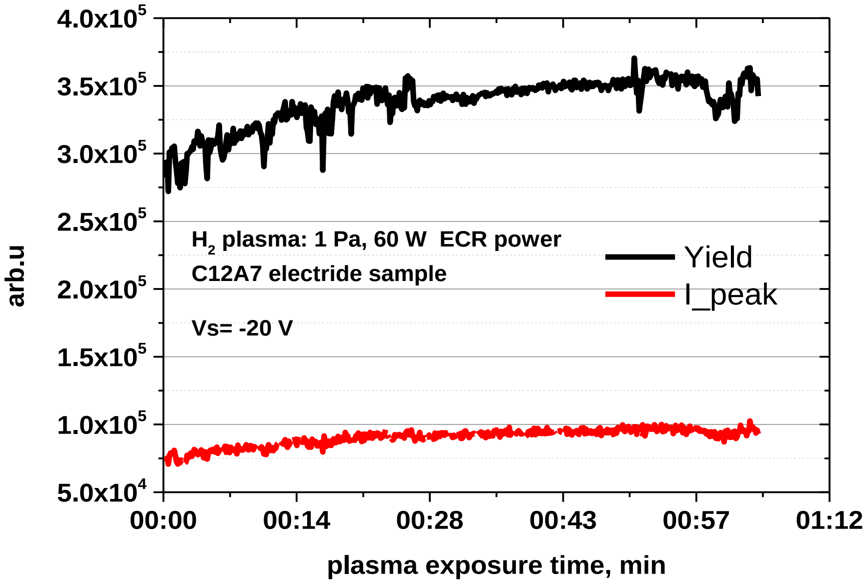

Figure 5.5 Time evolution of NI yield and NIEDF peak intensity measured on C12A7 electride surface biased at -20 V in H_2 plasma (1 Pa, 60 W)

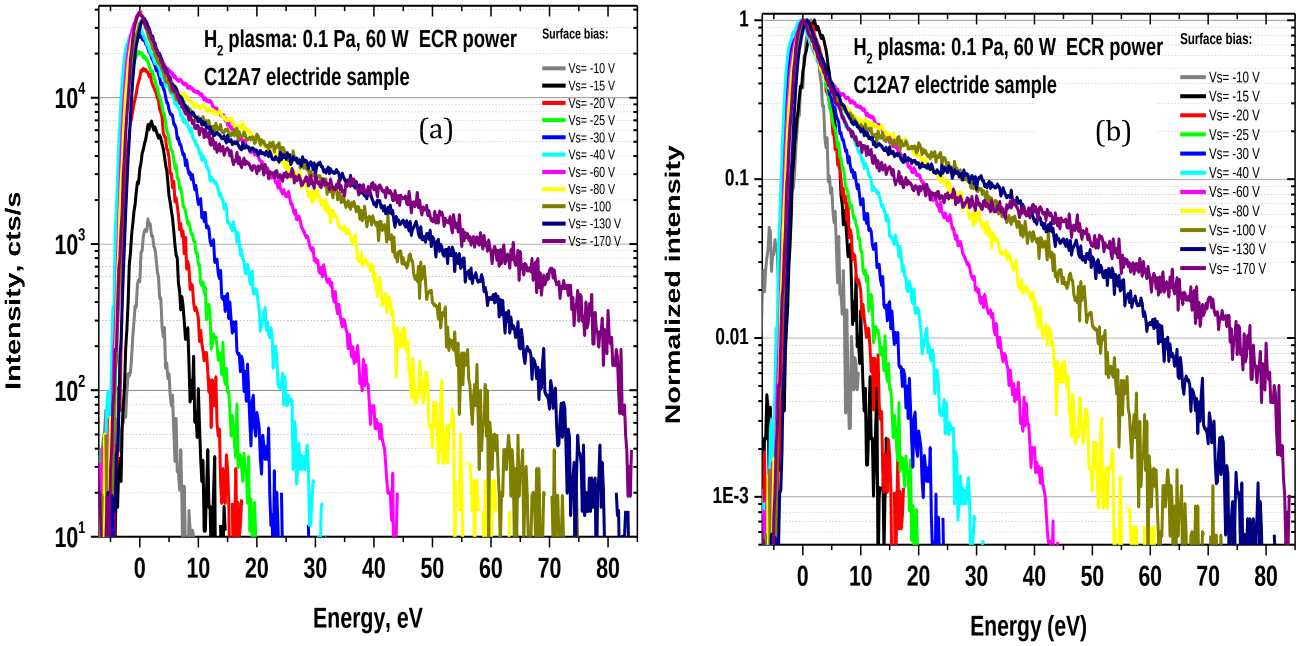

Figure 5.6(a) NIEDF measurements on C12A7 electride surface for different surface bias in H_2 plasma at 0.1 Pa of gas pressure and 60 W of ECR power (b) Normalized NIEDF measurements on C12A7 electride surface for different surface bias in H_2 plasma at 0.1 Pa of gas pressure and 60 W of ECR power

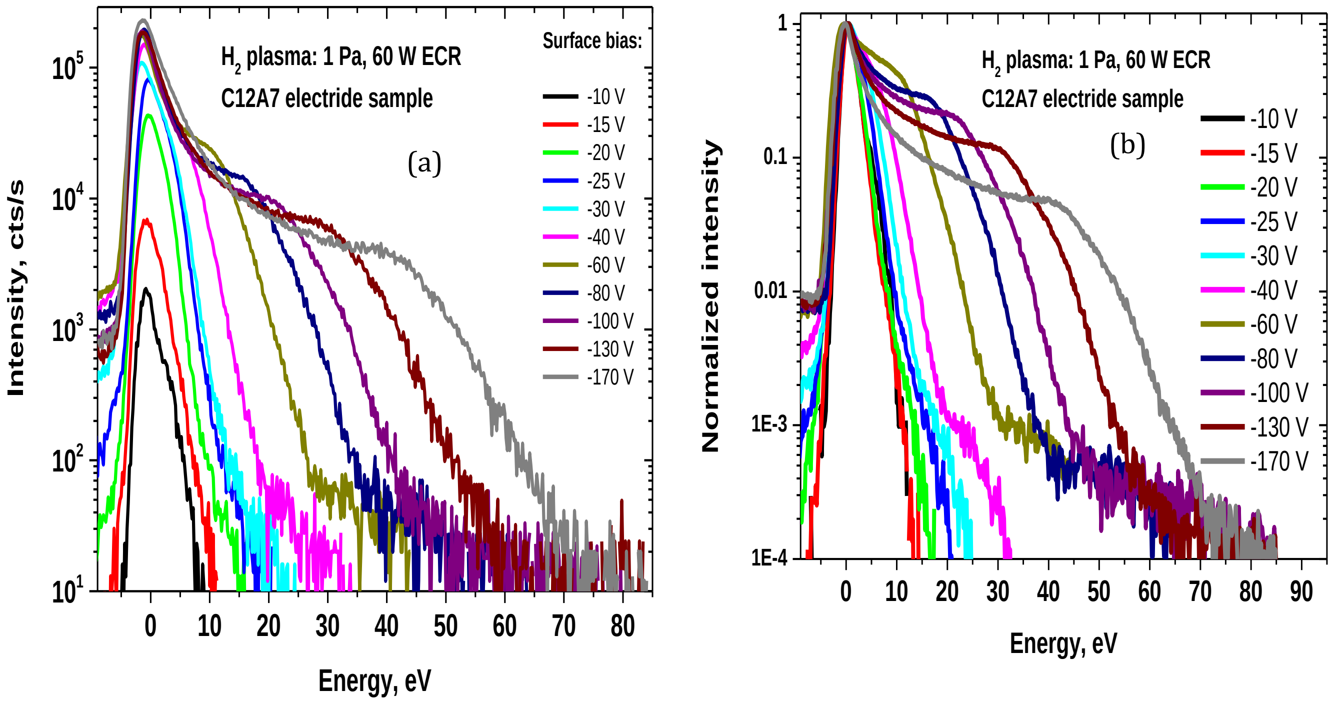

Figure 5.7(a) NIEDF measurements on C12A7 electride surface for different surface bias in H_2 plasma at 1 Pa of gas pressure and 60 W of ECR power (b) Normalized NIEDF measurements on C12A7 electride surface for different surface bias in H_2 plasma at 1 Pa of gas pressure and 60 W of ECR power

The influence of surface bias variation on NI surface production in the case of C12A7 electride surface is similar to the case of HOPG surface (see **Figure 5.8** and **Figure 5.9**). The signal is increasing with time when starting measurements with a pristine material. The positive ion bombardment leads to change on the surface that are favorable state to NI surface production (creation of defects and/or hydrogenation and change of electronics properties). The highest NIEDF peak intensity has been measured at -170 V for HOPG surface, same result is found for C12A7 electride surface where NIEDF peak intensity measured for C12A7 electride surface is 120 times higher than the one measured at -10 V.

It was discussed in **Chapter 3**, that the NI yield increase on HOPG with surface bias can only be explained by an increase of backscattering/ or sputtering yields. The same increase probably occurs also for C12A7 electride surface and it can probably be reinforced by an increase of the ionization probability.

The increase of the NIEDF tail means that mean energy of produced NI increases. This latter observation may be favorable for NI surface production. Indeed, NI surface production on low work function materials is expected to increase with increasing perpendicular velocities of outgoing particles. For HOPG we have demonstrated that energy and angle of outgoing particles do not influence much ionization probability, but this assumption cannot be made a priori for the electride material. Therefore, we must keep in mind that ionization probability might increase with surface bias and explain at least partly the increase of signal.

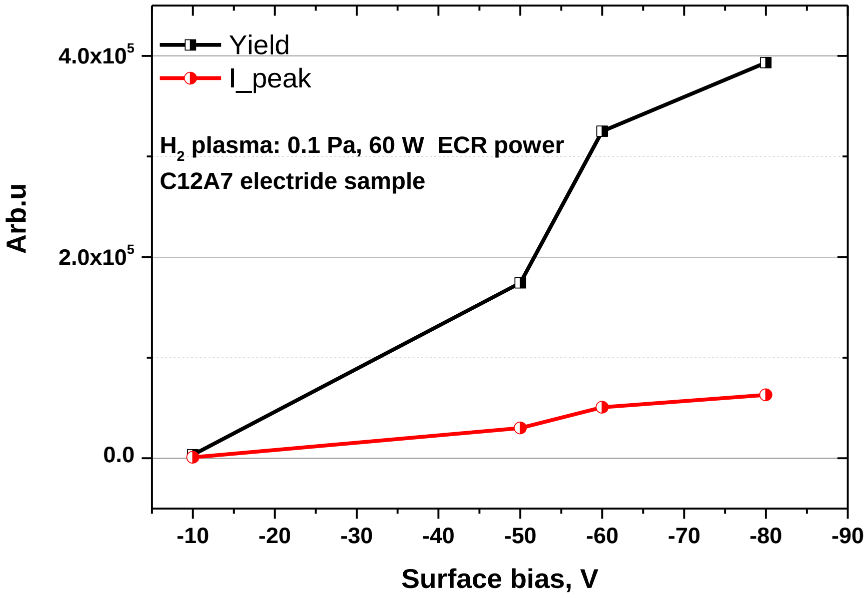

Figure 5.8 NI yield and NIEDF peak intensity measured for different surface bias on two fresh C12A7 electride material samples compared to NI yield and NIEDF peak intensity measured on HOPG sample, H_2 plasma (0.1 Pa, 60 W

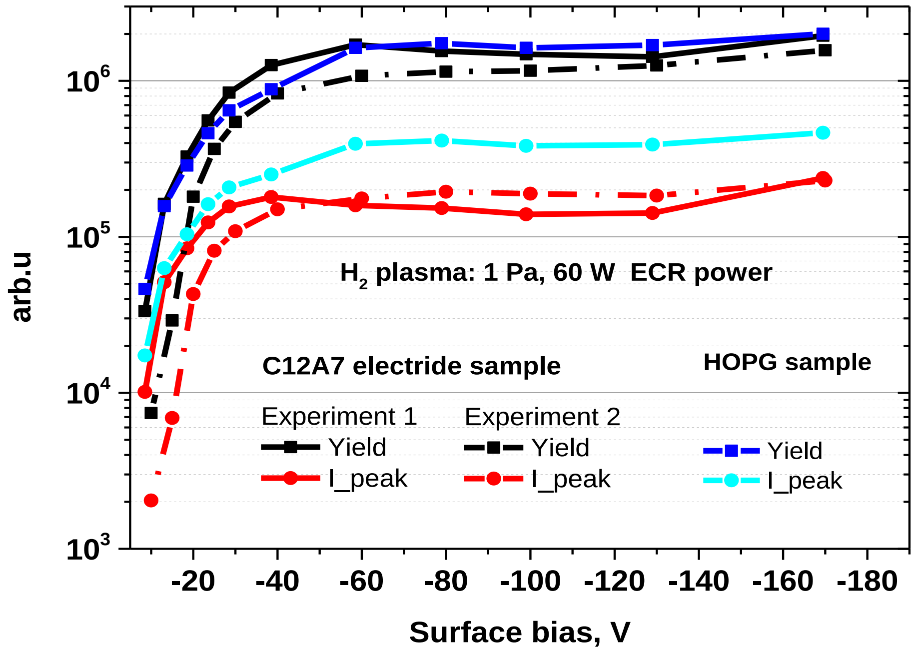

Figure 5.9 NI yield and NIEDF peak intensity measured for different surface bias on two fresh C12A7 electride material samples compared to NI yield and NIEDF peak intensity measured on HOPG sample, H_2 plasma (1 Pa, 60 W)

To investigate further the role of positive ion bombardment we made NIEDF measurements at low bias just after high bias exposure. C12A7 electride surface is first exposed at V_s= -170 V for 10 minutes (the used sample surface in this experiment is not a fresh one and it was exposed to plasma). Then NIEDF measurement is done at V_s = -20 V at steady state (signal takes 5 min to reach steady state as it is shown in **Figure 5.10** and compared to the measured one at Vs= -20 V before high bias exposure as it shown in **Figure 5.11**.

One can see on **Figure 5.10** that NI yield (and peak) is higher at Vs = - 20 V after high bias exposure confirming that, contrary to HOPG, after high energy bombardment the surface is changed in a way to be more favorable to NI surface production. This could be a sign of an increase of the ionization probability. **Figure 5.11** shows that the signal at – 20 V after high bias exposure is increasing with time probably due to a further re-arrangement of the surface. So, we can conclude that surface bombardment by energetic positive ions leads to change of the surface in a way to be more favorable to NI surface production.

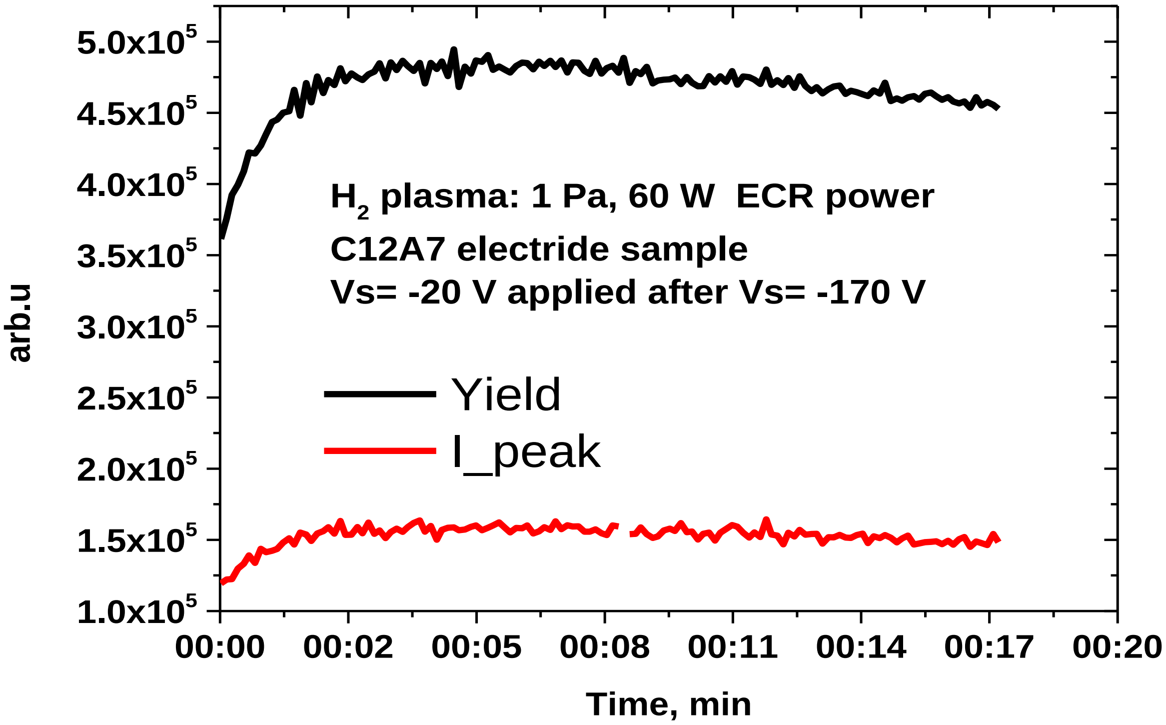

Figure 5.10 Time evolution of NI yield and NIEDF peak intensity measured on C12A7 electride surface biased at Vs= -20 V just after the end of NIEDF acquisition at Vs= -170 V

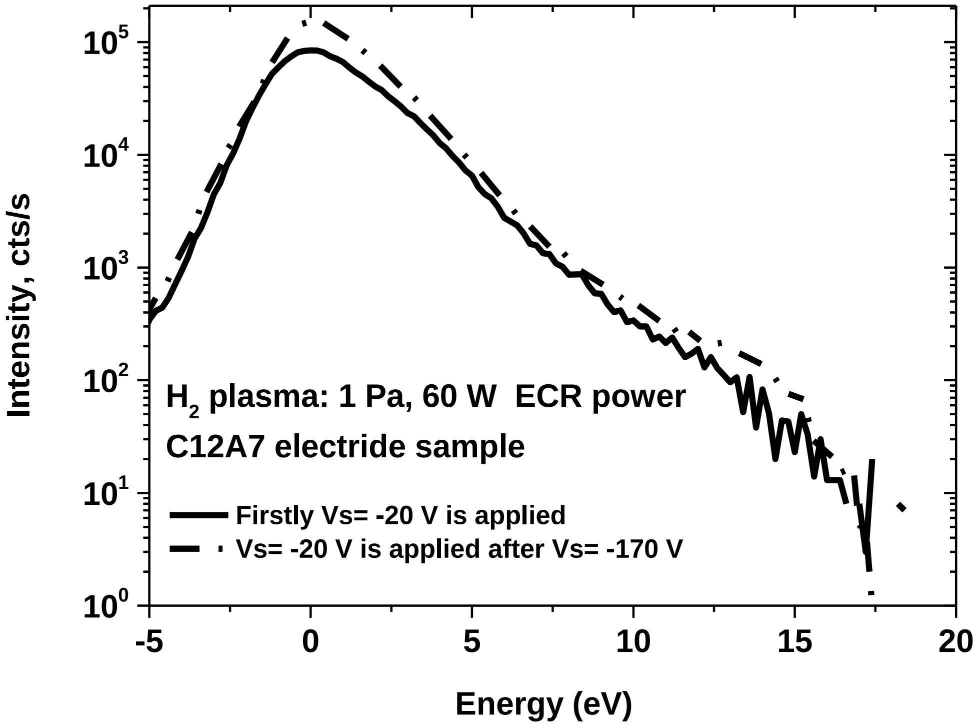

Figure 5.11 Comparison of NIEDF measured for C12A7 electride surface firstly biased at Vs= -20 V (solid line) and NIEDF measured at Vs= -20 V just after -170 V (dotted line)

To investigate the role of the positive ion fluence on the increase of signal at Vs = - 20V, we have varied the exposure time at high bias. First the fresh surface is biased under -20 V and the NIEDF is measured. After the end of this measurement the surface is biased under Vs= -130 V for 10 min and NIEDF is also measured. No evolution of the signal is observed during these 10 min. Then, we come back directly to Vs= -20 V and we do NIEDF measurement. The NIEDF at Vs = -20 V taken before high energy bombardment at -130 V is compared to the measured one after bombardment and is shown in **Figure 5.12**. The signal is increased by a factor 1.5 after 10 min of bombarding at -130 V. This result is identical to the one obtained at – 170V. This experiment has been repeated for different bombardment duration (10 min (red line), 30 min (green line) and 4 h (blue line)) as shown in **Figure 5.12**. As one can see the signal increase is the same for different bombardment duration and 10 min is enough to change surface properties and increase NI surface efficiency.

After 10 min of high energy bombardment the relative contribution of sputtering mechanism to NI production increases compared to the observed one before bombardment. This can be the reason of measuring a signal almost 2 times bigger on bombarded C12A7 electride surface biased at -20 V. The increase of sputtering mechanism contribution to NI surface production can be related to the variation of hydrogen surface coverage. So, we can say that after a high energy bombardment we obtain a C12A7 electride surface with a higher hydrogen coverage than the pristine one.

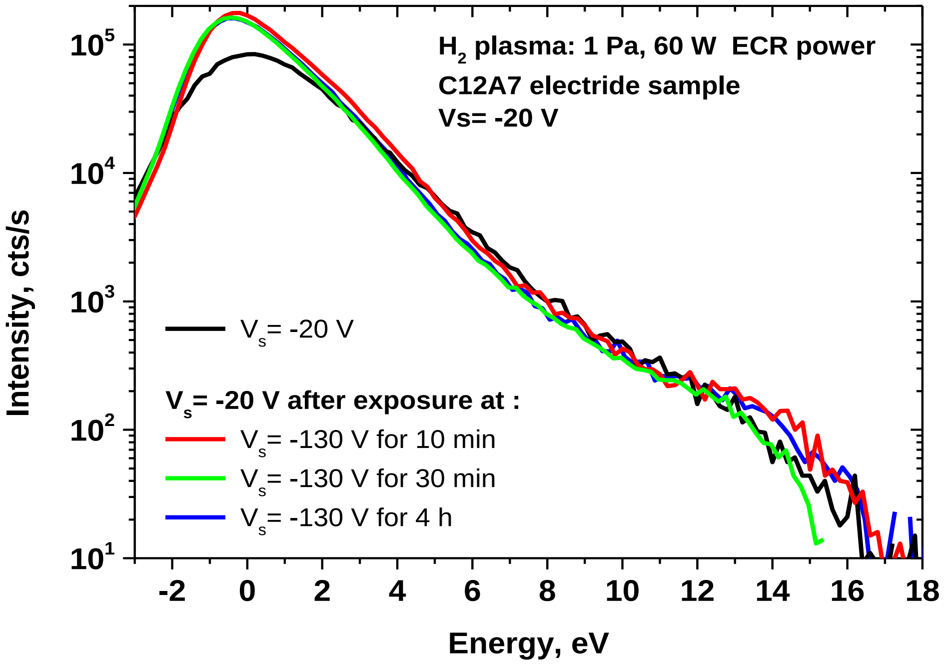

Figure 5.12 Comparison of NIEDF measured for C12A7 biased firstly at Vs= -20 V with the one measured at same conditions after 10 min (red line), 30 min (green line), 4 hours (blue line) of high energy bombardment

This hypothesis is tested hereafter by heating experiment. C12A7 electride surface biased at V_s= -130 V in H_2 plasma is heated from RT to 500°C. We expect that hydrogen desorption from sample surface occurs if we reach a critical value of surface temperature. We have no a priori idea of this critical temperature. The maximum temperature has been chosen in order to prevent damage of our heating system (600°C).

Figure 5.13 (a) shows NIEDF's measured on C12A7 electride surface biased at -130 V for different surface temperature going from RT to 500°C. As one can see in **Figure 5.13** (d) the NI yield and NIEDF peak intensity start decrease with surface temperature above 200°C. The NIEDF peak intensity measured at 44°C and 100°C is almost the same. Therefore, we can conclude that in our experimental conditions the threshold temperature for hydrogen desorption is around 200°C. As shown in **Figure 5.13** (d), NI surface production on C12A7 electride surface behave in a very similar way to NI surface production on HOPG when increasing surface temperature. This is reinforcing the relevance of interpretations based on HOPG analogy. In **Figure 5.13** (d), the significant decrease of NIEDF signal at 300°C is probably caused by the decrease of the amount of hydrogen on the surface. The signal continues its decrease for higher temperature (350°C, 400°C, and 500°C). In this temperature range the majority of NI are probably produced by backscattering mechanism as shown by the high increase of the tail contribution compared to the peak contribution. (**Figure 5.13** (b)). The shape of NIEDFs measured at different temperature is not the same. By analogy with HOPG, the change of NIEDF shape is related to the change of relative contribution of NI surface production mechanisms. As one can see in **Figure 5.13** (b), the normalized NIEDF measured at 500°C has a larger tail than the measured one at 44°C indicating a decrease of sputtering contribution and an increase of backscattering one.

The variation of hydrogen negative ion signals after baking of the sample was also measured. Before the baking, several hours of biasing experiment in an ECR plasma of 60 W had been carried out (1 Pa, 60 W, V_S = - 130 V). Then, 520° C baking was applied in vacuum for 50 min. During heating, a mass scan of hydrogen H_2 and H_2O variation was recorded, and the amount of hydrogen increased 3 times during heating and the amount of H_2O increase 24 times during heating, after cooling down, an ECR hydrogen plasma was ignited (1 Pa, 60 W, V_S = - 20 V). In **Figure 5.14** , the time behaviors of NI yield (total negative ion) produced and NIEDF peak intensity of the spectra right after the application of – 20 V bias voltage are shown by black and red lines, respectively. The negative ion peak intensity increased by a factor of 11.7 the first 5 min, and it increased then slowly. For comparison purpose **Figure 5.14** also presents the time behaviors of total negative ion produced and peak current of the spectra right after the application of – 20 V bias voltage without any baking. In this case, the sample has been exposed to a long ECR plasma exposure at 1 Pa, 60 W, V_S = - 130 V before the measurements at V_s = - 20 V. We can see that in this case the peak intensity increases only by a factor 1.7 instead of 11.7. It clearly shows that hydrogenation of the material is of major importance for efficient NI production on C12A7 Electride surface. Hydrogenation favors NI production through sputtering but might also change electronic properties of C12A7 electride surface. At Vs = - 130 V the strong contribution of sputtering to NI production is obvious if one refers to NIEDF obtained with HOPG material. At low bias, it is harder to conclude if hydrogenation is enhancing sputtering. If one refers to **chapter 3**, sputtering contribution was assumed to be low at Vs = - 20V for HOPG material. As explained in **chapter 4**, the shift of NIEDF peak position is an indication of surface bias variation. So, we can conclude that surface conductivity is temperature dependent, and that C12A7 electronic properties are changing with temperature and so with hydrogen coverage (**Figure 5.13** (c)). However, we have not eliminated the possibility that hydrogenation changes material properties. Indeed, it can be observed on Figure 21 that NIEDF peak position is shifted from its initial position at room temperature when increasing surface temperature. **Figure 5.13** (c) shows the shift of NIEDF peak position as a function of surface temperature.

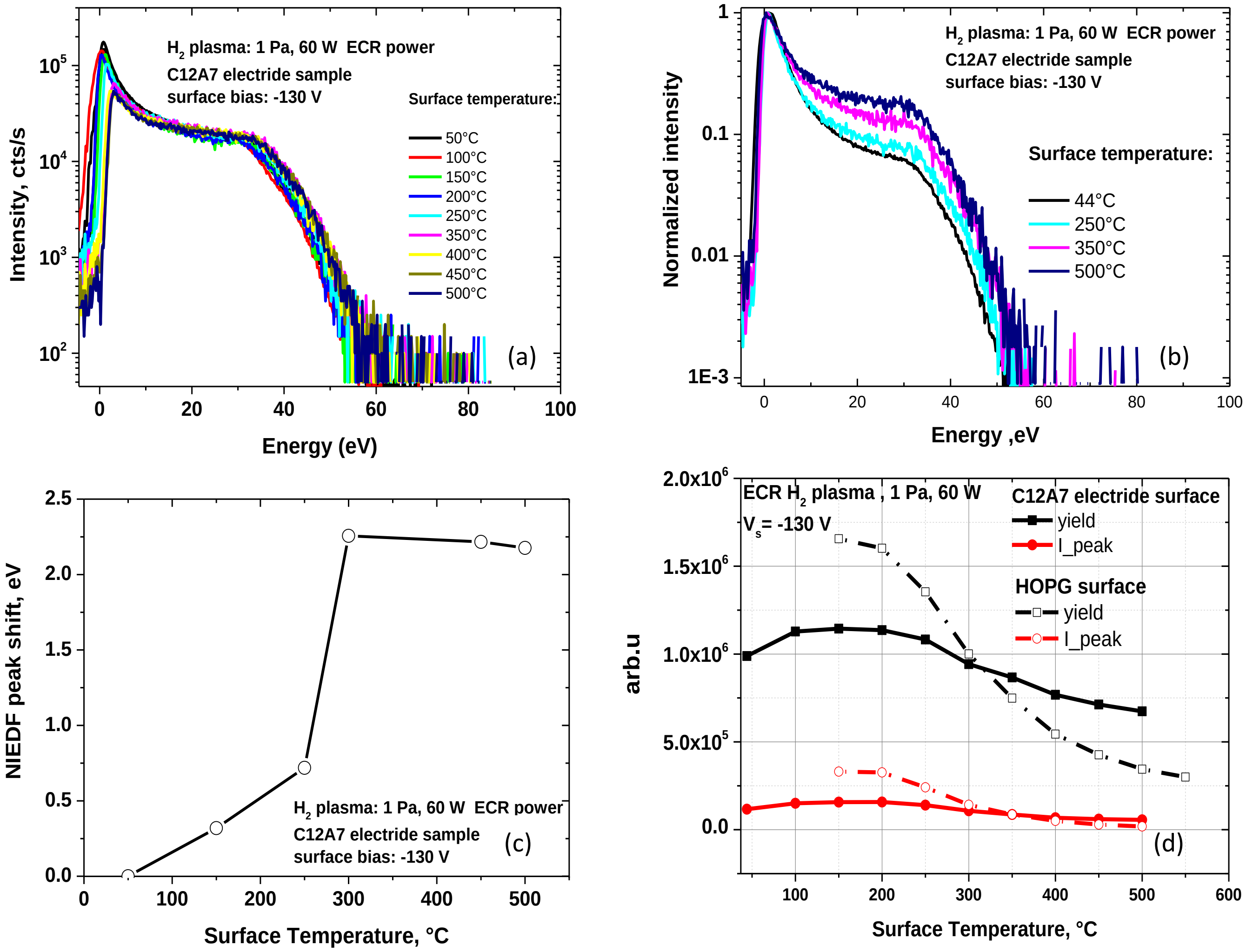

Figure 5.13(a) NIEDF measured in H_2 plasma on C12A7 electride surface biased at -130 V for different surface temperature (b) Normalized NIEDF measured in H_2 plasma on C12A7 electride surface biased at -130 V for different surface temperature (c) NIEDF peak shift measured in H_2 plasma on C12A7 electride surface biased at -130 V for different surface temperature (d) NIEDF peak intensity and NI yield measured in H_2 plasma on C12A7 electride and HOPG surfaces biased at -130 V for different surface temperature .

To study further the importance of the sputtering mechanism, normalized energy spectra measured at steady state of hydrogen negative ions from the C12A7 electride bombarded by hydrogen and by argon ions were compared as shown in **Figure 5.15.**

In both measurements, the target was pre-treated with an exposure to hydrogen ECR plasma (1 Pa H_2, 60 W) at Vs= -130 V for 10 min. Then, hydrogen plasma at 1 Pa, 60 W, or argon plasma at 0.1 PA, 30 W for different surface bias (Vs= -20 V, -40 V, -60 V, -80 V) were performed and NIEDFs were recorded. A dominant peak shown in the low energy region below 10 eV was observed for different surface bias.

The sputtering of pre-implanted hydrogen particles in C12A7 electride surface can be the origin of this dominant peak below 10 eV. This experimental observation can be a sign of non-negligible sputtering contribution at low bias Indeed, in Ar plasma the majority of negative ion H^- are produced by sputerring and a minority is produced by the backscaterring of hydrogen impurities. So, this analysis cannot be accurate if we don't take into account the contribution of hydrogen impurities in H^- production during Ar plasma experiment.

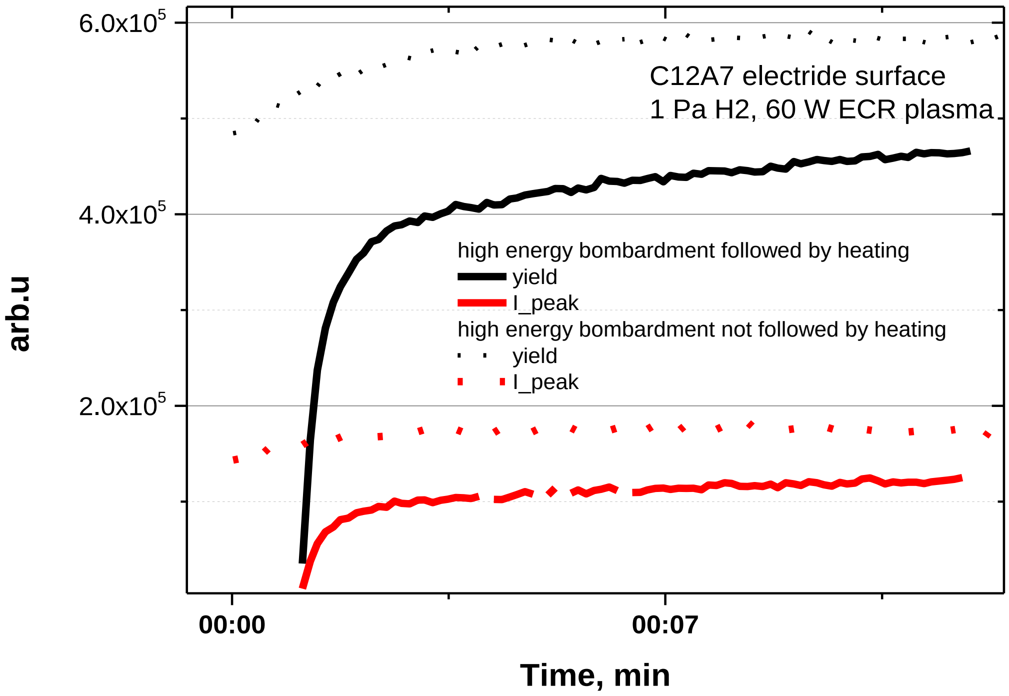

Figure 5.14 Time evolution of the negative ion yield after 10 min of high energy bombardment followed by heating in vacuum or without heating in vacuum

To eliminate the contribution of H impurities in H^- production during Ar plasma experiment, a precise procedure was followed. First, the target was pre-treated with an exposure to hydrogen ECR plasma (1 Pa H_2, 60 W) at Vs= -130 V for 10 min. Second, the target was putted in the load lock system, outside the diffusion chamber (plasma doesn't reach load lock system). An Ar plasma was ignited under same previous conditions (0.1 Pa, 30 W of ECR power), the chamber is cleaned by Ar plasma, and a PIEDF scan of hydrogen positive ions is done in parallel. After 30 min of Ar plasma ignition in diffusion chamber, H^+, H_2^+ and H_3^+ signals decrease and reach background value; hydrogen impurities are almost removed from Ar plasma.

After ensuring removing hydrogen impurities, the sample is biased at Vs= -60 V, and directly immersed in the diffusion chamber, the time evolution of NIEDF signal is measured and it is compared to the measured one without cleaning, comparison is shown in **Figure 5.16.**

As one can see in **Figure 5.16**, when hydrogen impurities are not removing from Ar plasma, the NI peak intensity has a starting value (at t= 0) 10 times higher than the measured one when hydrogen impurities are removed, this value decrease quickly with time and reach a constant value after 7 min of surface bombardment by Ar plasma. This is not the case for the signal measured after removing hydrogen impurities from Ar plasma, where the signal continues to decrease slowly with time (the peak intensity is 2 times lower after surface bombardment by Ar plasma). Therefore, the impurities cannot be neglected in our measurement and must be taken into account while understanding results. In order to get a direct information about impurities contribution to NI surface production in Ar plasma, the normalized NIEDF signal measured in Ar plasma on C12A7 surface biased at -60 V, in the case of chamber cleaning is compared to the measured in the case of non-removing of hydrogen impurities. The comparison is done for NIEDF measured at the start of time evolution measurement and at its end (see **Figure 5.17**). Normalized NIEDF measured in Ar plasma with and without cleaning are always located below 10 eV.

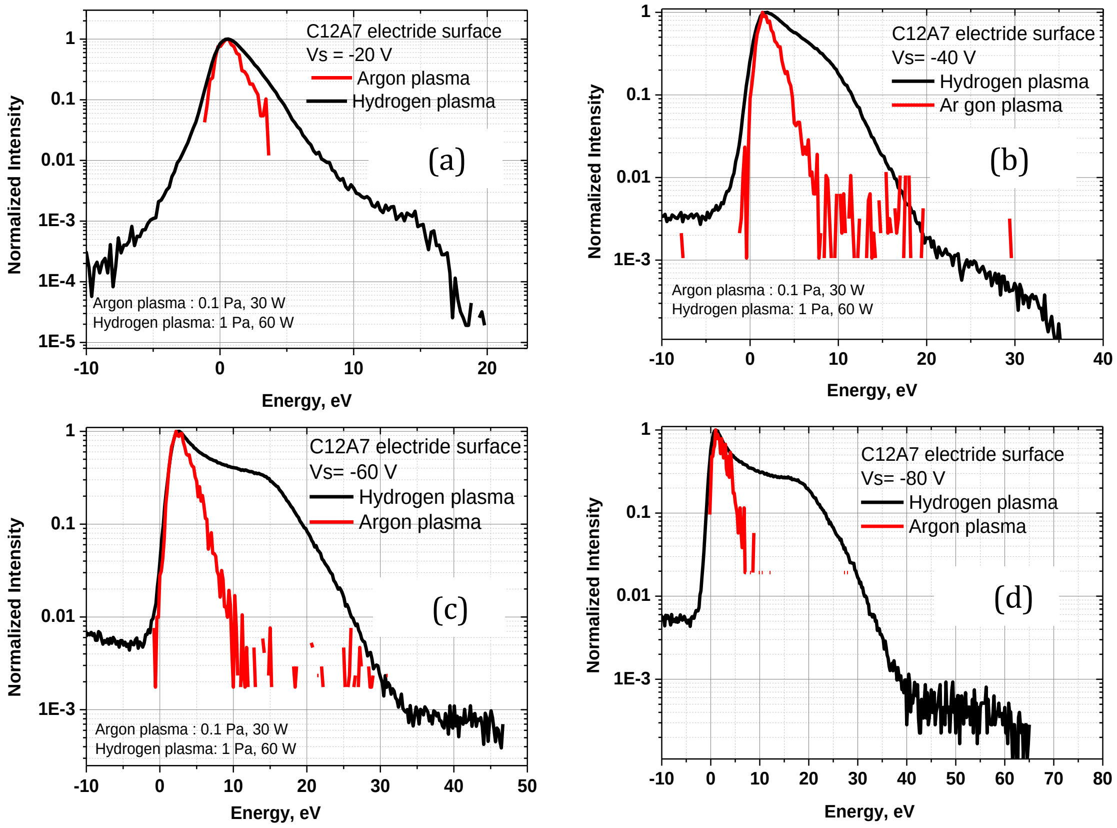

Figure 5.15 Comparison of the normalized NIEDF spectra measured in an ECR Ar plasma (red line) under 0.1 Pa and 30 W, and in ECR H_2 plasma (black line) under 1 Pa 60 W at (a) V_s= -20 V (b) V_s= 40 V (c) V_s= -60 V (d) V_s= -80 V after the sample was treated for 10 min in an ECR H_2 plasma (1 Pa 60 W and V_s= -130 V)

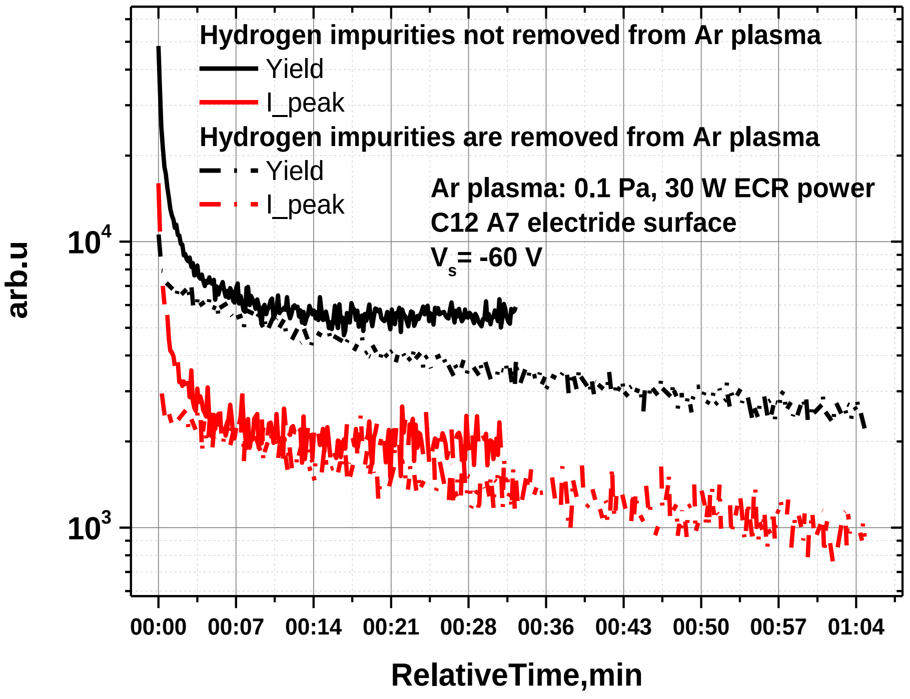

Figure 5.16 Time evolution of the negative ion yield after 10 min of high energy bombardment followed by cleaning in vacuum or without cleaning in Ar plasma

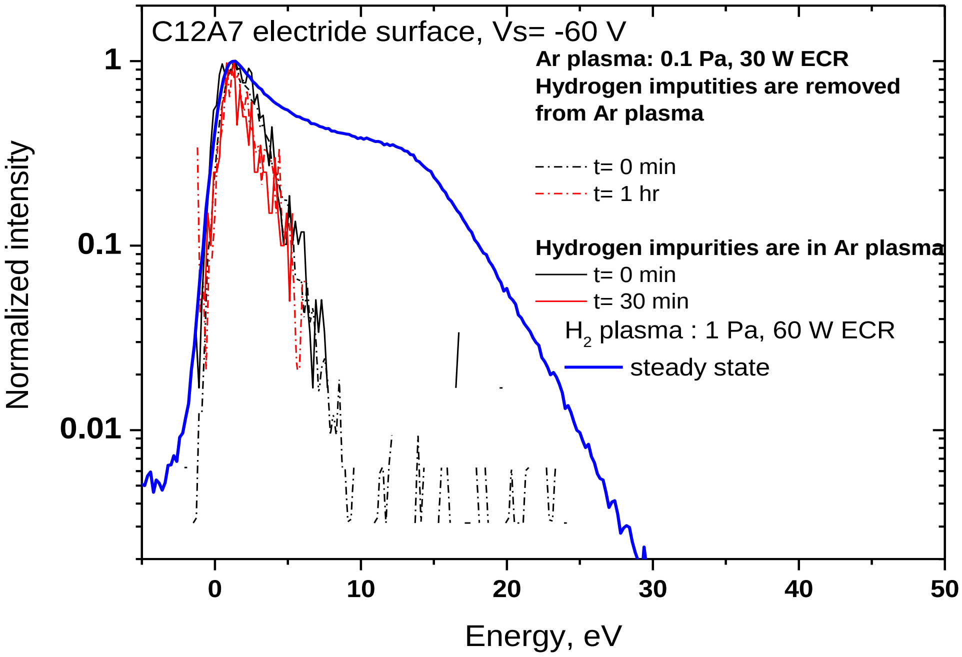

Figure 5.17comparison of normalized NIEDF measured at t= 0 and at the end of time evolution measurement showed in Figure 5.16 with cleaning and without cleaning in Ar plasma. The normalized NIEDF measured in H2 plasma is compared to normalized NIEDFs measured in Ar plasma.

As a conclusion, the sputtering mechanism and/or the surface hydrogenation has an important contribution to NI surface production on C12A7 electride surface. This contribution can be increased by high energy bombardment which probably favor hydrogen implantation or adsorption

5.4.2Variation of NI surface production efficiency with surface bias mode

In **chapter 4,** the method of pulsed bias was presented. It is developed to enable the study of NI production on surfaces of insulating materials. The study of NI production on insulator surface is not the only advantage of this technique. Indeed, pulsed mode bias allows biasing a fresh sample for a very short exposure time and therefore studying surface modifications due to PI bombardment. In this section, the total negative ion signal is measured on C12A7 electride surface (conductor surface) in pulsed mode and compared to DC mode for different temperature. The aim of this comparison is to conclude the effect of plasma exposure time on C12A7 electride surface state and on its electronic properties variation during ion bombardment.

The pulsed DC bias measurement is performed on C12A7 electride surface in H_2 plasma at different temperature starting from RT to 600°C under usual experimental conditions: 1 Pa, ECR power of 60 W. The NIEDF were measured in the case of V_a= -130 V using optimized pulsed bias parameters: f= 1 kHz, T_{pulse}= 10 µs, T_{acq}=8 µs, T_{delay}=12.5 µs.

As a starting point, NIEDF measured at RT were compared for pulsed mode and DC mode for fresh samples of C12A7 electride. NIEDF measurement in pulsed mode and DC mode are done on two fresh sample, NIEDF measurements are done in steady state. The comparison of NIEDF for constant and pulsed bias at RT shown in **Figure 5.18** reveals that the distribution maximum has increased by nearly two times for C12A7 electride surface in pulsed mode. This increase of total negative-ion signal measured at room temperature between DC and pulsed mode was observed previously for the three tested materials: HOPG, MCBDD and MCD

NIEDF measurements versus surface temperature in pulsed bias mode is shown in **Figure 5.19**. One can notice the decrease of the NI signal with surface temperature down to a saturation at 200°C. The decrease of the signal below 200°C is attributed to the decrease of hydrogenation, leading to a decrease of the negative ion creation by sputtering, and probably to change of electronic properties, which may become less favorable to surface ionization. The signal saturation after 200°C can be related to a complete desorption of hydrogen from surface (the NI yield is saturated, and the relative contribution of different surface production mechanism is unchanged for T> 200°C) and a constant ionization probability (the NIEDF peak intensity is saturated for T°C> 200°C).

To improve our understanding of plasma exposure effect on electride surface, results are compared to HOPG and diamond surfaces. Concerning HOPG, NIEDF measured at room temperature are different in pulsed and DC mode where an increase of the signal (factor 2) is observed due to the higher material hydrogenation. At higher temperature, as shown previously, hydrogen is desorbed from HOPG surface and the graphite material is recovered, leading to a strong decrease of the signal. A similar increase is observed at room temperature for C12A7 electride surface. However, one can see in **Figure 5.20** that the results are different from the ones observed on HOPG at higher temperature. An increase of the signal by a factor 2 for the whole range of temperature (starting from room temperature to 600°C) is measured in pulsed mode and the NI signal reaches a saturation level after 200°C.

It is observed that the pulsed bias mode leads to higher negative ion signal for all materials at room temperature. For all materials, the hydrogenation of the top layer seems higher in pulsed mode than in DC mode. However, this is not enough to explain the increase observed for the whole range of temperature on electride surface. This can be attributed to the weak number of defects created on electride surface at low duty cycle. As it was discussed previously for diamond, the electride surface biased in pulsed mode is close to the pristine surface which electronics properties are probably favorable to surface ionization of outgoing hydrogen particles.

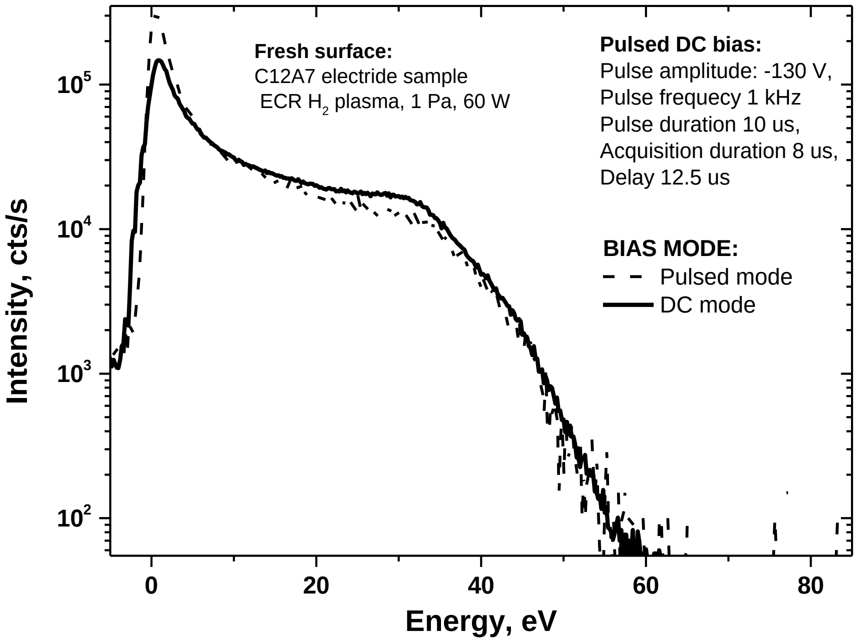

Figure 5.18 comparison of NIEDF measured for constant and pulsed bias at -130V (solid and dotted curves correspondingly) on C12A7 electride surface.at RT.

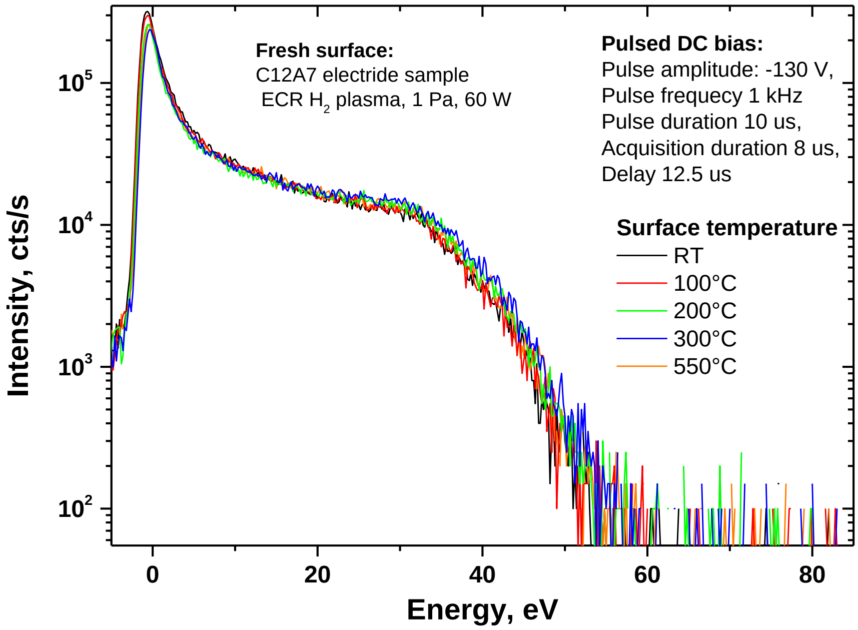

Figure 5.19 NIEDF measured on C12A7 electride surface as a function of sample surface temperature for pulsed bias mode at Vs = -130 V

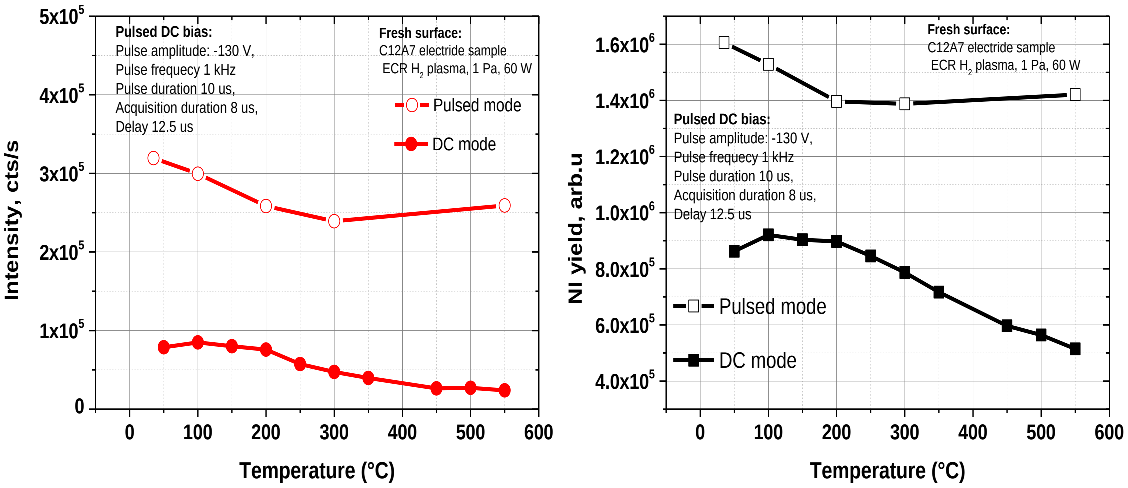

Figure 5.20 NIEDF peak intensity (red color) and NI yield (black color) dependence on surface temperature for C12A7 electride surface for constant bias (solid symbols) and pulsed bias (empty symbols)

5.5 Potential of using C12A7 electride surface in non cesiated NI source

As the absolute production rate of negative hydrogen ions (H^-) on C12A7 cannot be obtained with the mass spectrometer, we have compared it with the one from a clean molybdenum surface to get an idea of the figure of merit of this material. Wada et al.[117] measured the work function dependence of the H- production rate of a cesiated molybdenum surface[118] immersed in a hydrogen plasma, at bias voltage of -100, -200 and -300 V. Using a pseudo exponential work function dependence, they obtain a ratio between H^- yield from the cesiated molybdenum surface with the lowest work function and from a clean molybdenum surface (4.3 eV) of approximately 40 at 100 V. As it shown in **Figure 5.21**, the ratio of the total H^- yield from a C12A7 electride surface bombarded at -80 V to that from a clean molybdenum surface is approximately 10. This ratio increases to 50 at bias voltage Vs= -20 V. This value is consistent to previous indirect measurement done in Doshisha University. In this experiment the electric current due to negative hydrogen ions leaving the C12A7 surface upon the exposure to atomic hydrogen (H^0) flux was measured. This current was at a similar level to that obtained from a low work function bi alkali covered molybdenum surface.

Let us note that measurements in **Figure 5.21** is done an RF plasma under condition: 2 Pa D2, 250 W of RF power. The dominant ion is H_3^+. Plasma parameters are: T_e is almost 3 eV and ne is almost $10^8/cm^3$.

Together with the present direct observation of the negative hydrogen ions, it is likely that this material has a potential to produce a similar level of negative ions as that of the cesiated molybdenum surface in an H^- **source** where a plasma grid is bombarded with relatively low energy particles.

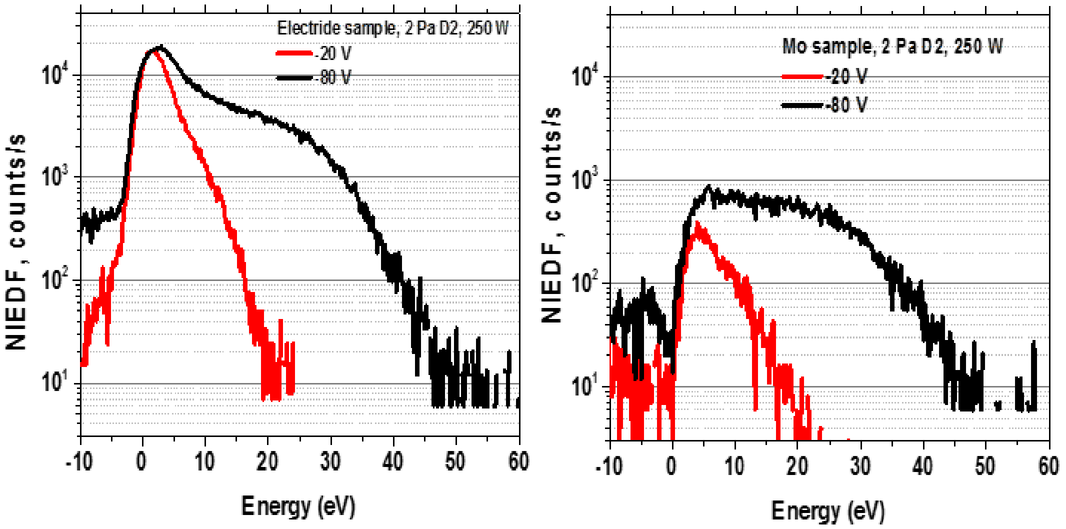

Figure 5.21 Negative ion spectrum from a C12A7 electride and molybdenum in RF plasma. The red and black lines show those obtained when the target bias was -20 *V* and -80 V, respectively.

Conclusion

The negative ion surface production on C12A7 electride surface is studied versus bias amplitude, bias mode and surface temperature. It has been shown that for C12A7 electride surface that the sputtering mechanism and/or the surface hydrogenation has an important contribution to NI surface production on thie material surface. This contribution can be increased by high energy bombardment which probably favor hydrogen implantation or adsorption

The analyzed novel C12A7 electrie material is air stable, mechanically robust, and machinable, with potentials to be used as a production surface of cesium free negative ions sources.

General Conclusion

This thesis is a contribution to the understanding of NI surface production in H_2/D_2 plasmas. In the first section of the manuscript, the modeling of negative ions energy and angle distribution function of negative ions emitted from the surface has been presented. In second section the impact of positive ion energy on carbon surfaces production of negative ion has been discussed and analyzed. In the third section, the pulsed bias approach used to extend our experimental study to insulator surface is discussed. In the fourth section, the study of negative ion surface production on new interesting material (C12A7 electride) is presented using knowledge acquired with materials previously studied.

Modeling of NIEDF (Negative Ion Energy Distribution Function) performed previously has shown remarkable agreement with experiment for HOPG confirming that the negative ion ionization probability is probably constant whatever the particle angle and energy of emission. This has also validated the choice of SRIM to provide the correct initial distribution for carbon materials. An improvement of SRIM calculation has been done here by considering the realistic energy distribution function of positive ions impacting on the surface. A new method of calculation of transmission function is also proposed. The method has been validated here, and it is faster than the method used previously.

In second section, we focused on the analysis of change in negative ion surface production yields on carbon surface with positive ion energy. It is shown that defect creation by positive ion bombardment has opposite effects on diamond and graphite. A special focus is put on low energy exposure as it is relevant to low ion/ atom impact energies on cesiated grid in real NI source for NBI systems. We have studied the possibility to self-extract the ions at low bias, and extraction was ensured even at a voltage difference of 10 V between sample surface and mass spectrometer. The experimental behavior of NI yield versus the surface bias was analyzed using modeling of ion transport and collection. However, SRIM calculations at low energy in the range of 10 eV are not accurate and numerical solution of the problem could not be obtained. Nevertheless, it t was showed that the surface state of HOPG is probably similar at all bias, only the depth of modified layer is changing. Indeed, due to the layer structure of HOPG, when positive ion energy is increased a new layer is reached and fast modified. For MCBDD, the accumulation of impacts at increasing energy slowly destroy the hard structure of the diamond material and the signal decreases.

In third section, the method of pulsed bias was developed to enable the study of NI production on surfaces of insulating materials. The idea is to apply a brief DC bias pulse on the surface and perform a synchronized negative-ion acquisition. Between pulses the surface is let floating to ensure unload. The present technique has enabled to study NI surface production on MicroCrystalline Diamond (MCD) for a temperature range starting from RT to 750°C. The pulsed-bias was studied by measuring sample current and surface voltage versus time and comparing them to a simple electrical model. . It has been shown that the MCD sample behaves in plasma as a RC circuit loaded by a constant current (the positive ion saturation current) during the pulse. A low duty cycle is required (<10 %) to ensure between bias pulses a complete removal of charges accumulated during the pulse. A pulse duration of 10 µs with a repetition frequency of 1 kHz allows for measurements on MCD material under the present low positive-ion flux experimental conditions.

The total negative-ion signal strongly increases between DC and pulse mode, for the three materials tested: HOPG, MicroCrystalline Boron Doped Diamond and MCD. Factors from 1.5 (HOPG) to around 10 have been observed and the highest negative-ion yield ever measured under the present experimental conditions have been obtained in pulsed mode at high temperature using diamond materials. The results bring us to the conclusion that in pulsed bias case the diamond surface is less degraded and more hydrogenated, which is favorable for NI surface production. This situation is similar to biasing a fresh diamond sample with constant DC bias for a very short exposure time. Most probably, under ion bombardment, diamond samples lose their attractive electronic properties. With a very short exposure time, or using the pulsed bias technique, it is possible to maintain electronic properties close to the pristine diamond ones and obtain higher NI yields.

Pulsing the bias at low duty cycle is a solution only for fundamental studies and could not be used in a real NI source due to the low time average negative-ion production. However, the present study shows that electronic properties of diamond are favorable for NI production, and diamond placed in appropriate experimental conditions could be potentially interesting for NI surface production as also shown in beam experiments[**Erreur ! Signet non défini.**]. Considering the overall result of the pulsed bias measurements, one can conclude that to optimize the NI yield on diamond, one has to work with a less degraded surface. This can be obtained by rising the surface temperature to 400°C–500°C which allows restoring intrinsic properties of diamond. The less degraded surface state can also be obtained by reducing positive ion energy.

A new material with interesting electronics properties for NI surface production has been studied in the last section. The knowledge acquired on NI production mechanisms and surface state influence on NI surface production was used to understand negative ion surface production on nanoporous $12CaO.7Al_2O_3$ electride surface or C12A7 electride surface for short. This material characterized by a low work function (2.4 eV) was compared to our reference material HOPG, and our reference material for low work function metals Gadolinium.

C12A7 is a candidate to enhance negative-ion surface production in negative-ion sources. Therefore, we have studied NI surface production as a function of bias voltage, including low biases which are relevant for NI sources. It has been shown that the sputtering mechanism and the surface hydrogenation has an important contribution to NI surface production on this material surface. The hydrogenation can be increased by high energy bombardment preceding measurements at low energy. Hiogh energy bombardment probably favors hydrogen implantation or adsorption.

The analyzed novel C12A7 electride material is air stable, mechanically robust, and machinable, with potentials to be used to enhance surface production in cesium-free negative ions sources.

As a perspectives, the absolute NI yield in our experimental setup phisis must be measured in order to compare it to NI yield produced in a real NI source. An in situ surface diagnostic must be installed on the experimental device in order to have an accurate idea about surface state during plasma exposure.

Bibliography

[1] Irving Langmuir, '"Method and Apparatus For Electric- Arc Welding"', 4 February 1930, https://patentimages.storage.googleapis.com/9b/ce/ac/065dd3f59b8475/US1746196.pdf.

[2] Paul K. Chu, 'Applications of Plasma-Based Technology to Microelectronics and Biomedical Engineering', *Surface and Coatings Technology* 203, no. 17–18 (June 2009): 2793–98, https://doi.org/10.1016/j.surfcoat.2009.02.131.

[3] Hyun Woo Lee et al., 'Atmospheric Pressure Plasma Jet Composed of Three Electrodes: Application to Tooth Bleaching', *Plasma Processes and Polymers* 7, no. 3–4 (22 March 2010): 274–80, https://doi.org/10.1002/ppap.200900083.

[4] Michael Keidar, 'Plasma for Cancer Treatment', *Plasma Sources Science and Technology* 24, no. 3 (20 May 2015): 033001, https://doi.org/10.1088/0963-0252/24/3/033001.

[5] Robert W. Conn, '"Nuclear Fusion"', Last Updated 2018.

[6] 'Https://Www.Euro-Fusion.Org/Fusion/Fusion-on-the-Sun/.', n.d.

[7] Craig Freudenrich, 'How Nuclear Fusion Reactors Work', 4 August 2015.

[8] 'HyperPhysics. Nuclear Fusion,August 4, 2015', n.d.

[9] Dmitry Kogut, 'Study Of Wall Conditioning in Tokamaks with Application to ITER. Doctoral Thesis', 2014.

[10] G. Khatri, '"Toroidal Equilibrium Feedback Control at EXTRAP T2R", Doctoral Thesis', 2010.

[11] T.J.M. Boyd and J.J Sanderson, 'The Physics of Plasma', 2003.

[12] James E Huheey, Ellen A Keiter, and Richard L Keiter, '"Inorganic Chemistry: Principles of Structure and Reactivity",4th Edition. New York: HarperCollinsCollege Publisher', 1993.

[13] 'CRC Handbook of Chemistry and Physics, 88th Ed Editor-in-Chief: David R. Lide (National Institute of Standards and Technology) CRC Press/Taylor & Francis Group: Boca Raton, FL. 2007. 2640 Pp. $139.95. ISBN 0-8493-0488-1.', *Journal of the American Chemical Society* 130, no. 1 (January 2008): 382–382, https://doi.org/10.1021/ja077011d.

[14] Kostiantyn Achkasov, '"Evaluation of Beam Emission Spectroscopy as a Diagnostic Tool for The TJ- II Stellarator." Master Thesis, Erasmus Mundus FUSION-EP Program', 2012.

[15] John Wesson, 'ToKamaks (Clarendon Press, Oxford, England, 2004).', n.d.

[16] A. Chutjian, A. Garscadden, and J.M. Wadehra, 'Electron Attachment to Molecules at Low Electron Energies', *Physics Reports* 264, no. 6 (January 1996): 393–470, https://doi.org/10.1016/0370-1573(95)00022-4.

[17] John Wesson, '"The Science Of Jet." 2nd Edition, JETJoint Undertaking, Abingdon', n.d.

[18] 'EFDA-JET (NowEUROfusion)', n.d.

[19] 'Https://Www.Iter.Org/Proj/Inafewlines', n.d.

[20] R. J. Hawryluk et al., 'Confinement and Heating of a Deuterium-Tritium Plasma', *Physical Review Letters* 72, no. 22 (30 May 1994): 3530–33, https://doi.org/10.1103/PhysRevLett.72.3530.

[21] A. Simonin, '"Towards an Efficient Neutral Beam Injection System for the Future Thermonuclear Fusion Reactors". Memoire de HDR', 2013.

[22] T. Asai et al., 'Experimental Evidence of Improved Confinement in a High-Beta Field-Reversed Configuration Plasma by Neutral Beam Injection', *Physics of Plasmas* 7, no. 6 (June 2000): 2294–97, https://doi.org/10.1063/1.874121.

---

[23] K. Watanabe et al., ‘Development of a Large Volume Negative-Ion Source for ITER Neutral Beam Injector’, *Review of Scientific Instruments* 73, no. 2 (February 2002): 1090–92, https://doi.org/10.1063/1.1431422.

[24] R. S. Hemsworth, A. Tanga, and V. Antoni, ‘Status of the ITER Neutral Beam Injection System (Invited)’, *Review of Scientific Instruments* 79, no. 2 (2008): 02C109, https://doi.org/10.1063/1.2814248.

[25] L. Schiesko et al., ‘First Experiments with Cs Doped Mo as Surface Converter for Negative Hydrogen Ion Sources’, *Journal of Applied Physics* 118, no. 7 (21 August 2015): 073303, https://doi.org/10.1063/1.4928861.

[26] P Franzen et al., ‘Magnetic Filter Field Dependence of the Performance of the RF Driven IPP Prototype Source for Negative Hydrogen Ions’, *Plasma Physics and Controlled Fusion* 53, no. 11 (1 November 2011): 115006, https://doi.org/10.1088/0741-3335/53/11/115006.

[27] A.R.P Rau, ‘"Astronomy-Inspired Atomic and Molecular Physics”, Page 60-61.’, n.d.

[28] Gwenaël Fubiani, ‘“Modeling of the Negative Ion Source and Accelerator of the ITER Neutral Beam Injector.”Doctoral Thesis, University of Toulouse (Paul Sabatier),’ 2016.

[29] M Bacal, ‘Physics Aspects of Negative Ion Sources’, *Nuclear Fusion* 46, no. 6 (June 2006): S250–59, https://doi.org/10.1088/0029-5515/46/6/S05.

[30] S. Béchu et al., ‘Multi-Dipolar Microwave Plasmas and Their Application to Negative Ion Production’, *Physics of Plasmas* 20, no. 10 (October 2013): 101601, https://doi.org/10.1063/1.4823466.

[31] R. Middleton, ‘A Survey of Negative Ions from a Cesium Sputter Source’, *Nuclear Instruments and Methods* 144, no. 3 (August 1977): 373–99, https://doi.org/10.1016/0029-554X(77)90001-5.

[32] R. Middleton, ‘A Versatile High Intensity Negative Ion Source’, *Nuclear Instruments and Methods in Physics Research* 214, no. 2–3 (September 1983): 139–50, https://doi.org/10.1016/0167-5087(83)90580-X.

[33] Y. Takeiri et al., ‘Negative Hydrogen Ion Source Development for Large Helical Device Neutral Beam Injector (Invited)’, *Review of Scientific Instruments* 71, no. 2 (February 2000): 1225–30, https://doi.org/10.1063/1.1150433.

[34] Yu.I. Belchenko, G.I. Dimov, and V.G. Dudinkov, ‘A Powerful Injector of Neutrals with a Surface-Plasma Source of Negative Ions’, Nucl. Fusion 113 1974.

[35] C. F. A. van Os, P. W. van Amersfoort, and J. Los, ‘Negative Ion Formation at a Barium Surface Exposed to an Intense Positive-hydrogen Ion Beam’, *Journal of Applied Physics* 64, no. 8 (15 October 1988): 3863–73, https://doi.org/10.1063/1.341340.

[36] P. McNeely et al., ‘Development of a Rf Negative-Ion Source for ITER Neutral Beam Injection’, *Review of Scientific Instruments* 77, no. 3 (March 2006): 03A519, https://doi.org/10.1063/1.2166246.

[37] F. Gaboriau, R. Baude, and G. J. M. Hagelaar, ‘Experimental Evidence of the Increased Transport Due to the Wall Bounded Magnetic Drift in Low Temperature Plasma’, *Applied Physics Letters* 104, no. 21 (26 May 2014): 214107, https://doi.org/10.1063/1.4880717.

[38] P. Sonato et al., ‘Status of PRIMA, the Test Facility for ITER Neutral Beam Injectors’ (THIRD INTERNATIONAL SYMPOSIUM ON NEGATIVE IONS, BEAMS AND SOURCES (NIBS 2012), Jyväskylä, Finland, 2013), 549–58, https://doi.org/10.1063/1.4792827.

[39] R. Pasqualotto et al., ‘Diagnostics of the ITER Neutral Beam Test Facility’, *Review of Scientific Instruments* 83, no. 2 (February 2012): 02B103, https://doi.org/10.1063/1.3662017.

---

[40] S. Mochalskyy, A. F. Lifschitz, and T. Minea, ‘Extracted Current Saturation in Negative Ion Sources’, *Journal of Applied Physics* 111, no. 11 (June 2012): 113303, https://doi.org/10.1063/1.4727969.

[41] S. Mochalskyy, A.F. Lifschitz, and T. Minea, ‘3D Modelling of Negative Ion Extraction from a Negative Ion Source’, *Nuclear Fusion* 50, no. 10 (October 2010): 105011, https://doi.org/10.1088/0029-5515/50/10/105011.

[42] S. Mochalskyy et al., ‘Origin of Extracted Negative Ions by 3D PIC-MCC Modeling. Surface vs Volume Comparison’ (SECOND INTERNATIONAL SYMPOSIUM ON NEGATIVE IONS, BEAMS AND SOURCES, Takayama City, (Japan), 2011), 30–38, https://doi.org/10.1063/1.3637372.

[43] S. Mochalskyy, A. F. Lifschitz, and T. Minea, ‘“Modeling of the Negative Ions Extraction from a Hydrogen Plasma Source. Application to ITER Neutral Beam Injector”, 19th International Symposium on Plasma Chemistry (ISPC). Bochum,Germany, July 26-31, Conference Proceeding’, 2009.

[44] D. Todorov et al., ‘Spatial Distribution of the Plasma Parameters in a Radio-Frequency Driven Negative Ion Source’, *Review of Scientific Instruments* 85, no. 2 (February 2014): 02B104, https://doi.org/10.1063/1.4826540.

[45] U. Fantz, R. Gutser, and C. Wimmer, ‘Fundamental Experiments on Evaporation of Cesium in Ion Sources’, *Review of Scientific Instruments* 81, no. 2 (February 2010): 02B102, https://doi.org/10.1063/1.3258428.

[46] L Schiesko et al., ‘Caesium Influence on Plasma Parameters and Source Performance during Conditioning of the Prototype ITER Neutral Beam Injector Negative Ion Source’, *Plasma Physics and Controlled Fusion* 53, no. 8 (1 August 2011): 085029, https://doi.org/10.1088/0741-3335/53/8/085029.

[47] Gilles Cartry et al., ‘Alternative Solutions to Caesium in Negative-Ion Sources: A Study of Negative-Ion Surface Production on Diamond in H_2 /D_2 Plasmas’, *New Journal of Physics* 19, no. 2 (23 February 2017): 025010, https://doi.org/10.1088/1367-2630/aa5f1f.

[48] ‘Https://Www.Iter.Org/Fr/Sci/Iterandbeyond’, n.d.

[49] Ahmad Ahmad et al., ‘Negative-Ion Production on Carbon Materials in Hydrogen Plasma: Influence of the Carbon Hybridization State and the Hydrogen Content on H^- Yield’, *Journal of Physics D: Applied Physics* 47, no. 8 (26 February 2014): 085201, https://doi.org/10.1088/0022-3727/47/8/085201.

[50] R.W Boswell, ‘“Very Efficient Plasma Generation by Whistler Waves near the Lower Hybrid Frequency”, Plasma Physics and Controlled Fusion, Vol. 26, No. IO, Pp, 1147 to 1162, 198’, n.d.

[51] A Ahmad et al., ‘Negative-Ion Surface Production in Hydrogen Plasmas: Modeling of Negative-Ion Energy Distribution Functions and Comparison with Experiments’, *Plasma Sources Science and Technology* 22, no. 2 (18 February 2013): 025006, https://doi.org/10.1088/0963-0252/22/2/025006.

[52] P Kumar et al., ‘Enhanced Negative Ion Yields on Diamond Surfaces at Elevated Temperatures’, *Journal of Physics D: Applied Physics* 44, no. 37 (21 September 2011): 372002, https://doi.org/10.1088/0022-3727/44/37/372002.

[53] L Schiesko et al., ‘H^- Production on a Graphite Surface in a Hydrogen Plasma’, *Plasma Sources Science and Technology* 17, no. 3 (1 August 2008): 035023, https://doi.org/10.1088/0963-0252/17/3/035023.

[54] L Schiesko et al., ‘A Comparative Study of H^- and D^- Production on Graphite Surfaces in H_2 and D_2 Plasmas’, *Plasma Sources Science and Technology* 19, no. 4 (1 August 2010): 045016, https://doi.org/10.1088/0963-0252/19/4/045016.

---

[55] L. Schiesko et al., 'Negative Ion Surface Production through Sputtering in Hydrogen Plasma', *Applied Physics Letters* 95, no. 19 (9 November 2009): 191502, https://doi.org/10.1063/1.3258352.

[56] R.S. Hemsworth and T. Inoue, 'Positive and Negative Ion Sources for Magnetic Fusion', *IEEE Transactions on Plasma Science* 33, no. 6 (December 2005): 1799–1813, https://doi.org/10.1109/TPS.2005.860090.

[57] 'Http://Nanoprobes.Aist-Nt.Com/Apps/HOPG%20info.Htm', n.d.

[58] L. Diederich et al., 'Electron Affinity and Work Function of Differently Oriented and Doped Diamond Surfaces Determined by Photoelectron Spectroscopy', *Surface Science* 418, no. 1 (November 1998): 219–39, https://doi.org/10.1016/S0039-6028(98)00718-3.

[59] L Diederich et al., 'Electron Emission and NEA from Differently Terminated, Doped and Oriented Diamond Surfaces', *Diamond and Related Materials* 8, no. 2–5 (March 1999): 743–47, https://doi.org/10.1016/S0925-9635(98)00339-2.

[60] M Belhaj et al., 'The Effects of Incident Electron Current Density and Temperature on the Total Electron Emission Yield of Polycrystalline CVD Diamond', *Journal of Physics D: Applied Physics* 43, no. 13 (7 April 2010): 135303, https://doi.org/10.1088/0022-3727/43/13/135303.

[61] P Wurz, R Schletti, and M. R. Aeling, '"Hydrogen and Oxygen Negative Ion Production by Surface Ionization Using Diamond Surfaces", Surface Science 373 (1997) 56-66', n.d.

[62] F Silva et al., 'Microwave Engineering of Plasma-Assisted CVD Reactors for Diamond Deposition', *Journal of Physics: Condensed Matter* 21, no. 36 (9 September 2009): 364202, https://doi.org/10.1088/0953-8984/21/36/364202.

[63] A. Simonin et al., 'R&D around a Photoneutralizer-Based NBI System (Siphore) in View of a DEMO Tokamak Steady State Fusion Reactor', *Nuclear Fusion* 55, no. 12 (1 November 2015): 123020, https://doi.org/10.1088/0029-5515/55/12/123020.

[64] Katsuro Hayashi et al., '"Light-Induced Conversion of an Insulating Refractory Oxide into a Persistent Electronic Conductor", Nature Volume 419, Pages 462–465 (03 October 2002)', n.d.

[65] Hideo Hosono, 'Exploring Electro-Active Functionality of Transparent Oxide Materials', *Japanese Journal of Applied Physics* 52, no. 9R (1 September 2013): 090001, https://doi.org/10.7567/JJAP.52.090001.

[66] S. Matsuishi, 'High-Density Electron Anions in a Nanoporous Single Crystal: [Ca24Al28O64]4+(4e-)', *Science* 301, no. 5633 (1 August 2003): 626–29, https://doi.org/10.1126/science.1083842.

[67] M. Miyakawa et al., 'Fabrication of Highly Conductive 12CaO·7Al2O3 Thin Films Encaging Hydride Ions by Proton Implantation', *Advanced Materials* 15, no. 13 (4 July 2003): 1100–1103, https://doi.org/10.1002/adma.200304925.

[68] Y. Toda et al., 'Work Function of a Room-Temperature, Stable Electride [Ca24Al28O64]4+(E−)4', *Advanced Materials* 19, no. 21 (5 November 2007): 3564–69, https://doi.org/10.1002/adma.200700663.

[69] G J M Hagelaar et al., 'Modelling of a Dipolar Microwave Plasma Sustained by Electron Cyclotron Resonance', *Journal of Physics D: Applied Physics* 42, no. 19 (7 October 2009): 194019, https://doi.org/10.1088/0022-3727/42/19/194019.

[70] R. Janev and W. Langer, '"Elementary Processes in Hydrogen-Helium Plasmas: Cross Sections and Reaction Rate Coefficients", (Berlin: Spriger-Verlag)', 1987.

[71] J F Ziegler, J P Biersack, and M D Ziegler, '"SRIM—The Stopping and Range of Ions in Matter"(Morrisville, NC: Lulu Press),' 2008.

---

[72] G. Cartry et al., ‘Production of Negative Ions on Graphite Surface in H_2/D_2 Plasmas: Experiments and SRIM Calculations’, *Physics of Plasmas* 19, no. 6 (June 2012): 063503, https://doi.org/10.1063/1.4725188.

[73] J. P. J. Dubois et al., ‘Negative-Ion Surface Production in Hydrogen Plasmas: Determination of the Negative-Ion Energy and Angle Distribution Function Using Mass Spectrometry’, *Journal of Applied Physics* 119, no. 19 (21 May 2016): 193301, https://doi.org/10.1063/1.4948949.

[74] D Kogut et al., ‘Reconstruction of Energy and Angle Distribution Function of Surface-Emitted Negative Ions in Hydrogen Plasmas Using Mass Spectrometry’, *Plasma Sources Science and Technology* 26, no. 4 (7 March 2017): 045006, https://doi.org/10.1088/1361-6595/aa5d7b.

[75] ‘SIMION Website, Http://Simion.Com’, n.d.

[76] M. m. Bredov, I. G. Lang, and N. M. Okuneva, ‘Zh. Tekh. Fiz. 28, 252 (1958) Sov.Phys.-Tech. Phys. 3, 228 1958)’, n.d.

[77] H Goldstein, ‘Classical Mechanics, 2nd Ed. (Addison-Wesley, Reading 1980) Chap. 3’, n.d.

[78] W. Eckstein, ‘Computer Simulation of Ion Solid Interaction, Springer Ser.’, n.d.

[79] J Ziegler, J Biersack, and U. Littmark, ‘“The Stopping and Range of Ions in Solids”, Pergamon, New York,1985.’, n.d.

[80] J F Ziegler, M D Ziegler, and J P Biersack, ‘Nuclear Instruments and Methods in Physics Research B 268 (2010) 1818–1823.’, n.d.

[81] ‘Http://Www.Srim.Org/SRIM/SRIM%2008.Pdf’, n.d.

[82] J. P. Biersack and L. H. Haggmark, ‘Nucl. Instrum. Methods 174, 257 (1980)’, n.d.

[83] J. P. Biersack and W. Eckstein, ‘Appl. Phys. A 34, 73 (1984)’, n.d.

[84] W Jacob, ‘Surface Reactions during Growth and Erosion of Hydrocarbon Films’, *Thin Solid Films* 326, no. 1–2 (August 1998): 1–42, https://doi.org/10.1016/S0040-6090(98)00497-0.

[85] A. von Keudell, W. Mo¨ller, and R. Hytry, ‘Diamond Rel. Mater. 2 (1993) 251.’, n.d.

[86] A. von Keudell, W. Mo¨ller, and R. Hytry, ‘Appl. Phys. Lett. 62 (1993) 937.’, n.d.

[87] W. Jacob and M. Unger, ‘Experimental Determination of the Absorption Strength of C–H Vibrations for Infrared Analysis of Hydrogenated Carbon Films’, *Applied Physics Letters* 68, no. 4 (22 January 1996): 475–77, https://doi.org/10.1063/1.116418.

[88] A. von Keudell and W. Jacob, ‘Interaction of Hydrogen Plasmas with Hydrocarbon Films, Investigated by Infrared Spectroscopy Using an Optical Cavity Substrate’, *Journal of Vacuum Science & Technology A: Vacuum, Surfaces, and Films* 15, no. 2 (March 1997): 402–7, https://doi.org/10.1116/1.580498.

[89] A. Annen and W. Jacob, ‘Chemical Erosion of Amorphous Hydrogenated Boron Films’, *Applied Physics Letters* 71, no. 10 (8 September 1997): 1326–28, https://doi.org/10.1063/1.119885.

[90] R.M.A. Heeren et al., ‘Energetic “Self-Extracted” H- Ions in a Ba Surface Conversion Source’, *Applied Surface Science* 70–71 (June 1993): 332–36, https://doi.org/10.1016/0169-4332(93)90453-I.

[91] B.T. Kelly, ‘Physics of Graphite, Applied Science Publishers, London, 1981.’, n.d.

[92] ‘W. Moller, in: R.E. Clausing, L.L. Horton, J.C. Angus, P. Koidl (Eds.), Diamond and Diamond-Like Films and Coatings, NATOASI Series B: Physics, Vol. 266, Plenum Press, New York, 1991, p.229.’, n.d.

[93] Wolfhard Möller, ‘Modelling and Computer Simulation of Ion-Beam- and Plasma-Assisted Film Growth’, *Thin Solid Films* 228, no. 1–2 (May 1993): 319–25, https://doi.org/10.1016/0040-6090(93)90625-Y.

---

[94] P. Reinke, W. Jacob, and W. Möller, ‘Influence of the Ion Energy on the Growth and Structure of Thin Hydrocarbon Films’, *Journal of Applied Physics* 74, no. 2 (15 July 1993): 1354–61, https://doi.org/10.1063/1.354892.

[95] D. R. Lide, ‘CRC Handbook of Chemistry and Physics, 75th Ed., CRC Press, Boca Raton, FL, 1994.’, n.d.

[96] C. F. A. van Os, R. M. A. Heeren, and P. W. van Amersfoort, ‘Negative Ion Formation at a Barium Surface in Contact with a Hydrogen Plasma’, *Applied Physics Letters* 51, no. 19 (9 November 1987): 1495–97, https://doi.org/10.1063/1.98613.

[97] D. A. Dahl, ‘“SIMION for the Personal Computer in Reflection”, Int. J. Mass Spectrom. 200 (2000) 3–25.’, n.d.

[98] D. A. Dahl, ‘SIMION 3D v.7 User’s Manual, Idaho National Engineering and Environmental Laboratory, Idaho Falls, ID,2000.’, n.d.

[99] ‘American Mass Spectrometry Society, Http://Www.Asms.Org/Default.Aspx?Tabid=220 , Accessed February 04, 2008.’, n.d.

[100] I. V. Veryovkin, W. F. Calaway, and M. J. Pellin, ‘Nucl. Instrum.Methods Phys. Res. Sect.A Accel. Spectrom. Detect. Assoc. Equip. 519 (2004) 363.’, n.d.

[101] ‘Modélisation d’un Analyseur En Masse et En Énergie, Pasquet Timothée, Rapport Du Stage, Licence Physique Appliquée et Instrumentation, 2010.’, n.d.

[102] D. O’Connell et al., ‘Comparison of Measurements and Particle-in-Cell Simulations of Ion Energy Distribution Functions in a Capacitively Coupled Radio-Frequency Discharge’, *Physics of Plasmas* 14, no. 10 (October 2007): 103510, https://doi.org/10.1063/1.2795634.

[103] W. Eckstein and H M Urbassek, ‘2007 Sputtering by Particle Bombarment (Topicsin Applied Physics Vol 110) (Berlin:Springer)’, n.d.

[104] K. Achkasov et al., ‘Pulsed DC Bias for the Study of Negative-Ion Production on Surfaces of Insulating Materials in Low Pressure Hydrogen Plasmas, Submitted to Journal of Applied Physics’, n.d.

[105] A. Davydova et al., ‘H^+ Ion-Induced Damage and Etching of Multilayer Graphene in H_2 Plasmas’, *Journal of Applied Physics* 121, no. 13 (7 April 2017): 133301, https://doi.org/10.1063/1.4979023.

[106] A.R. Dunn, D.M. Duffy, and A.M. Stoneham, ‘A Molecular Dynamics Study of Diamond Exposed to Tritium Bombardment for Fusion Applications’, *Nuclear Instruments and Methods in Physics Research Section B: Beam Interactions with Materials and Atoms* 269, no. 14 (July 2011): 1724–26, https://doi.org/10.1016/j.nimb.2010.12.009.

[107] D de Rooij, ‘Molecular Dynamics Simulations of Interactions between Hydrogen and Fusion-Relevant Materials (Utrecht University)’, n.d.

[108] D. Kogut et al., ‘Single-Crystal and Polycrystalline Diamond Erosion Studies in Pilot-PSI’, *Journal of Nuclear Materials* 500 (March 2018): 110–18, https://doi.org/10.1016/j.jnucmat.2017.12.028.

[109] Y. Yamazaki et al., ‘Structure of Diamond Surface Defective Layer Damaged by Hydrogen Ion Beam Exposure’, *Diamond and Related Materials* 15, no. 4–8 (April 2006): 703–6, https://doi.org/10.1016/j.diamond.2005.12.021.

[110] V Martirosyan, ‘Atomistic Simulations of H2 and He Plasmas Modification of Thin-Films Materials for Advanced Etch Processes (Grenoble Alpes University)’, n.d.

[111] V Šamara et al., ‘A Dc-Pulsed Capacitively Coupled Planar Langmuir Probe for Plasma Process Diagnostics and Monitoring’, *Plasma Sources Science and Technology* 21, no. 6 (1 December 2012): 065004, https://doi.org/10.1088/0963-0252/21/6/065004.

---

[112] S.-B. Wang and A. E. Wendt, 'Control of Ion Energy Distribution at Substrates during Plasma Processing', *Journal of Applied Physics* 88, no. 2 (15 July 2000): 643–46, https://doi.org/10.1063/1.373715.

[113] P. Kudlacek, R. F. Rumphorst, and M. C. M. van de Sanden, 'Accurate Control of Ion Bombardment in Remote Plasmas Using Pulse-Shaped Biasing', *Journal of Applied Physics* 106, no. 7 (October 2009): 073303, https://doi.org/10.1063/1.3225690.

[114] Edward Barnat and T.-M. Lu, 'Pulsed Bias Magnetron Sputtering of Thin Films on Insulators', *Journal of Vacuum Science & Technology A: Vacuum, Surfaces, and Films* 17, no. 6 (November 1999): 3322–26, https://doi.org/10.1116/1.582060.

[115] K Achkasov, 'Study of Negative Ion Surface Production in Cesium-Free H2 and D2 Plasmas Application to Neutral Beam Injectors for ITER and DEMO (Doctoral Thesis), Chapter of Pulsed Bias Approach p.157', n.d.

[116] Mamiko Sasao et al., 'Negative-Hydrogen-Ion Production from a Nanoporous 12CaO · 7Al $_2$ O $_3$ Electride Surface', *Applied Physics Express* 11, no. 6 (1 June 2018): 066201, https://doi.org/10.7567/APEX.11.066201.

[117] M. Wada, R. V. Pyle, and J. W. Stearns, 'Dependence of H $^-$ Production upon the Work Function of a Mo Surface in a Cesiated Hydrogen Discharge', *Journal of Applied Physics* 67, no. 10 (15 May 1990): 6334–39, https://doi.org/10.1063/1.345153.

[118] M. Sasao et al., 'Negative Ion Formation from a Low-Work-Function Nanoporous Inorganic Electride Surface' (FIFTH INTERNATIONAL SYMPOSIUM ON NEGATIVE IONS, BEAMS AND SOURCES (NIBS 2016), Oxford, United Kingdom, 2017), 020005, https://doi.org/10.1063/1.4995711.